

Evaluation of Electrolyte Challenges, Anode Surface Modification, and Current Collector Stability for Aluminum Batteries

Zur Erlangung des akademischen Grades eines
DOKTORS DER NATURWISSENSCHAFTEN

(Dr. rer. nat.)

von der KIT-Fakultät für Chemie und Biowissenschaften des
Karlsruher Instituts für Technologie (KIT)
genehmigte

DISSERTATION

von

Frau M.Sc. Fatemehsadat Rahide

Referent: Prof. Dr. rer. nat. Helmut Ehrenberg

Korreferentin: Prof. Dr. rer. nat. Sonia Dsoke

Tag der mündlichen Prüfung: 15.12.2023

ABSTRACT

Aluminum batteries (AlBs) hold promise as a sustainable energy storage substitute for Lithium-ion batteries (LiBs). Among potential alternatives to Lithium, Al stands out due to its abundance and theoretical capacity. However, practical implementation has been impeded by the corrosive nature of electrolytes required for effective Al plating and stripping. This thesis has illustrated the use of aluminum trifluoromethanesulfonate ($\text{Al}(\text{OTF})_3$) as a non-corrosive substitute for Al chloride (AlCl_3) in the electrolyte, with urea and N-methylacetamide (NMA) or ethyl-Isopropyl-Sulfone (EiPS) solvents. Our electrochemical investigation of $\text{Al}(\text{OTF})_3$ -based electrolytes reveals unforeseen challenges. Reversibility of Al redox reactions is hindered when utilizing these non-corrosive electrolytes, particularly on substrates *e.g.*, Al, molybdenum (Mo), titan (Ti) other than platinum (Pt) or copper (Cu). This unearths complexities in the practical application of $\text{Al}(\text{OTF})_3$ electrolytes for Al plating and stripping, which are vital processes for battery function. Conventional electrolyte, which is able to eliminate the Al_2O_3 oxide passivation film for effective plating and stripping, pose stability issues within AlBs. To mitigate this, the non-corrosive NMA-based electrolyte has been investigated. While this electrolyte avoids corrosiveness, it struggles with Al plating and stripping due to the inability to remove the Al_2O_3 oxide passivation film. Surface modifications to the Al electrode do not yield the possibility of Al plating and stripping, underscoring the intricate role of the electrolyte and electrode surface in interphase layer formation, which directly affects the success of Al plating and stripping. The presence of an amorphous Al_2O_3 oxide passivation film on Al substrates has been a persistent challenge, impeding cyclic performance by acting as an electron/ion insulator. This study reveals that the two sides of Al foils (optically seen as shiny and non-shiny) possess distinct surface properties. The non-shiny side, with higher surface roughness (S_a), exhibits enhanced Al plating and stripping due to increased active sites. Al surface immersion pretreatment (treatment) involving an $[\text{EMImCl}]/\text{AlCl}_3$ as AlCl_3 -based electrolyte leads to a modified interphase layer rich in Al, Cl, and N, thereby facilitating improved Al diffusion during plating and stripping. Extended cycling (500 cycles) of Al foils highlights issues such as dendritic Al deposition, active site appearance, and localized corrosion, impacting the mechanical attributes of the cycled foil. The interplay between treatment, foil surface characteristics, and interphase layer formation is crucial for the feasibility

and reversibility of Al plating/stripping. This comprehensive exploration delves into the intricate relationship between electrolyte composition, electrode surface properties, and electrode-electrolyte interphase formation, unravelling the complex mechanisms that dictate the success of Al plating and stripping processes. These insights emphasize the importance of optimizing electrolyte formulations and surface engineering strategies to unlock the full potential of AIBs for future energy storage applications. In addition, the stability of different metallic current collectors (CCs) in an AlCl_3 -based ILE for AIBs is evaluated herein. The study involves immersion tests of Ni, Ti, Mo, Ta, and W foils in the electrolyte, followed by surface analysis using scanning electron microscope (SEM) and energy-dispersive X-ray spectroscopy (EDX). Linear sweep voltammetry (LSV) and cyclic voltammetry (CV) techniques are used to assess their electrochemical behavior, revealing varying corrosion susceptibility. Ni and Ti foils react significantly with AlCl_3 -based ILE, leading to corrosion, while Mo and W foils also exhibit reactivity. In contrast, Ta foils resist corrosion. XPS analysis shows oxide layers on pristine metal samples, while CCs display residues of nitrogen, aluminum, and chlorine from cycling. Ni CCs show features consistent with NiCl_2 , indicating potential corrosion. Moreover, Mo and W rods were evaluated as CCs in Swagelok cell setups using an AlCl_3 -based ILE. CV experiments unexpectedly showed reactivity of the Mo substrate with the electrolyte, resulting in oxidative and reduction peaks in the CV data. This reaction was attributed to interactions between Mo and aluminum chloride complexes. Consequently, Mo rod (with 99.97% purity and specified impurities as mentioned) is not recommended as CCs/CE in Swagelok cells.

Zusammenfassung

Aluminiumbatterien (AlBs) sind ein vielversprechender Ersatz für Lithium-Ionen-Batterien (LiBs) als nachhaltige Energiespeicher. Unter den potenziellen Alternativen zu Lithium sticht Aluminium aufgrund seines Vorkommens und seiner theoretischen Kapazität hervor. Die praktische Umsetzung wurde jedoch durch die korrosive Natur der Elektrolyte behindert, die für eine effektive Al-Beschichtung und Ablösung erforderlich sind. In dieser Arbeit wurde die Verwendung von Aluminiumtrifluormethansulfonat ($\text{Al}(\text{OTF})_3$) als nicht korrosiver Ersatz für Al-Chlorid (AlCl_3) im Elektrolyten mit Harnstoff und N-Methylacetamid (NMA) oder Ethyl-Isopropyl-Sulfon (EiPS) als Lösungsmittel untersucht. Unsere elektrochemische Untersuchung von Elektrolyten auf $\text{Al}(\text{OTF})_3$ -Basis zeigt unvorhergesehene Herausforderungen. Die Reversibilität von Al-Redoxreaktionen wird bei der Verwendung dieser nicht korrosiven Elektrolyte behindert, insbesondere auf Substraten wie Al, Molybdän (Mo), Titan (Ti) und nicht Platin (Pt) oder Kupfer (Cu). Dies führt zu Schwierigkeiten bei der praktischen Anwendung von $\text{Al}(\text{OTF})_3$ -Elektrolyten für die Al-Beschichtung und das Strippen, die für die Funktion der Batterie entscheidend sind. Herkömmliche Elektrolyte, die in der Lage sind, die Al_2O_3 -Oxidpassivierungsschicht für eine effektive Beschichtung und Ablösung zu beseitigen, werfen Stabilitätsprobleme in AlBs auf. Um dies zu entschärfen, wurde der nicht korrosive Elektrolyt auf NMA-Basis untersucht. Dieser Elektrolyt ist zwar nicht korrosiv, hat aber Probleme mit der Al-Beschichtung und dem Strippen, da er die Al_2O_3 -Oxid-Passivierungsschicht nicht entfernen kann. Oberflächenveränderungen an der Al-Elektrode führen nicht zur Möglichkeit der Al-Abscheidung und des Strippings, was die komplizierte Rolle des Elektrolyten und der Elektrodenoberfläche bei der Bildung der Interphasenschicht unterstreicht, die sich direkt auf den Erfolg der Al-Abscheidung und des Strippings auswirkt. Das Vorhandensein eines amorphen Al_2O_3 -Oxid-Passivierungsfilms auf Al-Substraten ist ein anhaltendes Problem, das die zyklische Leistung behindert, da es als Elektronen/Ionen-Isolator wirkt. Diese Studie zeigt, dass die beiden Seiten von Al-Folien (optisch gesehen als glänzend und nicht glänzend) unterschiedliche Oberflächeneigenschaften aufweisen. Die nicht glänzende Seite mit höherer Oberflächenrauigkeit (S_a) weist eine verbesserte Al-Beschichtung und Ablösung auf, da sie mehr aktive Stellen aufweist. Die Vorbehandlung der Al-Oberfläche durch Eintauchen in einen $[\text{EMImCl}]/\text{AlCl}_3$ -Elektrolyten auf AlCl_3 -Basis führt zu einer

modifizierten Interphasenschicht mit hohem Al-, Cl- und N-Gehalt, wodurch die Al-Diffusion während der Abscheidung und des Strippings verbessert wird. Eine längere Zyklusdauer (500 Zyklen) von Al-Folien zeigt Probleme wie dendritische Al-Ablagerungen, das Auftreten aktiver Stellen und lokale Korrosion, die sich auf die mechanischen Eigenschaften der zyklierten Folie auswirken. Das Zusammenspiel zwischen der Behandlung, den Oberflächeneigenschaften der Folie und der Bildung von Zwischenschichten ist entscheidend für die Durchführbarkeit und Reversibilität der Al-Beschichtung/des Abbeizens. Diese umfassende Untersuchung befasst sich mit der komplizierten Beziehung zwischen der Elektrolytzusammensetzung, den Eigenschaften der Elektrodenoberfläche und der Bildung von Elektroden-Elektrolyt-Zwischenschichten und entschlüsselt die komplexen Mechanismen, die für den Erfolg von Al-Beschichtungs- und Abbeizprozessen entscheidend sind. Diese Erkenntnisse unterstreichen, wie wichtig es ist, die Elektrolytformulierungen und die Strategien der Oberflächentechnik zu optimieren, um das volle Potenzial von AIBs für zukünftige Energiespeicheranwendungen zu erschließen. Darüber hinaus wird hier die Stabilität verschiedener metallischer Stromkollektoren (CCs) in einer AlCl_3 -basierten ILE für AIBs bewertet. Die Studie umfasst Immersionstests von Ni, Ti, Mo, Ta und W-Folien im Elektrolyten, gefolgt von einer Oberflächenanalyse mittels Rasterelektronenmikroskop (SEM) und energiedispersiver Röntgenspektroskopie (EDX). Das elektrochemische Verhalten der Folien wird mit Linear Sweep Voltammetry (LSV) und Cyclic Voltammetry (CV) untersucht, wobei sich eine unterschiedliche Korrosionsanfälligkeit zeigt. Ni- und Ti-Folien reagieren deutlich mit AlCl_3 -basierter ILE, was zu Korrosion führt, während Mo- und W-Folien ebenfalls eine Reaktivität aufweisen. Im Gegensatz dazu sind Ta-Folien korrosionsbeständig. Die XPS-Analyse zeigt Oxidschichten auf unbehandelten Metallproben, während CCs Rückstände von Stickstoff, Aluminium und Chlor aus dem Zyklus aufweisen. Ni-CCs weisen Merkmale auf, die mit NiCl_2 übereinstimmen und auf eine mögliche Korrosion hinweisen. Darüber hinaus wurden Mo- und W-Stäbe als CCs in Swagelok-Zellaufbauten unter Verwendung einer AlCl_3 -basierten ILE bewertet. CV-Experimente zeigten unerwartet eine Reaktivität des Mo-Substrats mit dem Elektrolyten, was zu oxidativen und reduzierenden Spitzen in den CV-Daten führte. Diese Reaktion wurde auf Wechselwirkungen zwischen Mo und Aluminiumchloridkomplexen zurückgeführt. Daher werden Mo-Stäbe nicht als CCs/CE in Swagelok-Zellen empfohlen.

Acknowledgment

After more than three years of studying literature, identifying issues and bottlenecks in aluminum battery progress, finding solutions for challenges, countless attempts and efforts devoted to cell assembling and data analysis, and writing manuscripts, it's time to express my gratitude to those who have influenced my personal and scientific journey.

Foremost, my supervisor Prof. Helmut Ehrenberg deserves credit for guiding me through this thesis. His support, patience, and encouragement were invaluable during my PhD.

I'm thankful to Prof. Sonia Dsoke, my scientific advisor, for her insightful input on improving my findings and projects.

During my abroad research visit (August-October 2022 and May-July 2023) at the Department of Mechanical, Materials & Aerospace Engineering, University of Liverpool, United Kingdom. I was kindly hosted by Prof. B. Layla Mehdi. It really was a magnificent experience to get trained and educated on the transmission electron microscope (TEM) by Dr. Mounib Bahri. Working and delving into the TEM with Dr. Xiaodong was such a valuable experience.

I would like to thank Prof. Magda Titirici for her nice hospitality during my collaborative visiting research (May-June 2023) at the Faculty of Engineering, Department of Chemical Engineering at Imperial College London, United Kingdom. Getting skilled in such a high-tech battery technology laboratory was a big honour and opportunity for me.

Thanks to Prof. Helge Stein and Prof. Christine Kranz for providing access to conduct XPS and AFM analysis on my samples. I thank Dr. Angelina Sarapulova for the enlightening advices on my PhD journey. A very special thank you to Almut Kriese for her patience, kindness, and support which makes official bureaucracy easier for me. I extend special thanks to the present and past member of the institute, Dr. Michael Knapp, Dr. Anna-Lena Hansen, Dr. Sylvio Indris, Liuda Mereacre, Heinz-Robert Goebel, Julian Hansen, Philip Richter, Udo Geckle, and Luis Martin Sanchez Neudeck.

I'm indebted to Ali Dashti for his support, encouraging me at all times, especially in those disappointing and stressful moments of my PhD, and making life abroad easier for me. My special gratitude goes to my parents and sisters for teaching me, supporting me even from a far distance, and making every bit of my life unique. They have always been a supportive voice of reason for all of my decisions that remain so to this day.

In closing, my heartfelt appreciation to everyone who played a role in this journey.

Publications

1. **F. Rahide**, E. Zemlyanushin, G.-M. Bosch, and S. Dsoke, "Open Challenges on Aluminum Triflate-Based Electrolytes for Aluminum Batteries," *J Electrochem Soc*, vol. 170, no. 3, p. 030546, Mar. 2023, doi: 10.1149/1945-7111/acc762.[1]
2. **F. Rahide**, et al., "Hindered aluminum plating and stripping in urea/NMA/Al(OTf)₃ as a Cl-free electrolyte for Al batteries", *J Electrochem Soc*, Dec. 2023, doi: 10.1149/1945-7111/ad1553. [2]
3. **F. Rahide**, K. Palanisamy, J. K. Flowers, J. Hao, H. S. Stein, C. Kranz, H. Ehrenberg, S. Dsoke, "Modification of Al surface via acidic treatment and its impact on plating and stripping", *ChemSusChem*, Oct. 2023, doi: 10.1002/cssc.202301142.[3]
4. **F. Rahide**, M. Guidat, M. Löw, J. Kim, M.M. May, H. Ehrenberg, S. Dsoke, "In Situ Monitoring of the Al(110)-[EMImCl]:AlCl₃ Interface by Reflection Anisotropy Spectroscopy," *Batter Supercaps*, Oct. 2023, doi: 10.1002/batt.202300394.[4]
5. N. Sabi, K. Palanisamy, **F. Rahide**, S. Daboss, C. Kranz, S. Dsoke, "Surface Properties-Performance Relationship of Aluminum Foil as Negative Electrode for Rechargeable Aluminum Batteries," *Batter Supercaps*, Sep. 2023, doi: 10.1002/batt.202300298.[5]

Conference participations, presentations and posters

F. Rahide, E. Zemlyanushin, and S. Dsoke, 2021. On the way towards non-corrosive electrolytes for aluminum batteries, the 72nd ISE annual meeting organized by International Society of Electrochemistry.

F. Rahide, 2021. On the way towards non-corrosive electrolytes for aluminum batteries, new generation – Batteries and talents symposium organized by post lithium storage cluster of excellent.

F. Rahide, J. Hao, and S. Dsoke, 2022. Investigation and study of the aluminum anode surface using different Treatments, the 32nd ISE topical meeting organized by the International Society of Electrochemistry.

F. Rahide, M. Guidat, M.M. May, and S. Dsoke, 2022. Investigation of electrochemical and optical properties of Al(110)-electrolyte interface by Reflection Anisotropy Spectroscopy, ISE regional meeting organized by the International Society of Electrochemistry.

F. Rahide, 2022. Investigation and study of different electrode materials in different electrolytes for AlBs, Internal aluminum symposium organized by Institute of Applied Material- Energy Storage System.

F. Rahide, E. Zemlyanushin, G.-M. Bosch, and S. Dsoke, 2022. Open challenges on Aluminum Triflate-based electrolytes for Aluminum batteries, POLIS Conclave Meeting organized by post lithium storage cluster of excellent.

Faraday Institution ECR Conference, 2022, University of Warwick, United Kingdom.

Microscience Microscopy Congress, 2023, Manchester, United Kingdom.

F. Rahide, J. K. Flowers, J. Hao, H. S. Stein, H. Ehrenberg, S. Dsoke, 2023. Hindered aluminum plating and stripping in urea/NMA/Al(OTF)₃ as a Cl-free electrolyte for Al batteries, ISE annual Meeting organized by the International Society of Electrochemistry.

Declaration of collaborations

All the collaborative projects during this PhD, not presented in this PhD thesis, are as follows:

1. *In-situ* Monitoring of the Al(110)-[EMImCl]:AlCl₃ Interface by Reflection Anisotropy Spectroscopy was carried out in collaboration with Margot Guidat, Mario Löw, and Jongmin Kim in the laboratory supervised by Dr. Mathias M. May at Ulm University, and Tübingen University, Germany. 2022-2023 [4].
2. Operando Raman spectroscopy of Aluminum Graphite Dual-Ion Batteries, was carried out in collaboration with Anastasia Teck in the laboratory supervised by Prof. Magda Titirici at Imperial College London, United Kingdom. 2023.
3. Transmission electron microscopy (TEM) of the Aluminum dendrites in Aluminum batteries was carried out in collaboration with Dr. Mounib Bahri, and Dr. Xiaodong Liu, in the laboratory supervised by Prof. Layla B. Mehdi at the University of Liverpool, United Kingdom. 2023.
4. *In-situ* Analytical Techniques: Solid Electrolyte Interphase Analysis of Al Anode Materials was carried out in collaboration with Krishnaveni Palanisamy, in the laboratory supervised by Prof. Christine Kranz at Ulm University, Germany. 2022.
5. *In-situ* TEM of Zn-air Batteries was carried out in collaboration with Dr. Mounib Bahri, and Dr. Xiaodong Liu, in the laboratory supervised by Prof. Layla B. Mehdi at the University of Liverpool, United Kingdom. 2023.

The majority of the experimental work included in this thesis was completed by the author alone. Some of the measurements and analysis were reached in association with other scientists and people. A detailed description of the collaborations is presented as follows.

In Chapter 3: The coupled Thermogravimetric Analysis (TGA) and Fourier transform infrared (FTIR) spectroscopy measurement of the prepared Al(OTF)₃- based electrolytes done by Liuda Mereacre and interpreted with the scientific help of George Bosch from Karlsruhe Institute of the Technology. The *ex-situ* X-ray photoelectron Spectroscopy (XPS) of the Al, Pt electrodes has been measured and interpreted by Jackson K. Flowers from the Institute of Physical Chemistry (IPC), and Karlsruhe Institute of Technology (KIT).

In Chapter 4: The *ex-situ* XPS of the surface modified and cycled Al foils have been measured and interpreted by Jackson K. Flowers from Institute of Physical Chemistry (IPC), and Karlsruhe Institute of Technology (KIT). Furthermore, atomic force microscopy (AFM) of the surface modified and cycled Al foils has been done and interpreted by Krishnaveni Palanisamy from the Institute of Analytical and Bioanalytical Chemistry, Ulm University.

In Chapter 5: The *ex-situ* XPS analysis of pristine and cycled current collectors (CCs) have been measured and interpreted by Jackson K. Flowers from the Institute of Physical Chemistry (IPC), and Karlsruhe Institute of Technology (KIT).

List of Acronyms

1W	1 week
1M	1 month
Al	aluminum
AlBs	aluminum batteries
AlCl ₃	aluminum chloride
Al-NSH	non-shiny side of Al foil
Al-SH	shiny side of Al foil
Al-NSH-6h	non-shiny Al foil after immersion pretreated for 6 hours
Al-NSH-18h	non-shiny Al foil after immersion pretreated for 18 hours
ACN	acetonitrile
AlCl ₄ ⁻	tetrachloroaluminate
Al ₂ Cl ₇ ⁻	heptachlorodialuminate
AlCl ₃ -based E	[EMImCl]/AlCl ₃ electrolyte
AFM	atomic force microscopy
Al(OTF) ₃	aluminum trifluoromethanesulfonate
Al(OTF) ₃ - based urea/EiPS/Al(OTF) ₃ and urea/NMA/Al(OTF) ₃	electrolyte
Al(TFSI) ₃	aluminum bis(trifluoromethanesulfonyl)imide
Ag	silver
Ag quasi-RE	silver wire quasi-reference electrode
Al quasi-RE	aluminum wire quasi-reference electrode
Ar	argon
AT	atomic percentage of an element (atomic [%])
Au	gold
[BMIM]OTF	1-Butyl-3-methylimidazolium trifluoromethanesulfonate
CA	chronoamperometry
CE	counter electrode
Cl	chlorine
CV	cyclic voltammetry

Cu	copper
(CH ₃) ₂ SO ₂	dimethyl sulfone
DMC	dimethyl carbonate
EMImCl	1-Ethyl-3-methylimidazolium chloride
EDX	energy-dispersive X-ray spectroscopy
EiPS	ethyl-Isopropyl-Sulfone
EiPS-based E	urea/EiPS/Al(OTF) ₃ electrolyte
EIS	impedance spectroscopy
EtOH	ethanol
Fe	iron
FIB	focused ion beam
FT-IR	fourier-transform infrared spectroscopy
FWHM	Full-width, half-max
GC	glassy Carbon
GNP	graphene nanoplatelets
h	hours
HER	hydrogen evolution reaction
SHE	standard hydrogen electrode
IFFT	Inverse Fast Fourier Transform
ILE	ionic liquid electrolyte
iPsBs	isopropyl-s-butyl sulfone
Li	lithium
LIBs	lithium-ion batteries
LSV	linear sweep voltammetry
MeOH	methanol
Mo	molybdenum
M-Al	surface-modified (<i>i.e.</i> immersion pretreated) Al
N	nitrogen
Ni	nickel
NMA	N-methyl acetamide

NMA-based E	urea/NMA/Al(OTF) ₃ electrolyte
NT	non-pretreated
NT-Al-NSH	non-shiny side of non-pretreated Al foil
NT-Al-SH	shiny side of non-pretreated Al foil
Pt	platinum
quasi-RE	quasi-reference electrode
RE	reference electrode
RT	room temperature
RTILEs	room-temperature ionic liquid electrolytes
S _a	surface roughness
SA	sodium alginate
SEI	solid electrolyte interphase
SEM	scanning electron microscope
Si	silicon
SPM	scanning probe microscopy
SS	stainless steel
TEM	transmission electron microscope
THF	tetrahydrofuran
TGA	thermogravimetric analysis
Ta	tantalum
Ti	titan
TiN	Titanium nitride
TSC-SC	TSC surface cell
TSC1600-CC	TSC 1600 closed cell
treatment	immersion pretreatment
treated	immersion pretreated
vs.	<i>versus</i>
W	tungsten
WE	working electrode
WT	weight percentage of an element (weight [%])

XPS

x-ray photoelectron spectroscopy

List of Figures

Figure 1-1. A Schematic of the state-of-the-art AIBs.	3
Figure 1-2. A schematic of the overall motivation of this PhD study.	4
Figure 1-3. A schematic of the main specific objectives of this PhD research study.	5
Figure 3-1. (a) Arrhenius plots of the ionic conductivity σ and viscosity η (b) Density ρ in the 20–80°C	30
Figure 3-2. TGA of (a) the pure chemicals and (b) the two electrolyte mixtures. C, and d) DSC and TGA curves of NMA and EiPS.	32
Figure 3-3. FT-IR spectra of the pure substances and the two electrolyte mixtures in the range for (a) N-H vibration bands for the two electrolyte compositions and (b) S=O vibration bands for the EiPS-based E.	34
Figure 3-4. (a) Recorded CVs with the scan rate of 20 mV s ⁻¹ on a Pt disc as a WE and Al quasi-RE in NMA-based E. Ferrocene as an internal RE (b) Al quasi-RE(c) Ag quasi-RE. TSC1600-CC with a Pt as a CE.	35
Figure 3-5. Recorded LSV for AlCl ₃ -free electrolytes at 25°C in TSC1600-CC recorded on a) a GC disc at the scan rate of 10 mV s ⁻¹ and b) a Pt disc at the scan rate of 5 mV s ⁻¹ with Ag quasi-RE and Pt CE.	36
Figure 3-6. Recorded CV on a Pt disc in TSC1600-CC in (a) NMA-based E (b) EiPS-based E. (c) EiPS-based E and EiPS/Al(OTF) ₃ with Ag quasi-RE and Pt CE.	37
Figure 3-7. Recorded CV on a Pt foil as WE vs. Ag quasi-RE in TSC-SC with GC CE. And oxidation and reduction capacities, and Coulombic efficiency at 20 mV s ⁻¹ in (a), and (b) NMA-based E. (c) and (d) in EiPS-based E in TSC1600-CC with Ag quasi-RE and Pt CE.	38
Figure 3-8. Recorded CVs on a Pt disc as WE vs. Ag quasi-RE in TSC1600-CC with Pt CE, oxidation and reduction capacity, and Coulombic efficiency at 20 mV s ⁻¹ (a-b-c) in NMA-based E at two potential windows -1.5 to 0.7 V and -1 to 0.7 V (d-e-f) in EiPS-based E at two potential windows -1.5 to 0.5 V and -1.8 to 0.5 V.	40
Figure 3-9. Recorded CVs on a Pt disc as WE vs. Ag quasi-RE in TSC1600-CC with Pt CE, oxidation and reduction capacity, and Coulombic efficiency at 20 mV s ⁻¹ (a-b-c) in NMA-based E at two	

potential windows -1.5 to 0.7 V and -1 to 0.7 V (d-e-f) in EiPS-based E at two potential windows -1.5 to 0.5 V and -1.8 to 0.5 V.	41
Figure 3-10. Recorded CVs on a Pt WE vs. Ag quasi-RE in TSC1600-CC with Pt CE, at the temperature range of 20 to 50°C (a-b) in NMA-based E, and (c-d) in EiPS-based E. b and d are a magnification of a and c.	43
Figure 3-11. (a) Recorded CVs on a Pt WE vs. Ag quasi-RE in TSC1600-CC with Pt CE, at 20 and 30°, (b-c) oxidation and reduction capacity, and Coulombic efficiency at 20 mV s ⁻¹ in NMA-based E.	43
Figure 3-12. (a) Recorded CVs on a Pt WE vs. Ag quasi-RE in TSC1600-CC with Pt CE, at 20 and 30°, (b-c) oxidation and reduction capacity, and Coulombic efficiency at 20 mV s ⁻¹ in EiPS-based E.	44
Figure 3-13. Recorded CVs on Pt, GC, Ti, Mo, Cu and Al WE vs. Ag quasi-RE in TSC-SC with GC CE in (a,c,d) NMA-based E, and (b) EiPS-based E.	46
Figure 3-14. Recorded CVs with a scan rate of 20 mV s ⁻¹ on pristine Al WE in TSC-SC with GC CE in (a) Al(OTF) ₃ -based vs. Ag quasi-RE and (b) AlCl ₃ -based E vs. Al quasi-RE (c) CVs comparison. (d) on M-Al foil in Al(OTF) ₃ -based vs. Ag quasi-RE.	51
Figure 3-15. SEM images and EDX images and spectra of (a) pristine, (b) cycled Al foil, and (d) M-Al in NMA-based E.	52
Figure 3-16. Recorded CAs at -1 V, corresponding to Al deposition on Pt electrode from (a) AlCl ₃ -based E with Al quasi-RE and on (b) Pt (c) Al electrode from NMA-based E with A quasi-RE.	53
Figure 3-17. XPS fine spectra with peak assignments for Pt foil after Al electrodeposition from AlCl ₃ -based E.	57
Figure 3-18. XPS fine spectra with peak assignments for Al electrode after applied CA technique in NMA-based E.	58
Figure 3-19. XPS fine spectra with peak assignments for Pt electrode after applied CA technique in NMA-based E.	59
Figure 4-1. SEM images and corresponding EDX results and observed elements on the surface of the pristine (a-b) Al-NSH and (c-d) Al-SH.	65

Figure 4-2. (a) AFM surface topography of the pristine Al-NSH and Al-SH recorded in Ar atmosphere. (b) Bar graph of mean S_a values for Al-NSH and Al-SH.	66
Figure 4-3. CVs recorded on (a) NT-Al-SH and NT-Al-NSH and (b - c) Al-NSH-6h and Al-NSH-18h in $AlCl_3$ -based E. (d) The Al plating/stripping capacity of the NT-Al-NSH and Al-NSH-18h.	68
Figure 4-4. SEM images of the cycled (a) NT-Al-NSH and (b) NT-Al-SH.	69
Figure 4-5. SEM images of (a) Al-NSH-6h (b) Al-SH-6h (c) Al-NSH-18h (d) Al-SH-18h after treatment in $AlCl_3$ -based E.	70
Figure 4-6. EDX results and observed elements on the surface of (a) Al-NSH-6h (b) Al-SH-6h (c) Al-NSH-18h (d) Al-SH-18h after treatment in $AlCl_3$ -based E.	71
Figure 4-7. AFM topographic images of (a) Al-NSH-6h and Al-NSH-18h, (b) Al-SH-6h and Al-SH-18h after treatment in $AlCl_3$ -based E. (c) Bar graph of mean S_a values comparison with respect to S_a : before and after cycling.	73
Figure 4-8. SEM images of cycled (a) Al-NSH-6h, and (b) Al-NSH-18h.	73
Figure 4-9. XPS fine spectra with peak assignments for pristine Al-NSH and Al-NSH-18h. $Cl2p$ and $N1s$ were taken only for Al-NSH-18h.	75
Figure 4-10. (a) AFM topography images of cycled NT-Al-NSH, Al-NSH-6h, Al-NSH-18h, (b) Bar graph of mean S_a values comparison with respect to S_a .	77
Figure 4-11. 500-cycled recorded CV on NT-Al-NSH in $AlCl_3$ -based E. (b) corresponding SEM and (c) EDX result and observed elements.	79
Figure 4-12. (a) AFM topographic images of the 500-cycled NT-Al-NSH. (b) Bar graph of mean S_a values.	79
Figure 4-13. (a) Nanomechanical properties, and (b) Nanomechanical characterization (recorded image of height, adhesion force, deformation and Young's modulus. Scale = $5 \times 5 \mu m^2$.) of pristine and cycled Al in $AlCl_3$ -based E.	81
Figure 5-1. SEM images of the pristine and immersed (a)Ni (b)Ti (c)Mo (d)W (e)Ta metallic CCs.	89
Figure 5-2. EDX images and spectra of the pristine and immersed Ni foils in $AlCl_3$ -based ILE.	90
Figure 5-3. EDX images and spectra of the pristine and immersed Ti foils in $AlCl_3$ -based ILE.	91
Figure 5-4. EDX images and spectra of the pristine and immersed Mo foils in $AlCl_3$ -based ILE.	92
Figure 5-5. EDX images and spectra of the pristine and immersed W foils in $AlCl_3$ -based ILE.	93
Figure 5-6. EDX images and spectra of the pristine and immersed Ta foils in $AlCl_3$ -based ILE.	94

Figure 5-7. Recorded LSV on Ni, Ti, Mo, W, Ta foil in AlCl ₃ -based ILE in TSC-SC Al quasi-RE and GC CE.	96
Figure 5-8. Recorded CVs on (a)Ni, (b)Ti, (c)Mo, (d) W (e)Ta (f) CV comparison in AlCl ₃ -based ILE in TSC-SC Al quasi-RE and GC CE.	99
Figure 5-9. SEM images of the cycled Ni, Ti, Mo, W, Ta CC in AlCl ₃ -based ILE.	101
Figure 5-10. Fine spectra from cycled Ni CC AlCl ₃ -based ILE. Peaks in a given column are scaled on the same intensity scale.	105
Figure 5-11. Fine spectra from cycled Ti CC in AlCl ₃ -based ILE. Peaks in a given column are scaled on the same intensity scale.	106
Figure 5-12. Fine spectra from cycled Mo CC in AlCl ₃ -based ILE. Peaks in a given column are scaled on the same intensity scale.	107
Figure 5-13. Fine spectra from cycled W CC in AlCl ₃ -based ILE. Peaks in a given column are scaled on the same intensity scale.	108
Figure 5-14. Fine spectra from cycled Ta CC in AlCl ₃ -based ILE. Peaks in a given column are scaled on the same intensity scale.	109
Figure 5-15. The Cl2p fine spectra from each metal foil, displayed on a single intensity scale. Peaks around 198 eV, corresponding to AlCl ₃ , are rendered in red. Peaks over 199 eV, corresponding to foil corrosion species, are rendered in blue.	110
Figure 5-16. Recorded CVs on Mo CC in AlCl ₃ -based ILE in (a) Swagelok cell 1, cell 2, and cell 3 at 5 mV s ⁻¹ and (b) CVs' comparison of Mo CCs in two TSC-SC and Swagelok at 0.5 mV s ⁻¹ . (c-d) CVs' comparison of Mo and W CC in Swagelok at 0.5 mV s ⁻¹ .	112
Figure 5-17. Recorded CVs in AlCl ₃ -based ILE at scan rate of 0.5 mV s ⁻¹ on (a) GNP coated on Mo CC in coin cell (contributed by Anastasia Teck from Titirici Group, Imperial College London) (b) Mo foil as CC in Swagelok cell, and (c) Mo foil as CC in TSC-SC.	113

List of Tables

Table 3-1. List of electrolyte compositions reported in the literature.	22
Table 3-2. Physicochemical properties of Al(OTF) ₃ -base electrolytes at 30°C.	30
Table 3-3. Melting and boiling points of the electrolyte components	31
Table 3-4. Binding energies, assignments, and a rough estimate of surface composition by atomic percent for the XPS spectrum of Pt foil after Al electrodeposition from AlCl ₃ -based E.	57
Table 3-5. Binding energies, assignments, and a rough estimate of surface composition by atomic percent for the XPS spectrum of Al electrode after Al electrodeposition NMA-based E.	58
Table 3-6. Binding energies, assignments, and a rough estimate of surface composition by atomic percent for the XPS spectrum of Pt electrode after applied CA technique in NMA-based E.	59
Table 4-1. A table of binding energies in eV, assignments, and % signal content for each species on each foil surface.	75
Table 2. Summarized reported ALBs using [EMImCl]: AlCl ₃ electrolyte.	83
Table 5-3. A table of binding energies in eV, assignments, and % signal content for each species on cycled Ni CC surface.	105
Table 5-4. A table of binding energies in eV, assignments, and % signal content for each species on cycled Ti CC surface.	106
Table 5-5. A table of binding energies in eV, assignments, and % signal content for each species on Mo CC surface.	107
Table 5-6. A table of binding energies in eV, assignments, and % signal content for each species on W CC surface.	108
Table 5-7. A table of binding energies in eV, assignments, and % signal content for each species on Ta CC surface.	109

Table of content

ABSTRACT	II
ZUSAMMENFASSUNG	IV
ACKNOWLEDGMENT	VI
PUBLICATIONS.....	VII
CONFERENCE PARTICIPATIONS, PRESENTATIONS AND POSTERS	VIII
DECLARATION OF COLLABORATIONS	IX
LIST OF ACRONYMS	XI
LIST OF FIGURES	XV
LIST OF TABLES.....	XIX
1 INTRODUCTION.....	1
1.1 Background	1
1.2 Motivation	3
1.3 Scope of the Project.....	4
1.3.1 Objectives and Research Questions.....	4
1.3.2 Contributions, Innovation, and Challenges	8
2 EXPERIMENTAL METHODS	12
2.1 Materials and Electrolyte Preparation	12
2.2 Electrolyte Characterization	13
2.3 Electrode Preparation and Characterization	14
2.4 Electrochemical Setup and Techniques.....	17

3	THE ADVANCEMENT AND CHALLENGES OF ALUMINUM TRIFLATE-BASED ELECTROLYTES.....	22
3.1	Research Background and Methodology	22
3.2	Open Challenges on Aluminum Triflate-based Electrolytes.....	27
3.2.1	Findings and Discussion	28
3.2.2	Conclusions and Outlook	46
3.3	Hindered Aluminum Plating and Stripping in Urea/NMA/Al(OTF) ₃ Electrolyte	47
3.3.1	Findings and Discussion	48
3.3.2	Conclusions and Outlook	59
4	COMPREHENSIVE INSIGHT INTO THE PERFORMANCE OF THE ALUMINUM ANODE MATERIAL: IMPACTS OF SURFACE MODIFICATION ON ITS THE SURFACE PROPERTIES.....	61
4.1	Research background and Methodology.....	61
4.2	Impact of Al Surface Modification on Al Surface Properties and Plating/Stripping	64
4.2.1	Findings and Discussion	64
4.2.2	Conclusions and Outlook	82
5	EVALUATION OF METALLIC CURRENT COLLECTORS IN AL DUAL-ION BATTERIES	83
5.1	Research background and Methodology.....	83
5.2	Criterion for the level of the instability of the Current Collectors in [EMImCl]: AlCl ₃ electrolyte	86
5.2.1	Findings and Discussion	87
5.2.2	Conclusions and Outlook	114
6	CONCLUSIONS.....	115
	REFERENCES.....	117
	APPENDIX.....	132

1 Introduction

1.1 Background

Global energy challenges have boosted the growth of electrochemical energy storage, especially rechargeable batteries [6]. They are in high demand for electric vehicles, renewable energy, and industry. Rechargeable battery technology has evolved from lead-acid to Li-ion. Li-ion, with its high energy density and durability, dominates the market since 1991 [6]. Next-gen Li-ion batteries are now under extensive exploration to meet rising demands for improved electrochemical performance [6]. Rechargeable Lithium-ion batteries (LiBs) as the established technology within the battery industry [7]. Metallic Li is known for its notable volumetric capacity (2062 mAh cm^{-3}) and the highest gravimetric capacity among alkali metals (3857 mAh g^{-1}) [8], [9]. However, the high cost and scarcity of Li (0.0065% of the earth's crust) and safety concerns stemming from the use of volatile organic electrolytes [10], [11] drive researchers to explore alternatives. Aluminum batteries (AlBs) have gained attention as a promising alternative to LiBs due to aluminum's sustainability, supported by a well-established aluminum foil industry [12]. Al is a much more abundant element ($\sim 8\%$ of the earth's crust mass fraction) than Li and has a volumetric capacity of 8040 mAh cm^{-3} that is about four times higher than Li [12], [13]. This is attributed to its unique capacity for three electrons exchange per redox center. Consequently, AlBs hold the potential for providing high specific power and energy [14], [15], [16]. Additionally, Al is cost-effective, recyclable, and readily available [15], [16], [17]. Hence, AlBs with metallic Al as an anode hold promise for sustainability and improved energy density. Since Dai *et al.* [18] demonstrated a stable and ultrafast AlBs in 2015 using an aluminum anode, a graphite cathode, and an [EMImCl]/ AlCl_3 electrolyte (AlCl_3 -based E), there has been growing interest in studying AlBs [18]. A schematic of the state-of-the-art AlBs is presented in Figure 1-1. Numerous studies have employed Al as the anode in various AlBs configurations, including Al dual ion batteries [19], [20], [21], Al-air batteries, and Al-S batteries [22]. AlBs encompass two distinct electrochemical mechanisms: 1) conversion or intercalation transpiring at the cathode, and 2) reversible dissolution and deposition of Al metal at the anode during the charge and discharge cycles [23], [24]. AlBs can be categorized into two groups based on their choice of electrolyte, either aqueous or non-aqueous [25]. Aqueous systems face limitations in using Al foil as a negative electrode due to hydrogen

evolution reaction (HER) occurring at potentials higher than Al plating. The negative standard reduction potential of Al anode occurs at -1.662 V vs. standard hydrogen electrode (SHE) [25]. The challenges faced in achieving successful Al plating and stripping in aqueous electrolytes, due to the competitive H_2 evolution reaction, have driven researchers to seek alternatives that allow for reversible Al plating and stripping. Non-aqueous room-temperature ionic liquid electrolytes (RTILEs) have been employed in AIBs due to their wide electrochemical potential window and low vapor pressures [26], [27], and nonvolatile and nonflammable properties [25]. While RTILEs lack the Al^{3+} cation, they contain Tetrachloroaluminate ($AlCl_4^-$) and Heptachlorodialuminate ($Al_2Cl_7^-$), the latter being the only active species, which allow reversible Al plating/stripping [26]. Various RTILEs have been investigated so far [28], [29], [30], [31], however, Imidazolium chloride and $AlCl_3$ -based melts being the most widely utilized compositions for enabling reversible Al plating and stripping [16], [32]. This combination ([EMImCl]: $AlCl_3$ (1:1.5)), has good ionic conductivity and outstanding plating and stripping behavior [33]. The success of [EMImCl]: $AlCl_3$ in Al plating and stripping is attributed to the presence of $Al_2Cl_7^-$, which forms when the molar ratio of $AlCl_3$ to [EMIm]Cl exceeds one [28], [31], [34]. Depending on the molar ratio between these components, the Al species primarily exist as monovalent complex anions, including $[Al_2Cl_7^-]$ and $[AlCl_4^-]$ [35]. However, the strong coordination of Al^{3+} and Cl^- impedes the existence of Al^{3+} [25]. Consequently, based on the utilized positive electrode material, different charge carriers are involved (*e.g.*, $AlCl_4^-$, $AlCl_2^+$, $AlCl_2^{2+}$), often resulting in a “dual ion” storage mechanism rather than Al-ion shuttling [36]. In principle, during charge and discharge, $[Al_2Cl_7^-]$ converts to Al^{3+} and $[AlCl_4^-]$ and *vice versa* [14], [37]. A significant challenge arises from the corrosive and aggressive nature of IL- $AlCl_3$ -based electrolytes, which restricts the choice of cathode materials and auxiliary components of the battery (*e.g.*, binders, separator, current collector (CC), and battery casing) [38]. The corrosivity of the chloroaluminate-based ILs is associated with the existence of Cl^- in $[Al_2Cl_7^-]$ and $[AlCl_4^-]$ species, and the Lewis acidity of the solution, dependent on the molar ratio between $AlCl_3$ and the IL. Additionally, $AlCl_3$ makes the electrolyte highly sensitive to moisture [14], [37], [39].

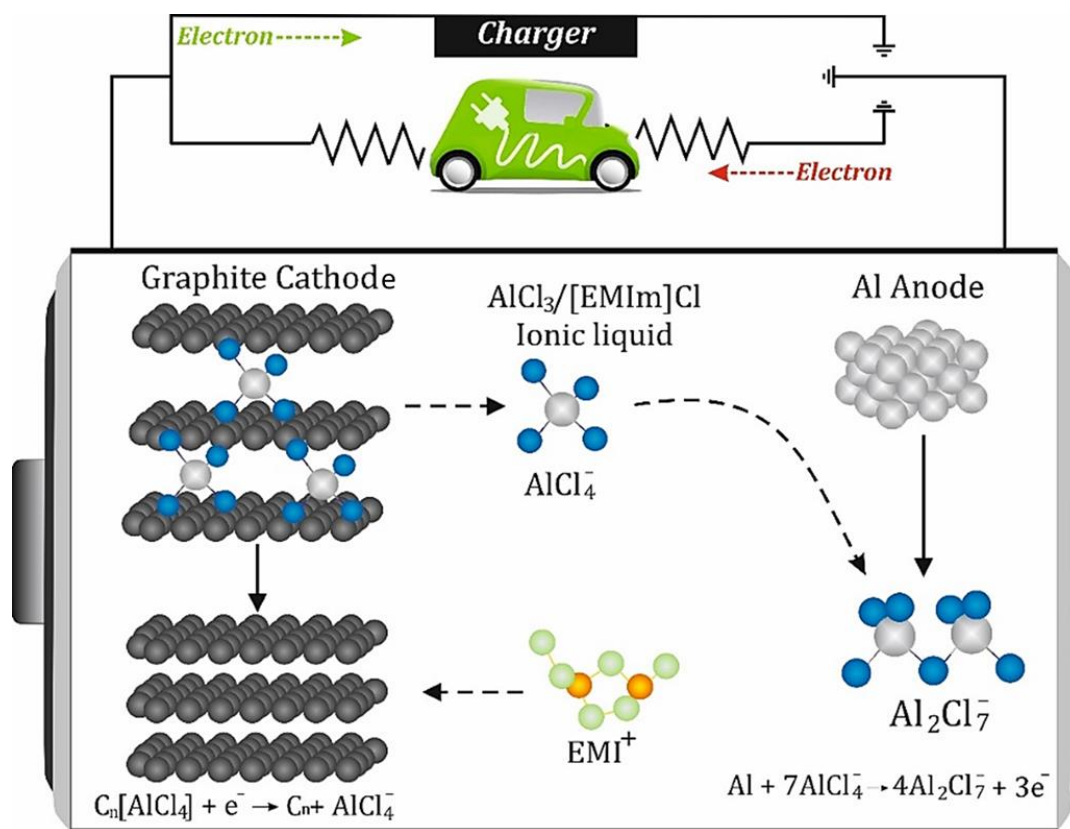


Figure 1-1. A Schematic of the state-of-the-art AIBs.

1.2 Motivation

This research is driven by the pursuit of AIBs as sustainable energy storage alternatives to LiBs. Al offers promise due to its abundance and higher charge capacity potential. However, corrosivity of the practical electrolytes hinders application of AIBs. The non-corrosive $Al(OTf)_3$ salt provides an opportunity. Chapter 3 aims to understand $Al(OTf)_3$ -based electrolyte behavior, assess feasibility, and uncover challenges, providing vital insights for future AIBs advancements. Chapter 4 aims to understand the hindrance caused by the Al_2O_3 oxide passivation film on Al substrates, exploring its impact on processes like Al plating and stripping. Chapter 5 aims to thoroughly evaluate the performance and stability of diverse metal foil CCs in AIBs with a non-aqueous ionic liquid electrolyte (ILE). The goal is to understand their electrochemical behavior, corrosion mechanisms, and safety implications. By establishing guidelines for optimal CCs' materials, the study contributes to enhancing battery design and technology. The overview of motivation behind this PhD research study demonstrated in Figure 1-2.

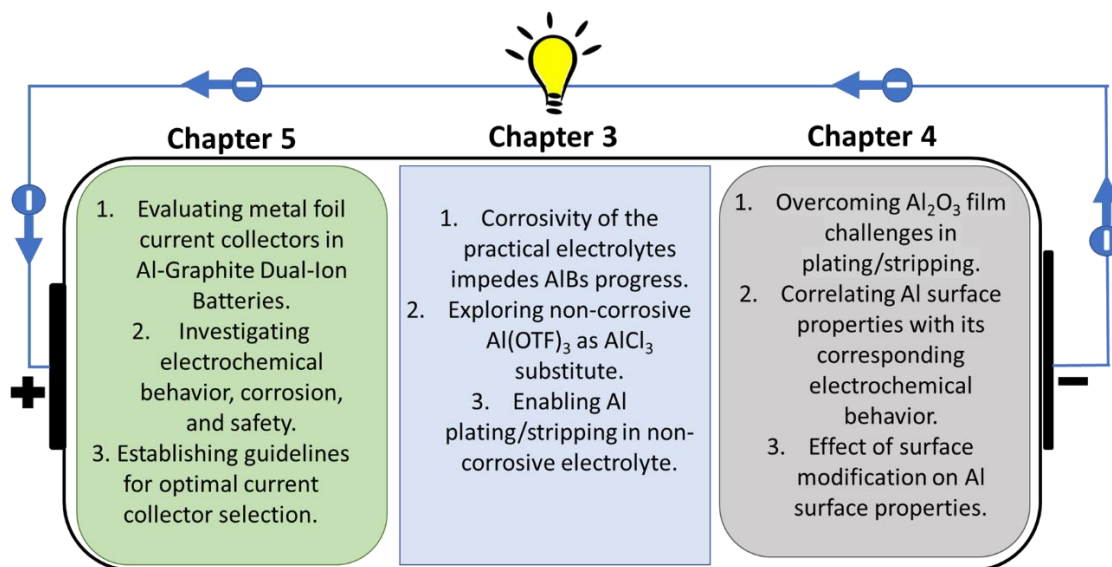


Figure 1-2. A schematic of the overall motivation of this PhD study.

1.3 Scope of the Project

1.3.1 Objectives and Research Questions

The primary aim of this PhD research study is to advance the progress towards rechargeable AIBs. This involves addressing the obstacles hindering the development of non-corrosive, AlCl_3 -free electrolytes, as well as implementation of the metallic Al substrate as anode material in AIBs. This encompasses the identification of critical challenges, uncovering overlooked and underexplored factors contributing to these issues. The main objectives are outlined in Figure 1-3. Each objective is listed with a brief description as follow.

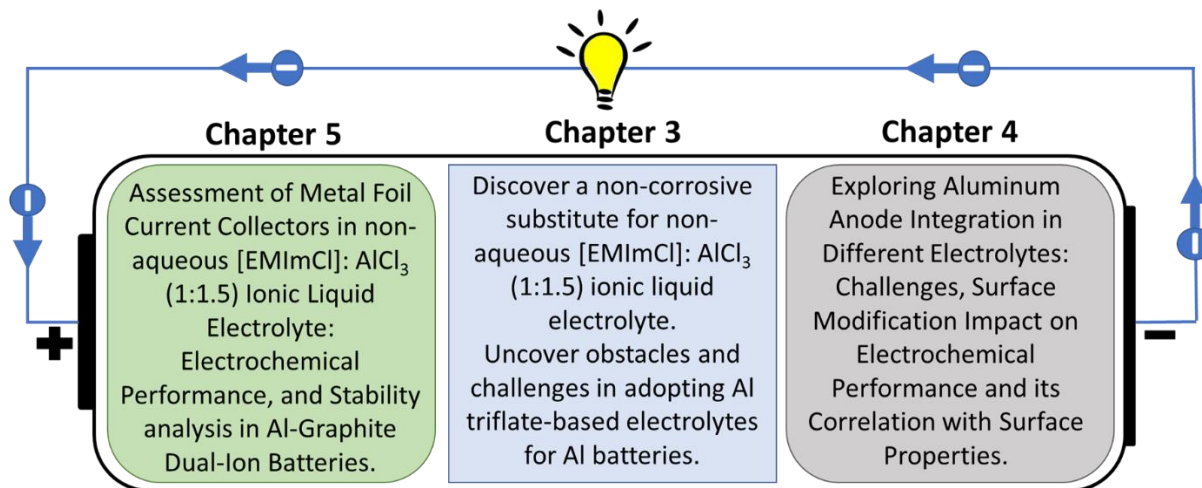


Figure 1-3. A schematic of the main specific objectives of this PhD research study.

The following specific objectives serve as the stepping stones towards the achievement of the overall goal:

Objective 1: Discovering a non-corrosive substitute for the state-of-the-art common non-aqueous ILEs. Furthermore, uncovering and exploring obstacles and challenges in adopting Al triflate-based electrolytes for AIBs. This objective centres on addressing the following questions:

1. What is the non-corrosive alternative to the common available electrolyte?
2. What are the non-corrosive alternative salts to be able to plate and strip Al?
3. How effective is Al plating/stripping from Al(OTF)₃-based E compared to [EMImCl]/AlCl₃ (AlCl₃-based E)?
4. What are the advantages and disadvantages of the Al(OTF)₃-based electrolytes?
5. How does the electrochemical performance of the Al(OTF)₃-based electrolytes differ?

Each question aligns with the overarching objective and contributes to a comprehensive investigation of the potential non-corrosive alternatives and challenges associated with Al triflate-based electrolytes for AIBs. It is significant to highlight that this thesis delves into the examination of two distinct Al(OTF)₃-based electrolytes within this context. Notably, the pursuit of this specific objective is detailed in chapter 3 of the thesis.

Objective 2: Application of the metallic Al anode in in both AlCl₃-based and Al(OTF)₃-based electrolytes and addressing challenges and the weakness of the Al(OTF)₃-based electrolytes in Al

plating and stripping on the Al substrate. This objective centres on addressing the following questions:

1. How does the behavior of the metallic Al anode differ between AlCl_3 -based and $\text{Al}(\text{OTF})_3$ -based electrolytes?
2. What are the primary challenges encountered when applying the metallic Al anode in AlCl_3 -based and $\text{Al}(\text{OTF})_3$ -based electrolytes?
3. How do the challenges differ between the AlCl_3 -based and $\text{Al}(\text{OTF})_3$ -based electrolytes during Al plating and stripping?
4. What are the weaknesses exhibited by $\text{Al}(\text{OTF})_3$ -based electrolytes in Al plating and stripping processes on the Al substrate?
5. Can modifications or optimizations be introduced to mitigate the challenges and weaknesses associated with Al anode application and $\text{Al}(\text{OTF})_3$ -based electrolytes?
6. How can the knowledge be gained from addressing challenges and weaknesses contribute to the advancement of Al anode-based electrochemical processes?

This PhD research study investigates the electrochemical performance of both nonmodified and surface-modified Al (M-Al) foil as negative electrodes. This particular objective is thoroughly examined in chapters 3 and 4. Moreover, chapter 3 specifically sheds light on the challenges associated with Al plating/stripping in $\text{Al}(\text{OTF})_3$ -based electrolytes. Furthermore, chapter 4 delves into the investigation of the electrochemical performance and surface characteristics of the as-received and M-Al substrate in an AlCl_3 -based E.

Objective 3: Exploring Al anode integration in AlCl_3 -based E: challenges, surface modification impact on electrochemical performance and its correlation with surface properties, considering the dual optical characteristics of shiny and non-shiny sides of Al foil. This objective centres on addressing the following questions:

1. How do the surface properties of the shiny and non-shiny sides of the Al metal foil differ?
2. What are the electrochemical differences observed between the shiny and non-shiny sides of the Al metal foil?
3. How can surface modifications affect the surface properties of both the shiny and non-shiny sides of the Al metal foil?

4. Can surface modification strategies harmonize the electrochemical responses of the shiny and non-shiny sides?
5. What is the relationship between the surface properties of each side and their corresponding electrochemical behavior?
6. How can the electrochemical differences between the two sides be exploited for electrochemical applications?
7. Can surface modifications provide insights into the origins of dual-side electrochemical differences?
8. Which surface modification strategies are effective in mitigating electrochemical differences and enhancing overall performance?

This PhD research study explores the differences in electrochemical performance in correlation with surface properties between nonmodified and M-Al foil, taking into account optically both sides of Al foil. This focused objective is comprehensively addressed in chapter 4. Within this chapter, there is a particular emphasis on establishing a connection between surface properties and the ensuing electrochemical behaviors of each side of the Al foil.

Objective 4: Evaluation and assessment of different metal foil CCs in a non-aqueous [EMImCl]: AlCl₃ (1:1.5) (AlCl₃-based) ILE present a multifaceted exploration encompassing both electrochemical performance and stability analysis within the context of AIBs. This objective centres on addressing the following questions:

1. How does the electrochemical behavior of different common metal foils molybdenum (Mo), tungsten (W), titan (Ti), nickel (Ni), tantalum (Ta)) vary when used as CCs in AlCl₃-based ILE?
2. What are the key factors influencing the electrochemical performance of different metal foils as CCs in AlCl₃-based ILE?
3. How does the long-term cycling stability of batteries with different metal foils as CCs compare in AlCl₃-based ILE?
4. What are the corrosion mechanisms exhibited by the chosen metal foils when immersed in acidic AlCl₃-based ILE?
5. How does corrosion of CCs impact the overall electrochemical performance and stability of Al Dual-ion batteries?

6. Can specific CC-electrolyte combinations mitigate or exacerbate corrosion effects in AlCl_3 -based ILE?
7. What are the safety implications of corrosion-induced changes in CCs' materials for Al Dual-ion batteries?
8. Can guidelines for selecting optimal CCs' materials in ILEs be established based on a balance between electrochemical performance and stability considerations?

This PhD research study provides a comprehensive framework for investigating the behavior of common CCs in AlCl_3 -based ILE and their stability within the context of Al Dual-ion batteries. Chapter 5 stands out as a key component, providing an in-depth grasp of the chemical and electrochemical stability of a range of diverse metal foil CCs, namely Ti, Mo, Ni, W, and Ta.

1.3.2 Contributions, Innovation, and Challenges

This PhD research study has made significant contributions to the science of ALBs. The study's outcomes, presented across chapters 3, 4, and 5. A list of the contributions, innovation, and challenges from each chapter are presented as follows:

Chapter 3

Contributions:

This chapter contributes by presenting an electrochemical study of two distinct electrolyte compositions based on the non-corrosive $\text{Al}(\text{OTF})_3$ salt, urea, and two different solvents (NMA and EiPS). The investigation aims to assess the electrochemical behavior of these alternative electrolytes under various conditions. In addition, this chapter addresses the challenges of utilizing the urea/NMA/ $\text{Al}(\text{OTF})_3$ electrolyte (NMA-based E), which is non-corrosive but suffers from inadequate Al plating and stripping. The study investigates the role of the electrolyte and the Al electrode surface in influencing the formation of the electrode-electrolyte interphase.

Innovations:

The study innovatively evaluates; 1. the suitability of $\text{Al}(\text{OTF})_3$ -based electrolytes as a non-corrosive alternative to traditional AlCl_3 -containing electrolytes, 2. unexpected behavior with substrates other than Pt or Cu is explored to uncover challenges that might arise with different electrode materials, and 3. the impact of the electrolyte and electrode surface on electrode-

electrolyte interphase formation to provide novel insights into the challenges of Al plating and stripping in NMA-based E.

Challenges:

The study identifies challenges related to; 1. the reversibility of redox reactions when using $\text{Al}(\text{OTF})_3$ -based electrolytes, highlighting potential limitations in achieving efficient plating and stripping, 2. limitations identification in achieving effective Al plating and stripping in the NMA-based E due to the inability to remove the Al_2O_3 oxide passivation film, and 3. challenges arise from the formation of electrode-electrolyte interphase containing $\text{Al}(\text{OH})_3$, AlF_3 , and re-passivated Al oxide, which obstructs pathways for successful Al plating and stripping.

Chapter 4

Contributions:

This chapter contributes by addressing the challenge posed by the presence of an amorphous Al_2O_3 oxide passivation film on Al substrates, which hinders the cyclic performance of metallic Al in rechargeable ALBs. The study investigates the influence of this electron/ion insulating film on the activation of the anode and the Al plating and stripping processes. Moreover, this chapter delves into the impact of surface properties (*i.e.* microstructures, surface roughness, and morphology) on Al plating and stripping, focusing on the visually distinct sides of Al foils (shiny and non-shiny). The study investigates how differences in surface roughness (S_a) and microstructure influence the efficiency of these electrochemical processes. In addition, this chapter explores the effects of treatment in AlCl_3 -based E on the surface properties of Al foils. The study investigates the formation of interphase layer rich in Al, Cl, and Ni and how it facilitates Al diffusion during plating and stripping.

Innovations:

The study innovatively explores; 1. how the Al_2O_3 oxide passivation film retards the activation of the anode and impedes Al plating and stripping, identifying a critical obstacle in ALBs, 2. the impact of surface characteristics, including roughness and microstructure, introduced by the Al_2O_3 oxide passivation film on the electrochemical processes, 3. the relationship between S_a , active sites concentration, and current density during Al plating and stripping, 4. the visually distinct sides of Al foils introduces a novel perspective on how surface attributes affect battery performance, 5. how treatment results in the formation of an interphase layer that enhances pathways for Al

diffusion during electrochemical processes, 6. the impact of this specific electrolyte on surface properties and interphase layer formation introduces new insights.

Challenges:

The study identifies challenges related to; 1. the presence of the Al_2O_3 oxide passivation film introduces electron/ion insulating properties, inhibiting efficient charge transfer and plating/stripping processes, 2. the form of dendritic Al deposition, contributing to local corrosion, electrode pulverization, and ultimately affecting cyclic performance, 3. uneven active site concentrations between the shiny and non-shiny sides, affecting the distribution of current density during electrochemical processes, 4. the non-shiny side's increased S_a , while conducive to Al plating and stripping, introduces challenges in maintaining uniform current distribution, 5. the composition and stability of the interphase layer formed through treatment, including its influence on long-term battery performance, 6. enhanced Al diffusion and interphase layer formation, while beneficial, may contribute to challenges such as escalated local corrosion and electrode pulverization over extended cycles.

Chapter 5

Contribution:

This research study contributes to the understanding of metallic CCs' stability when exposed to an AlCl_3 -based ILE in the context of AIBs. The study employs a combination of immersion tests, surface analysis techniques, and electrochemical assessments to evaluate the corrosion susceptibility of various metallic CCs foils. The findings reveal differing degrees of reactivity among the foils, with Ni and Ti showing significant corrosion susceptibility, while Mo and W exhibit reactivity, and Ta demonstrates enhanced resistance. These insights are valuable for selecting appropriate CCs for AIBs applications.

Innovation:

The innovation in this research lies in its investigation of the suitability of CCs (Mo and W rods) in Swagelok cell configurations using an AlCl_3 -based ILE. The unexpected reactivity between Mo and the electrolyte is identified, resulting in oxidative and reduction peaks in the CV data. This novel insight highlights the electrochemical interactions between Mo and aluminum chloride complexes, ultimately concluding that Mo rods (with 99.97% purity and specified impurities as

mentioned) are not recommended as CC in Swagelok cells, which expands our understanding of materials' behavior in specific battery configurations.

Challenges:

The reactivity of Mo, and W with ILE presents a challenge in terms of material selection for CCs. Overcoming these challenges is essential to provide reliable recommendations for practical battery applications and to further advance the understanding of metallic CCs' behavior in ILE.

2 Experimental methods

2.1 Materials and Electrolyte Preparation

In this PhD research study, anhydrous acetonitrile (ACN) (99.8%) and anhydrous methanol (MeOH) (99.8%), dimethyl carbonate (DMC) (99.99%), anhydrous aluminum chloride (AlCl_3) (99.99%), and 1-Ethyl-3-methylimidazolium chloride (EMImCl) (95%) were purchased from Sigma Aldrich company. A commonly used ionic liquid (IL) electrolyte in AIBs, [EMImCl]/ AlCl_3 (AlCl_3 -based) ILE with a molar ratio of 1:1.5 [40] was prepared by gradually adding the calculated amount of AlCl_3 salt to the appropriate amount of [EMImCl] salt while stirring inside an argon-filled (Ar-filled) glovebox (MBraun, O_2 and H_2O level < 0.5 ppm temperature 28 to 30°C). While the two solids are being mixed, they transform into a yellowish clear liquid. Ethyl Isopropyl sulfone (EiPS) (97.00%) was purchased from TCI company. Aluminum trifluoromethanesulfonate ($\text{Al}(\text{OTf})_3$) (99.9% trace metal basis), N-methylacetamide (NMA) (99%), urea (99%) were all purchased from Sigma-Aldrich company. $\text{Al}(\text{OTf})_3$ and urea were dried in a glass oven (BÜCHI Glass Oven B-585) under vacuum at 80°C for 48 h and then stored in an Ar-filled glovebox (MBraun, O_2 and H_2O level < 0.5 ppm) before being used. Molecular sieves (MS) of 3 Å (beads, 4 - 8 mesh) were purchased from Sigma-Aldrich company. EiPS was dried over MS for 10 days at room temperature (RT) till the water content became less than 20 ppm. The initial measured water content in the as-received NMA solvent was about 4476 ppm; therefore, NMA was dried with MS for 10 days until the water content was less than 25 [1]. A Karl Fisher titrator (Titroline[®] 7500 KF trace) was used to measure the water content. Urea and $\text{Al}(\text{OTf})_3$ were vacuum-dried at 80°C for 48h in a glass oven (BÜCHI Glass Oven B-585) before being transferred to an Ar-filled glovebox (MBraun, O_2 and H_2O level < 0.5 ppm) and used later for the preparation of the NMA-based E [1], [41]. NMA was firstly melted at 40°C and then dried for each water content measurement. NMA-based ternary electrolyte with a final molar ratio of 0.19:0.75:0.05 was prepared first by melting NMA at 40°C [41]. Then the appropriate amounts of dried $\text{Al}(\text{OTf})_3$ and urea were added and stirred for 12h at RT inside the glovebox. The second electrolyte based on urea/EiPS/ $\text{Al}(\text{OTf})_3$ (EiPS-based E), with a molar ratio of 0.30:0.65:0.05 based on better solubility, was prepared by mixing the appropriate amounts of $\text{Al}(\text{OTf})_3$ and EiPS and adding the required amounts of urea. The mixture was stirred for 12h at RT inside the glovebox. The EiPS-based E has been prepared considering the ability to

form Al^{3+} complex with six surrounding urea molecules [42], [43], [44]. Therefore, due to the 1:6 metal-to-ligand molar ratio between urea and $\text{Al}(\text{OTF})_3$, the molar ratio of 0.30:0.65:0.05 was chosen for EiPS-based E. Based on the experience, the 1:7 metal-to-ligand molar ratio results in a solubility issue. To calibrate the reference electrode (RE), electrolytes containing Ferrocene (0.02 mol L^{-1}) as an internal reference were prepared. Ferrocene (98.00%) was purchased from Sigma-Aldrich company. All the prepared AlCl_3 -based E and EiPS-based E and NMA-based E were kept sealed in the glovebox for the following electrochemical experiment. The Al foils (0.075 mm, 0.025 mm thicknesses and 99.0% purity), Ti foil (0.025 mm thickness and 99.6% purity), Ta foil (0.025 mm thickness and 99.99% purity), Ni foil (0.025 mm thickness and 99.99% purity), W foil (0.025 mm thickness and 99.96% purity), and Mo foil (0.025 mm thickness and 99.9% purity) were purchased from Goodfellow company. Mo rod with 99.97% purity, containing impurities such as Al (Max. $1 \frac{\mu\text{g}}{\text{g}}$), Cr (Max. $3 \frac{\mu\text{g}}{\text{g}}$), Cu (Max. $2 \frac{\mu\text{g}}{\text{g}}$), Fe (Max. $5 \frac{\mu\text{g}}{\text{g}}$), K (Max. $6 \frac{\mu\text{g}}{\text{g}}$), Ni (Max. $1 \frac{\mu\text{g}}{\text{g}}$), Si (Max. $2 \frac{\mu\text{g}}{\text{g}}$), C (Max. $13 \frac{\mu\text{g}}{\text{g}}$), N (Max. $5 \frac{\mu\text{g}}{\text{g}}$), O (Max. $6 \frac{\mu\text{g}}{\text{g}}$), Cd (Max. $1 \frac{\mu\text{g}}{\text{g}}$) and W rod with 99.97% purity, including impurities such as Al (Max. $15 \frac{\mu\text{g}}{\text{g}}$), Fe (Max. $30 \frac{\mu\text{g}}{\text{g}}$), Si (Max. $20 \frac{\mu\text{g}}{\text{g}}$), H (Max. $5 \frac{\mu\text{g}}{\text{g}}$), Cd (Max. $5 \frac{\mu\text{g}}{\text{g}}$), Cr (Max. $20 \frac{\mu\text{g}}{\text{g}}$), K (Max. $10 \frac{\mu\text{g}}{\text{g}}$), Mo (Max. $100 \frac{\mu\text{g}}{\text{g}}$), N (Max. $5 \frac{\mu\text{g}}{\text{g}}$), Hg (Max. $1 \frac{\mu\text{g}}{\text{g}}$), Cu (Max. $10 \frac{\mu\text{g}}{\text{g}}$), Ni (Max. $20 \frac{\mu\text{g}}{\text{g}}$), C (Max. $30 \frac{\mu\text{g}}{\text{g}}$), O (Max. $20 \frac{\mu\text{g}}{\text{g}}$), Pb (Max. $5 \frac{\mu\text{g}}{\text{g}}$), were purchased from PLANSEE. The platinum (Pt) foil (0.4 mm thickness and 99.9% purity) was supplied from rhd Instruments GmbH & Co. KG (Germany). Copper (Cu) foil (9 μm thickness and > 99.8% purity) was purchased from MTI Corporation. Graphene NanoPlatelets (GNPs) with a thickness of 15 nm (xGnP Grade-H) was purchased from XG Sciences (USA). Carbon black (CB; Super-P) conductive agent ($\geq 99\%$) were supplied by Alfa Aesar (USA). Sodium alginate (SA) and Glass microfiber separators (Whatman GF/A) were purchased from Sigma-Aldrich Company.

2.2 Electrolyte Characterization

In chapter 3, the physical properties of the NMA-based E were previously documented in work of Mandai and Johansson [41]. For the EiPS-based E, its density, viscosity, and ionic conductivity were characterized across temperatures ranging from 20 to 80°C. Density and viscosity measurements were conducted using a DMA 4100 (Anton Paar) viscosimeter. Temperature-

dependent ion-conductivity of the EIPS-based E solution was determined via electrochemical impedance spectroscopy (EIS). The EIS measurements were performed using a TSC 1600 closed cell (TSC1600-CC) with a cell constant (K_{cell}) of 1.3 cm^{-1} , in combination with a Microcell HC setup (rhd instruments GmbH & Co. KG) [45]. The entire procedure took place inside an Ar-filled glovebox (MBraun, O_2 and H_2O level $< 0.5 \text{ ppm}$). The cell, filled with 1.0 mL of the sample solution, was sealed and transferred to a test station (cell stand) outside the glovebox. The Microcell HC temperature facilitated automated temperature adjustments using a Peltier element technique, ensuring a high level of precision (0.1°C accuracy). The EIS measurements were conducted with a Biologic VMP potentiostat (France) equipped with EC-Lab software. Impedance data were evaluated using the RelaxIS 3[®] software suite (rhd instruments GmbH & Co. KG). Impedance spectra were recorded over frequency range from 1 Hz to 100 KHz (20 points per decade) with an AC voltage amplitude of 10 mV at various temperatures (20 to 80°C with 10°C intervals). To ensure thermal equilibrium, a 0.5h hold time was employed after reaching the temperature set-point before initiating the EIS experiment. TGA and Fourier-transform infrared spectroscopy (FT-IR) of the electrolytes were carried out using a Bruker Tensor 27 FT-IR spectrometer, all within the Ar-filled glovebox (MBraun, O_2 and H_2O level $< 0.1 \text{ ppm}$).

2.3 Electrode Preparation and Characterization

All handling and preparation of the electrodes were conducted within an Ar-filled glovebox (MBraun, O_2 and H_2O level $< 0.5 \text{ ppm}$). To remove residual electrolyte, surface-modified and cycled electrodes were rinsed either in anhydrous ACN, or DMC, or MeOH inside an Ar-filled glovebox (MBraun, O_2 and H_2O level $< 0.5 \text{ ppm}$) and subsequently vacuum-dried for 12h at RT in a glass oven (BÜCHI Glass Oven B-585). All glassware and components, including magnetic stir bars, underwent vacuum drying at 80°C overnight prior to their placement within the glovebox.

In chapter 3, for the treatment of the Al foil ($1 \text{ cm} \times 1 \text{ cm}$ with a thickness of 0.025 mm), it was immersed in $900 \mu\text{L}$ of AlCl_3 -based E for 18h. The Pt foil, after undergoing chronoamperometry (CA) technique in AlCl_3 -based E, and the immersed Al electrode before being used as the working electrode (WE) in $\text{Al}(\text{OTf})_3$ -based electrolyte, were washed three times with anhydrous ACN to ensure the removal of any residual electrolyte. Afterward, they were vacuum-dried in a glass oven (BÜCHI Glass Oven B-585) at RT. Similarly, the Al and Pt electrodes, following each applied electrochemical technique in $\text{Al}(\text{OTf})_3$ -based electrolyte, were rinsed three times in fresh

anhydrous MeOH to eliminate any residual electrolyte and then dried under vacuum in a glass oven (BÜCHI Glass Oven B-585) at RT. Scanning electron microscope (SEM) imaging and energy-dispersive X-ray spectroscopy (EDX) of the Al and Pt electrodes were performed using a JEOL JSM 7500F machine with acceleration voltages of 5 kV and 10 kV, respectively. For XPS measurements of the Al and Pt electrodes, a Specs EnviroESCA NAP-XPS 52 was utilized within a nitrogen-filled (N-filled) glovebox (GS, O₂ and H₂O level < 0.5 ppm). During the XPS measurements, the NAP features were not used, and the pressure was approximately 10⁻⁶ mbar. Survey spectra were acquired with a pass energy of 100 eV and an energy resolution of 1 eV, while fine spectra were taken with a pass energy of 30 eV and a resolution of 0.1 eV.

In chapter 4, treated and cycled Al foils underwent a thorough washing process (three times) utilizing anhydrous ACN within the glovebox. Subsequently, the foils were dried under vacuum for a period of 12h within BÜCHI Glass Oven B-585. The preparation of treated electrodes followed these steps: Al foils were immersed in 900 µL of AlCl₃-based E for durations of 6h and 18h, then being cleaned washed and dried for post-mortem surface analysis. SEM images of pristine, treated, and cycled Al foils were captured using JEOL JSM 7500F instruments at an acceleration voltage of 5 kV. Elemental analysis of the Al foil was conducted through EDX with an acceleration voltage of 10 kV. All AFM assessments for pristine, treated, and cycled Al foils were conducted utilizing an AFM microscope (Park NX10, Park Systems) positioned within an Ar-filled glovebox (MBraun, O₂ and H₂O level < 0.1 ppm). The evaluation of morphological changes and roughness in pristine, treated, and cycled Al foils was accomplished using a closed-loop scanner in non-contact mode. Measurements were taken before and after 100 and 500 cycles. High aspect ratio silicon AFM probes (PPP-NCHR, NanoWorld AG, Switzerland) with a resonant frequency of 330 kHz and a tip radius of 10 nm were used for non-contact mode experiments. The AFM images recorded at a scan speed of 0.7 Hz. The force constant of the cantilevers ($k = 42 \text{ Nm}^{-1}$) was determined using the thermal noise method method [46]. Nanomechanical properties of pristine and cycled electrodes were assessed utilizing diamond-coated AFM probes (DT-NCHR, Nanoworld AG, Switzerland) with a resonant frequency of 400 kHz and a tip radius of 10 nm. Images were recorded at a scan speed of 0.2 Hz. Roughness data (mean surface roughness (S_a)) and nanomechanical data were analyzed using Park's imaging processing tool for Scanning Probe Microscopy (SPM) data (XEI 5.2, Park Systems). The Pinpoint nanomechanical mode was utilized

to avoid lateral shear forces, minimizing the potential for surface damage. This mode allowed for simultaneous imaging of surface topography alongside Young's modulus, deformation, and adhesion. The employed cantilevers were calibrated using a piece of Si wafer prior to measuring the Al samples. XPS measurements of the pristine and M-Al foil were conducted using a Specs EnviroESCA NAP-XPS [47], operating without NAP features, and at an approximate pressure of 10^{-5} mbar. These measurements took place within a N-filled glovebox (GS, O₂ and H₂O level < 0.5 ppm). All of the Al electrodes are denoted as follows: Al-NSH (non-shiny side of Al foil), Al-SH (shiny side of Al foil), Al-NSH-6h (non-shiny immersion treated for 6h), and Al-NSH-18h (non-shiny treated for 18h).

In chapter 5, the preparation and handling of the electrodes have been carried out inside an Ar-filled glovebox (MBraun, O₂ and H₂O level < 0.5 ppm). The corrosivity test involved immersing metal foils in 1000 μ L of AlCl₃-based E durations of 24h, 48h, 1 week, and 1 month. Subsequently, the foils were rinsed in anhydrous ACN to remove residual ILE. Following each electrochemical characterization, the electrodes were washed thrice with anhydrous ACN inside the glovebox, followed by a 12h drying period in a vacuumed glass oven (BÜCHI Glass Oven B-585). SEM imaging of the electrodes was conducted using a JEOL JSM 7500F machine with an acceleration voltage of 5 kV. Elemental analysis was carried out using EDX with a 10 kV, and 15 kV acceleration voltage. XPS measurements of cycled electrodes were performed using a Specs EnviroESCA NAP-XPS [47] (without making use of the near-ambient pressure (NAP) features, so at roughly 10^{-6} mbar) via a N-filled glovebox (GS, O₂ and H₂O level < 0.5 ppm). More specifically, not using NAP features means that we are operating at the minimum of roughly 10^{-6} mbar, instead of the up to 10 mbar that the machine can reach. Survey spectra were captured with a pass energy of 100 eV and energy resolution of 1 eV. Fine spectra were acquired using a pass energy of 30 eV and a resolution of 0.1 eV. Spectra were taken of pristine and current collector samples of Mo, Ta, Ti, W, and Ni. For the pristine samples, fine spectra were taken of the relevant transition metal, carbon, oxygen, and any visible impurities. All pristine samples were calibrated by setting the major C1s peak to 284.8 eV for C-C / C-H, with the exception of the Mo sample, for which that peak was already at 284.8 eV. Spectra were fit with CasaXPS [48], using the CasaXPS LA lineshape function for all peaks; non-metals were fit using a standard Gaussian-Lorentzian shape, while conductive metal peaks were fit with ad-hoc asymmetric line shapes. For the coin cell setup, the

Al foil (taken as anode) was prepared as follows. Initially, the Al foil was subjected to ultrasonication in anhydrous ethanol (EtOH) for 5 minutes, followed by immersion in 8 molar HNO₃ for an additional 5 minutes to eliminate surface impurities. Subsequent to this treatment, the foil underwent thorough rinsing with water until a neutral pH was attained. It was then dried using acetone before being vacuum-dried and transferred into an Ar-filled glovebox (MBraun, O₂ and H₂O level < 0.1 ppm). Each Metallic foil CCs, firstly were cut (15 mm diameter) then was subjected to ultrasonication in anhydrous EtOH for 5 minutes, followed by immersion in deionized water for an additional 5 minutes to eliminate surface impurities. In addition, the foil underwent thorough rinsing with acetone, then being dried for 12h at 80°C in vacuum oven before being transferred into an Ar-filled glovebox (MBraun, O₂ and H₂O level < 0.1 ppm). Concerning GNP electrode (as cathode) preparation procedure [49], GNP slurry compositions (GNP: SA: CB) by mass = 75:15:10) were created by blending 0.75 g of GNPs, 0.15 g of SA, and 0.10 g of CB with 8–10 mL of deionized water. The mixture was subjected to magnetic stirring overnight until a uniform slurry consistency was achieved. This slurry was then applied onto metallic foil CCs tab (already cut, washed, dried, and weighted) using a drop-coating technique. To restrict the coated area (12 mm diameter), paper tape was utilized. After a drying period at RT lasting 2-3h, the tape was taken off, and any remaining adhesive was cleaned off with acetone. Before determining the precise loading, the GNP-coated was vacuum-dried at 80°C overnight to eliminate residual moisture. The active material's actual loading was computed by dividing the weight difference between the coated and uncoated metallic CCs by the coating area and then multiplying it by the GNP mass fraction in the 0.75 slurry. This approach, which exclusively accounts for GNP's mass contribution, facilitated a direct comparison of the specific discharge capacity obtained.

2.4 Electrochemical Setup and Techniques

All electrochemical experiments were conducted within an airtight, closed and sealed rhd cells, supplied by rhd Instruments GmbH & Co. KG (Germany), Swagelok and coin cells purchased from Alfa Aesar. All electrochemical cells were assembled, operated, disassembled inside an Ar-filled glovebox (MBraun, O₂ and H₂O level < 0.1 ppm). To prevent any contamination and dirt from affecting the cell, after each electrochemical experiments all cell auxiliaries were cleaned, rinsed and washed with absolute EtOH, deionized water while being in ultrasonic bath and finally rinse in acetone, then all components of the cell were subjected to overnight vacuum drying at

temperatures ranging from 80 to 90°C. This process was implemented to eliminate any potential moisture present in the raw materials. The schematic of the whole electrochemical setup which have been taken in this PhD study are presented in Figure A-2- 1. The configuration and handling of each electrochemical setups in each chapter are presented as follow:

In chapter 3, TSC1600-CC was taken for study the electrochemical performances of the electrolytes. The measuring TSC1600-CC (from rhd Instruments) is equipped with a Pt crucible, which serves both as a sample container and a counter electrode (CE). Due to its large surface area, the Pt CE can efficiently support the current generated at the WE. To establish cell connections to the potentiostat, the Microcell HC cell stand was utilized. The temperature-dependent ion-conductivity of the EiPS-based E was evaluated through electrochemical EIS using this setup. The electrolyte used was in large excess, with a volume of 1.0 mL. This setup allows for a maximized distance between the CE and WEs, effectively minimizing the influence of oxidative reaction products formed at the CE on the processes occurring at the WE during the first reduction (plating) process. Glassy Carbon (GC) and Pt discs as WE, each with a geometric area of 0.07 cm², were meticulously polished using 250 nm diamond polishing paste before being utilized in the experiments. The Silver (Ag) wire quasi-RE were polished 1 μm diamond suspension and also prepared accordingly. The Al quasi-RE underwent an additional treatment by soaking it in a mixture of H₂SO₄/H₃PO₄/HNO₃ (25/70/5 by volume) for 5 to 15 minutes to remove any dirt or residual oxide [41]. Subsequently, the Al quasi-RE was thoroughly washed with acetone and dried under vacuum just before the measurements.

TSC surface cell (TSC-SC) was taken for study the electrochemical performances of metallic anode foils (Al, Pt, Mo, Cu, Ti) as WE for anode application in chapter 3, Al meal foil as WE for anode application in chapter 4, and metallic foils (Mo, W, Ni, Ti, and Ta) as WE for CCs application in chapter 5. The TSC-SC consists of a gold-plated thermo-block with an integrated Pt100 temperature sensor and a PEEK housing, which facilitates testing air- and moisture-sensitive samples. The GC and Pt discs (each with a radius of 6 mm) served as CEs, while Ag and Al wires were used as quasi-REs. The TSC-SC consisted of WE with a geometric area of 0.28 cm², which were either Pt, Mo, Al, Cu, W, Ni, Ta, or Ti foils, depending on the specific experiment in each chapter. Before and after each electrochemical test, the GC electrode was polished using 250 nm diamond polishing paste and rinsed with deionized water to ensure a clean electrode surface.

Similarly, the Al quasi-RE was polished and cleaned using a mixture of $\text{H}_2\text{SO}_4/\text{H}_3\text{PO}_4/\text{HNO}_3$ (25/70/5 by volume) to remove any dirt and residual oxide [41]. The Ag quasi-RE was polished with a 1 μm diamond suspension and rinsed with deionized water.

In chapter 5 Swagelok cell was taken to study the chemical and electrochemical stability of Mo, and W CCs. Swagelok cell typically consists of three main electrodes: a WE, a RE, and a CE. The setup allows for precise control and measurement of electrochemical reactions. The utilized materials in this PhD are as follows: 300 μL of AlCl_3 -based E was utilized for three-electrode Swagelok cell. The metallic CCs including Mo, and W foil (12 mm diameter) as WE and CE, and Al foil (0.075 mm thickness, 99.99% purity) with 12mm diameter cut as RE were taken in Swagelok cell. All cell components cell body, caps, the O-rings or gaskets installed at the appropriate places to ensure a proper seal. This prevents leakage of the electrolyte. Once the cell is filled with electrolyte and purged of air, close and tighten all caps and ports to ensure a secure and leak-free assembly. The two/three-electrode Swagelok cells were conducted with a Biologic VMP potentiostat (France) equipped with EC-Lab software.

In Chapter 5 the coin cell was taken to study the electrochemical performances of GNP coated on metallic CCs. Typically coin cell consists of two main electrodes: cathode, anode electrode material. The coin cell assembly protocol proceeds as follows. The required materials, including the stainless steel (SS) top/positive coin cell case, Mo spacer and spring, SS button/negative coin cell case, Glass microfiber separators Whatman (GF/A), Al foil as the anode, graphite nanoplates (GNP) as the cathode material coated on a CC, EtOH, electrolyte, clean tissue, silicon mat, plastic tweezers, and a pneumatic crimping machine (the MSK-PN110-S) are gathered. The assembly process begins with ensuring that all coin cell components are thoroughly cleaned. The parts are immersed first in absolute EtOH, then in deionized water and cleaned for 20 minutes in an ultrasonic bath. After being vacuumed dried overnight at 80°C , the cleaned, dried components are transport to Ar-filled glovebox (MBraun, O_2 and H_2O level < 0.1 ppm), then arranged on a clean tissue placed over a silicon mat. The assembly process is initiated by positioning the Mo spacer (16 mm diameter) into the negative case cap, with attention to the orientation of any sharp edges towards the stainless-steel top/negative coin cell case. The Al foil (anode) is then centrally positioned onto the Mo spacer, with care taken to orient any sharp edges towards the spacer and cap. Next, the GF/A separator (16 mm diameter) is gently positioned onto the anode,

ensuring that the separator is not punctured by the plastic tweezers. The electrolyte, distributed evenly (150 μL), is introduced onto the separator using a pipette. The cathode electrode (GNP coated on a metallic CC) is positioned onto the separator with the coated side facing the separator, employing plastic tweezers. Two Mo spacers are placed on top of the cathode electrode using plastic tweezers. The stainless-steel Mo spring is positioned onto the Mo spacers atop the cathode. The final step involves utilizing a pneumatic crimping machine (e.g., MSK-PN110-S) to apply approximately 5 bar pressure to crimp the cell. This sealing action establishes proper contact among the coin cell components, effectively preventing any potential leakage. Following this protocol, a functional coin cell can be successfully assembled for utilization in electrochemical experiments in chapter 5.

The electrochemical techniques corresponding to each chapter are outlined as follows:

In section 2 of chapter 3: to test the electrochemical performance of the triflate-based electrolytes, cyclic voltammetry (CV) was employed using sealed, closed, and airtight TSC1600-CC. For the determination of the anodic stability of the electrolyte on the two different electrode substrates (Pt and GC), Linear sweep voltammetry (LSV) was performed with a scan rate of 5 mV s^{-1} using the TSC1600 closed cell equipped with an Ag quasi-RE. Additionally, to investigate the Al plating and stripping on varied metal foils in triflate-based electrolytes, CV was recorded with a scan rate of 20 mV s^{-1} . Investigating metal foils as WEs (anodes) in contact with the liquid electrolyte was accomplished using the measuring TSC-SC.

In section 3 of chapter 3: CV and CA measurements were performed using a biologic potentiostat (VMP12) at a temperature of 25°C in TSC-SC. CVs were recorded with a scan rate of 20 mV s^{-1} in a potential range of 0.5 to 1.0 V vs. Al quasi-RE in the AlCl_3 -based E, and in a potential range of -1.7 to 0.5 V vs. Ag quasi-RE in the $\text{Al}(\text{OTf})_3$ -based E. These CVs allowed the study of possible Al reduction and oxidation reactions. Considering the stability window of the NMA-based E and the stability of the quasi-RE for Al plating and stripping, this potential range (-1.7V to 0.5V vs. Ag quasi-RE), was derived from prior study [1] where it had proven to be a reliable and effective window for Al electrodeposition and dissolution. On the other hand, CA was conducted by applying a constant voltage of -1 V (vs. Ag quasi-RE in NMA-based E, and vs. Al quasi-RE in AlCl_3 -based E) for 5h to investigate the potential electroplating of Al on the Al and Pt electrodes in TSC-SC.

In chapter 4: To study the impact of the Al surface modification of via acidic treatment on Al surface properties and Al plating and stripping, CVs (100 and 500 cycles) were recorded with a biologic potentiostat (VMP12) in AlCl_3 -based E at 25°C , with the scan rate of 20 mV s^{-1} and in a potential range of $-0.5 - 1.0 \text{ V vs. Al quasi-RE}$ in TSC-SC.

In chapter 5: To test the electrochemical stability of the metallic CCs (W, Mo, Ni, Ti, Ta foils), CV was employed using sealed, closed, and airtight TSC-SC with a scan rate of 0.5 mV s^{-1} at a potential window of 0.3 to $2.2 \text{ V vs. Al quasi-RE}$. The W, Mo, Ni, Ti, Ta foils were taken as WE and GC was taken as CE. Complementary to CV, for the determination of the cathodic stability of CCs, LSV was performed with a scan rate of 0.05 mV s^{-1} using the TSC-SC equipped with an Al quasi-RE. To test the electrochemical stability of Mo and W substrates as CC in Swagelok cell setup, the following materials have been taken; Mo, and W rods as CE, Al foil as RE, and GF/A separator. The separator made of glass fiber (GF) are widely used in small-scale labs. Its primary function is to maintain an adequate separation distance between the anode and cathode, effectively preventing any potential short-circuiting issues. Notably, GF/A separator allow the unhindered movement of AlCl_4^- and Al_2Cl_7^- ions between the electrodes during the cyclic processes. CVs were recorded with a scan rate of 0.5 mV s^{-1} at a potential range of 0.3 to $2.2 \text{ V vs. Al quasi-RE}$ and also with a scan rate of 5 mV s^{-1} at different potential ranges of 0 to 1.2 V , 0 to 1.5 V , and 0.5 to 2.5 V . The same CV setup were taken for coin cell consisting of Al foil as anode and coted NP on each metallic CCs as cathode. An overall experimental setup of each chapter is presented in appendix (Figure A-2-2, Figure A-2-3, Figure A-2-4).

3 The advancement and Challenges of Aluminum Triflate-based electrolytes

The presented scientific findings within this chapter have undergone thorough analysis, meticulous review, and subsequent publication in an international peer-reviewed journals:

1. **F. Rahide**, E. Zemlyanushin, G.-M. Bosch, and S. Dsoke, "Open Challenges on Aluminum Triflate-Based Electrolytes for Aluminum Batteries," J Electrochem Soc, vol. 170, no. 3, p. 030546, Mar. 2023, doi: 10.1149/1945-7111/acc762.
2. **F. Rahide**, et al., "Hindered aluminum plating and stripping in urea/NMA/Al(OTF)₃ as a Cl-free electrolyte for Al batteries", J Electrochem Soc, Dec. 2023, doi: 10.1149/1945-7111/ad1553.

3.1 Research Background and Methodology

[EMImCl]: AlCl₃ faces limitations such as being expensive, highly corrosive, hygroscopic, moisture-sensitive, and susceptible to hydrolysis [50], [51]. As a result, efforts have been made to discover alternatives that are Cl-free electrolytes. AlCl₃-free electrolytes, including mixtures containing non-corrosive alternative salts such as aluminum trifluoromethanesulfonate (Al(OTF)₃) and aluminum bis(trifluoromethanesulfonyl)imide (Al(TFSI)₃) have been explored recently [51]. These alternatives aim to address the reactivity concerns associated with chloroaluminate systems. Table 3-1 presents some of the investigated AlCl₃-free electrolytes.

Table 3-1. List of electrolyte compositions reported in the literature.

electrolyte compositions	WE	references
Al(OTF) ₃ /1-butyl-3-methylimidazolium trifluoromethanesulfonate ([BMIM]OTF)	Al	[50]
Al(TFSI) ₃ /acetonitrile	Mo	[52]
aluminum hexafluorophosphate (Al(PF ₆) ₃)/Dimethyl sulfoxide (DMSO)	Cu	[53]
aluminum trifluoromethanesulfonate (Al(OTF) ₃)/propylene carbonate/tetrahydrofuran (THF)		[54]
Al(OTF) ₃ /2-methoxy ethyl ether (diglyme)	Al	[55], [56]
Al(OTF) ₃ /THF	GC, and Au	[57]
Al(OTF) ₃ /LiCl/THF	Au	[58]
aluminum hexa-methylimidazole bis(trifluoromethansulfonyl)imide [Al(MIm) ₆]/[TFSI] ₃	Pt	[59]

aluminum hexa-butylimidazole bis(trifluoromethanesulfonyl)imide [Al(BIm) ₆]/[TFSI] ₃ aluminum hexa-dimethyl sulfoxide [Al(DMSO) ₆]/[TFSI] ₃ [Al(DMSO) ₆]/[OTF] ₃		
Al(OTF) ₃ /tetrabutylammonium chloride (TBAC)/diglyme	Al	[60]
urea/Al(OTF) ₃ /N-methyl acetamide (NMA)	Pt	[41]

Slim and Menke [58] conducted a detailed investigation into the impact of Cl⁻ on the electrochemistry and Al speciation in various systems, including Al(OTF)₃/THF, Al(OTF)₃ plus LiCl in THF, and AlCl₃/THF. Their study, which combined theoretical and experimental methods, revealed that Cl⁻ significantly enhances the electrochemical activity of Al-ions, facilitating easy Al plating. However, one observed drawback is that the presence of Cl⁻ makes the electrolyte corrosive [58]. Given these significant drawbacks, there is an urgent need to explore innovative electrolytes, preferably without chloride content. Key properties desired in an electrolyte include high conductivity, low viscosity, and a wide electrochemical stability window. However, the strong Coulombic interaction between the Al³⁺ cation and its counter anions in common organic solvents limits the solubility of Al-salts, resulting in relatively low ionic conductivity for Al-based electrolytes [38]. To address this, Al(OTF)₃ and Al(TFSI)₃ have recently emerged as non-corrosive alternatives to AlCl₃ [52], [61], [62]. For instance, Chiku *et al.* [52] proposed Al(TFSI)₃ in anhydrous ACN as a new chloride-free electrolyte with a broad electrochemical window and low overpotential for Al deposition or dissolution. This Al(TFSI)₃ in ACN demonstrates an electrochemical window of approximately 3.6 V, surpassing that of traditional ILEs (2.5 V) [52]. Another approach pursued by Mandai and Johansson [59] involves combining AlCl₃ with specific ligands to synthesize a variety of cationic aluminum coordination complexes. By replacing MIm with BIm in [Al(alkylimidazole (RIm))₆][TFSI]₃, where R can be butyl or methyl, they obtained a room-temperature molten cationic Al-solvated quasi-IL. This new [Al(BIm)₆][TFSI]₃ exhibits unique properties as a non-moisture-sensitive Al-based quasi-ionic liquid, displaying both cathodic and anodic current due to the deposition and dissolution of Al metal, respectively [59]. In other study, Wang *et al.* [61] investigated an IL electrolyte formed by mixing 1-Butyl-3-methylimidazolium trifluoromethanesulfonate ([BMIM]OTF) with the corresponding aluminum salt (Al(OTF)₃). Their study demonstrated that the Al(OTF)₃/[BMIM]OTF IL electrolyte exhibited a broader

electrochemical stability window compared to the AlCl_3 -based E, with an anodic stability of up to 3.25 V vs. Al^{3+} on a GC WE. However, it was observed that increasing the concentration of $\text{Al}(\text{OTf})_3$ led to a pairing phenomenon, resulting in enhanced conductivity and reduced viscosity of the electrolyte [61]. Meanwhile, Reed *et al.* [63] conducted a study on the physicochemical characteristics of $\text{Al}(\text{OTf})_3$ in 2-methoxy-ethyl ether diglyme, combining experimental data with Density Functional Theory calculations. According to their calculations, the electrochemical window varied from 7.2 V for neat diglyme to 3.5 V for a highly concentrated electrolyte. Additionally, the study indicated that the oxidative stability of the triflate and the reductive stability of the $[\text{Al}(\text{diglyme})_2]^{3+}$ complex played crucial roles in controlling the cathodic and anodic edges of the electrochemical window [63]. Mandai and Johansson [41] conducted a study on room-temperature ternary electrolytes composed of mixtures of $\text{Al}(\text{OTf})_3$, NMA, and urea. They found that the conductivity of these mixtures, which relies on interactions between multivalent metal cations and corresponding counter anions, could be improved by adjusting the amount of urea. They identified the most suitable molar ratio of NMA-based E, which exhibited optimal ionic conductivity ($2.5 \times 10^{-3} \text{ S cm}^{-1}$) and strong solvation ability, to be 0.19/0.76/0.05 [41]. This selected formulation was electrochemically tested on a Pt electrode, demonstrating the potential for Al plating and stripping. However, further electrochemical studies are required to fully assess the suitability of this electrolyte formulation for AlBs. Additionally, it is crucial to explore alternative sustainable solvents to replace the harmful NMA. With this respect, one promising class of solvents is sulfones, which exhibit weak coordination strength with Al^{3+} . Previous research on Al deposition has shown that Al can be plated in dimethyl sulfone ($(\text{CH}_3)_2\text{SO}_2$) and AlCl_3 [64]. However, the high melting point of dimethyl sulfone restricts electrochemical plating to temperatures above 100°C. Linear sulfones have been investigated as solvents for supercapacitors [65] and for Li-ion and Mg-ion batteries [66], [67]. Ethyl-Isopropyl-Sulfone (EiPS) has been utilized in AlBs, with one work attempting to replace corrosive AlCl_3 with $\text{Al}(\text{BF}_4)_3$ without success, as the BF_4^- anion led to the formation of a stable passivating layer on the negative electrode [68], blocking further Al plating and stripping [69]. This work highlights and claims that the presence of AlCl_3 is fundamental for Al deposition and dissolution [68]. Among sulfone-type solvents, *i.e.* ethyl isobutyl sulfone (EiBS) or isopropyl-*s*-butyl sulfone (iPsBs), EiPS stands out due to its low viscosity and high permittivity, likely influenced by a greater interaction between the

more branched alkyl chains [61]. The same effect was investigated by Das *et al.* [70] for room-temperature ionic liquids. EiPS has low melting (-8°C) and high boiling (265°C) points, making it a suitable solvent. The low melting point of EiPS has a correlation with its viscosity, which is due to the weak intermolecular force of EiPS [65]. Moreover, EiPS has good thermal stability with no significant degradation or evaporation up to 85°C [71]. Its high stability is due to its low reactivity with H_2O [65]. Pure EiPS has an electrochemical stability window (ESW) of 3.7 V [65] and even 3.9 V [71]. Furthermore, the reported sulfone-based electrolyte consisting of the mixture of AlCl_3 and dialkylsulfone exhibited an excellent performance, including no corrosion and no Al dendrite formation, as well as relatively good charge/discharge capacity in AIBs [69]. In seeking an ideal electrolyte, it is essential to have a solvent with sufficient solvating power to form a liquid electrolyte at RT. Acetamide and urea mixtures have been found to have optimal solvation properties and be capable of dissolving salts of divalent metal ions like $\text{Mg}[\text{OTF}]_2$ [72]. Since there are many analogies between Mg and Al in terms of the electrochemical properties, this knowledge can potentially be transferred to Al-batteries. The desired solubility is related to the ability of carbonyl and primary amino groups to coordinate with various cations and anions, leading to salt dissociation through relaxation of hydrogen-bond interactions between the organic compound and ion-ion interactions. In addition, the strength of these coordination bonds affects the bond strength. The deformation of the hydrogen bonds also affects the bond strength, which should also result in a Raman frequency shift and lower thermal stability. However, excessively strong coordination bonds can cause substantial polarization and large overpotential [72].

The NMA-based E possesses a wider electrochemical stability window compared to $[\text{EMImCl}]:\text{AlCl}_3$ [41]. Despite this advantage, it exhibits insufficient electrochemical Al plating and stripping on Al substrate, as presented in this chapter [1]. Many other AlCl_3 -free electrolytes (summarized in Table 3-1) also demonstrate poor performance in terms of plating and stripping Al. The $\text{Al}(\text{OTF})_3$ salt shows poor plating and stripping not only in a mixture with urea and NMA, but also with other solvents like diglyme [1], [41], [55], [56]. Al electrodeposition on Mo substrate from 1-butylimidazole bis(trifluoromethanesulfonyl) imide demonstrates quasi-reversible plating/stripping, but this is reversible only for a limited number of cycles or with significant side reactions [59]. $\text{Al}(\text{TFSI})_3$ in anhydrous ACN on Mo substrate and $\text{Al}(\text{PF}_6)_3$ in dimethyl sulfoxide on Cu substrate shows similar quasi-reversible behavior with significant plating/stripping

overpotentials (> 1.5 V) [52], [53]. For successful Al plating and stripping in non-corrosive environments, two approaches have been proposed: either modifying the Al anode or the electrolyte. The Al anode can be modified through techniques such as anode amorphization [73], anode alloying [74], [75], and surface modification [76], [77], [78], [79]. This modification of the anode-electrolyte interphase plays a vital role in enabling the plating and stripping processes. Similarly, the electrolyte can be altered by developing concentrated electrolytes [80], adding water scavengers [81], [82], and incorporating additives [60], [83].

The amount of active Al species in the electrolyte significantly influences the appearance of Al deposits [15]. A chlorine-free electrolyte alone cannot guarantee reversible Al plating and stripping without an appropriate electrode-electrolyte interphase which allows for the plating and stripping process [50], [84]. The solid electrolyte interphase (SEI) can be formed artificially before cell assembly or during the initial cell operation when reduced byproducts of the solvent deposit on the anode surface [85], [86], [87]. The study of Loaiza, *et al.* [88] revealed that the initial passivation layer formed upon contact with ILE is porous and intricate, comprised of an outer inorganic/organic layer and an inner oxide-rich layer. A stable and robust electrode-electrolyte interphase layer can improve the cyclic stability of the battery cell by preventing additional solvent reduction and anode component disintegration (as it is well-known from the lithium battery technologies) [29], [79]. Without this protection, byproducts of ILE breakdown can be deposited again onto newly generated surfaces, and the interfaces may become unstable due to the ongoing process of dissolution and deposition [89]. Regardless of the type of electrolyte, Al metal electrodes are considered state-of-the-art anode materials in AIBs [16], [33], [77], [90]. The state of the Al foil surface and the electrode-electrolyte interphase significantly impact the performance of AIBs [23], [24], [89], [90].

The amorphous ion-insulator Al_2O_3 oxide passivation film covering the metallic Al anode blocks the anode's activation and affects the attainability of the reversible reaction of Al plating and stripping, leading to substantial overpotential [15], [77], [89]. However, at the same time, this passivation layer provides protection against corrosion induced by the ILE, so a good balance between exposed and covered Al sites is desirable [77]. Al_2O_3 oxide passivation film can be dissolved locally, enabling adequate Al plating/stripping reaction when it is in contact with ILE [90], [91]; this can be considered as an Al surface modification that can be done before cell

assembly. Surface modification of the Al foil, such as partial removal or modification of the Al_2O_3 oxide passivation film, plays a crucial role in enhancing battery cell performance. Al surface modification guarantees adequate electrolyte penetration of the Al metal anode. This modification as an extra and time-consuming step has hampered the development and real application of alternative and non-corrosive non-aqueous electrolytes [50]. The Al_2O_3 oxide passivation film removal, as a surface modification, determines the reversibility of the Al plating/stripping at the electrode/electrolyte interface [34], [50]. Complete removal of Al_2O_3 oxide passivation film can be detrimental as it prevents Al metal electrode disintegration. Studies have shown that removing the thick oxide film layer during surface treatment is essential for improving battery cell performance. Go *et al.* [79] claimed that the etched and electropolished Al foil has the greatest effect on AIBs' performance [79]. A surface treatment (as a type of surface modification) can typically be achieved by immersing the Al foil in ILE to partially remove or modify the Al_2O_3 oxide passivation film and build an Al, Cl, and N-rich layer at the surface, thus creating an "artificial interphase" [84]. Long *et al.* [92] demonstrated that, with this method, the dissolved Al_2O_3 oxide passivation film in the ILE is replaced by an interphase layer rich in Cl and O species. On the other side, a complete removal of Al_2O_3 oxide passivation film may be detrimental as this oxide prevents Al metal electrode disintegration [16], [93]. The morphological changes of Al metal as a function of immersion time in the ILE were also examined by Lee *et al.* [89], who found that a new oxide layer with a particular lattice plane was formed on the Al surface. These findings confirmed that removing the thick oxide film layer during treatment is crucial for enhancing battery cell performance [50]. However, the function of both the native and electrolyte-derived passivation layers is not fully understood despite their significant influence on the electrochemical performance of the Al anode in both aqueous [94] and non-aqueous [50], [84], [89] systems.

3.2 Open Challenges on Aluminum Triflate-based Electrolytes

Motivated by the studies on chloroaluminate-free electrolytes mentioned earlier, we performed an electrochemical investigation of two electrolyte compositions utilizing the $\text{Al}(\text{OTF})_3$ salt. Specifically, we studied a composition based on NMA-based E and another one based on EiPS-based E. Our investigation involved systematically varying conditions such as temperature and

electrode substrates, which allowed us to uncover significant challenges that hinder the practical application of these so-called "non-corrosive" electrolytes in real AIBs.

3.2.1 Findings and Discussion

The subsequent section presents the outcomes pertaining to the physical properties of the $\text{Al}(\text{OTF})_3$ -based electrolytes. In Figure 3-1(a) and (b), we can observe the ionic conductivity, viscosity, and density of the EiPS-based E across a temperature range of 20 to 80°C. Figure 3-1(c) presents the temperature-dependent impedance spectra displayed as Bode plots, where impedance is plotted against the measuring frequency. The plateau value in the Bode plot represents the bulk resistance for ion movement. As the temperature increases, the plateau value decreases due to the enhanced conductivity of the electrolyte. Density and viscosity values can be found in Table 3-2. The corresponding physical parameters for the NMA-based E have been documented in the study by Mandai and Johansson [41]. Typically, the conductivity of common electrolytes is directly related to their viscosity; however, the NMA-based E exhibits an interesting characteristic of high conductivity despite having high viscosity and low fluidity [41]. Specifically, the optimized molar ratio of NMA-based E (0.19/0.76/0.05) displays an impressive ionic conductivity value of $2.5 \times 10^{-3} \text{ S cm}^{-1}$ at 30°C [41]. In contrast, the EiPS-based E (0.65:0.05:0.30) exhibits a lower conductivity of 0.38 mS cm^{-1} at 30°C. In summary, the EiPS-based E demonstrates high viscosity, leading to a relatively lower ionic conductivity, whereas the NMA-based E (0.19/0.76/0.05) formulation achieves high conductivity despite its higher viscosity [41]. Solvents with a high dielectric constant (ϵ_r) have the effect of moderating the strong electric field induced by charged species, thus weakening salt dissociation and ion-ion interactions [95]. The ionic conductivity plays a crucial role in determining the rate of charge transport for active ions. The small and trivalent Al^{3+} ion (ionic radius of 0.050 nm) with its strong electric field influences the polarization of the solvated ions. Moreover, the dissociation of ternary electrolytes is strongly correlated with their composition. For example, it has been demonstrated that a minor substitution of NMA with urea reduces the dissociation of $\text{Al}(\text{OTF})_3$, while additional substitution enhances salt dissociation [41]. NMA, being one of the most self-associated liquids, possesses a high static dielectric constant and high conductivity compared to other molecular liquids [95]. In the NMA-based E, NMA serves as a solvent for $\text{Al}(\text{OTF})_3$, and a small substitution of NMA by urea

surprisingly promotes the dissociation of $\text{Al}(\text{OTF})_3$. However, a mixture of NMA and urea has a lower dielectric constant ($\epsilon_r=81.3$) than pure NMA ($\epsilon_r=178$) [41], [95]. Urea's role in the electrolyte's properties is still a subject of discussion [41], [96], [97]. Urea facilitates further dissociation of the $\text{Al}(\text{OTF})_3$ salt-solvent complex through bidentate hydrogen bonding with OTF- in deep eutectic solvents [98]. On the other hand, at 25°C, pure EiPS ($\epsilon_r=55$) has a lower dielectric constant compared to pure NMA, which implies higher ionic conductivity for NMA-based E [65], [95]. EiPS has a relatively low melting point of -8°C and a high boiling point of 265°C, with a viscosity of 5.6 mPa.s at 25°C [71], whereas NMA's melting point ranges from 26 to 28°C, with a high boiling point of 204 to 206°C [99]. This suggests that EiPS may have a wider operable temperature window compared to the NMA-based E. Additionally, at 20°C, the electrolyte containing 100% EiPS exhibits a viscosity of 12.3 mPa.s with a conductivity of 3.5 mS cm⁻¹ [71]. In summary, the EiPS-based E exhibits lower ionic conductivity and higher viscosity but possesses high thermal stability due to its wider operating temperature range. A summary of the physicochemical properties of $\text{Al}(\text{OTF})_3$ -based electrolytes is presented in Table A-3- 1.

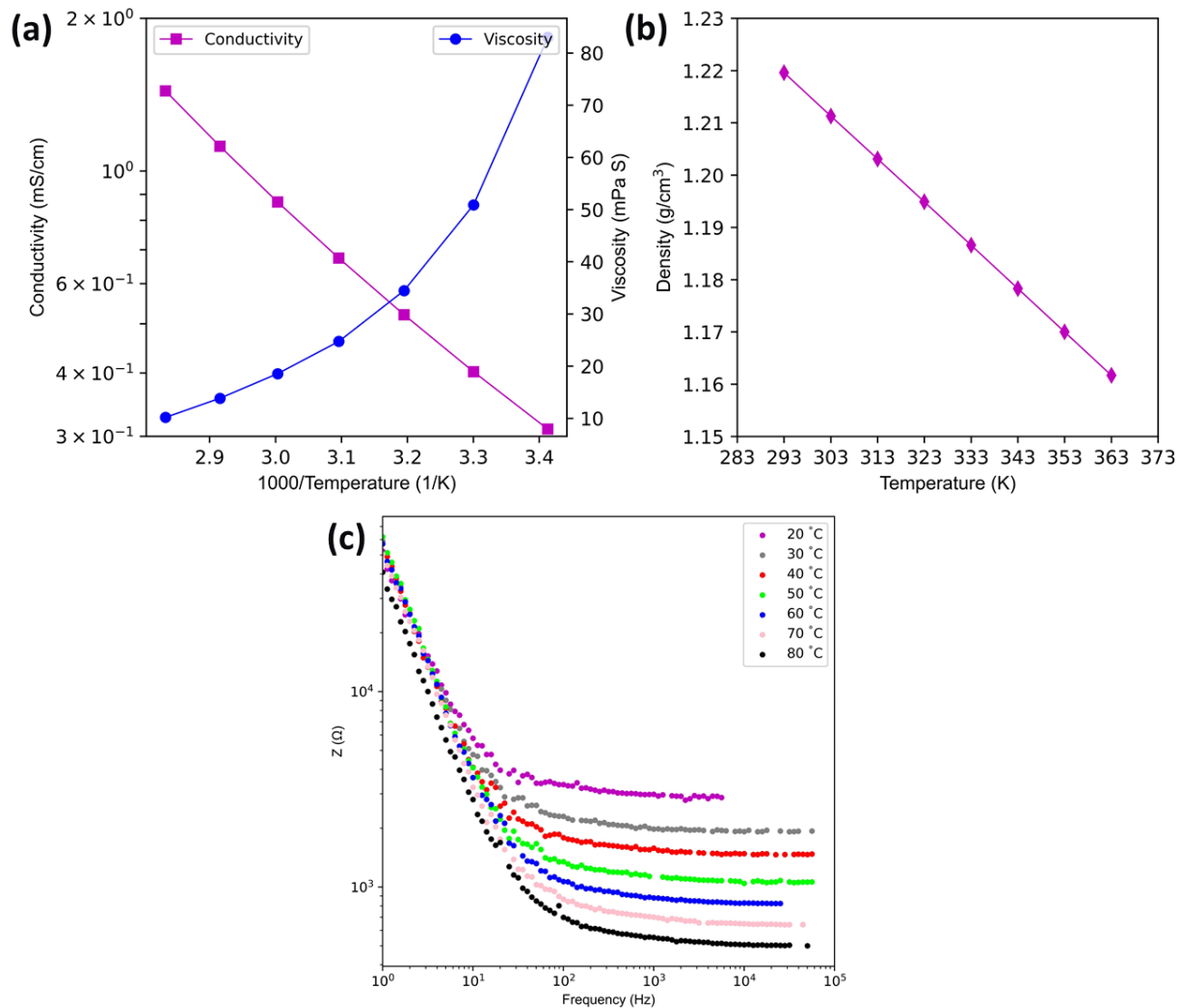


Figure 3-1. (a) Arrhenius plots of the ionic conductivity σ and viscosity η (b) Density ρ in the 20–80°C

Table 3-2. Physicochemical properties of Al(OTF)₃-base electrolytes at 30°C.

	ρ [g/cm ³]	η [mPa.s]	σ [mS cm ⁻¹]	ϵ_r solvent
urea/NMA/Al(OTF) ₃ [41]	1.11	33.4	2.4 at 30°C	178 at 30°C[95]
urea/EiPS/Al(OTF) ₃	1.21	50.90	0.4 at 30°C	55 at 25°C[65]

The following section showcases the findings concerning the intermolecular interactions and thermal stability of the electrolyte. Intermolecular interactions in ternary solvents play a significant role in influencing ion mobility and conductivity, therefore, to gain insight into these interactions, we conducted TGA coupled with differential scanning calorimetry (DSC) and Fourier Transform Infrared Spectroscopy (FT-IR). This combined approach allowed us to investigate the interaction between the different substances in the electrolyte. Additionally, thermal analysis is

crucial in understanding the thermal stability of the individual components present in the electrolyte. By studying the thermal behavior of the electrolyte components, we can better comprehend their stability under different temperature conditions. The melting and boiling points of the four components, namely NMA, EiPS, urea, and Al(OTF)₃, are presented in Table 3-3. At the initial conditions of the TGA-DSC measurement, which is an ambient temperature of 35°C, NMA and EiPS exist in liquid form, while urea and Al(OTF)₃ are in solid states.

Table 3-3. Melting and boiling points of the electrolyte components

	Melting point [°C]	Boiling point [°C]
N-methylacetamid (NMA) [99]	27	205
1-Ethyl isopropyl sulfone (EiPS)	-8[65]	265[65]
Urea	133 [100](decomposition)	-
Aluminum trifluoromethane sulfonate (Al(OTF) ₃)	300	N/A

Figure 3-2(a) depicts a TGA measurement conducted on the four chemicals, within a temperature range from 35 to 90°C with a heating rate of 1 K min⁻¹. Two solid chemicals, namely urea and Al(OTF)₃, demonstrate no weight loss throughout the entire temperature range, indicating their high thermal stability. On the contrary, NMA and EiPS, which are in liquid form within this temperature range and have not yet reached their boiling points, exhibit a continuous decrease in mass. Despite being in liquid state, these substances experience a loss of mass during the TGA measurement. The DSC measurement (Figure 3-2(c) and (d)) reveals no signs of decomposition for the substances under investigation. The observed mass loss during the TGA measurement can be attributed to the continuous gas flow surrounding the sample. This enables a continuous removal of material in the gas phase, leading to the observed mass reduction. The mass loss is directly linked to evaporation, as there is a constant concentration balance in the gas phase above the liquid. The vapor pressure, which reflects the intermolecular interactions within the solution, allows us to infer the strength of these interactions from the mass loss under the given conditions. Comparing the mass loss of NMA to that of EiPS (Figure 3-2(a)), we observe that the mass loss of NMA is approximately twice as much as that of EiPS. This finding is also consistent with the boiling points of the two liquids reported in Table 3-3. The higher mass loss and lower boiling point of NMA suggest that NMA molecules exhibit weaker intermolecular interactions compared to the molecules of EiPS. This difference in intermolecular interactions can be attributed to the additional van-der-Waals interactions present between the isopropyl and ethyl groups in EiPS.

Figure 3-2 (b) shows the TGA results of the electrolyte mixtures, measured under the same conditions as the individual components. The measurement was done between 35 and 90°C with a heating rate of 1 K min⁻¹. In both cases, a continuous decrease in mass is observed. Notably, the mixture based on NMA exhibits a significantly lower mass loss, only 5%, compared to the pure NMA. Conversely, the electrolyte with EiPS shows a substantial mass loss of 26%. The evaporation rate in the mixture is significantly reduced in comparison to the pure NMA. This difference in mass loss indicates that the intermolecular interactions are strengthened when adding the other two components (urea and Al(OTF)₃) in the ternary electrolyte. Interestingly, there are no significant changes in mass loss when comparing the EiPS electrolyte mixture with pure EiPS. This observation suggests that there are no strong intermolecular interactions between EiPS and the other two substances in the ternary electrolyte, which maintains the vapor pressure unchanged. However, NMA can effectively interact with the trivalent Al³⁺ ion, leading to a strong solvation effect.

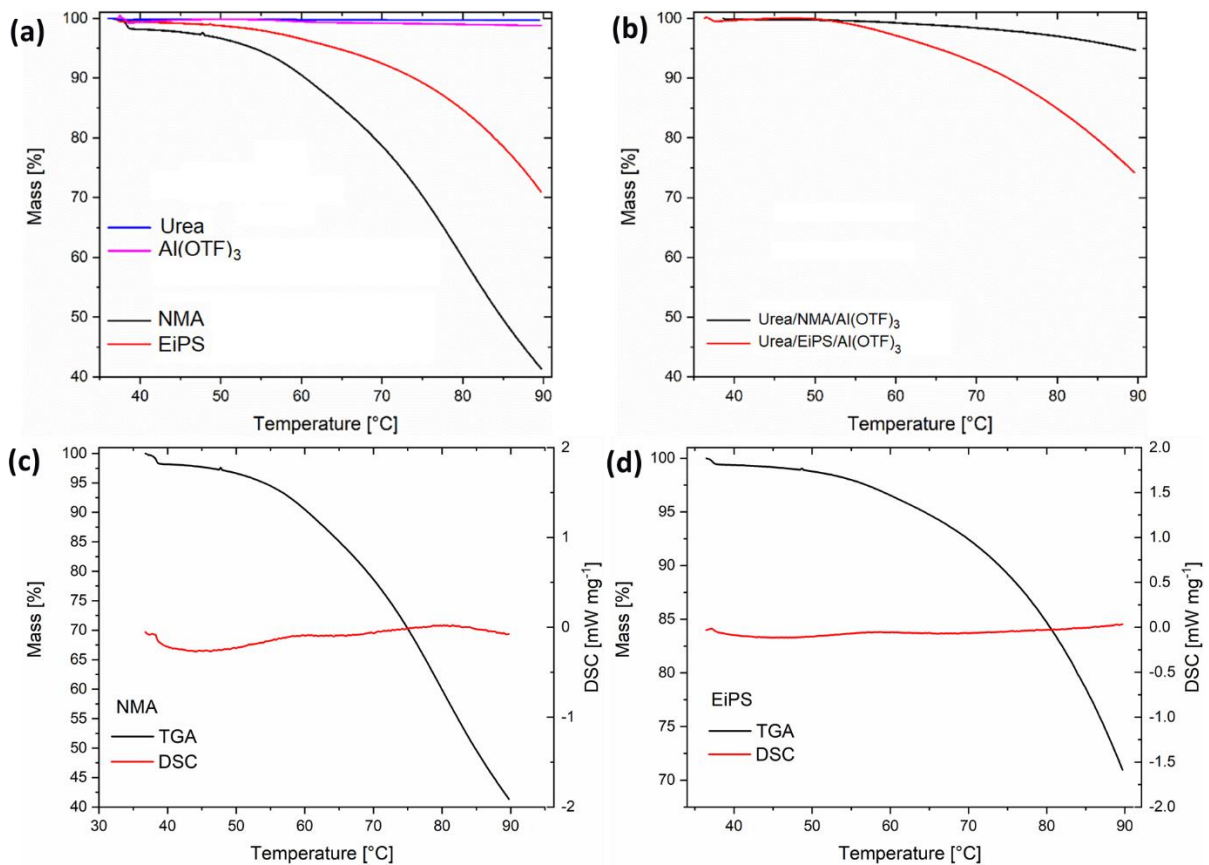


Figure 3-2. TGA of (a) the pure chemicals and (b) the two electrolyte mixtures. C, and d) DSC and TGA curves of NMA and EiPS.

NMA forms hydrogen bonds with urea, providing further intermolecular interactions [41]. Consequently, the high charge concentration of the Al^{3+} ion is distributed over the solvent, enhancing the stability of the electrolyte. In contrast, in $[\text{Al}(\text{EiPS})_3]^{3+}$, the strong Al–O bond, as confirmed by Y. Nakayama *et al.* [69] prevents successful Al plating. However, the strategic addition of urea weakens the Al-EiPS interaction, leading to the formation of a hybrid complex with urea, which is expected to be electrochemically active and allows for desirable Al plating and stripping behavior. Figure 3-3 shows the FT-IR spectra of the two electrolyte mixtures in comparison with the pure components. The full spectra are available Figure 3-3(c) and (d). The analysis focuses on studying the interactions of urea, NMA, and EiPS with Al^{3+} and their respective mixtures. The FT-IR spectra provide valuable insights into the molecular vibrations and functional groups present in the samples, allowing us to understand the nature of the interactions between the components in the electrolyte mixtures. It is well-established that urea forms coordinative bonds with Al^{3+} cations through the free electron pairs of oxygen, effectively transferring an electron from oxygen to the Al^{3+} cation, thus lowering the electron density at the oxygen [44]. As a result, the electron density at the oxygen is reduced, leading to a shift in electron density within the urea molecule and a stronger attraction of protons to the N atoms. This enhanced binding of the amino groups can be observed in the FT-IR spectrum, serving as an indicator of the coordination of urea to Al^{3+} . The vibrational bands corresponding to the N-H bonds can be observed in the range of 3600 and 3200 cm^{-1} [101]. In Figure 3-3(a), a comparison of the two electrolytes along with the pure chemicals is presented. The bands related to the N-H vibration of pure urea at 3425 and 3325 cm^{-1} are shifted to higher wavenumbers in the two electrolyte mixtures due to the formation of Al-complexes and the strengthening of the binding caused by intermolecular interactions. Similar interactions are also expected for NMA, but since the bands of NMA and urea largely overlap, a clear distinction cannot be made based on the FT-IR spectrum alone. Likewise, it can be presumed that a similar interaction occurs between the S=O groups of EiPS and the Al^{3+} cation, similar to the C=O group of urea. However, in Figure 3-3(b), which displays the relevant range of the FT-IR spectrum from 1500 to 1100 cm^{-1} , no significant shift in the vibrational bands for EiPS is observed when urea is present in the mixture. This lack of a noticeable shift indicates that there is no strong interaction between the S=O groups of EiPS and

the Al^{3+} cation in the presence of urea. The full FT-IR spectra of each pure component and electrolyte mixtures are presented in Figure A-3- 1.

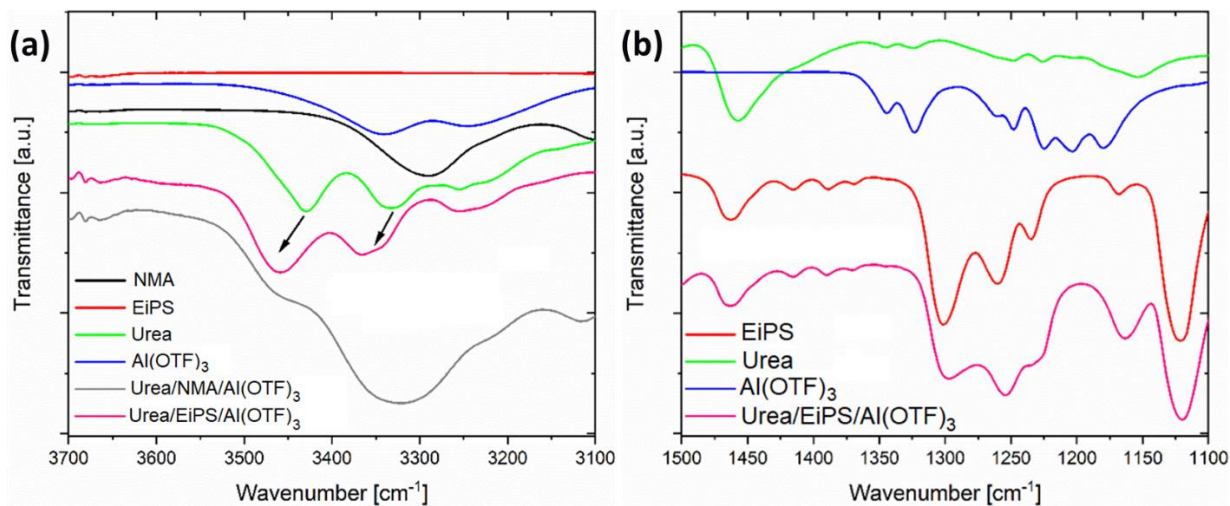


Figure 3-3. FT-IR spectra of the pure substances and the two electrolyte mixtures in the range for (a) N-H vibration bands for the two electrolyte compositions and (b) S=O vibration bands for the EiPS-based E.

In the subsequent section, the findings pertaining to the electrochemical characterization of the electrolytes are presented. The initial CV curve obtained on a Pt disc electrode in the NMA-based E shows agreement with previous literature¹⁶, despite using a different cell setup (Figure 3-4 cycle 1). However, a noticeable shift in the oxidation peak is observed as cycling progresses, while only one cycle was previously reported in the literature¹⁶. To investigate the reason behind this peak drift, a calibration of the Al quasi-RE against Ferrocene (used as an internal reference) was conducted. Figure 3-4(b) demonstrates that the redox peaks of Ferrocene against the Al quasi-RE exhibit significant shifts to lower potentials with increasing cycle number over 24h. This potential drift can be attributed to changes in the surface of the Al quasi-RE during cycling and its interaction with the electrolyte. In contrast, the potential measured using the Ag quasi-RE remains mainly stable during the 24-hour period (Figure 3-4(c)). Metallic Al is commonly used as a RE in Al battery-related literature, and reference calibration has not been previously reported. Based on these findings, it is evident that the Al quasi-RE is unsuitable for studying these electrolytes, and employing an Ag quasi-RE would be a more appropriate choice.

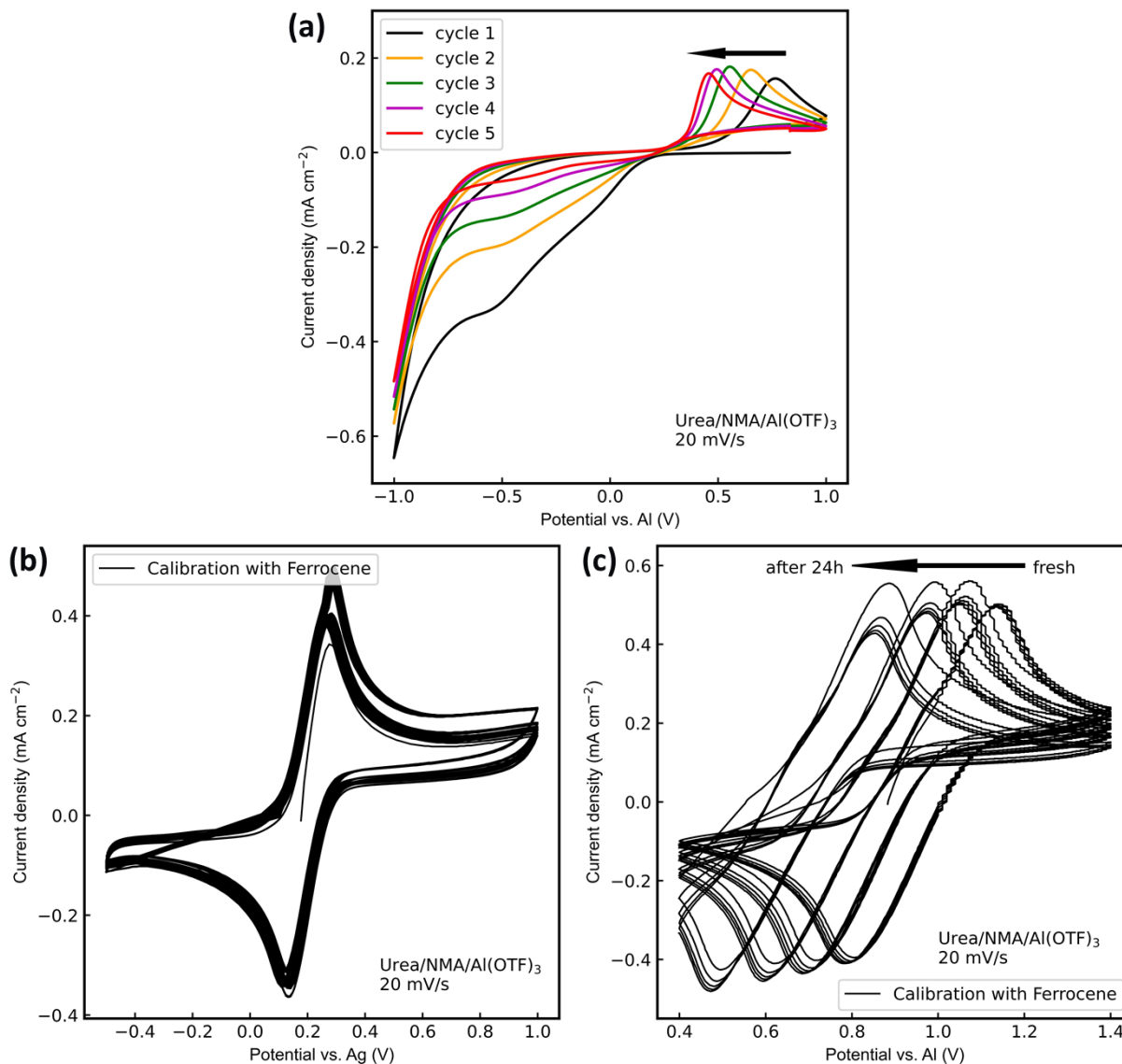


Figure 3-4. (a) Recorded CVs with the scan rate of 20 mV s^{-1} on a Pt disc as a WE and Al quasi-RE in NMA-based E. Ferrocene as an internal RE (b) Al quasi-RE (c) Ag quasi-RE. TSC1600-CC with a Pt as a CE.

The anodic stability of the electrolytes was evaluated using LSV performed on Pt and GC discs as WEs, with the Ag quasi-RE (Figure 3-5). The cell potential was recorded from the open circuit potential (OCP) to +3 V at scan rates of 10 and 5 mV s^{-1} until an increase in current was observed. A current of 0.2 mA cm^{-2} was chosen as the criterion to determine the potential limit. Figure 3-5 illustrates that the anodic potential limit of the EiPS-based E is greater than that of the NMA-based E, regardless of the electrode substrate used.

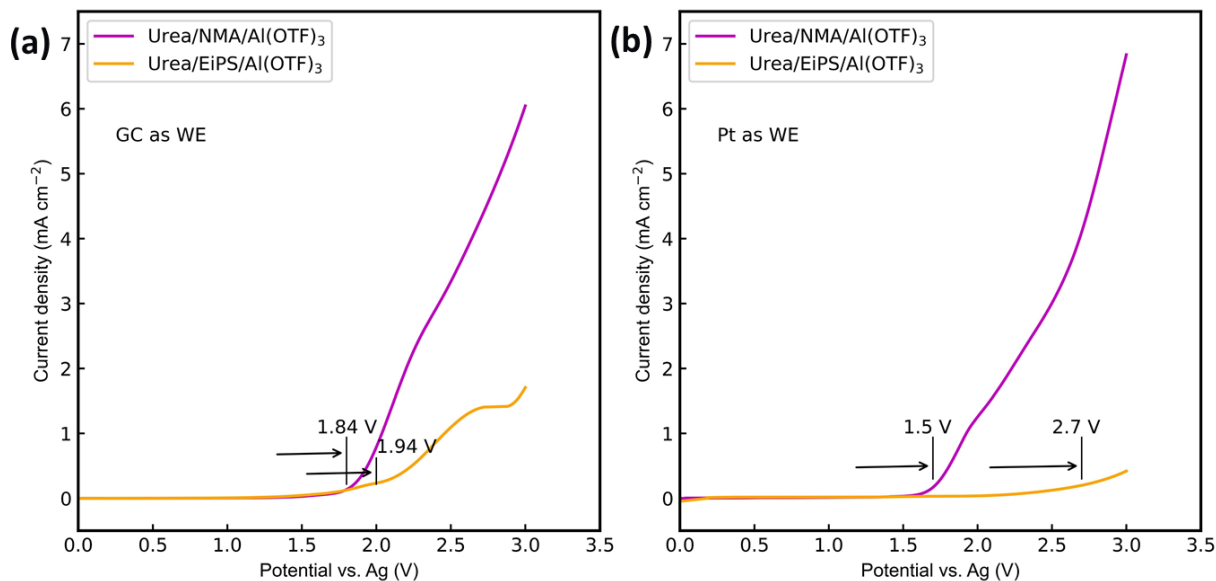


Figure 3-5. Recorded LSV for AlCl_3 -free electrolytes at 25°C in TSC1600-CC recorded on a) a GC disc at the scan rate of 10 mV s^{-1} and b) a Pt disc at the scan rate of 5 mV s^{-1} with Ag quasi-RE and Pt CE.

As shown in Figure 3-6(a) and (b), an oxidation peak appears at -0.2 V vs. Ag on the Pt electrode in the $\text{Al}(\text{OTF})_3$ -based electrolyte. In the NMA-based E, two different types of Pt substrates, disc, and foil, with electrode surface areas of 0.07 cm^2 and 0.28 cm^2 , respectively, were used as WEs in two different cell configurations (Figure 3-6(a) and Figure 3-13). The crucial role of urea is evident in Figure 3-6(c), as the absence of urea completely disables the electrochemical reduction, highlighting the importance of the Al-urea interaction for Al plating and stripping. Urea plays a fundamental role in the desolvation process (i.e., weakening the interaction between EiPS and Al^{3+}), and without this component, the reduction of Al^{3+} is hindered. Urea also improves the dielectric properties of the electrolyte, consequently increasing the ionic conductivity by facilitating the dissociation of $\text{Al}(\text{OTF})_3$ [25]. The solvent's dielectric constant (ϵ_r) directly impacts salt dissociation and ion-ion interactions, with lower dielectric constants leading to lower conductivity and less salt dissociation. Therefore, the degree of salt dissociation depends on the competitive interactions of ion-ion and ion-solvent. The improvement of $\text{Al}(\text{OTF})_3$ dissociation with the addition of urea has been demonstrated in NMA-based E [41]. The molar ratio between the solvent and urea significantly affects the solvation ability, as even a small amount of urea initiates the $\text{Al}(\text{OTF})_3$ dissociation [25]. Considering the relatively low dielectric constant of EiPS (55) [65], the addition of urea as a substitution for EiPS would likely enhance the dissociation of

Al(OTF)₃. However, despite indications of possible plating and stripping, the capacities over consecutive CV cycles and coulombic efficiency of both Al(OTF)₃-based electrolytes on Pt electrodes (Figure 3-7) are much smaller compared to those reported for "standard" AlCl₃/ILEs[41]. Additionally, the coulombic efficiency remains too low for practical battery applications.

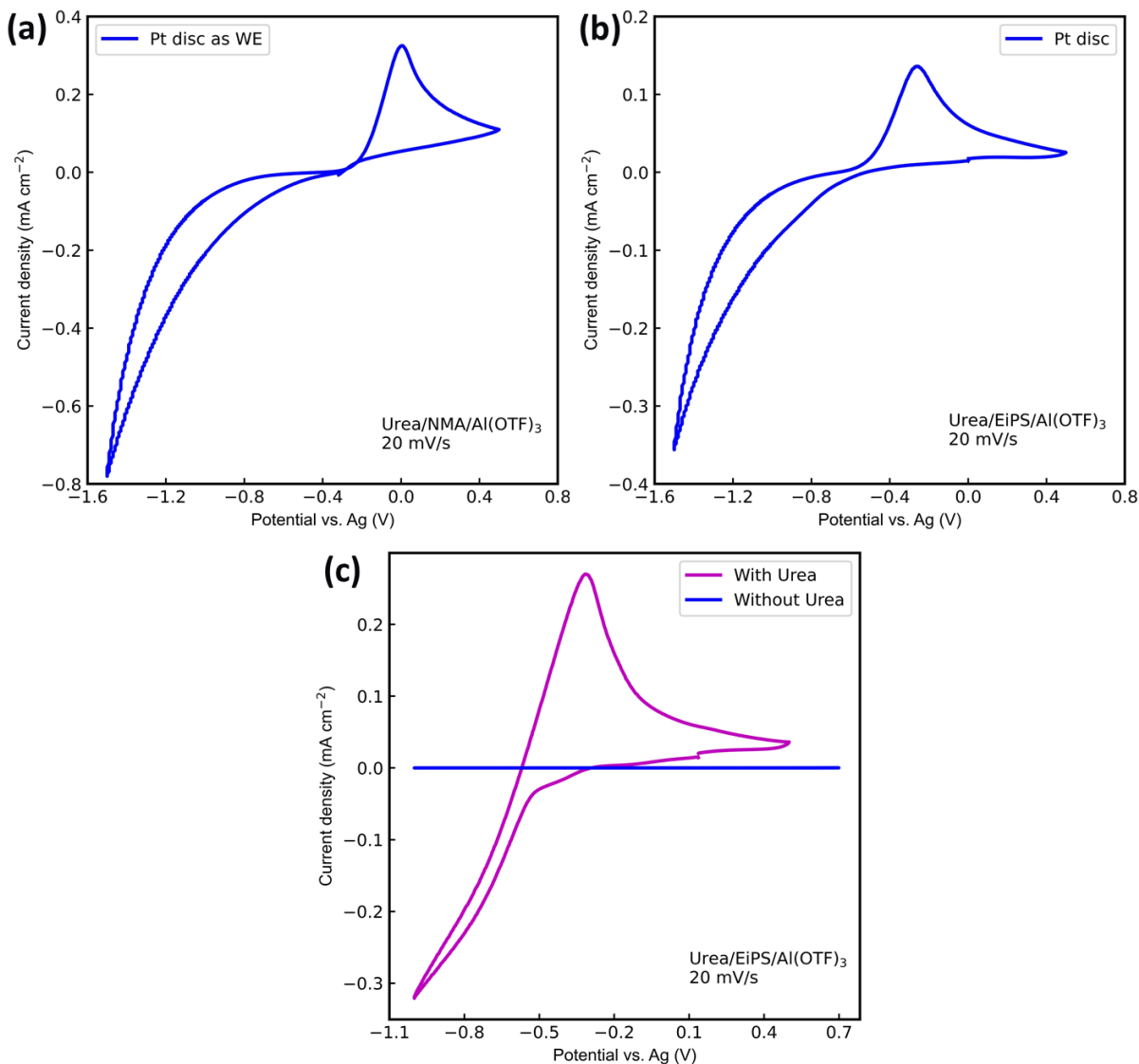


Figure 3-6. Recorded CV on a Pt disc in TSC1600-CC in (a) NMA-based E (b) EiPS-based E. (c) EiPS-based E and EiPS/Al(OTF)₃ with Ag quasi-RE and Pt CE.

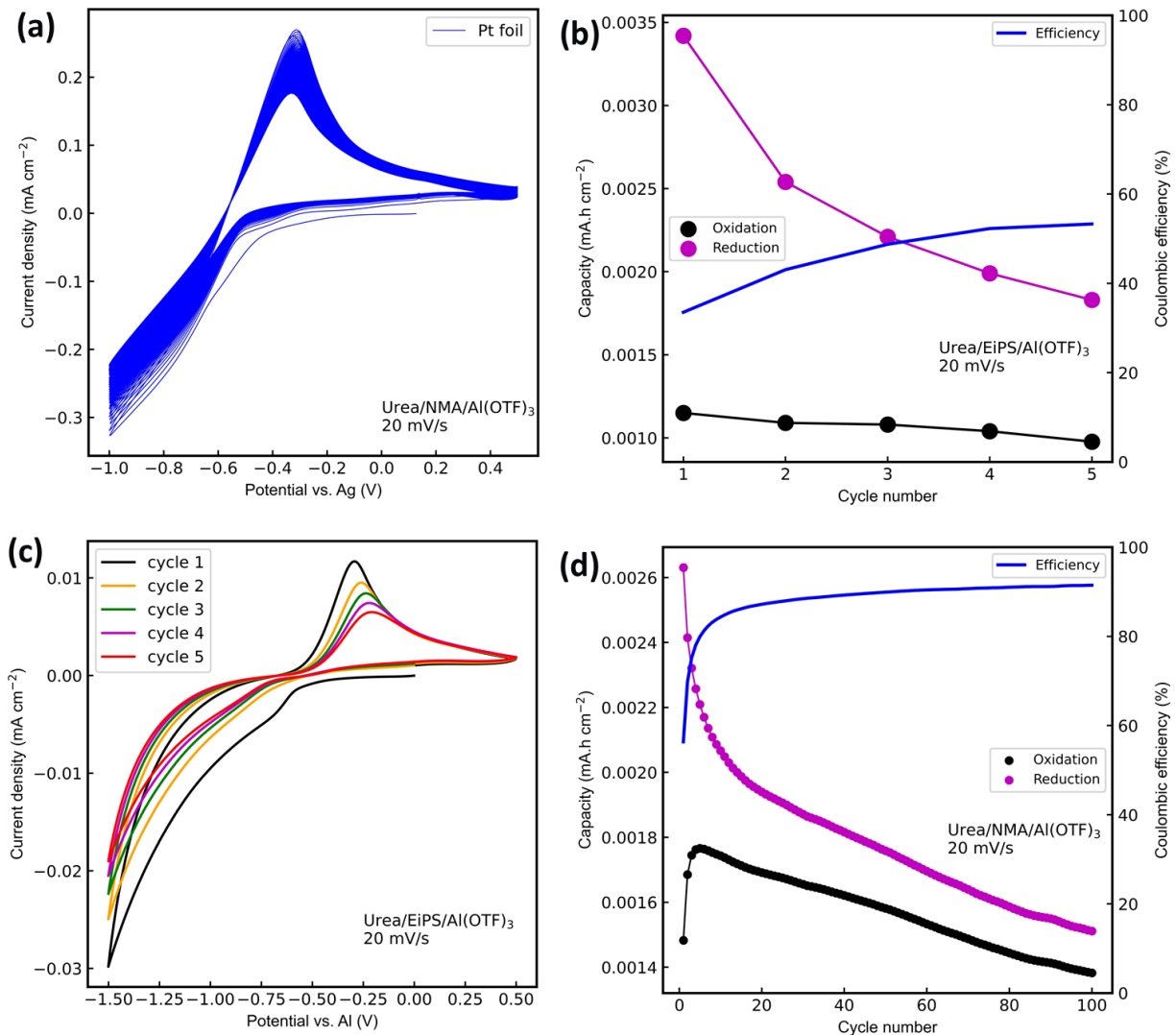


Figure 3-7. Recorded CV on a Pt foil as WE vs. Ag quasi-RE in TSC-SC with GC CE. And oxidation and reduction capacities, and Coulombic efficiency at 20 mV s⁻¹ in (a), and (b) NMA-based E. (c) and (d) in EIPS-based E in TSC1600-CC with Ag quasi-RE and Pt CE.

In the following results related to the effect of the cathodic potential limit are presented. The applied voltage range plays a crucial role in determining the performance of the electrolyte as it defines the limits of electrolyte decomposition and regulates the potential range for the desired reactions. To gain a better understanding of the reversibility of the redox reaction of interest, various cathodic potentials were tested, with the lower potential limit set at -1 V and -1.5 V vs. Ag (Figure 3-8). It is important to note that the observed reduction/oxidation currents could be attributed to either Al deposition/dissolution or possible electrolyte decomposition (or a combination of both reactions). The differentiation between these processes is critical for

assessing the stability and performance of the electrolyte in practical battery applications. In general, a low coulombic efficiency is often a consequence of undesirable and irreversible reactions that are unrelated to the battery's normal charge and discharge behavior. These reactions may be triggered by factors such as the presence of trace water or the irreversible decomposition of the electrolyte components. In the case of the NMA-based E, the strong coordination of NMA and urea with Al^{3+} ions results in a significant polarization, requiring a high overpotential for the desolvation process ¹⁶. This can shift the electrodeposition to lower potentials, leading to lower cycling efficiency. Additionally, side reactions that occur at larger cathodic limits can contribute to the decomposition of the electrolyte, further affecting cycling efficiency. Figure 3-8(a) shows that for the 5th cycle, the reduction reaction at the lower cathodic limit has a noticeable overpotential, indicating kinetic limitations. Consequently, a lower cut-off potential of -1.5 V yields a higher capacity due to increased irreversibility. However, a lower cut-off potential of -1.5 V also induces higher irreversibility, as shown in Figure 3-8(b) and (c). To mitigate this, the cathodic limit of -1 V has been chosen for further studies (Figure 3-8(b) and (c)). For the EiPS-based E, within the lower potential cut-off of -1 V, negligible current density is observed, necessitating a further decrease in potential. Figure 3-9(a) displays the 5th CV cycle of the EiPS-based E with two cathodic limits of -1.5 V and -1.8 V. With a cathodic limit of -1.8 V, the irreversibility increases dramatically, resulting in a smaller oxidation current. Hence, the optimum cathodic limit for the EiPS-based E is considered to be -1.5 V.

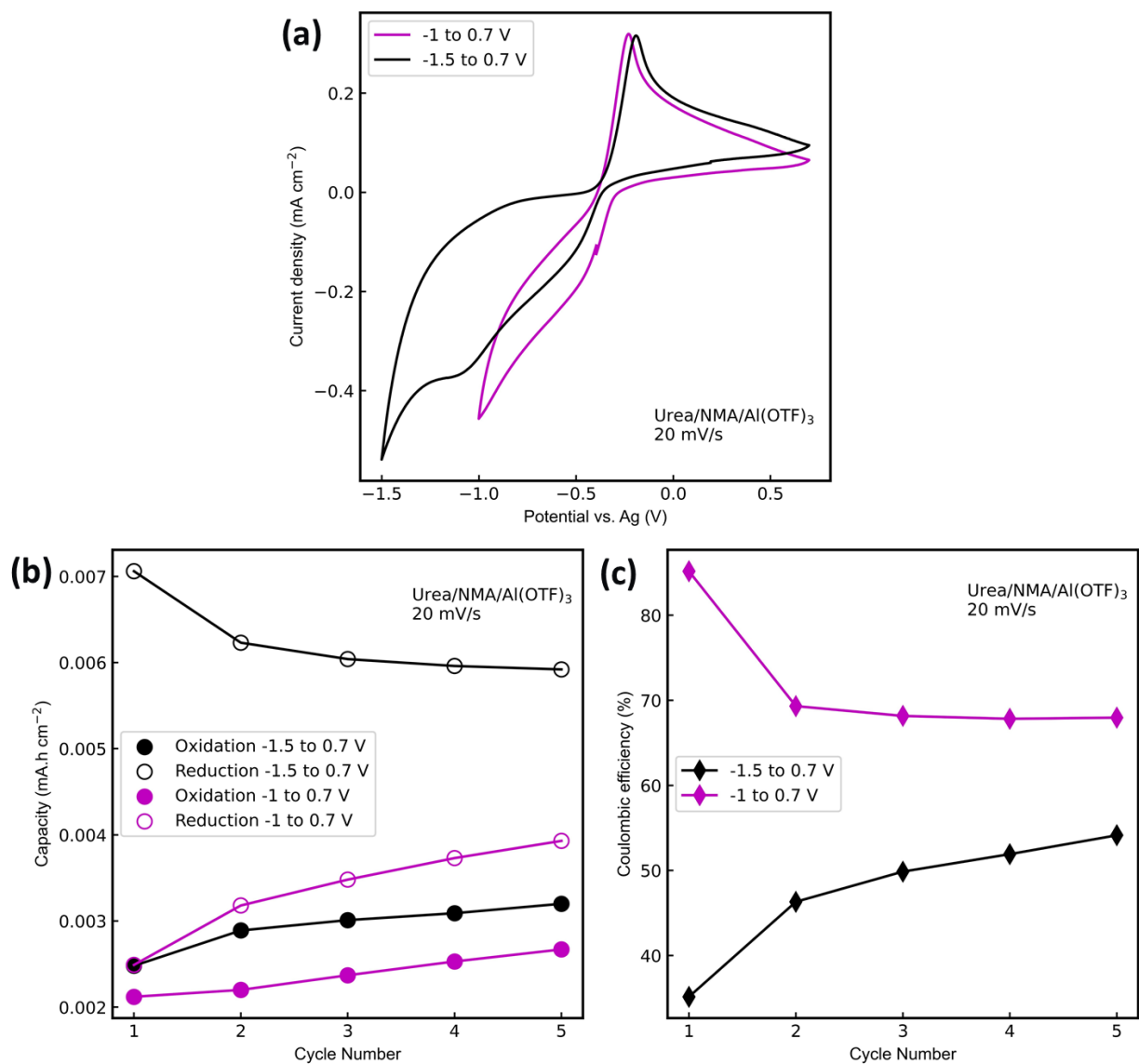


Figure 3-8. Recorded CVs on a Pt disc as WE vs. Ag quasi-RE in TSC1600-CC with Pt CE, oxidation and reduction capacity, and Coulombic efficiency at 20 mV s⁻¹ (a-b-c) in NMA-based E at two potential windows -1.5 to 0.7 V and -1 to 0.7 V (d-e-f) in EIPS-based E at two potential windows -1.5 to 0.5 V and -1.8 to 0.5 V.

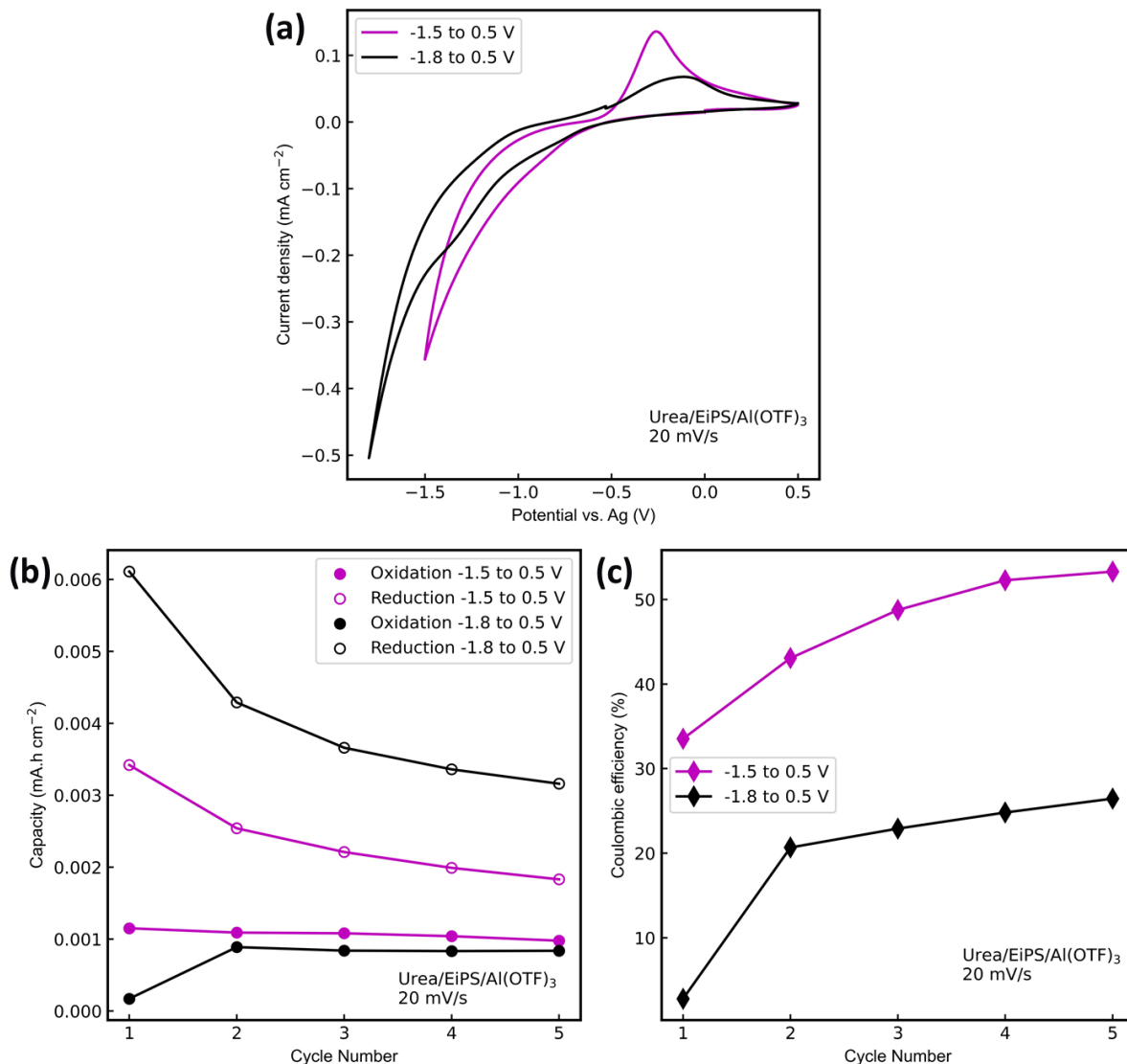


Figure 3-9. Recorded CVs on a Pt disc as WE vs. Ag quasi-RE in TSC1600-CC with Pt CE, oxidation and reduction capacity, and Coulombic efficiency at 20 mV s⁻¹ (a-b-c) in NMA-based E at two potential windows -1.5 to 0.7 V and -1 to 0.7 V (d-e-f) in EiPS-based E at two potential windows -1.5 to 0.5 V and -1.8 to 0.5 V.

In the subsequent section of the thesis, results related to the variation of operative temperature and the critical role of the electrode substrate are elaborated. As temperature increases, it generally leads to higher ion mobility and reduced viscosity. Furthermore, elevated temperatures can facilitate the dissociation of Al(OTF)₃. Figure 3-10 demonstrates a similar trend for both Al(OTF)₃-based electrolytes concerning temperature. Increasing the temperature from 20 to 50°C boosts the reduction current while hindering the oxidation current. Consequently, at higher temperatures, the reduction capacities exceed the oxidation capacities (as shown in Figure 3-10),

resulting in lower coulombic efficiency. Figure 3-11(a) illustrates that raising the temperature from 20 to 30°C reduces polarization and induces higher reduction/oxidation currents in the NMA-based E. Conversely, in the EiPS-based E, lower reduction/oxidation currents are observed at 30°C compared to 20°C (Figure 3-12(a)). As mentioned earlier, the high boiling point of EiPS (265°C) suggests that the EiPS-based E should have a broader operable temperature window compared to the NMA-based E. However, increasing the temperature leads to lower capacity and coulombic efficiency for both Al(OTf)₃-based electrolytes. This indicates that the temperature increase affects the kinetics of both the desired redox reaction (Al plating and stripping) and side (undesired) reactions. As the EiPS-based E contains a higher amount of urea, the results suggest that the decomposition of urea may be responsible for these effects at higher temperatures.

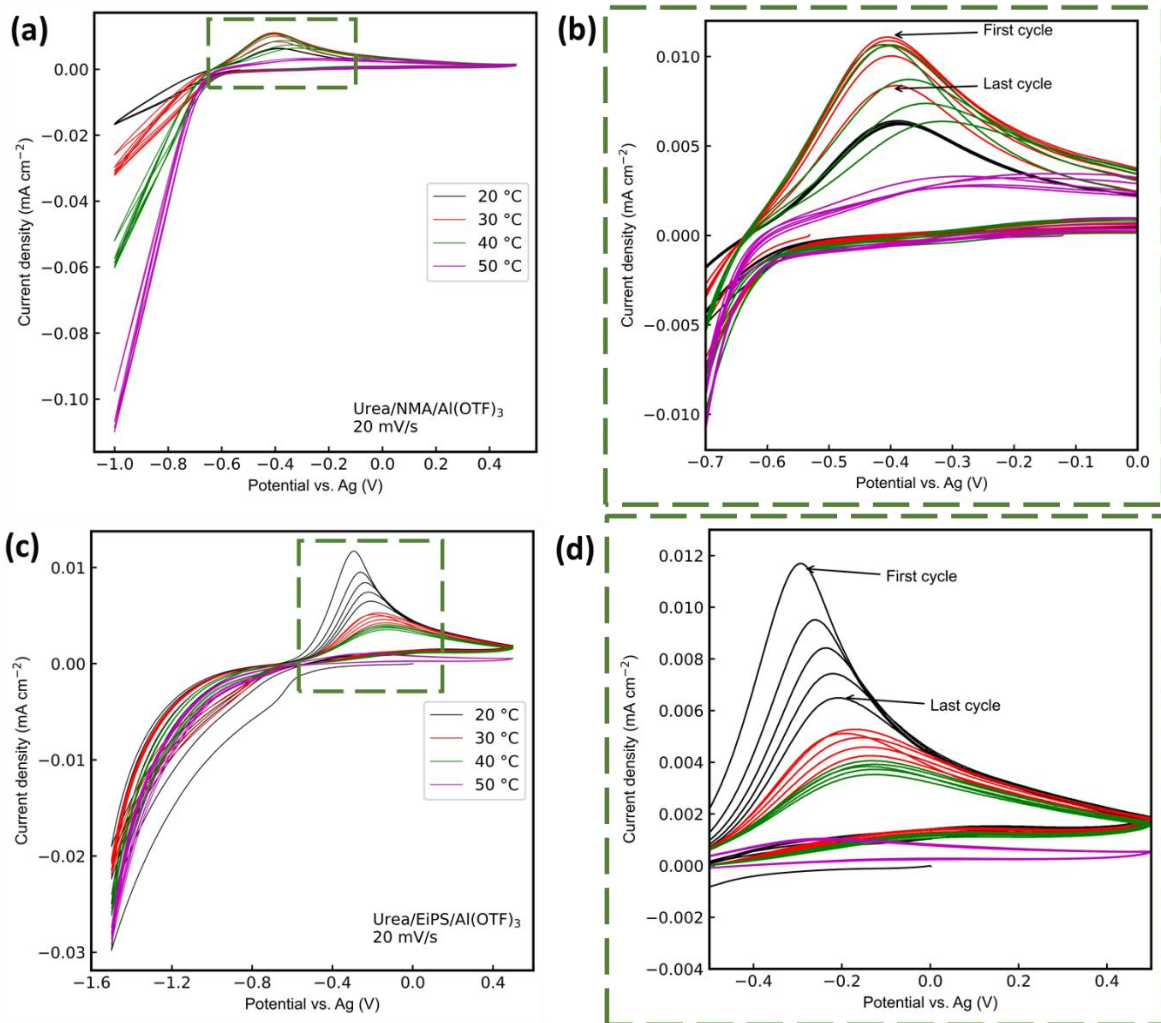


Figure 3-10. Recorded CVs on a Pt WE vs. Ag quasi-RE in TSC1600-CC with Pt CE, at the temperature range of 20 to 50°C (a-b) in NMA-based E, and (c-d) in EiPS-based E. b and d are a magnification of a and c.

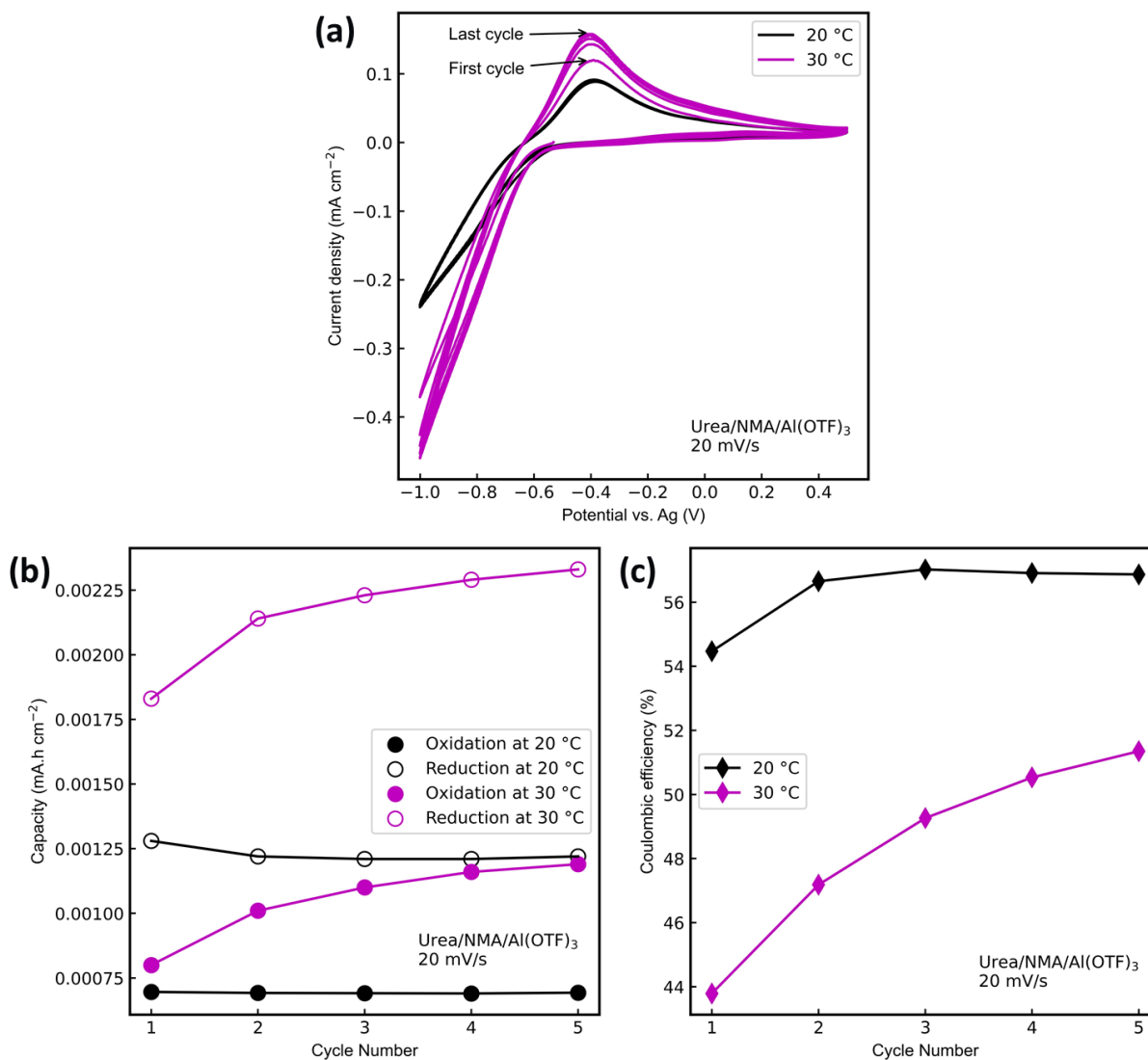


Figure 3-11. (a) Recorded CVs on a Pt WE vs. Ag quasi-RE in TSC1600-CC with Pt CE, at 20 and 30°, (b-c) oxidation and reduction capacity, and Coulombic efficiency at 20 mV s⁻¹ in NMA-based E.

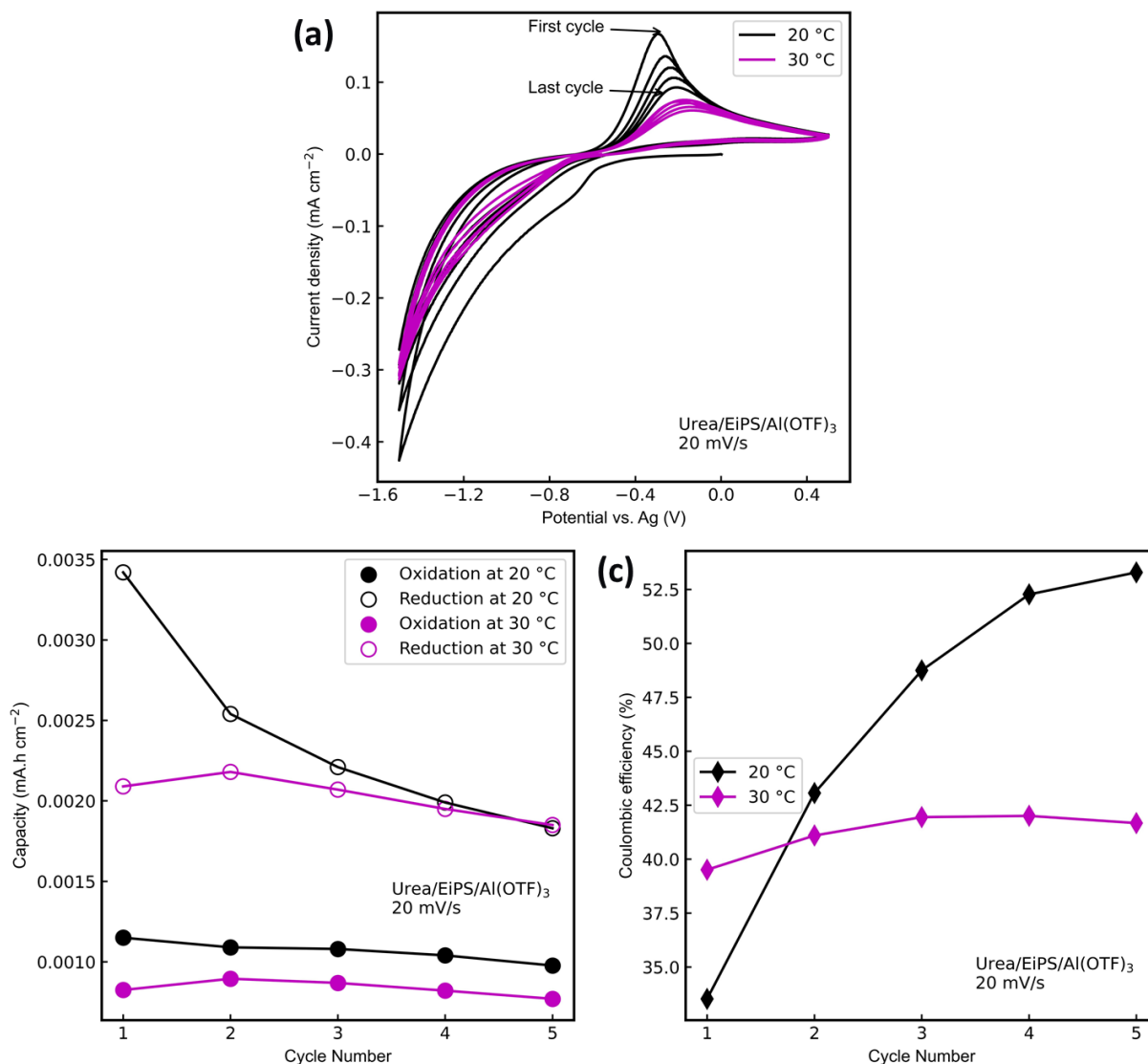


Figure 3-12. (a) Recorded CVs on a Pt WE vs. Ag quasi-RE in TSC1600-CC with Pt CE, at 20 and 30°, (b-c) oxidation and reduction capacity, and Coulombic efficiency at 20 mV s⁻¹ in EiPS-based E.

In addition to investigating the electrochemical behavior of Al(OTF)₃-based electrolyte on Pt discs, it is essential to understand the electrochemical reactions on other metallic substrates. The electrochemical activity of the NMA-based E has only been demonstrated on Pt electrodes [41]. However, for practical battery applications, it is crucial to consider more affordable and readily available metal substrates. In AIBs, the use of metallic Al as a negative electrode is a significant advantage, making it vital to assess the compatibility of such a metal anode with the electrolyte solution. Figure 3-13(a) and (b) depict the CV (2nd cycle) of Pt and GC disc electrodes in NMA-based and EiPS-based electrolytes, respectively. No redox reactions can be observed on

substrates such as GC, Ti, Mo, and Al foils, as illustrated in Figure 3-13(c). Cu, a metal that could potentially form an alloy with Al, shows different behavior. The CVs of Pt, Cu, and Al foils are compared in Figure 3-13(d). The Cu foil exhibits electrochemical activity with a broad reduction peak at -0.4 V vs. Ag followed by a cathodic current increase, similar to what is observed on Pt foil. However, the oxidation is shifted to a much higher potential, surpassing the limit of the electrolyte's oxidative decomposition. On the other hand, the Al foil shows differences from Cu and Pt: no evidence of electrochemical activity can be observed on the Al foil, ruling out any form of possible Al plating and stripping. This finding raises significant questions about the feasibility of establishing a non-corrosive practical electrolyte in ALBs with a metallic Al negative electrode. Two primary possibilities could explain this behavior: 1) the condition of the Al surface, which is generally covered by an oxide layer, hinders plating and stripping, or 2) the reaction observed on the Pt does not involve plating and stripping, but instead, other reactions are occurring. Since the overpotential for hydrogen evolution is low on Pt electrode substrates, there is a possibility that the reduction current observed in voltammograms recorded at a Pt electrode originates from the hydrogen evolution resulting from the electrochemical reduction of urea [102]. Given these results, the next section (section 3.3) is focused on addressing two aspects: i) shedding lights on formed electrode-electrolyte interphase on Pt, and Al WE in NMA-based E, and ii) modifying the Al surface through treatment methods.

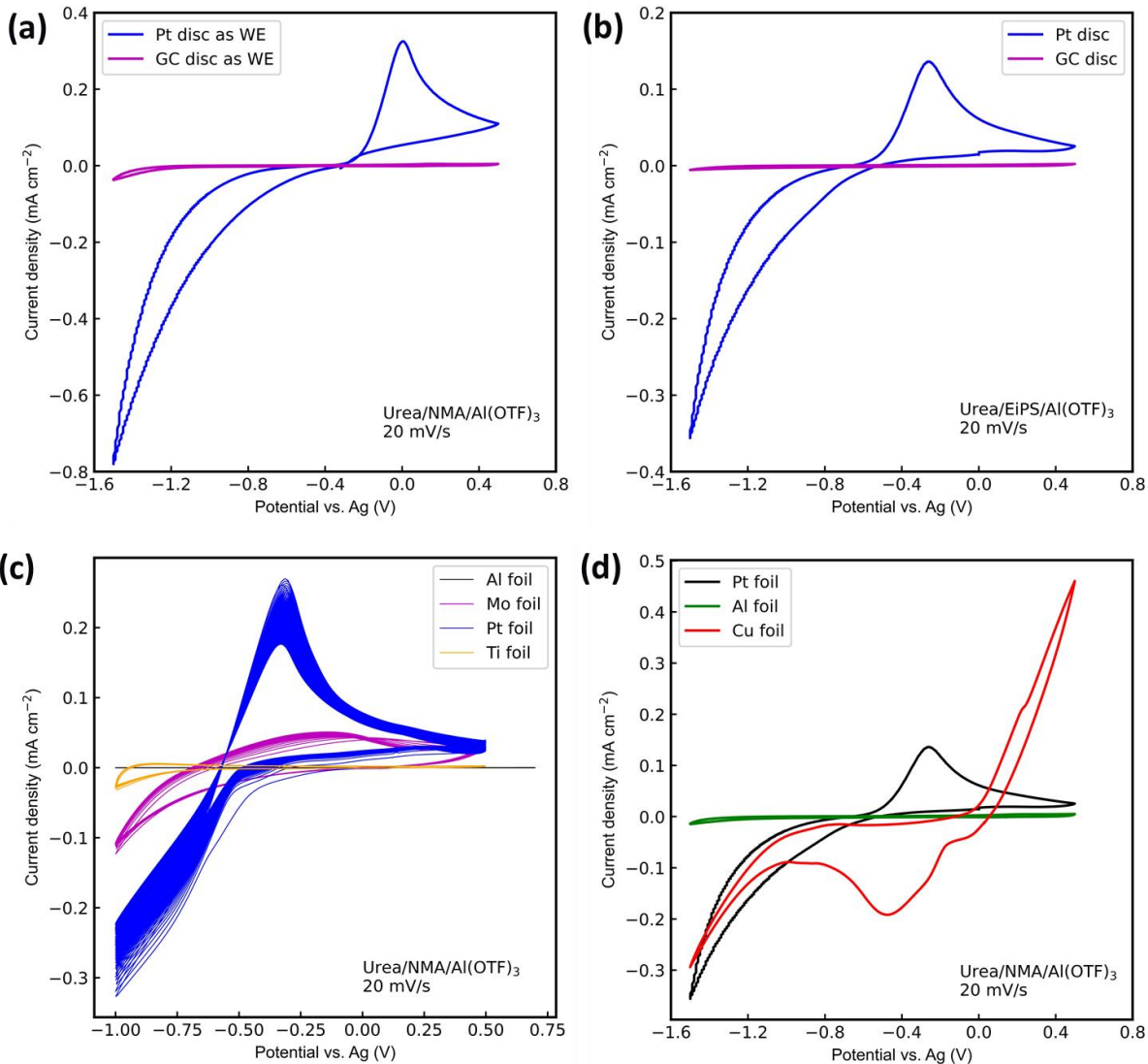


Figure 3-13. Recorded CVs on Pt, GC, Ti, Mo, Cu and Al WE vs. Ag quasi-RE in TSC-SC with GC CE in (a,c,d) NMA-based E, and (b) EiPS-based E.

3.2.2 Conclusions and Outlook

This study thoroughly investigated the electrochemical behavior of the Al(OTF)₃ salt as a promising and non-corrosive alternative to the acidic AlCl₃ salt. Two different electrolyte compositions were studied, with varying WE substrates and temperatures. A novel AlCl₃-free electrolyte was developed using EiPS, Al(OTF)₃, and urea. It was found that urea plays a crucial role in electrochemical reduction and ion conductivity, influencing both the desolvation process and the dielectric properties of the electrolyte. An important consideration for researchers in this field is the use of an Ag quasi-RE, which proved to be a stable RE in AlCl₃-free electrolytes, instead

of Al, for electrochemical studies of $\text{Al}(\text{OTf})_3$ -based electrolytes. The comparison between NMA-based and EiPS-based electrolytes revealed that the EiPS solvent has lower ionic conductivity and higher viscosity but exhibits higher thermal stability. Additionally, the EiPS solvent allows for operation at higher anodic potentials, enabling higher voltage battery cells compared to analogous electrolytes with NMA solvent. Temperature significantly affects the electrochemical performance of $\text{Al}(\text{OTf})_3$ -based electrolytes, as ionic conductivity increases with temperature. Literature routinely presents the RT as the ambient temperature where experiments are carried out. This study considered the sensitivity of electrochemical performance to temperature variations of 10°C at two "RT" boundaries, 20°C and 30°C . The results showed that the NMA-based E exhibited lower polarization and higher reduction/oxidation currents at 30°C compared to 20°C , whereas the EiPS-based E exhibited lower reduction/oxidation currents at 30°C compared to 20°C . The study also demonstrated that the choice of the cathodic potential limit is crucial. For the NMA-based E, a cathodic limit of -1 V exhibited lower irreversibility compared to -1.5 V . Conversely, the EiPS-based E system showed lower irreversibility at a cathodic limit of -1.8 V compared to -1.5 V . A crucial finding was the significance of the WE in affecting Al deposition/dissolution. Common metallic WEs, such as Ti, Al, and Mo foils, lacked Al deposition. To practically implement Al foil as a negative electrode in $\text{Al}(\text{OTf})_3$ -based electrolytes, surface modification is necessary to facilitate Al plating and stripping.

The study underscores the necessity for surface modification techniques to enable effective Al plating and stripping on commonly used WEs. This insight will likely drive ongoing research efforts focused on optimizing electrode-electrolyte interactions and facilitating stable cycling in $\text{Al}(\text{OTf})_3$ -based electrolytes. The next section (section 3.3) is centered on highlighting the intricate mechanisms of Al plating/stripping and side reactions at the electrode-electrolyte interface.

3.3 Hindered Aluminum Plating and Stripping in Urea/NMA/ $\text{Al}(\text{OTf})_3$ Electrolyte

The practical application of the active metallic Al anode material in NMA-based E as a Cl-free non-corrosive electrolyte has not been evaluated, and there are no reported studies on the interphase layer formed on the Al anode. Therefore, this part of the thesis aims to address the crucial issues that hinder Al plating and the performance of surface (non-)modified Al anodes in the NMA-based E. Bottlenecks of the NMA-based E concerning Al plating and stripping are investigated in the

following. One of the main challenges arises from the HER and the formation of an interphase layer containing $\text{Al}(\text{OH})_3$, Al-F, and re-passivated Al oxide, which subsequently obstructs the pathway for Al ions through the electrode-electrolyte interphase.

3.3.1 Findings and Discussion

The following research efforts are focused on refining surface modification techniques and further comprehending the obstacles encountered during the process of Al plating and stripping in NMA-based E. In the subsequent section, an in-depth investigation on the electrochemical performance of Al WE in NMA-based E is presented. Figure 3-14 illustrates the CVs recorded on the pristine Al foil in NMA-based E and AlCl_3 -based E. Considering the stability window of the urea/NMA/ $\text{Al}(\text{OTf})_3$ electrolyte and the stability of the Ag quasi-reference electrode for Al plating and stripping, this potential range (-1.7V to 0.5V), was derived from prior study [1] where it had proven to be a reliable and effective window for Al electrodeposition and dissolution. It's notable to mention that according to the evidence, the calibration of the quasi-reference electrode showed notable shifts in the redox peaks of Ferrocene (utilized as an internal reference) against the Al wire. Conversely, using the Ag wire as the quasi-reference maintained a remarkably stable potential throughout the 24-hour period [1]. Figure 3-14(a) demonstrates that only capacitive current, without any Al plating/stripping reaction, can be observed on the pristine Al foil in the NMA-based E. Conversely, in the AlCl_3 -based E (Figure 3-14(b)), the Al redox reaction is evident on the pristine Al foil. The peak current density related to Al stripping in the AlCl_3 -based E ranges from 0.4 to 4.027 mA cm^{-2} from the 1st cycle to the 100th cycle, indicating an activation process as the number of cycles increases (which should imply progressive Al_2O_3 dissolution). The native Al_2O_3 oxide passivation film on the Al foil should have a few defect sites during the initial cycles, allowing the electrolyte to pass through and react with the internal Al around the cracks and defect sites [16]. Subsequently, the native Al_2O_3 oxide passivation film gradually dissolves into the electrolyte since it cannot tolerate the acidic environment [77], leading to the exposure of new Al foil portions for Al plating/stripping. The complete progression of 100 cycles for both electrolytes can be seen in Figure A-3- 2. SEM images and EDX of the pristine and cycled Al electrode in NMA-based E (Figure 3-15 and Table 3-4) confirm the absence of any changes as no electrochemical reaction occurs on the Al electrode. It is assumed that Al_2O_3 is not removed due

to the non-acidic nature of the electrolyte therefore activation of Al plating/stripping has been impeded [12], [52], however it can be removed in Lewis acidic AlCl_3 -based E during cycling, owing to the existence of the chloroaluminate complexes. The continuous removal of the Al_2O_3 oxide passivation film results in the increase in Al plating/stripping capacity with the increasing cycle number. However, this same Al_2O_3 oxide passivation film deactivates the Al surface for any electrochemical reactions in the AlCl_3 -free electrolyte [50]. Therefore, when using the NMA-based E, treatment is necessary to activate electrode-electrolyte interfaces for the desired electrochemical reactions. Two crucial factors affect the possibility and reversibility of the Al plating/stripping process: 1) the appropriate electrode-electrolyte interphase driven by the state of Al_2O_3 oxide film covering the Al surface, 2) the water content of utilized electrolyte with the right ionic Al species. Therefore, firstly, we investigated if the state of the Al surface after 18 hours of immersion in 900 μl of AlCl_3 -based electrolyte enables Al plating/stripping. Figure 3-14(a) presents the recorded CV on the M-Al foil in NMA-based E, while Figure 3-14(d) shows the formation of an interphase layer rich in Al, N, and Cl species during the treatment, which aligns with previous studies [16], [78], [79]. Contrary to the expectations, no electrochemical activity can be observed for the M-Al electrode. Although an oxidation peak with high current density is observed, there is no corresponding reduction peak, indicating that this reaction is irreversible, as shown in Figure 3-14(d). This result contrasts with the findings which was presented in $\text{Al}(\text{OTF})_3/[\text{BMIM}]\text{OTF}$ ILE of Wang *et al.* [50]. The reactivity of the Al surface and the NMA-based E with Cl^- ions form an insulating interphase layer, leading to a high anodic current density. Consistent with the CV findings, it is evident that non-surface modified Al and M-Al demonstrated no observable morphological changes throughout their cycling within the NMA-based E. Detailed visual representation, as well as SEM images and accompanying EDX spectra, are provided in Figure 3-15. EDX results of the elements observed are presented in Table A-3- 2. To gain more insight into the possible Al deposition in the NMA-based E, the study explored the possibility of Al electrodeposition on a Pt WE [1], comparing it with the electroplated Al on Pt from an AlCl_3 -based E. Inspired by the work of Slim and Menke [58], CA was carried out to electroplate Al on both Al and Pt electrodes from the electrolyte medium. Figure 3-16 shows CAs in the AlCl_3 -based and NMA-based electrolytes. In both electrolytes, a cathodic current appears during the CA experiments. The oscillations in reductive currents during CAs could be attributed to the reductive

decomposition of the anions in the AlCl_3 -based E, as observed by Slim *et al.* [58] for other electrolyte compositions. Furthermore, the XPS spectra of $\text{Cl}2p$ support this notion, indicating the continued bonding of chlorine to both aluminum and $[\text{EMIm}]^+$ (Figure 3-18). Additionally, the slow current reduction recorded in Figure 3-16(a) is probably due to the reduced active surface area of the Pt substrate and Al deposition [58]. Another factor could be the facilitation of further Al deposition from the electrolyte because of the freshly deposited Al [15]. XPS analysis of the Al and Pt electrodes was performed to determine if the reductive current shown in Chronoamperograms correlates with the metallic Al deposition from active Al species in the electrolytes.

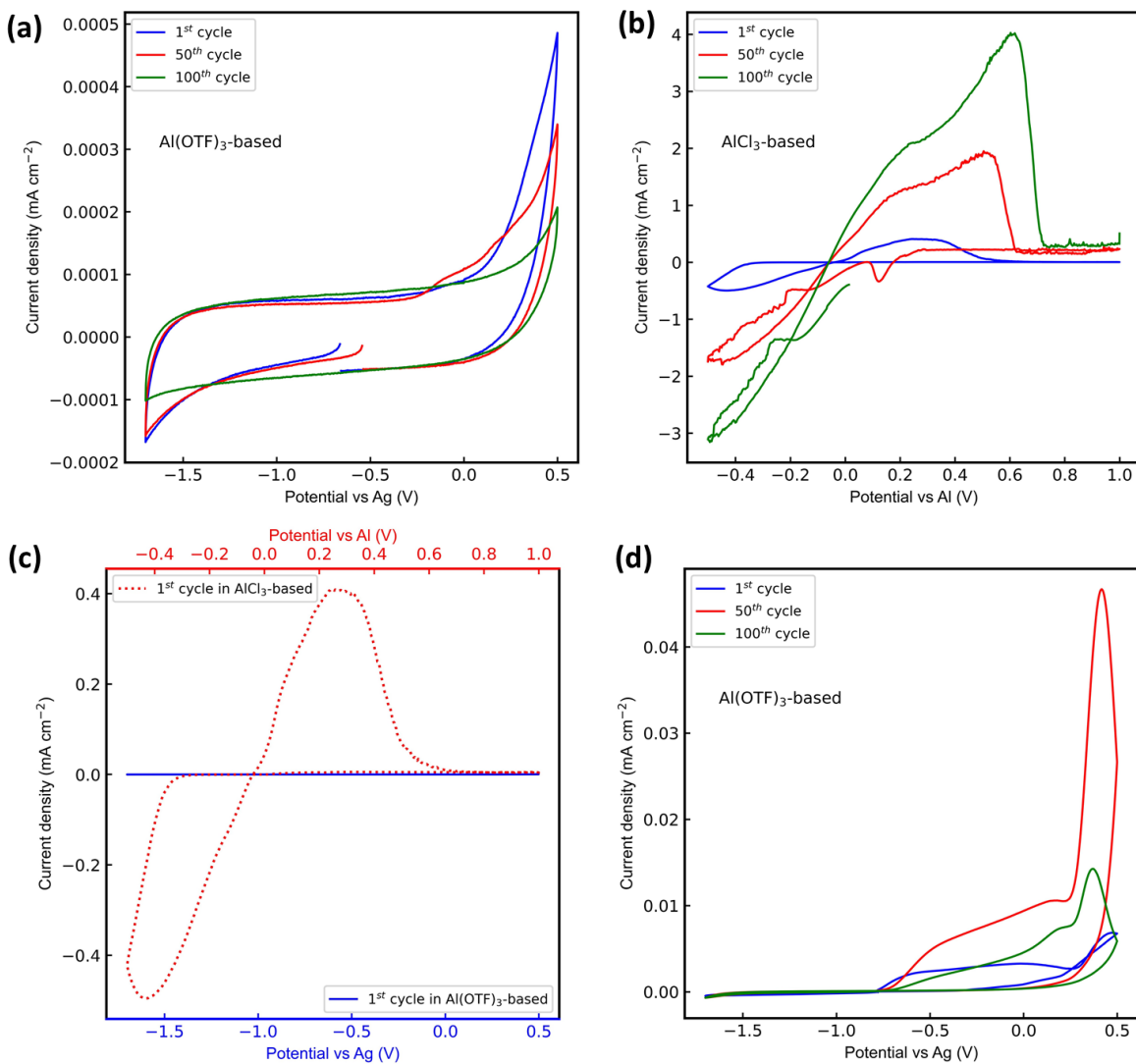


Figure 3-14. Recorded CVs with a scan rate of 20 mV s⁻¹ on pristine Al WE in TSC-SC with GC CE in (a) Al(OTF)₃-based vs. Ag quasi-RE and (b) AlCl₃-based E vs. Al quasi-RE (c) CVs comparison. (d) on M-Al foil in Al(OTF)₃-based vs. Ag quasi-RE.

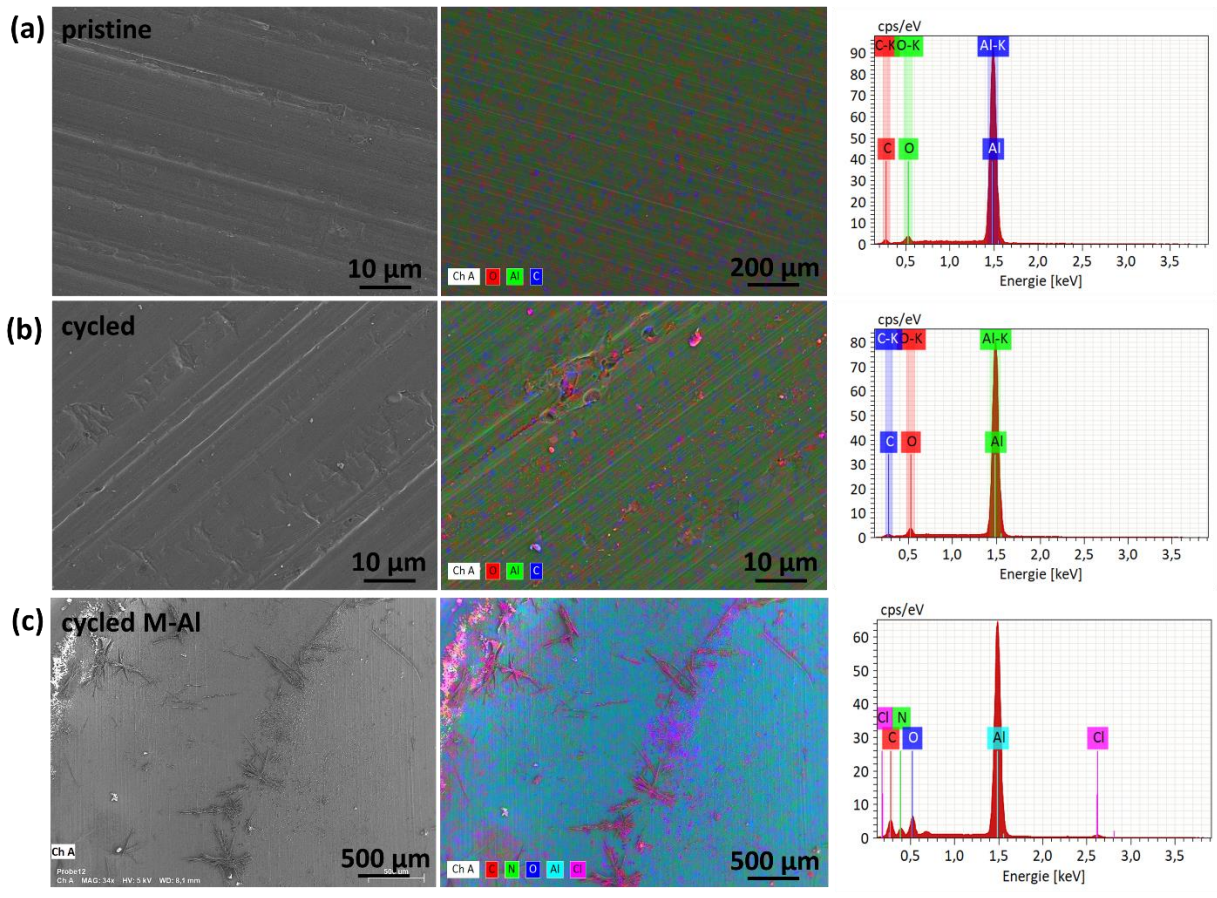


Figure 3-15. SEM images and EDX images and spectra of (a) pristine, (b) cycled Al foil, and (d) M-Al in NMA-based E.

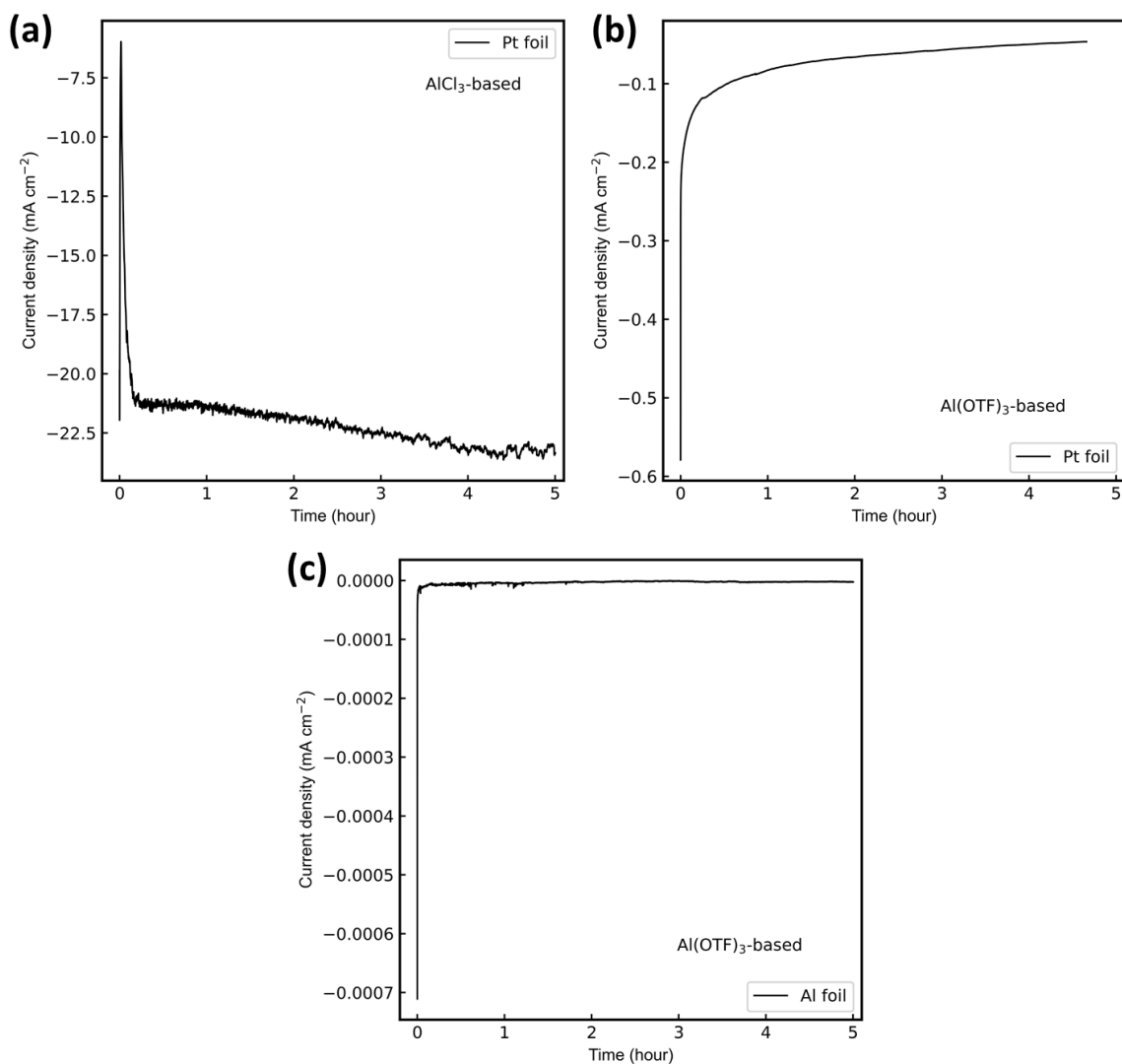


Figure 3-16. Recorded CAs at -1 V, corresponding to Al deposition on Pt electrode from (a) AlCl₃-based E with Al quasi-RE and on (b) Pt (c) Al electrode from NMA-based E with A quasi-RE.

XPS analysis was carried out on three electrodes: a Pt foil that had undergone CA to electroplate Al from an AlCl₃-based E, and Al and Pt electrodes after CA in NMA-based E. All spectra were analyzed using CasaXPS, and fits of the spectrum for each element and electrode are presented in Figure 3-17, Figure 3-18, and Figure 3-19. Note that energy window of the Pt4*f* spectrum does not extend far enough to capture the full asymmetric tail. Intensities are normalized for each spectrum individually. The lists of peaks for each spectrum can be found in Table 3-4, Table 3-5, and Table 3-6. The surface of the Pt foil, after Al electroplating with the AlCl₃-based E, was heavily covered with Al deposition products, resulting in Pt not being visible in the XPS spectrum, as expected. Figure 3-17 shows XPS fine spectra with peak assignments for Pt foil after Al

electrodeposition from AlCl_3 -based E. Spectra from the same element are normalized on the same intensity scale. In the fine spectra (Figure 3-17), performed on the C1s, N1s, O1s, Al2p, and Cl2p regions, the Al peaks showed clear bimodality, with two $\text{Al}2p_{3/2}$ peaks occurring at 74.6 and 71.6 eV, attributed to Al^{3+} and Al metal, respectively. The Cl2p spectrum contains two overlapping doublets, demonstrating that Cl^- remains bonded to both aluminum and [EMIm]. The AlCl_3 $\text{Cl}2p_{3/2}$ occurs at 198.7 eV and that of [EMIm]Cl at 197.6 eV, consistent with the results of Calisi *et al.* [103]. The C1s spectrum was fitted with three peaks: a C – C/C – H peak calibrated at 285 eV, a C – O / C – N peak at 286.1 eV, and an O – C = O peak at 289.1 eV. The N1s spectrum exhibited a larger peak at 401.7 eV arising from cationic N in imidazolium [104], and a smaller neutral C – N peak at 399.9 eV, indicating either a decomposition product of the imidazolium or residual anhydrous ACN from washing. Finally, the O1s spectrum was fitted with two overlapping peaks: a smaller peak at 530.8 eV, and a larger one at 532.2 eV. The O1s peak at 532.2 eV suggests that the primary surface Al^{3+} compound in the sample is $\text{Al}(\text{OH})_3$ [105], reconfirming AlCl_3 -based E as an effective electrolyte for Al plating [106]. This significant hydroxide peak observed on the surface might stem from the glovebox atmosphere. The intricate composition of the oxide passivation layer on the Al metal surface is susceptible to alterations caused by storage conditions [88], [107]. Factors such as temperature and humidity impact the absorption of elements like water, hydroxides, and carbon dioxide, thereby influencing the layer's overall composition [107]. It's notable that the observed fluctuation in CV (Figure 3-14(a)) can be attributed to the uneven current distribution across the electrode surface, highlighting the possibility of gas evolution from the Al metal's surface during cycling. This connection aligns with XPS observations, reinforcing the correlation between current distribution and gas evolution due to the presence of $\text{Al}(\text{OH})_3$. Moreover, this fluctuation is directly proportional to the scan rate. At higher scan rates like what has been deployed in this study (20 mV s^{-1}), it is hard to accurately measure the actual current response. Overall, the XPS analysis provides valuable insights into the composition and surface characteristics of the electrodes in different electrolytes, aiding in understanding the electroplating process of Al in the respective systems. The analysis of the Al electrode after CA measurement in the NMA-based E was challenging due to the difficulty in distinguishing deposited Al metal from the pre-existing Al on the sample. Unlike the Pt foil, the measured Al foil

lacked a thick deposition layer. Fine spectra were taken for F1s, O1s, C1s, and Al2p. In the Al2p spectrum, two doublets were observed, corresponding to Al metal and Al³⁺. The O1s spectrum exhibited two peaks at 532.3 eV and 531.1 eV, attributed to Al(OH)₃ / C – O and Al₂O₃ / O – C = O [105], respectively. The C1s spectrum displayed well-defined peaks at 285, 285.8, 289.5, 293.1, and 296.3 eV. These peaks were assigned to C – C, C – O, O – C = O / C – F, and -CF₃, respectively, with the C – F compounds clearly originating from the reduction of OTF⁻. The peak at 296.3 eV was tentatively assigned to CF₄ [108]. In the F1s spectrum, two peaks were observed: a larger one at 688.7 eV, characteristic of C – F bonding, and a smaller one at 685.6 eV, attributed to a small amount of AlF₃ [109]. The presence of AlF₃ is due to the reduction of the OTF⁻ anion containing fluorine [84], [110], [111]. Moreover, AlF₃ participates in the "re-passivation" process and may cause the overpotential of the HER over time [84]. Interestingly, the observed high water content (~ 28466 ppm) in the NMA-based E could be a source of HER during Al plating. The presence of water in the electrolyte solution can result in HER in the presence of Al, leading to the formation of Al(OH)₃ and H₂. This prevents the possibility of reversible Al plating and stripping. We verified that, although the components have been dried as reported in our previous study [1], high water content (about 28466 ppm) was still present in the Al(OTF)₃-based electrolyte. Another H₂ source could also arise from the decomposition of urea [1]. Water molecules can also serve as a source of oxygen for the creation of oxide films [112]. Another H₂ source could also arise from the decomposition of urea [1]. Thermodynamically and kinetically, an excess of H⁺/H₃O⁺ assists even in the earlier onset of hydrogen evolution [113], which may explain the trace hydroxide present in the sample. It is essential to note that the water content might have been introduced during the electrolyte preparation, despite the vacuum and drying of all electrolyte components before preparation, as previously reported in the literature [1]. The impact of water content in NMA-based E on Al plating has not been explored before [41], [59]. The water content would interfere with Al plating [86] because water in the electrolyte solution would result in HER in the presence of Al. As a primary cathodic reaction, the HER (2Al + 6H₂O → 2Al(OH)₃ + 3H₂) prevents the possibility of reversible Al plating and stripping [86]. Understanding the role of water content in the electrolyte is critical in the context of Al plating and the formation of surface oxides, influencing the reversibility of Al plating/stripping processes. The oxide film on the Al electrode can undergo re-passivation when the organic component degrades or dissolves in the electrolyte.

However, the first oxide layer formed after re-passivation is expected to be much less uniform and likely thinner than the initial layer on pristine Al. The passive oxide film production can occur in the pH-neutral range (4 to 8) [114]. The measured pH (4) of the electrolyte, is attributed to the polarized O-H bonds of water molecules coordinating Al^{3+} [84], [115]. This can hinder the transport of Al^{3+} due to the presence of the interphase/passivation layer containing AlF_3 , $\text{Al}(\text{OH})_3$, and re-passivated Al oxide. It should be noted that the Al-metal peak is not significantly enhanced compared to untreated samples, and the O1s structure shows a mixture of oxide and hydroxide, similar to what was observed in the pristine foil samples. Hence, it is possible that the oxide-hydroxide layer of the pristine foil was not attacked at all, or the oxide layer might have formed from trace oxygen and water between cycling and measurement. Regardless of the cause, considering the highly regular character of the oxide layer and the low concentration of electrolyte deposition products, it can be inferred that significant Al-deposition did not take place. A summary and approximate breakdown of the relative signal between spectra can be found in Table 3-5. The XPS analysis of the Pt foil, which underwent CA to electroplate Al from the NMA-based E, shows no indication of any interaction with the electrolyte. Only Pt metal is observed on the surface, along with trace impurities and adventitious carbon. This result may appear to contradict the reduction current observed in the recorded CV at a Pt electrode [1]. However, this current could be attributed to hydrogen evolution via the electrochemical reduction of urea. It is known that the overpotential for hydrogen evolution is low at Pt electrode substrates [1], [102]. A summary and approximate breakdown of the relative signal between spectra can be found in Table 3-6.

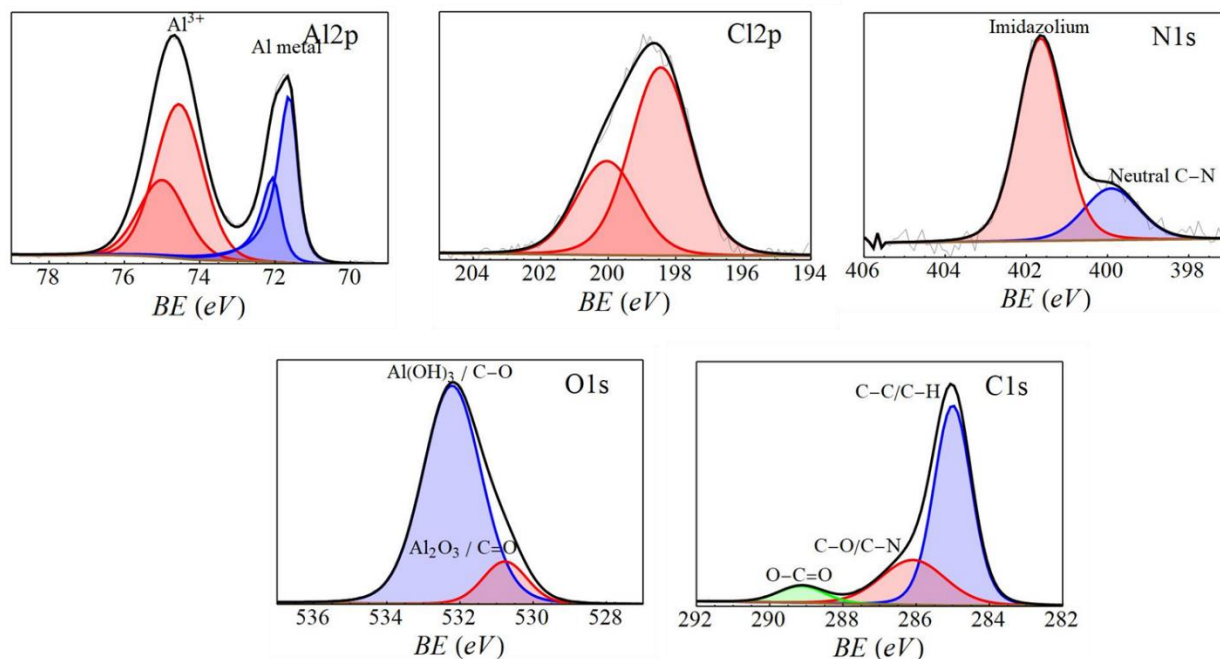


Figure 3-17. XPS fine spectra with peak assignments for Pt foil after Al electrodeposition from AlCl_3 -based E.

Table 3-4. Binding energies, assignments, and a rough estimate of surface composition by atomic percent for the XPS spectrum of Pt foil after Al electrodeposition from AlCl_3 -based E.

Spectrum	Binding Energy (eV)	Peak Area (cps×eV)	Est. % Content	Assignment
O1s	530.8	1297	3.2	Al_2O_3 / O – C = O
	532.2	8721	21.3	$\text{Al}(\text{OH})_3$ / C – O
N1s	399.9	125	0.5	neutral C – N
	401.6	413	1.6	Imidazolium
C1s	285	4114	29.5	C – C
	286.1	1590	11.4	C – N / C – O
	289.1	430	3.1	O – C = O
$\text{Cl}2p_{3/2}$	198.4	1105	5.2	AlCl_3 (and related anions)
$\text{Al}2p_{3/2}$	71.6	461	9.3	Al metal
	74.6	743	14.9	Al^{3+}

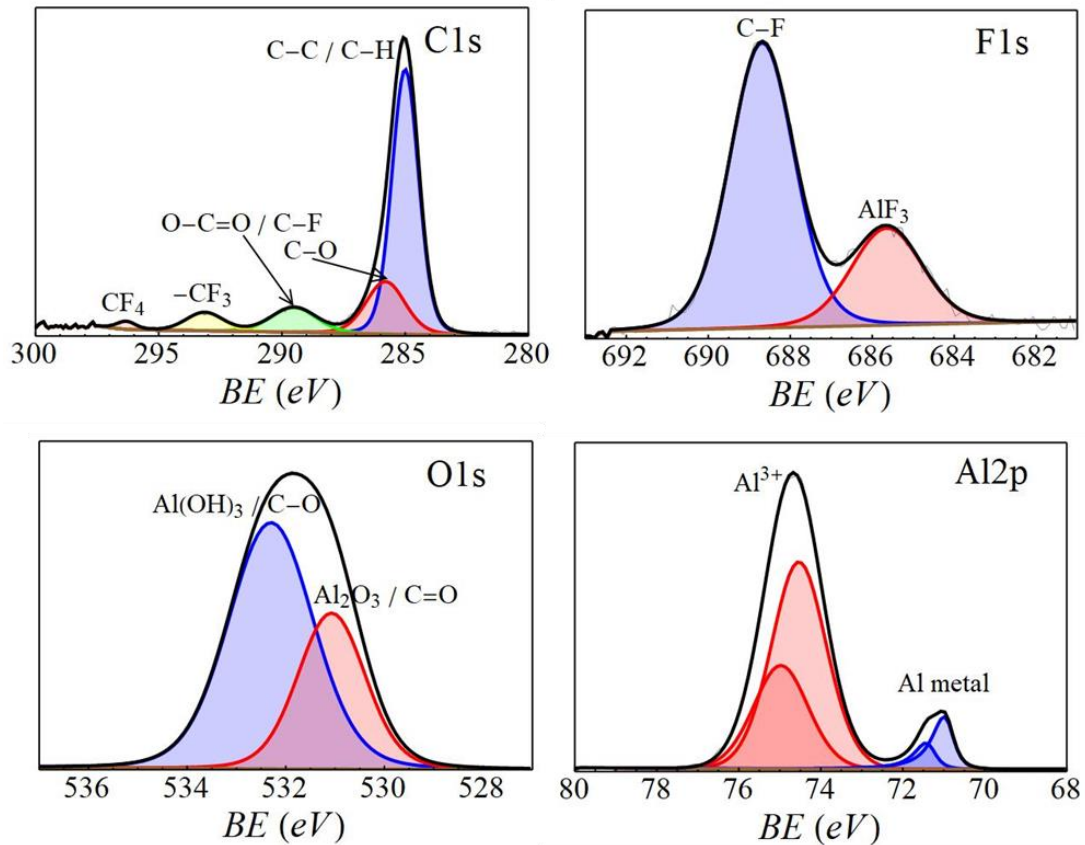


Figure 3-18. XPS fine spectra with peak assignments for Al electrode after applied CA technique in NMA-based E.

Table 3-5. Binding energies, assignments, and a rough estimate of surface composition by atomic percent for the XPS spectrum of Al electrode after Al electrodeposition NMA-based E.

Spectrum	Binding Energy (eV)	Peak Area (cpsxeV)	Est. Content (%)	Assignment
F1s	685.6	532	0.8	AlF ₃
	688.7	1412	2.1	C-F
O1s	531.1	6360	14.4	Al ₂ O ₃ / O-C=O
	532.3	12638	28.6	Al(OH) ₃ / C-O
C1s	285	1836	12.2	C-C
	285.7	556	3.7	C-O
	289.5	235	1.6	O-C=O / C-F
	293.1	146	1	-CF ₃
	296.3	36	0.2	CF ₄
Al2p _{3/2}	71	221	4.1	Al metal
	74.5	1668	31.2	Al ³⁺

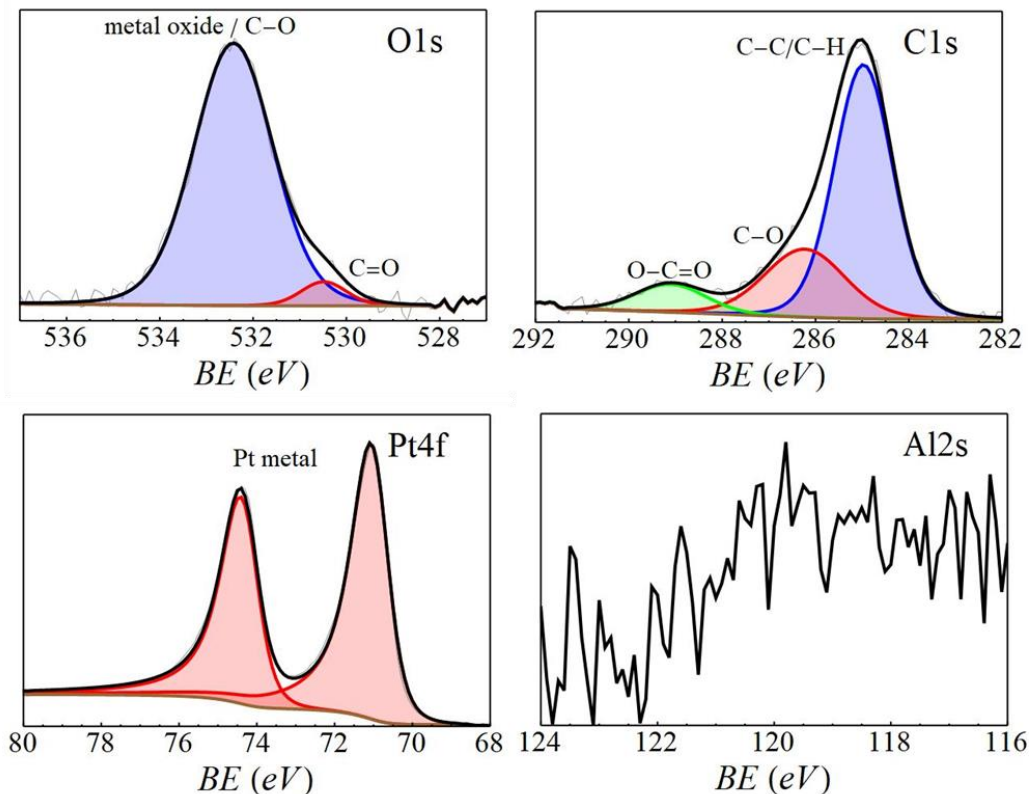


Figure 3-19. XPS fine spectra with peak assignments for Pt electrode after applied CA technique in NMA-based E.

Table 3-6. Binding energies, assignments, and a rough estimate of surface composition by atomic percent for the XPS spectrum of Pt electrode after applied CA technique in NMA-based E.

Spectrum	Binding Energy (eV)	Peak Area (cps×eV)	Est. % Content	Assignment
O1s	530.5	216	0.8	C = O
	532.4	4107	16.6	C – O
C1s	285	2328	27.5	C – C
	286.2	809	9.6	C – O
	289.1	268	3.2	C = O
Pt4f _{7/2}	70.7	29703	40.6	Pt metal

3.3.2 Conclusions and Outlook

The CV data gathered from both pristine and M-Al foils reveal a lack of successful Al plating and stripping in the NMA-based E. On the other hand, X-ray XPS analysis of the electrodeposited Al on the Pt electrode from the AlCl₃-based E demonstrates significant deposition of Al metal, with consideration that this Al metal may undergo oxidation post-deposition. Conversely, the XPS

analysis of the Al and Pt electrodes in NMA-based E provides no evidence of electroplated Al. Instead, a minor presence of C-F compounds is observed that can be linked to the reduction of OTF^- . The interphase layer formed on the Al electrode, comprising AlF_3 , $\text{Al}(\text{OH})_3$, and re-passivated Al oxide, correlates with the initiation of the hydrogen evolution reaction (HER) due to the elevated water content in the electrolyte. This observation confirms that the hindered Al plating arises from the composition of the formed interphase/passivation layer, containing AlF_3 , $\text{Al}(\text{OH})_3$, and re-passivated Al oxide.

This study encourages an in-depth exploration of the electrolyte's broader contributions, particularly in relation to other potential side reactions beyond the HER and $\text{Al}(\text{OTF})_3$ degradation. Promising strategies to mitigate the interaction between Al and water encompass the inclusion of water scavengers, additives, water-binding polymers, and additive-driven interfacial engineering.

4 Comprehensive insight into the performance of the aluminum anode material: Impacts of surface modification on its the surface properties

The presented scientific findings within this chapter have undergone thorough analysis, meticulous review, and subsequent publication in an international peer-reviewed journals:

1. **F. Rahide**, K. Palanisamy, J. K. Flowers, J. Hao, H. S. Stein, C. Kranz, H. Ehrenberg, S. Dsoke, "Modification of Al surface via acidic treatment and its impact on plating and stripping", ChemSusChem, Oct. 2023, doi: 10.1002/cssc.202301142.
2. N. Sabi, K. Palanisamy, **F. Rahide**, S. Daboss, C. Kranz, S. Dsoke, "Surface Properties-Performance Relationship of Aluminum Foil as Negative Electrode for Rechargeable Aluminum Batteries," Batter Supercaps, Sep. 2023, doi: 10.1002/batt.202300298.

4.1 Research background and Methodology

Al metals are employed as anodic materials for AIBs in the forms such as plates, foils, or particles [24]. The notable attributes of AIBs can be primarily related to the quality of the Al metal anode. The quality encompasses availability, economical cost [23], [24], gravimetric capacity (2980 mAh g⁻¹ [15]), and high volumetric capacity (8040 mAh cm⁻³, i.e. four times higher than metallic Li). Al exhibits a standard reduction potential of -1.66 V (vs. SHE) and possesses the capacity to transfer three electrons [24], [116]. Nevertheless, the utilization of metallic Al as an anode within AIBs introduces challenges like volume expansion, the development of insulating passive films, and inherent self-corrosion [24]. Several factors including Al purity, the formation of Al dendrites, the presence of Al₂O₃ oxide passivation film, grain size, crystal orientation, and microstructure [24] affect the performance of the Al anode. Reduced efficiency of the Al anode is attributed to the presence of impurities like Fe, Si, and Cu. These impurities can instigate localized galvanic cells, functioning as cathodic sites alongside Al and thereby accelerate the rate of self-corrosion [117], [118]. However, excellent purity incurs a greater cost for the Al anode [118], creating a delicate balance between performance and cost. Furthermore, the process of repeated Al plating and stripping accelerates the formation of dendritic Al [119], [120]. These Al dendrites have the potential to puncture the separator that leads to the disintegration of the anode and consequently failure of the cell[121]. Another concern arises from the loss of the Al active material as dead Al dendrites detach from the Al matrix [93]. Despite the ongoing debate

regarding the existence of Al dendrites [18], [122], they are indeed present but restricted under the barrier of Al_2O_3 oxide passivation film, contrary to the expected dendrite-free behavior [93]. The inherent Al_2O_3 oxide passivation film impedes the growth of Al dendrites, hence stabilizes the interface between the anode and electrolyte [92], [93]. Al_2O_3 oxide passivation film delays the initiation of the anode and complicates the achievement of the reversible potential that leads to a substantial overpotential or passivation [15], [24]. The amorphous Al_2O_3 oxide passivation film possesses characteristics of an electron/ion insulator, featuring defects and a few nanometres thickness. This structural setup allows for electron tunnelling and facilitates ion conduction and charge transfer [15], [121]. However, the correlation between the oxide film and the process of Al deposition is an ongoing discussion [16], [90], [93]. It has been documented that activating the interface between the Al electrode and the electrolyte involves pretreatment of the Al metal anode, leading to the partial removal of the Al_2O_3 oxide passivation film [121]. However, any increase in potential achieved after the removal of the oxide film could potentially pave the way for corrosion [15]. She *et al.* [78] proposed that the surface evolution of the Al electrode is an outcome of electrochemical corrosion, which consequently impacts the morphological characteristics of the Al electrode. The activity of Al dendrites, along with their size distribution, also play a role in altering ion concentration and current distribution, thereby influencing the evolution of the Al electrode surface [78]. Consequently, the design of Al anode treatment should not only enhance the active surface area of the Al anode and the capacity for Al deposition and dissolution but also control corrosion and dendrite growth [121]. Acid etching treatment and electro-polishing are two types of treatments used for the Al anode. While the elimination of the Al_2O_3 oxide passivation film increases the electrochemically active surface area of the Al metal, it can also result in a weaker or less stable electrode-electrolyte interphase layer [123], [124]. Treated Al surfaces exhibit multiple pits that serve as active sites during the charge/discharge cycles [79]. Acidic etching can be performed through (pre)immersion in a chloroaluminate-based ILE [125] and partially removes and modifies the surface oxide film to facilitate specific electrochemical reactions [50], [126]. However, intense protic acid etching [93] and electro-polishing [127] lead to the complete removal of the native surface oxide film, subsequently triggering dendritic Al electrodeposition, fracturing of the metal anode, severe corrosion, and even pulverization of the Al anode [126], [128]. Wu *et al.* [129] demonstrated that moderate

removal of the Al_2O_3 oxide passivation film enhances the coulombic efficiency of Al plating and stripping, while excessive removal does not yield any improvement. The duration of immersion impacts the extent of Al_2O_3 oxide passivation film removal and the activation of the Al surface for electrochemical reactions, as well as the stabilization of the anode/electrolyte interface [130]. Yang *et al.* documented that an immersion time of 6h is optimal in 1-butyl-3-methylimidazolium chloride ([BMIM]Cl): AlCl_3 (1:1.1) electrolyte [126]. The conventional ILE mixture for AlBs, [EMIm]Cl: AlCl_3 (1:1.5), becomes a Lewis acid only when the molar ratio AlCl_3 : [EMIm]Cl exceeds 1. The chloroaluminate complexes formed with this molar ratio (Al_2Cl_7^-) attack the surface of metallic Al, initiating a galvanic corrosion reaction and forming an electrode-electrolyte interphase layer that includes a modified passivation film (Al_2O_3) [131]. This leads to local dissolution of the Al surface during Al plating/stripping in the ILE [132]. Moreover, new passivation layers emerge under open circuit voltage conditions due to the deposition of decomposition products from the ILE [77]. These newly formed passivation layers provide some protection, but they eventually corrode and dissolve [89], [90], [92], leading to heterogeneous species distribution and restructuring of the electrode changes in porosity that affects interfacial resistance and ionic species diffusion. Lee *et al.* [89] conducted an analysis of the morphological changes on the Al surface to explore the chemical activity and stability of Al in ionic liquids (ILs). However, they presented the morphological changes on the Al metal surface in a qualitative manner, lacking detailed surface analysis [89].

The surface properties, structure, and topology of the interfacial layers remain inadequately understood. The native Al_2O_3 oxide passivation film possesses a complex composition and nature, influenced directly by manufacturing and storage conditions [107]. The temperature and humidity of storage and manufacturing environments dictate how adsorbed species such as water, hydroxides, and carbon dioxide affect the composition of the Al_2O_3 oxide passivation film. When the Al_2O_3 oxide film comes into contact with an ILE, a porous film with intricate characteristics is formed. The inner and outer layers of the film are rich in oxides and inorganic/organic materials, respectively [77]. This porous film expands upon exposure to open circuit voltage, concurrently redepositing and dissolving deposited products. Galvanostatic cycling, on the other hand, leads to pitting corrosion of the Al metal due to electrochemical etching [77].

4.2 Impact of Al Surface Modification on Al Surface Properties and Plating/Stripping

A comprehensive investigation of changes in microstructure and surface properties of surface-modified Al foil, along with their impact on electrochemical performance is missing in the literature. A systematic investigation of the correlation between Al surface properties and changes in Al microstructure, together with their influence on the reversibility and stability of Al plating and stripping, is notably absent. Within this investigation, the association between diverse electrochemical behaviors exhibited by each side of the Al foil and their unique surface properties are highlighted. Furthermore, we conducted an analysis of the impact of treatment on the mechanical surface properties of the Al foil following CV, comparing it to the pristine sample. The modification of the Al surface, particularly in terms of changes to its composition and microstructure, exerts a noticeable influence on the electrochemical performance and aging of the Al electrode. The enhancement of the Al surface, with a focus on microstructure modification, directly influences the kinetics of Al deposition/dissolution as well as the stability across cycles. To the best of our understanding, the available literature lacks in-depth electrochemical investigations into the distinct sides of Al foil. Typically, one side is explored individually, disregarding the potential performance disparities between both sides [5]. This study explores new perspectives by revealing changes in surface properties and modifications in the microstructure of different sides of Al foil after treatment and cycling in AlCl_3 -based electrolyte.

4.2.1 Findings and Discussion

Each commercial Al foil is characterized by two distinct sides with different mechanical surface properties such as roughness and microstructures, arising from the conditions of the manufacturing process [5], [107], [133]. These visually distinguishable sides are commonly referred to as shiny (Al-SH) and non-shiny (Al-NSH), with each side displaying unique characteristics in terms of the nature and composition of the Al_2O_3 oxide passivation film. In this study, the pristine Al foil was analyzed as received, without undergoing any treatment. Both sides of the pristine Al foil exhibit striking variations in surface morphology, as evidenced by the SEM images depicted in Figure 4-1. The quantitative elemental composition, including Al, C, and O, is illustrated by the EDX results. The distinct thicknesses and compositions of the Al_2O_3 oxide passivation film correspond to the varying proportions of Al and O. Figure 4-2 provides

AFM images of the pristine Al-NSH and Al-SH sides, revealing distinct surface microstructures and levels of roughness for each side. The Al-NSH side exhibits a higher S_a when compared to the Al-SH side. The AFM images were captured from three different spots, each covering an area of $30 \times 30 \mu\text{m}^2$. The average S_a values are represented in the bar graph displayed in Figure 4-2(b). Error bars reflect standard deviations from data for three different spots at one sample in Figure 4-2(b). S_a values of $123 \pm 11 \text{ nm}$ ($n=3$) and $89 \pm 7 \text{ nm}$ ($n=3$) were determined for Al-NSH and Al-SH, respectively. This data confirms that the Al-NSH side exhibits a higher S_a in comparison to the Al-SH side.

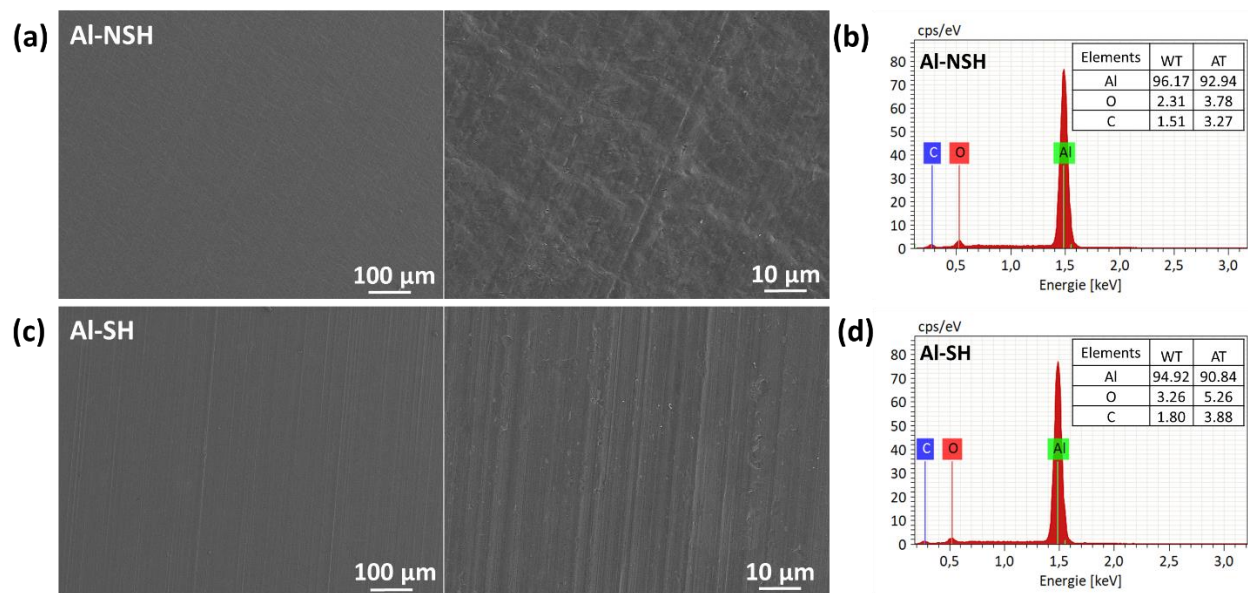


Figure 4-1. SEM images and corresponding EDX results and observed elements on the surface of the pristine (a-b) Al-NSH and (c-d) Al-SH.

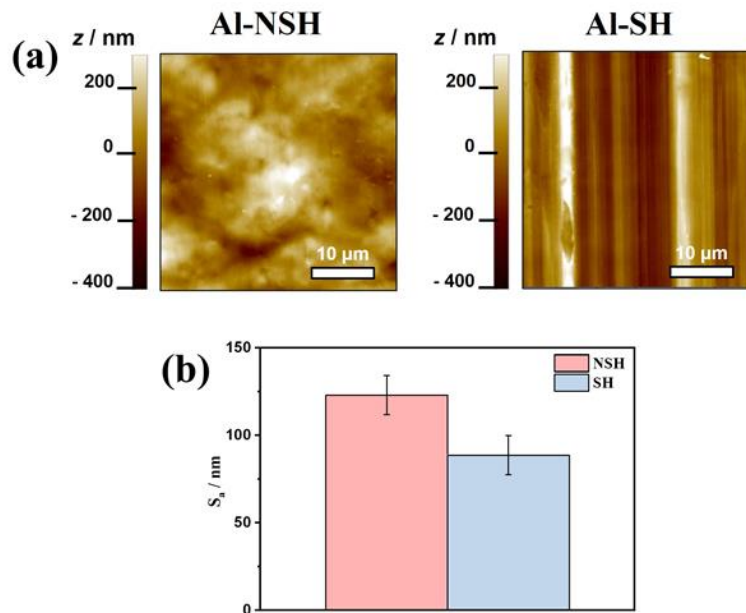


Figure 4-2. (a) AFM surface topography of the pristine Al-NSH and Al-SH recorded in Ar atmosphere. (b) Bar graph of mean S_o values for Al-NSH and Al-SH.

Figure 4-3 shows recorded CVs on non-shiny side of non-pretreated Al foil (NT-Al-SH) and shiny side of non-pretreated Al foil (NT-Al-SH) at a scan rate of 20 mV s^{-1} in AlCl_3 -based E. As depicted in Figure 4-3(a), a noticeable increase in current density occurs with cycles. Regardless of the side, the presence of the Al_2O_3 oxide passivation film impedes optimal Al deposition or dissolution during the initial cycle, leading to extremely low current density. This effect stems from the oxide film's interference with the electrochemically active surface area, making it more challenging for aluminum chloride complexes to access the Al surface. The initiation of electrochemical activity takes a few primary cycles, during which the inherent Al_2O_3 oxide passivation film is gradually eliminated and dissolved within the ILE. This phenomenon leads to a rise in current density with the cycle numbers. Consequently, the current densities for the first cycle are notably lower compared to the final cycle (Figure 4-3). This trend is consistent with literature findings, where Al plating/stripping peaks are initially modest and irregular but gradually increase and attain reversibility throughout cycling [134], [135]. The observed CVs for both sides indicate an increase in current density with cycling (Figure 4-3(a)), that in turn reveals the higher Al plating/stripping capacity. This current density directly correlates with capacity, reflecting the extent of current

flow through the active surface area. The current flow depends on the initial surface properties of Al foil. Hence, the observed different current densities for each side depend on the thickness and the nature of the passivation layer (Figure 4-3(a) and (b)). The local dissolution of the Al_2O_3 oxide passivation film generates active sites that affects the degree of Al plating/stripping reversibility and the aging of the electrode. The Al-SH side, characterized by lower S_a , suggests a homogenous Al_2O_3 oxide passivation film or less defects. This configuration blocked the tunnelling path for Al deposition or dissolution at the electrode/electrolyte interface that accounts for the lower current densities exhibited by NT-Al-SH (Figure 4-3(a)). In agreement with the CV results, SEM images (Figure 4-4(a) and (b)) of cycled NT-Al-NSH show more morphological surface alterations. This outcome can be attributed to the impact of the chloroaluminate Al_2Cl_7^- anion during Al electrodeposition, especially on the NT-Al-NSH side due to its higher initial S_a . The distinctive rock-like morphology observed in cycled NT-Al-NSH (Figure 4-4(a)) aligns with its higher S_a and the broader distribution of current flow attributed to a larger number of active sites.

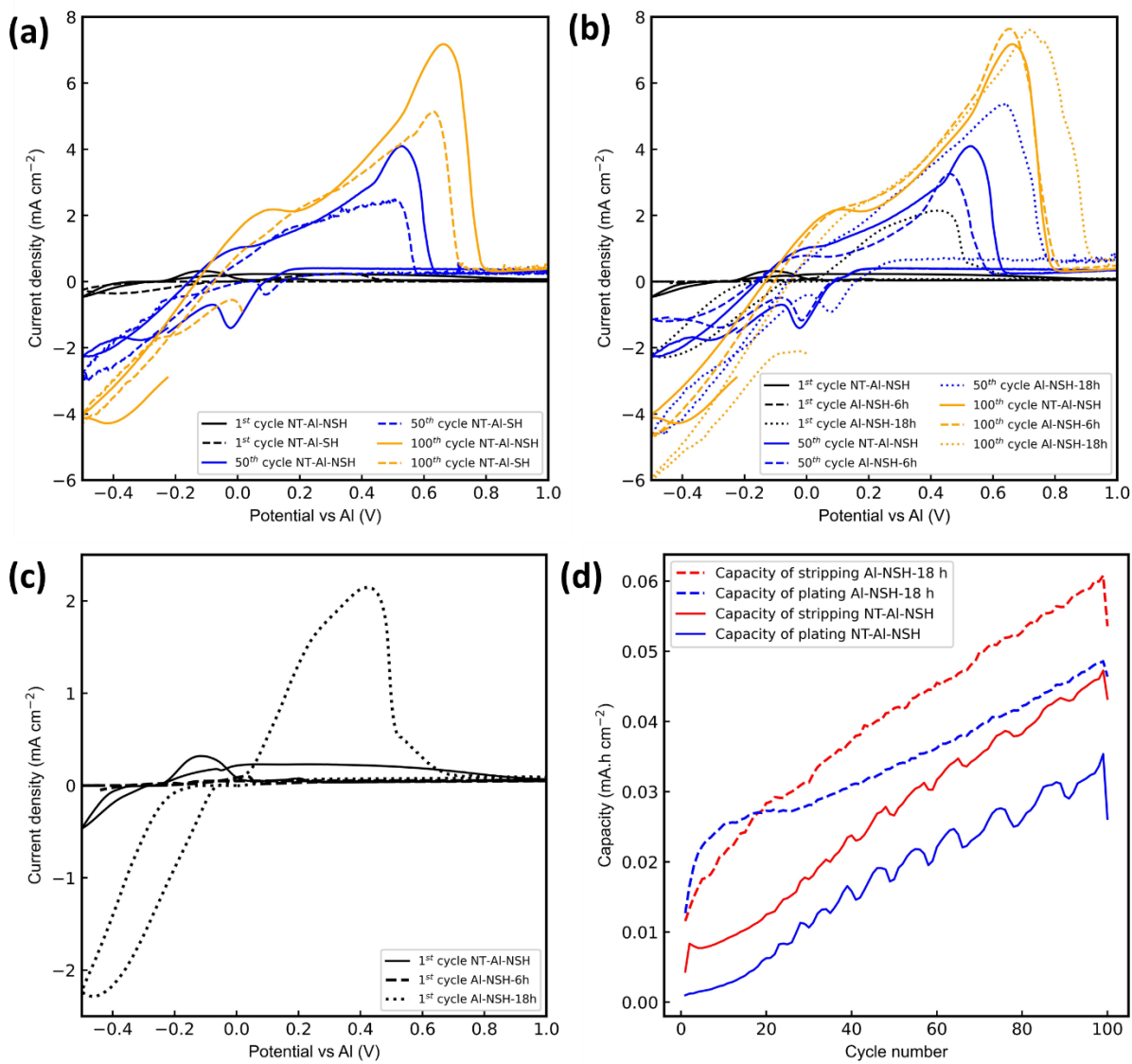


Figure 4-3. CVs recorded on (a) NT-Al-SH and NT-Al-NSH and (b - c) Al-NSH-6h and Al-NSH-18h in AlCl_3 -based E. (d) The Al plating/stripping capacity of the NT-Al-NSH and Al-NSH-18h.

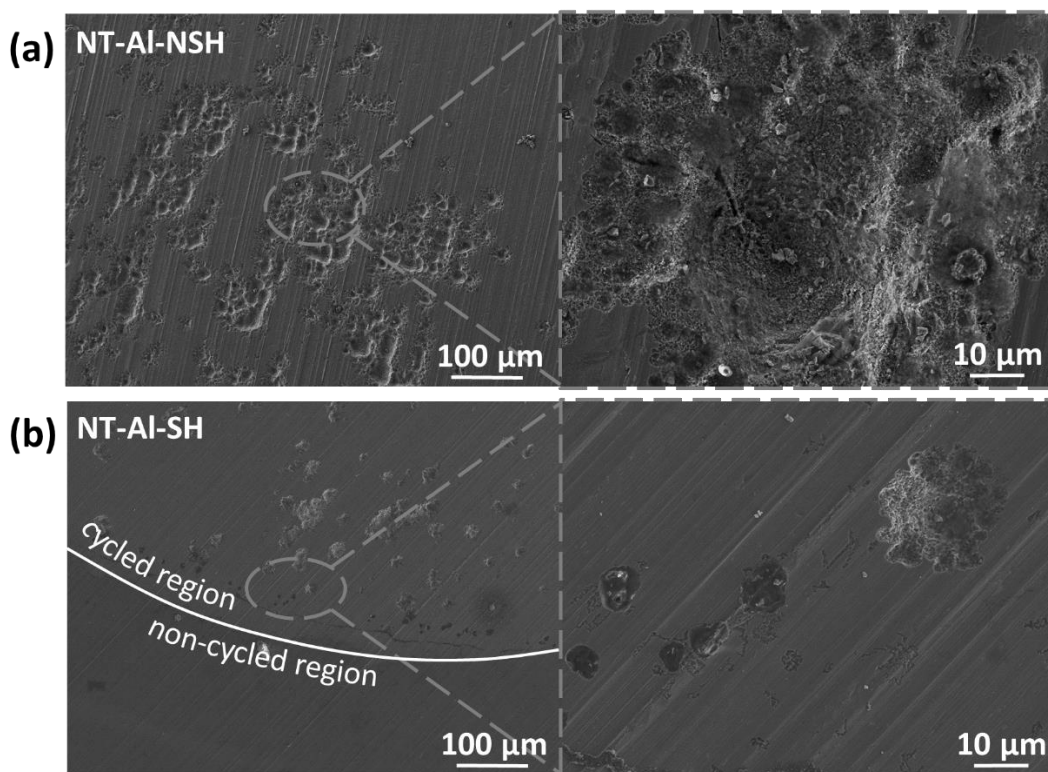


Figure 4-4. SEM images of the cycled (a) NT-Al-NSH and (b) NT-Al-SH.

Regarding the modification of the Al surface, the effectiveness of Al_2O_3 oxide passivation film removal depends on factors such as the mass and molar ratio of AlCl_3 -based E, immersion duration, and the initial surface characteristics of the Al electrode. To prevent galvanic corrosion and sustained/continuous surface attack by chloroaluminate complexes, the M-Al foils were washed and vacuum-dried before starting the electrochemical tests. Upon immersion of the Al foil in the ILE, spontaneous redox reactions take place at the electrode/electrolyte interface, leading to the formation of interphase/passivation layers. SEM images (Figure 4-5) and confirm that both sides of the M-Al foil exhibit alterations in surface morphology and roughness. In contrast to the pristine Al foil, the treated foil demonstrates a relatively rough and granular surface on either sides. EDX elemental analysis and the presence of different elements on both sides of the M-Al foil are shown in Figure 4-6.

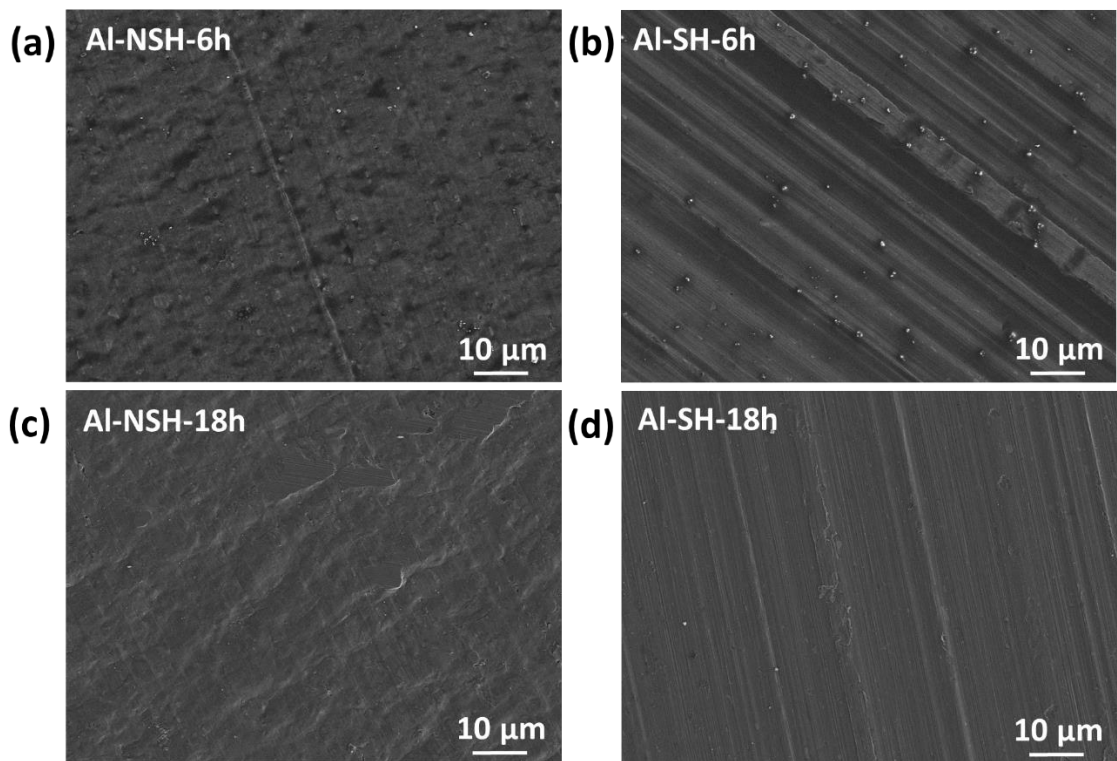


Figure 4-5. SEM images of (a) Al-NSH-6h (b) Al-SH-6h (c) Al-NSH-18h (d) Al-SH-18h after treatment in AlCl_3 -based E.

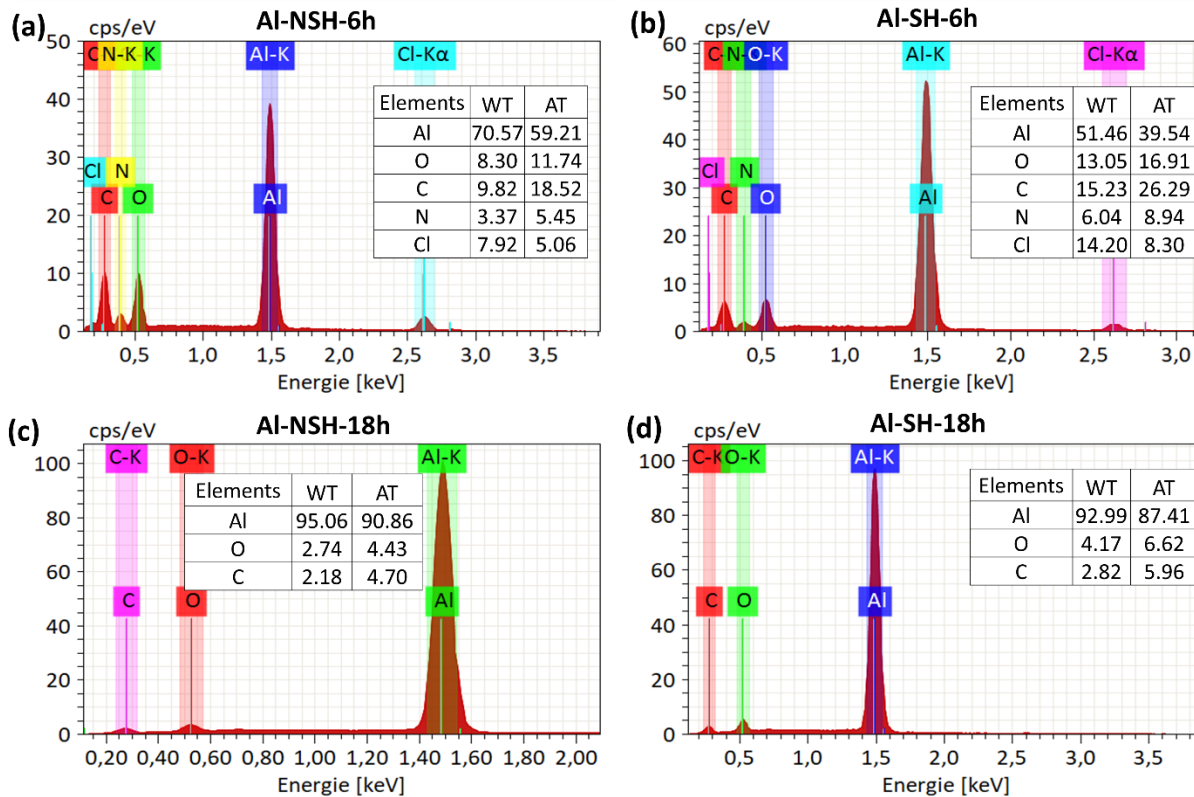


Figure 4-6. EDX results and observed elements on the surface of (a) Al-NSH-6h (b) Al-SH-6h (c) Al-NSH-18h (d) Al-SH-18h after treatment in AlCl_3 -based E.

The microstructures observed on the surfaces of the M-Al foil (Figure 4-7(a) and (b)) vary distinctly from those of the pristine Al foil. These differences extend to surface topography, roughness, morphology, and microstructure. In the case of Al-NSH, the S_a slightly decreases in the pristine sample (123 ± 11 nm ($n=3$)) to 102 ± 15 nm and 105 ± 7 nm, for 6 and 18h treatment, respectively. This decline in S_a can be attributed to the partial removal of the Al_2O_3 oxide passivation film from the Al-NSH surface. Notably, for Al-SH, S_a increases to 142 ± 14 nm ($n=3$) following 6h treatment, and further rises to 189 ± 11 nm ($n=3$) following 18h treatment (Figure 4-7(c)). Error bars reflect standard deviations from data for three different spots at one sample in Figure 4-7(c).

The S_a increase on Al-SH suggests the removal of the Al_2O_3 oxide passivation film from the Al foil's surface due to the action of the ILE, potentially accompanied by corrosion. Further electrochemical studies were focused on the Al-NSH side, considering the higher current density associated with its initial surface properties that have more active sites. Additionally, the observed less severe pitting corrosion is attributed to a broader and more uniform distribution of current. Figure 4-3(b) shows the recorded CVs for treated Al-NSH in comparison to the pristine

sample. Regardless of being treated or not, there is a rise in current density for Al plating/stripping with cycle number. However, in the first cycle, the greater current density observed in Al-NSH-18h compared to Al-NSH-6h proved the facilitated nature of Al plating/stripping. Figure 4-3(c) reveals the importance of treatment in accelerating the kinetics of the Al redox reaction. The modified Al surface that is enriched with elements such as Al, N, O, and Cl (Figure 4-9) shows more active sites for Al plating and stripping. In comparison to pristine Al-NSH, the higher current density during the initial cycle of Al-NSH-18h implies the ions movement and higher Al plating/stripping capacity (Figure 4-3 (d)). The observed occurrence of pitting corrosion (illustrated in Figure 4-8) is correlated to the duration which the surfaces are exposed to the electrolyte, as well as the electrochemical reactions induced by the applied potential. In agreement with the CV results, SEM images (Figure 4-8(a) and (b)) demonstrate that prolonged immersion durations lead to increased dissolution of both Al and Al₂O₃ oxide passivation film, and formation of more surface flaws, cracks, and defects. The treatment, by generating a greater number of active sites for Al electrodeposition and dissolution, plays a role in mitigating the extent of deep pitting corrosion. Furthermore, the formation of defects on the surface facilitates the process of Al electrodeposition and dissolution. In contrast, the effects of 6h immersion are distinct, resulting in more localized and profound pitting corrosion (for instance, comparing regions "a" and "b" in Figure 4-8(a)). Additionally, longer immersion times are observed to trigger greater localized Al metal pulverization due to the intensified consumption of Al metal within specific areas during cycling.

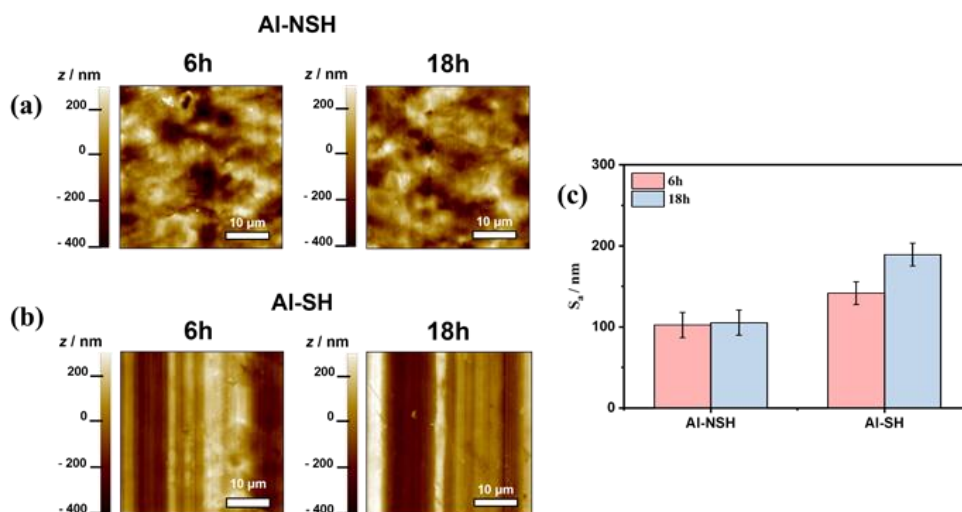


Figure 4-7. AFM topographic images of (a) Al-NSH-6h and Al-NSH-18h, (b) Al-SH-6h and Al-SH-18h after treatment in $AlCl_3$ -based E. (c) Bar graph of mean S_a values comparison with respect to S_a : before and after cycling.

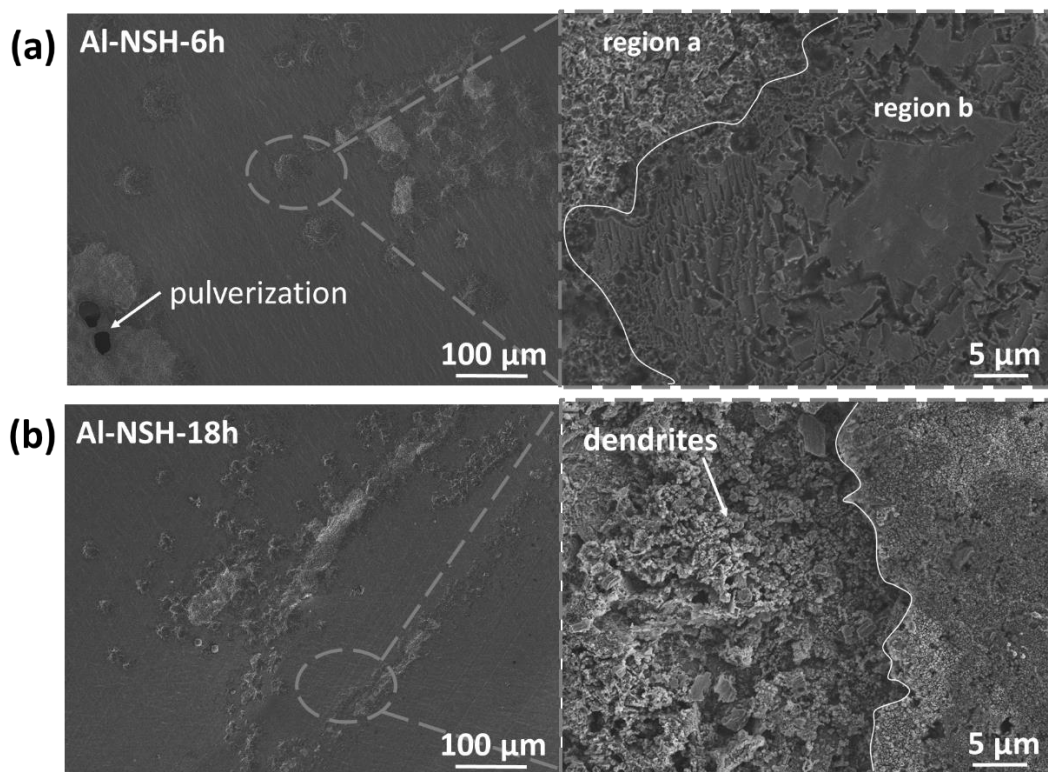


Figure 4-8. SEM images of cycled (a) Al-NSH-6h, and (b) Al-NSH-18h.

The *ex-situ* XPS analysis was conducted on both the pristine Al foil and the Al-NSH-18h sample (Figure 4-9). Spectra from the same element are normalized on the same intensity scale. Several survey spectra were collected for each sample to ensure surface homogeneity, followed by the

acquisition of one set of fine spectra. For the pristine Al-NSH, fine spectra for O1s, C1s, and Al2p were obtained. In the case of Al-NSH-18h, fine spectra for N1s and Cl2p were also recorded, alongside an F1s peak, presumably arising from contamination. The CasaXPS software was employed to fit the obtained spectra [48] and calibration was performed by setting the C – C peak to 285eV. Peaks were fit using a Shirley background and the CasaXPS LA lineshape was used for all peaks, with an ad-hoc asymmetric shape constructed for the conductive Al metal peaks. Each O1s spectrum is fit with two peaks, each C1s spectrum with three, and each Al2p spectrum with two doublets. The O1s spectra were fitted with two peaks, approximately at 531 eV and 532 eV, primarily attributed to Al(OH)₃ and Al₂O₃, respectively. The relative areal ratio of these peaks was roughly 30:70 for both the pristine and treated electrodes, implying that substantial alterations in the oxide's nature were unlikely. This suggests that the treatment might not have significantly affected the oxide or that it possibly regenerated from trace oxygen within the glovebox. The C1s spectrum of the pristine sample revealed the anticipated hydrocarbon contamination layer, featuring peaks corresponding to C-C, C-O, and O-C=O bonds at approximately 285 eV, 286 eV, and 289 eV, respectively. The peak at 286 eV experienced an increase in size and a slight shift towards higher binding energy in Al-NSH-18h, where it also accounted for C-N bonds in the imidazolium electrolyte present on the surface [104]. The Al2p spectra exhibited a pair of doublets, with Al2p_{3/2} peaks around 71 eV and 74.5 eV, attributed to Al metal and Al³⁺, respectively. The latter was exclusively assigned to the oxide film in the pristine Al-NSH, but it was also linked to AlCl₃ deposition resulting from the treatment. The Cl peaks observed in Al-NSH-18h were purely anionic, with two Cl2p_{3/2} peaks at 197.5 eV and 198.5 eV. The higher-energy peak corresponded to AlCl₃ [136] while the lower one likely represented EMImCl, in accordance with Calisi *et al.* [103] and our own previous results [2]. The N1s spectrum displayed a predominant peak at 401.8 eV and a minor peak at 399.8 eV. The major peak was attributed to the imidazolium cations of the electrolyte [104] and the minor peak is due to indeterminate neutral C – N species. The origin of these species could stem from the imidazolium cations interacting with the electrode surface, or from anhydrous ACN used for sample washing. Ultimately, it seems likely that these products are simply unmodified electrolyte residue, but the data is inconclusive as to whether treatment results in corrosion or, perhaps, robust electrode-electrolyte interphase layer

formation. The F1s spectrum has a major peak at 685.1 eV and a minor one at 688 eV. The latter indicates C – F bonding, though the peak is far too small to be visible in the C1s structure. The major peak was likely associated with Al oxyfluorides [137]. A summary and approximate breakdown of the relative signal between spectra can be found in Table 4-1.

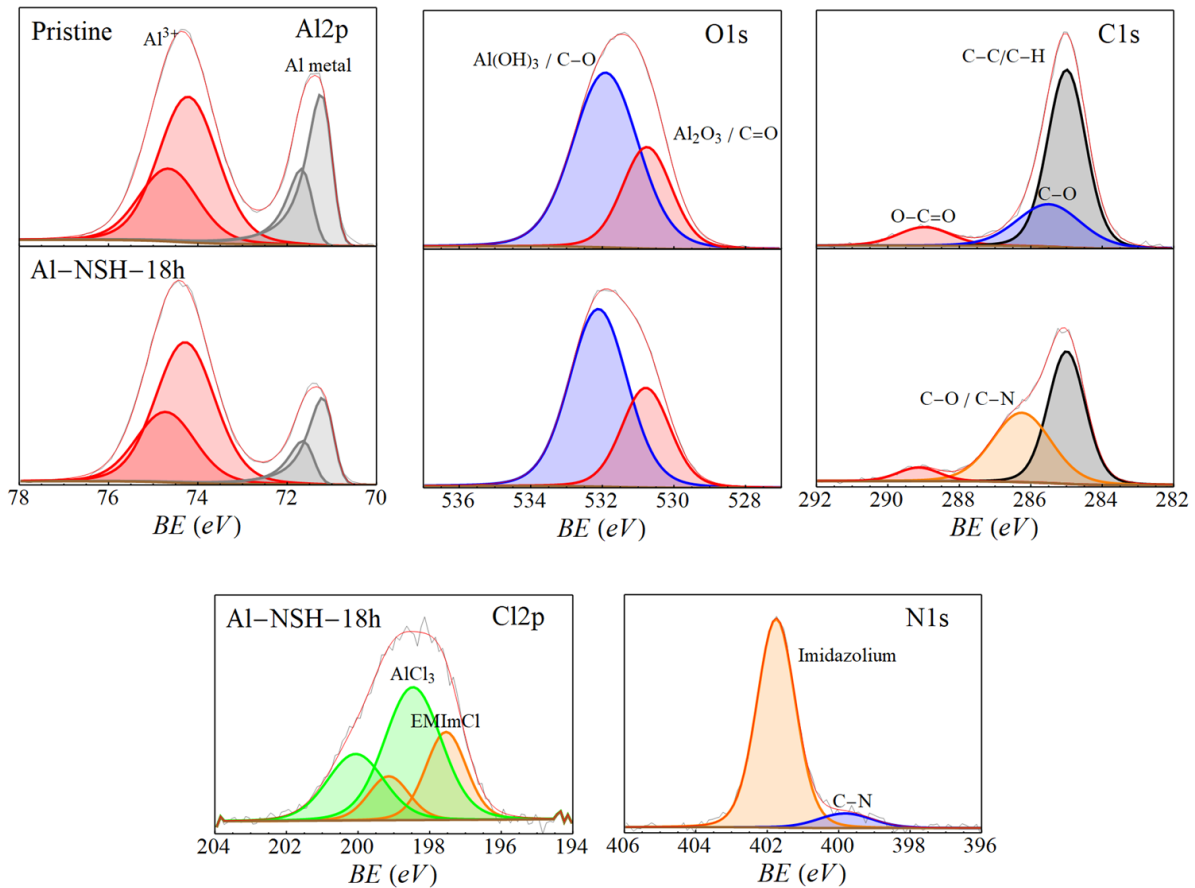


Figure 4-9. XPS fine spectra with peak assignments for pristine Al-NSH and Al-NSH-18h. Cl2p and N1s were taken only for Al-NSH-18h.

Table 4-1. A table of binding energies in eV, assignments, and % signal content for each species on each foil surface.

Peak	Pristine Al-NSH		Al-NSH-18h		Assignment
	Binding energy (eV)	% signal	Binding energy (eV)	% signal	
F1s	-	-	685.1	1.6	Al Oxyfluorides [137]
	-	-	688	0.2	C – F
O1s	530.7	11.2	530.8	11.2	Al ₂ O ₃ , C = O
	531.9	25.4	532.1	23.9	Al(OH) ₃ , C – O
N1s	-	-	399.8	0.2	neutral C – N [104]
	-	-	401.8	2.6	Imidazolium [103], [104]

C1s	285	17.1	285	13	C – C
	285.5	6.8	286.3	10.7	C – O, C – N
	289	2.5	289.1	1.5	O – C = O
Cl2p _{3/2}	-	-	197.5	1	[EMImCl] [103], [104]
			198.5	2.1	AlCl ₃ [136]
Al2p _{3/2}	71.1	12.8	71	7.6	Al metal
	74.2	24.2	74.3	24.4	Al ³⁺

The Changes in surface microstructure and roughness of cycled Al-NSH foils are depicted in Figure 4-10. The AFM images of the cycled Al foils unveil changes in microstructure in comparison to their pristine counterparts across/for all conducted experiments. These AFM images, as illustrated in Figure 4-10(a), were captured both before and after 100 cycles in AlCl₃-based E, following treatment of 6h and 18h. The cycled Al-NSH foils exhibit a combination of features such as cracks, fractures, and the evolution of granular structures after undergoing 100 cycles. The average S_a of the cycled Al-NSH foils, with and without prior treatment, is presented in Figure 4-10(b) using a bar diagram. Error bars reflect standard deviations from data for three different spots at one sample in Figure 4-10(b). All cycled samples display a considerable increase in mean S_a values when compared to the pristine Al foil prior to cycling. Among these, Al-NSH-18h exhibits the most prominent increase in mean S_a , reaching 889 ± 39 nm. Interestingly, the 6h treatment (Al-NSH-6h) results in a relatively lesser increase (264 ± 31 nm) in S_a even when compared to the sample without any treatment (426 ± 35 nm). Although the mean S_a values after treatment prior to cycling are similar, the effects become more obvious after 100 cycles. It seems that the longer duration of treatment yields more active sites for the Al redox reaction, as indicated by the CV data Figure 4-3(b). This suggests that longer treatment increases the density of active sites and potentially enhances the kinetics of the Al deposition and dissolution processes.

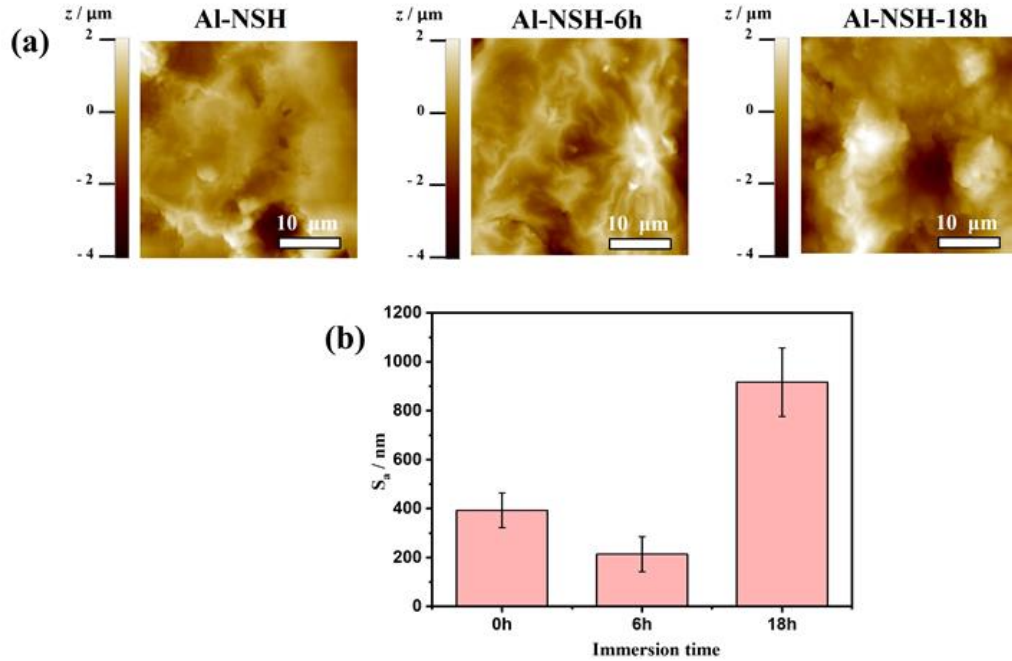


Figure 4-10. (a) AFM topography images of cycled NT-Al-NSH, Al-NSH-6h, Al-NSH-18h, (b) Bar graph of mean S_a values comparison with respect to S_a .

Figure 4-11(a) illustrates the behavior of Al-NSH during long-term cycling, shedding light on the process of electrode aging. After undergoing 300 cycles, a high level of polarization becomes evident that leads to a noticeable shift in the Al plating and stripping peaks towards lower and higher potentials, respectively. These shifts in both anodic and cathodic polarization can be attributed to several factors such as the substantial polarization due to a rise in resistance, the occurrence of Al pulverization, and particularly severe corrosion. The continuous removal of Al metal and oxide coupled with the generation of active sites accelerates local corrosion and consequent electrode pulverization during cycling. The role of dendritic Al deposition on the Al surface emerges as a critical factor influencing both the Al plating process and the corrosion observed during extended cycling. The presence of dendritic Al deposition suggests a heterogeneous current distribution, mainly concentrated within the generated active sites exhibiting deep pitting corrosion. This non-uniform current distribution within the active sites results in an unequal consumption of active Al, ultimately leading to an unstable electrode/electrolyte interface. Figure 4-11(b) presents SEM images of cycled Al-NSH to provide a visual evidence of severe corrosion and pulverization resulting from the extensive utilization of metallic Al during the stripping process. The presence of dendritic Al deposition, often exhibiting

pebble-like and spherical morphologies, is directly related to the unremoved Al_2O_3 oxide passivation film that covers the Al surface. The observed variation in dendritic morphologies reflects the increased current density during prolonged cycling, as indicated by the recorded CV in Figure 4-11(a). The identification of galvanic corrosion is confirmed by the EDX results, which reveal the presence of Fe, an impurity present in the Al foil at sites of severe corrosion on the Al surface (Figure 4-11(c)). Figure 4-12(a) shows an AFM image of the Al foil without any prior treatment after 500 cycles. The observed granular morphology is consistent with the SEM image depicted in Figure 4-11(b), providing visual evidence of dendritic Al deposition, corrosion, and pulverization that happened during the extended cycling. The corresponding roughness parameters are presented in a bar diagram in Figure 4-12(b), showcasing a decrease in the mean S_a value (299 ± 20 nm) after 500 cycles. In Figure 4-12(b), error bars reflect standard deviations from data for three different spots at one sample. This decrease aligns with both the SEM images and the recorded CV data. It's worth noting that the S_a value after 500 cycles is lower than what might be expected when comparing it to the NT-Al-NSH cycled for 100 cycles (426 ± 35 nm). This discrepancy could potentially be attributed to the limited number of examined samples and other variables influencing the surface morphology over prolonged cycling.

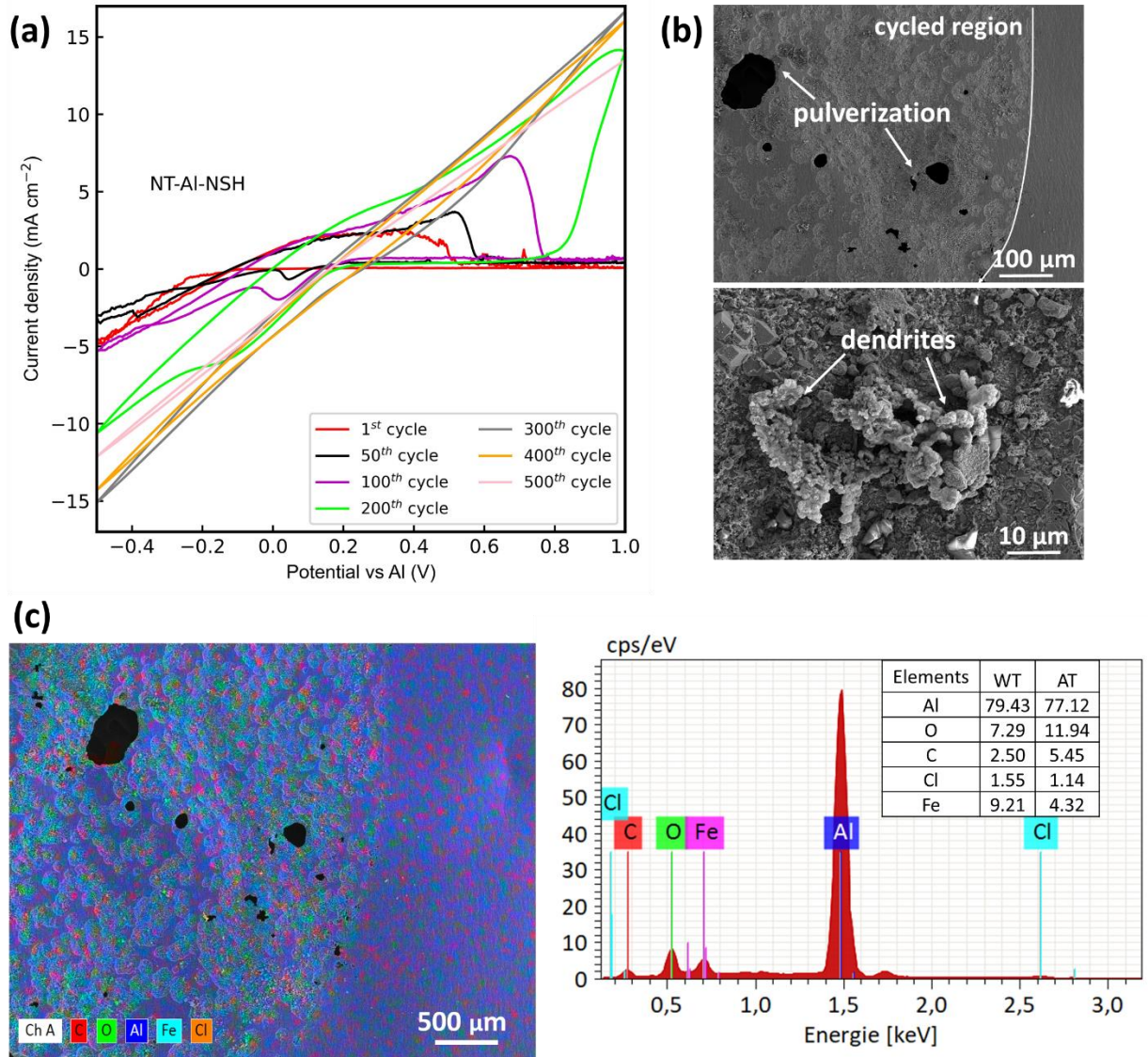


Figure 4-11. 500-cycled recorded CV on NT-Al-NSH in AlCl_3 -based E. (b) corresponding SEM and (c) EDX result and observed elements.

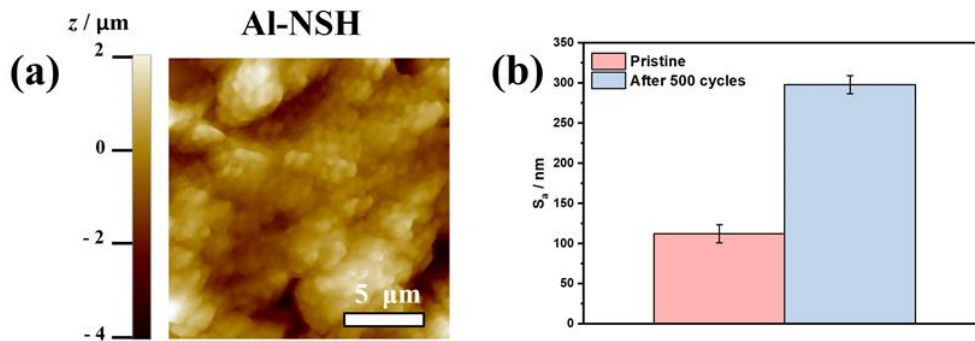


Figure 4-12. (a) AFM topographic images of the 500-cycled NT-Al-NSH. (b) Bar graph of mean S_0 values.

Figure 4-13 present summary of the nanomechanical characterization results before and after cycling. Figure 4-13(a) presents a bar graph illustrating the nanomechanical properties of both the pristine Al-NSH and the Al-NSH foil cycled for 100 cycles without any treatment in AlCl_3 -based E. Error bars represent standard deviations from data collected at three different spots on one sample. Corresponding AFM images are provided in Figure 4-13(b), revealing the topography, adhesion force, deformation, and Young's modulus of the pristine and cycled Al-NSH foils. It is important to emphasize that the data presented in these images and graphs reflect trends in nanomechanical properties rather than absolute values. This is due to the intricate and complex nature of the treated and cycled samples, which are influenced by various factors. The adhesion force of the pristine Al-NSH measures at 193.89 ± 24.24 nN ($n = 3$). This value significantly decreases to 24.24 ± 1.57 nN ($n = 3$) after 100 cycles. This change in adhesion force can be attributed to several factors. The diamond-coated AFM probes used for measurements are oxygen-terminated. According to the XPS data, it's obvious that the hydrophilic O-terminated diamond probe exhibits stronger adhesion with the oxide layer of the pristine sample. However, as a result of treatment and cycling, changes in surface groups, as revealed by XPS data, lead to a decrease in adhesion. Moreover, the increase in S_a over cycling could contribute to this observed reduction in adhesion [138]. Changes in deformation values are also observed after cycling. The cycled Al-NSH exhibits a deformation increase of 31 ± 4 nm compared to the pristine value of 5 ± 1 nm. These changes in deformation can be attributed to the corrosion reaction that takes place during the stripping process, leading to changes in the surface microstructure. The Young's modulus of the pristine Al foil measures at 1.88 ± 0.23 GPa, whereas it decreases to 1.13 ± 0.1 GPa after 100 cycles. The nanomechanical properties of such complex samples are influenced by many factors, such as changes in surface morphology along with the deposition of products. The observed decrease in both adhesion force and Young's modulus after cycling can potentially be attributed to the changes in surface microstructure caused by the partial or complete removal of the oxide passivation film (Al_2O_3) from the Al foil surface. Subsequent deposition of Al dendrites during the plating/stripping process in AlCl_3 -based E is also likely contributing to these changes.

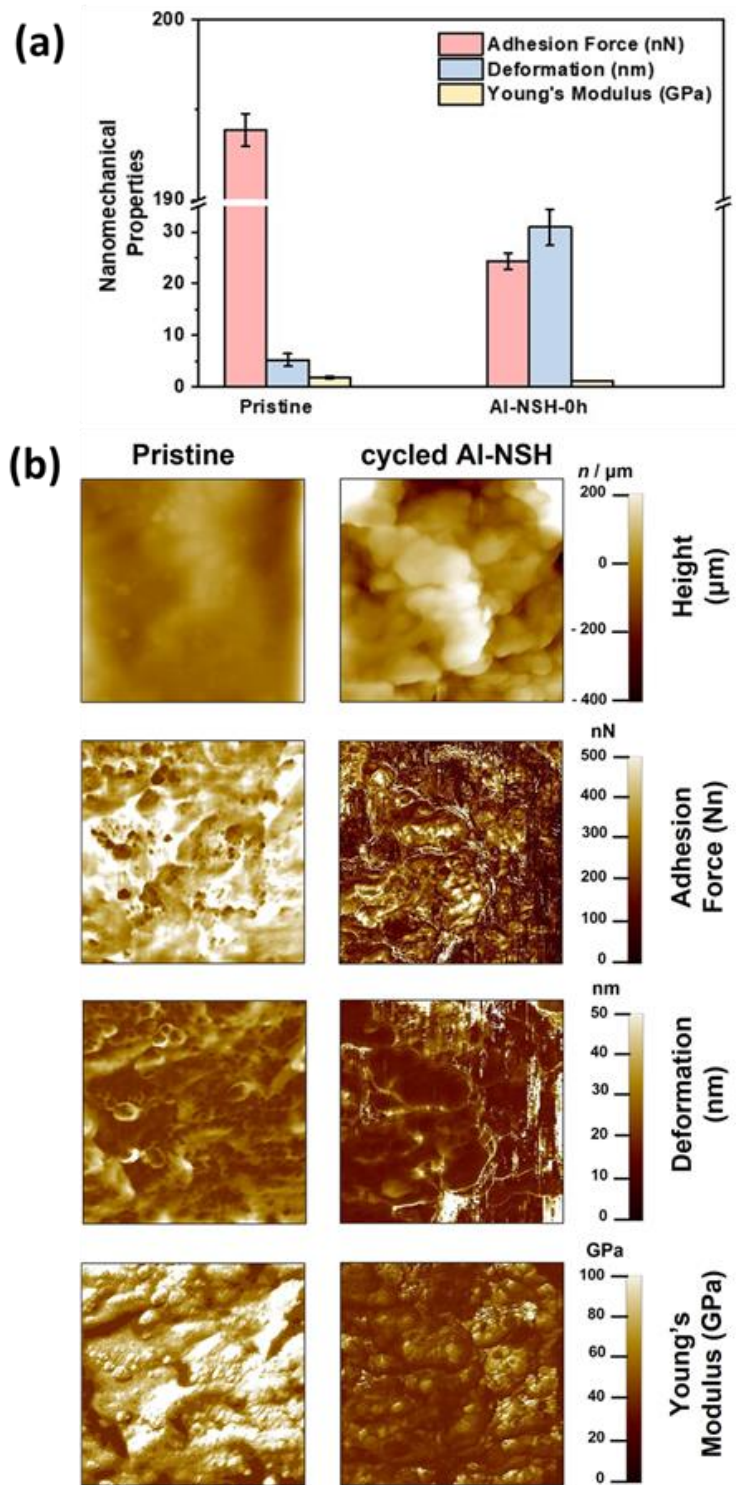


Figure 4-13. (a) Nanomechanical properties, and (b) Nanomechanical characterization (recorded image of height, adhesion force, deformation and Young's modulus. Scale = $5 \times 5 \mu\text{m}^2$.) of pristine and cycled Al in AlCl_3 -based E.

4.2.2 Conclusions and Outlook

This study has provided valuable insights into how the surface properties, specifically the roughness and microstructure of Al foils influence their electrochemical behavior and aging as potential negative electrodes in AIBs. Several important factors should be considered when investigating the role of surface modification on Al plating and stripping processes. The characteristics of the initial Al electrode surface, including its roughness and microstructure, play a significant role in determining its electrochemical performance. Differences between the shiny and non-shiny sides of the Al foil were observed, with the latter being more susceptible to be attacked by aluminum chloride complexes and undergoing surface changes. Moreover, the duration of treatment and the amount of AlCl_3 -based E can affect the surface properties of the Al electrode. Optimizing the treatment time (such as 18h) can lead to improved reversibility and cycling performance, ensuring that the M-Al foil can be cycled reversibly from the first cycle. The acidity and composition of the electrolyte, including the mass of AlCl_3 -based E used for treatment, can alter the surface properties of the Al foil. These factors need to be considered when studying the effects of surface modification on Al plating and stripping. Furthermore, the surface properties of the Al electrode directly impact the transport of electrons and ions at the electrode-electrolyte interface, affecting the overall electrochemical performance. The study also highlighted the role of surface properties in electrode aging and degradation. The changes in mechanical properties, such as adhesion force, deformation, and Young's modulus, are influenced by complex interactions between the surface microstructure, deposition of products, and corrosion processes. On top of that, given the complexity of the studied samples, qualitative trends were presented.

Further works such as *in-situ* studies and modelling, are necessary to gain a deeper understanding of the intricate interactions occurring at the electrode-electrolyte interface during cycling.

5 Evaluation of Metallic Current Collectors in Al Dual-Ion Batteries

5.1 Research background and Methodology

The interest in studying AIBs grew substantially after Dai *et al.* [18] demonstrated stable and ultrafast AIBs in 2015, utilizing an aluminum anode, a three-dimensional flexible graphite cathode, and an [EMImCl]/AlCl₃ ionic liquid electrolyte (ILE). In the pursuit of enhancing AIBs, researchers have explored widely the utilization of low-temperature molten salt electrolytes and room-temperature organic ionic liquids as viable electrolyte options [139], [140], [141], [142], [143], [144], [145], [146], [147], [148], [149], [150], [151], [152], [153], [154]. Some of the reported AIBs, offer wide operating temperature ranges, high conductivity, and non-flammability, reinforcing their potential as environmentally friendly and sustainable solutions [155], [156]. Table 2 displays a comprehensive summary of the reported cathode materials, mostly coated on Mo current collector in AIBs. These studies involve the utilization of a room-temperature ionic liquid electrolyte, [EMImCl]: AlCl₃, with varying molar ratios. Notably, different metallic current collectors (CCs) have been employed to coat the cathode active material, although the stability of these collectors in the acidic [EMImCl]: AlCl₃ ILE has not been systematically evaluated. This oversight raises important questions about the viability and durability of these CCs under specific electrolytic conditions, highlighting a crucial area for further investigation and optimization in AIB technology.

Table 2. Summarized reported AIBs using [EMImCl]: AlCl₃ electrolyte.

Cathode material	CC	Cell configuration	[EMImCl]: AlCl ₃
three-dimensional (3D) graphitic-foam cathode [157]	Ni	Pouch cell	1:1.3
pyrolytic graphite [157]	GC	Swagelok cell	1:1.3
commercial carbon paper [158]	Mo	Swagelok cell	1:1.3
3D foam graphite [159]	Ni	pouch cell	1:1.3
Ni ₃ S ₂ /graphene micro-flakes composite (Ni ₃ S ₂ @graphene) [152]	Ta	pouch cell	1:1.3
hexagonal NiS nanobelts (NiS) [150]	Ta	pouch cell	1:1.3
3D reduced graphene oxide-supported SnS ₂ nanosheets hybrid(G-SnS ₂) [151]	Mo	Swagelok cell	1:1.3
graphene aerogel [160]	Ni	coin cell	1:1.3
graphene aerogel [160]	Ta	pouch cell	1:1.3
metal-organic frameworks (MOF)-derived carbon [161]	Ni	coin cell	1:1.3
cobalt Sulfide@Carbon nanotube(Co ₉ S ₈ @CNTs-CNFs) [149]	free-standing	Swagelok cell, and pouch cell	1:1.3

porous microspheric copper oxide (PM-CuO) [153]	Ta	pouch cell	1:1.3
MOF-derived Co ₃ O ₄ @MWCNTs Polyhedron (Co ₃ O ₄ @MWCNTs) [162]	Mo	-	1:1.3
ultrasonic graphite flakes [163]	W	pouch cell	1:1.3
Sb ₂ Se ₃ nanorods with N-doped reduced graphene oxide hybrids [146]	Ta	pouch cell	1:1.18
ordered macroporous cobalt diselenide@carbon (3DOMCoSe ₂ @C) [145]	Ta	Swagelok cell	1:1.3
MOF-derived CoTe ₂ nanoparticles@nitrogen-doped porous carbon polyhedral composites (CoTe ₂ @N-PC) [144]	Mo	-	1:1.3
graphite/copper phthalocyanine (CuPc@graphite) [141]	Ni	pouch cell	1:1.4
acid-treated expanded graphite (AEG) and base-etched graphite (BEG) [154]	Mo	Swagelok cell	1:1.5
heterostructured Bi ₂ Te ₃ /Sb ₂ Te ₃ nanoflakes [142]	Mo	Swagelok cell	1:1.3
cobalt sulfide@carbon nanofibers composite films (CoS ₂ @CNFs)[148]	free-standing	pouch cell	1:1.3
SnSe nano-particles[147]	Mo	bottled battery	1:1.3
two-dimensional V ₂ C@Se (MXene) composite [143]	Mo	-	1:1.3
polycyclic aromatic hydrocarbons (PAHs)[140]	Mo	Swagelok cell	1:1.3
Co ₃ Sn ₂ wrapped with graphene oxide (Co ₃ Sn ₂ @GO)[139]	Mo	pouch cell	1:1.3

CCs are one of the essential components of ABs [164], [165], [166]. CCs play a crucial role in supporting active materials including conductive additives, binders, anode, and cathode materials. Moreover, CCs connect an external circuit with the whole anode and cathode structure [167]. It is crucial for the CC to exhibit specific attributes such as mechanical strength, a lightweight structure, and the ability to withstand chemical and electrochemical challenges posed by the electrolyte [167]. Changes have been made to the thickness, hardness, compositions, coating layers, and architectures of CCs in order to increase the charge/discharge cyclability, energy density, and rate performance of a cell, among other elements of battery performance [167], [168]. Considerations have been given to cheap, lightweight carbon fibers [169], clothing [170], and carbon derived from biomass [171]. These porous CCs can offer an efficient electrical transportation network and reduce the ion diffusion route. Moreover, the porous CCs have enough mechanical strength to withstand the strain and tension caused by the significant volume change of graphite cathodes. However, carbon-based materials cannot be used as CCs for AIBs, as both graphitic and amorphous carbon materials are potential active material for cathode [172]. A certain degree of graphitic character in the carbon material is considered to be necessary for CCs to provide adequate electrical conductivity, but materials acting as CCs should not have a graphitic nature, because this could cause the CCs to become electrochemically active. They will

host anions and cause volumetric changes, which means they will cause the active species to be separated from the cathode electrode and significantly reduce capacity [172]. Concerning (non-) metallic CCs in AIBs, the most frequently employed materials in descending order of usage as follows: Ni, Mo, stain steel, carbon paper, GC, Ta, W, Pt, and Ti [173]. It is revealed that Ni can't be a suitable choice among CCs in this context. Ni exhibits comparable activity to stain steel [174]. Based on an extensive overview of suitable metals and compounds for CCs within the potential range of 0 to 2.5 V in [EMImCl]:AlCl₃ ILE, chromium, SS, Al, Ti, and even Au proved to be active (react with ILE) [165]. In contrast, increased stability for materials such as Mo, GC, W, Chromium nitride (Cr₂N), and Titanium nitride (TiN) is documented [165]. V₂O₅ is considered as one of the promising cathode materials coated on SS capable of intercalating Al³⁺ ions in ILE in coin cell configuration [54]. However, the entire electrochemical contribution may not have originated from the active V₂O₅ material but rather from the SS components used in the system [175]. Chen *et al.* [176] identified Ta but also introduced Indium Tin oxide (ITO) as a novel and previously unexplored CC. Their research demonstrated that both Ta and ITO exhibited remarkable stability, capable of withstanding voltages up to 2.75 V vs. Al RE. This finding suggests that ITO, traditionally known for its use in transparent conductive coatings, could be a promising addition to the collection of stable CCs for advanced battery technologies. They found that Pt exhibited oxidation at approximately 1.8 V vs. Al RE, while Mo showed a similar behavior at around 2.0 V vs. Al RE [176]. This particular redox behavior for Mo is also corroborated [177]. However, it is worth noting that despite these observations, many studies employed Mo foil as a CC, revealing the negligible activity of Mo [177]. This suggests that the specific role and contribution of Mo as a CC may vary depending on the particular battery system and experimental conditions. Due to the corrosivity of the [EMImCl]:AlCl₃ ILE [165], [166], conventional CCs like SS, Cu, and Ni which are commonly used in other batteries cannot be utilized in AIBs. Some studies tend to downplay the significance of the Mo foil as a CC [174], [177], [178], [179]. Moreover, as CCs for AIBs, electrochemically inert foils such as W [166], Mo [164], and anticorrosive TiN-coated stain steel [165] were used. Surprisingly, only a few authors [176] have acknowledged the reactivity of the Mo foil. Yu *et al.* [177] noted an identical redox behavior of Mo CC as observed by other researchers but deemed it negligible when compared to the electrochemical activity of the graphite used as the positive electrode material. Similarly, Sun *et al.* [179] characterized the redox behavior as merely an

interface reaction between Mo CC and the electrolyte. These observations underscore the need for a more comprehensive understanding of the role and reactivity of Mo-foil as a CC, which has been overlooked in many prior studies. On the other hand, the W substrate employed as the cathode CC is one of the biggest cost contributors [172], [180]. Decreasing the volume and weight of inert components like CCs in batteries can directly increase their energy density. Therefore, other reasonably priced CC materials should take the place of the pricey W CC, because existing AIBs have a far lower specific energy density than LIBs (180 W h kg^{-1}) [180]. Chloroaluminate melts' high corrosivity and reactivity should be taken into account while conducting electrochemical testing and developing new electrochemical systems. The test cell's chemical and electrochemical stability should be confirmed before beginning any electrochemical evaluation. Reporting electrochemical reference measurements for the employed cell's stability is always advised. Furthermore, it is important to confirm that the electrode materials are stable in the utilized electrolyte. The stability of the inexpensive cell parts (CC, cell shell, separator, sealing glues) in chloroaluminate electrolytes has to be studied for the long-term development of this technology [165]. The stability of Mo and W appears to vary depending on the specific study. Oh *et al.* [174] report that Mo is more stable than W in this context, while Wang *et al.* [179] present contrasting findings, suggesting that W may exhibit greater stability. These discrepancies highlight the complex and nuanced nature of the interactions between different materials and the [EMImCl]: AlCl_3 ILE, underscoring the need for further investigation and a deeper understanding of these phenomena. The literature [139], [140], [141], [142], [143], [144], [145], [146], [147], [148], [149], [150], [151], [152], [153], [154] predominantly emphasizes cathode materials in the realm of battery research, overlooking the significance of CCs.

5.2 Criterion for the level of the instability of the Current Collectors in [EMImCl]: AlCl_3 electrolyte

There is a noticeable lack of practical studies dedicated to evaluating and investigating metallic CCs. This gap in research hampers comprehensive understanding of the entire battery system. This frontier study focuses on investigating the stability of metallic CCs within [EMImCl]: AlCl_3 ILE. Understanding how different metallic CCs endure in specific electrolyte environment is crucial. Unstable CCs can significantly affect the battery cycling performance. Corrosion or degradation of the collector material can lead to increased electrical resistance, hampering efficient

charge/discharge processes. This, in turn, results in diminished battery capacity, reduced energy efficiency, and ultimately shorter battery lifespan. This research not only sheds light on CCs durability but also challenges the stability of the metallic CC.

5.2.1 Findings and Discussion

The immersion tests of metal foils in AlCl_3 -based ILE were conducted to assess their corrosive resistance. All the metallic CCs including Ni, Ti, Mo, Ta, and W were immersed for durations of 24h, 48h, 1 week, and 1 month. After each immersion, the foils were cleaned with anhydrous ACN to eliminate residual electrolyte, followed by vacuum drying to prevent external interactions. Subsequently, the dried foils were examined using SEM to analyze any morphological changes. This approach provides information about surface changes, such as pitting, cracks, or irregularities, indicating susceptibility to corrosion. EDX as quantitative analysis technique was employed for a more objective evaluation of the degree of surface degradation for each foil type over different immersion periods. The SEM images of the immersed CC are presented in Figure 5-1. Upon close examination of SEM images, it became evident that the Ni foil experienced significant corrosion as the immersion time increased (Figure 5-1(a)). Within 24h, observable corrosion manifested as the outer layer of the Ni foil have initiated detachment and corrosion. This process intensified after 48h of immersion. As the immersion time extended, the degree of corrosion on the Ni surface proportionally escalated, resulting in the complete detachment of the outer Ni layer following immersion for both one week and one month. The corresponding EDX results (presented in Figure 5-2, Table A-5- 1) confirmed these findings, demonstrating a notable increase in the presence of elements such as Cl, N, and Al, indicative of the electrolyte's reactivity with the Ni substrate. This clear evidence suggested that Ni, as a metal, was not chemically stable when exposed to the AlCl_3 -based ILE. The reactivity of Ni begins as soon as it comes into contact with the AlCl_3 -based ILE. The surface undergoes a transformation, leading to the formation of NiO and Ni_2O_3 [174]. Comparable observations were made with respect to the behavior of Ti foil. SEM images (Figure 5-1(b)) captured the progression of severe pitting corrosion across the Ti foil's surface, with the extent of corrosion escalating in tandem with the immersion time. EDX analysis further underpinned these SEM findings by revealing an increasing concentration of Cl, N, and Al – all traceable to the interaction between the Ti substrate and AlCl_3 -based ILE (as shown in Figure

5-3 and Table A-5- 2). This alignment of SEM and EDX data affirmed the idea that Ti experienced instability within AlCl_3 -based ILE. Among Mo, W, and Ta foils, Mo experienced the highest degree of corrosion. The SEM images (Figure 5-1(c-d-e)) highlighted distinct pitting corrosion patterns on the Mo (presented in Figure 5-4, Table A-5- 3) and W foils (Figure 5-5, Table A-5- 4), alongside the emergence of Cl, N, and Al signals in the corresponding EDX results. These outcomes confirmed the substantial reactivity of Mo and W with the AlCl_3 -based ILE. There are indications that W also undergoes a reaction when exposed to AlCl_3 -based ILE [165]. In contrast, as demonstrated in Figure 5-6 and Table A-5- 5, the SEM-EDX analysis of the immersed Ta foil indicated a higher degree of resistance to corrosion within the same electrolyte, comparatively outperforming W, Mo, Ti, and Ni foils. This inference was drawn from the lack of prominent pitting corrosion and the minimal increase of Cl, N, and Al signals in the EDX spectrum. In fact, the investigation into the chemical and corrosive stability of various metallic CCs within ILE revealed the susceptibility of Ni, Ti, Mo, and W to varying degrees of corrosion. In contrast, Ta exhibited enhanced resistance against corrosive degradation. It's important to highlight that, following the immersion test, the color of the ILE underwent a slight change from yellow/orange to dark brown or red for all the CCs except Ta foil.

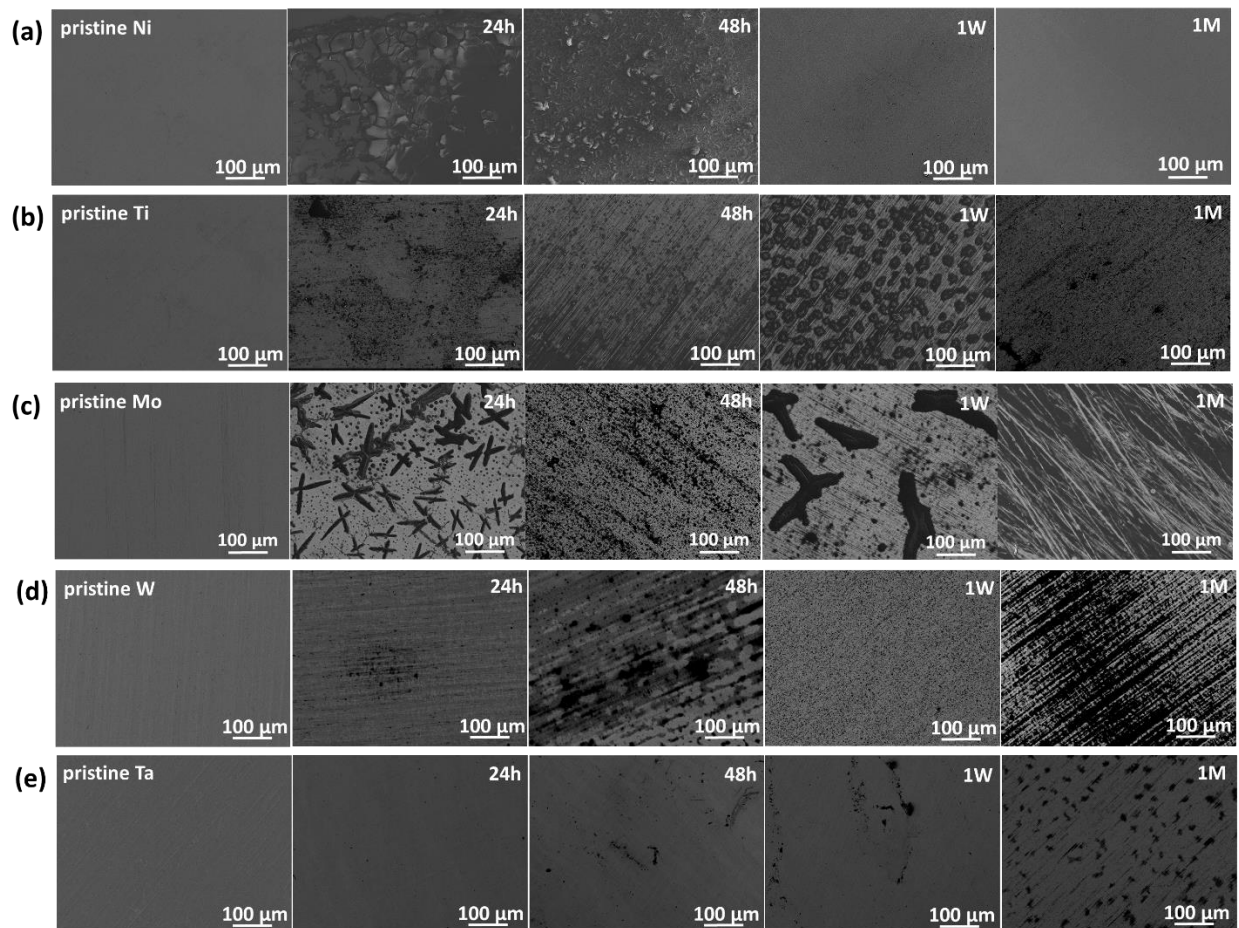


Figure 5-1. SEM images of the pristine and immersed (a)Ni (b)Ti (c)Mo (d)W (e)Ta metallic CCs.

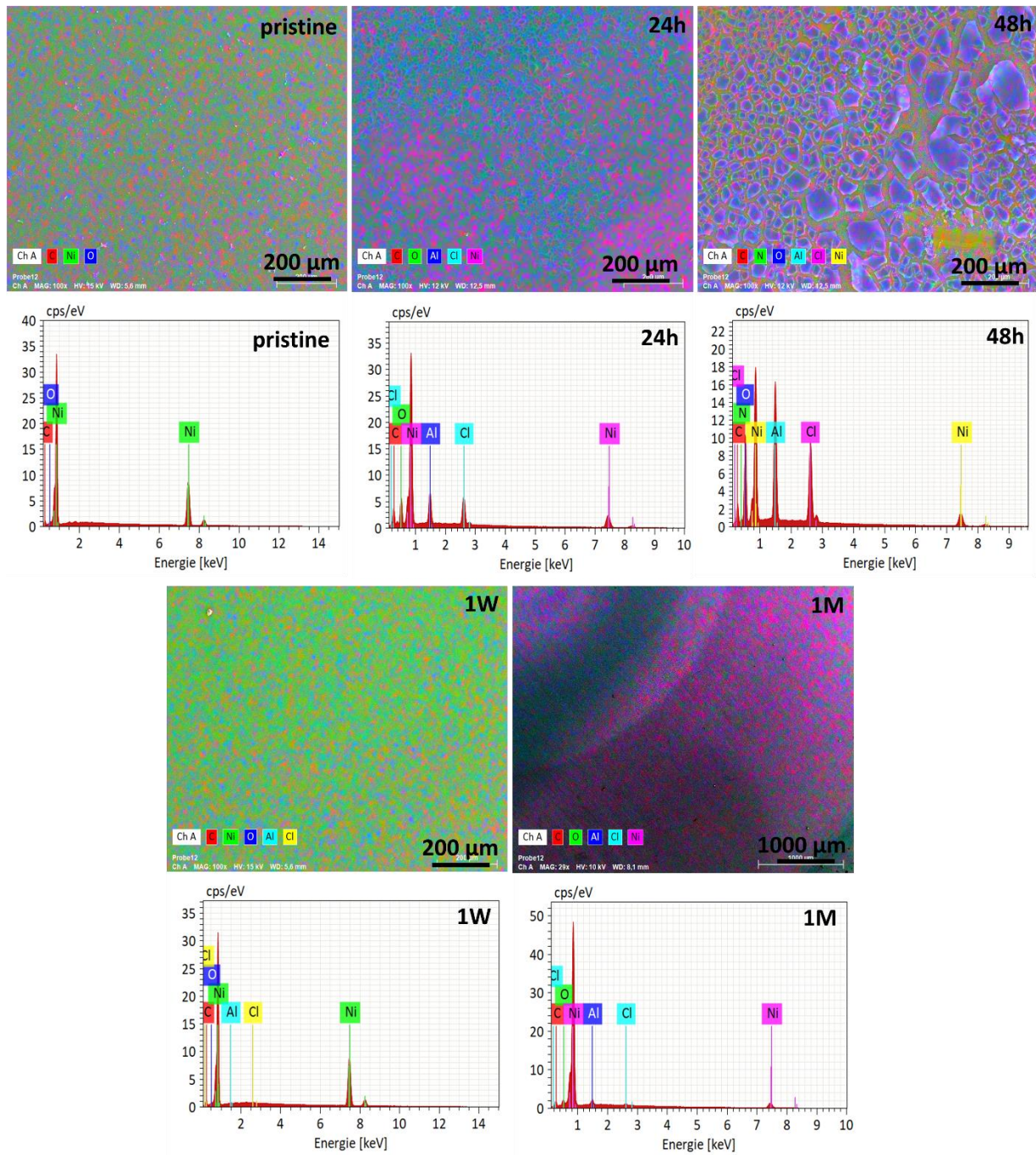


Figure 5-2. EDX images and spectra of the pristine and immersed Ni foils in AlCl_3 -based ILE.

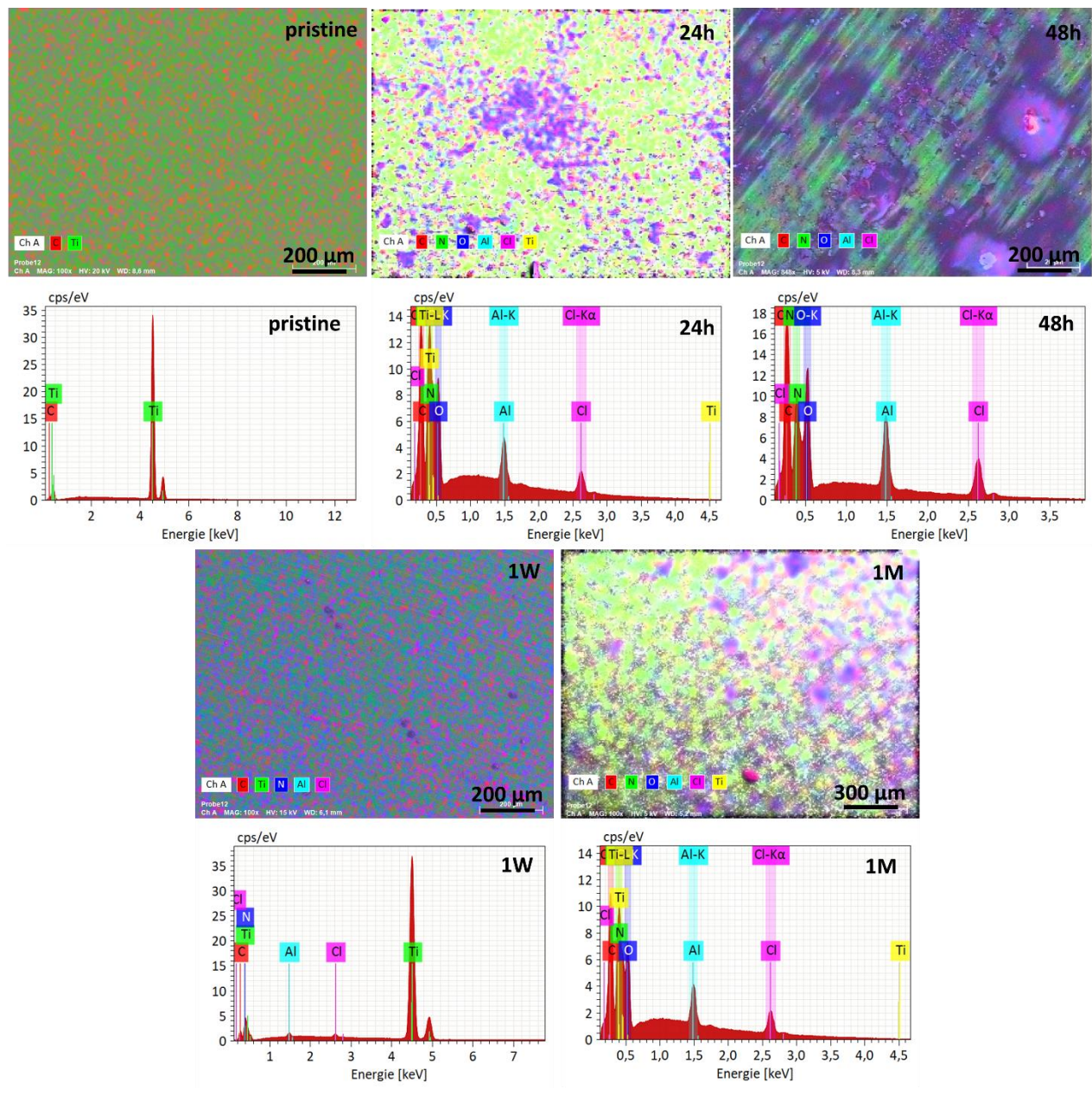


Figure 5-3. EDX images and spectra of the pristine and immersed Ti foils in AlCl₃-based ILE.

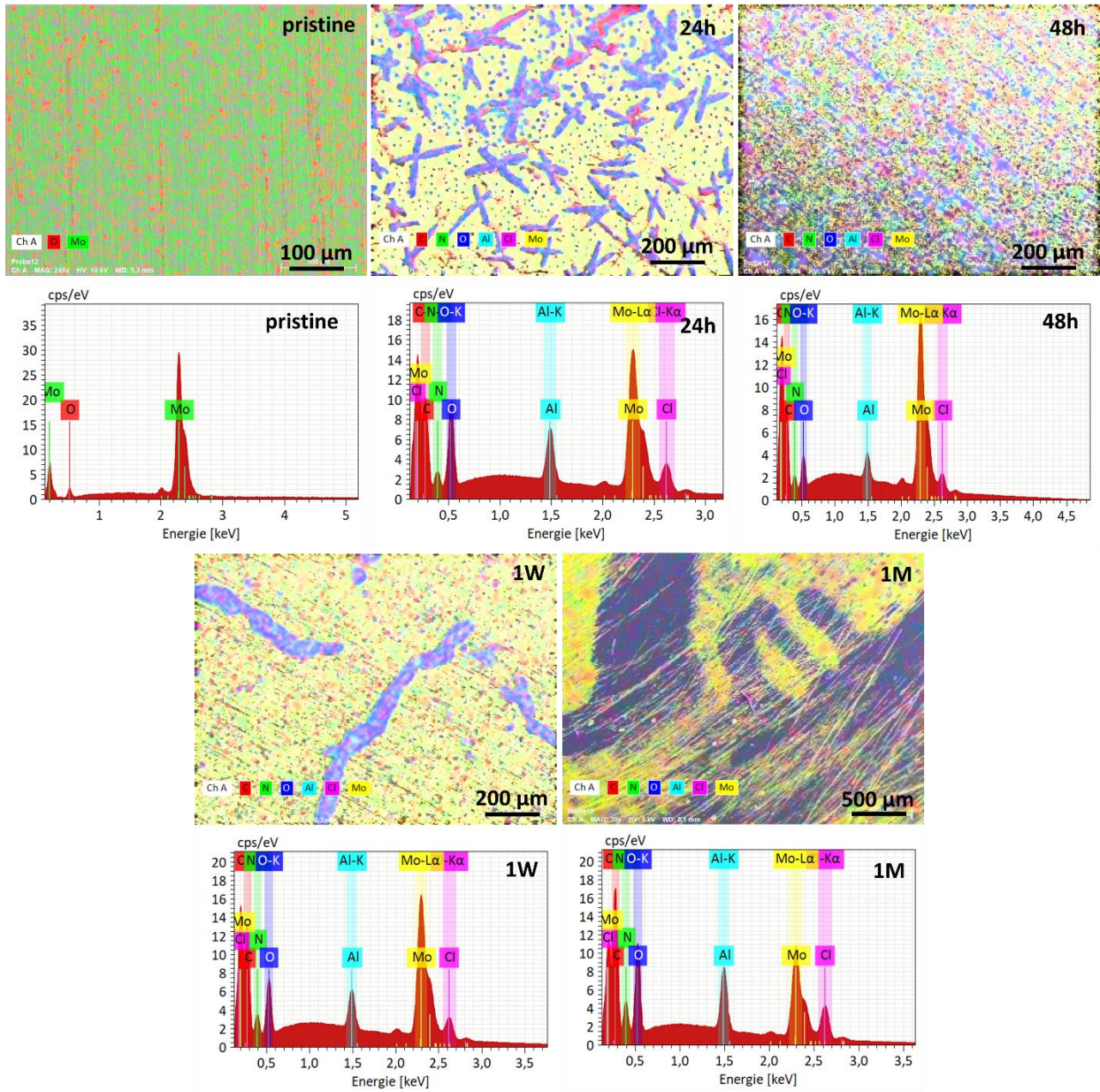


Figure 5-4. EDX images and spectra of the pristine and immersed Mo foils in AlCl₃-based ILE.

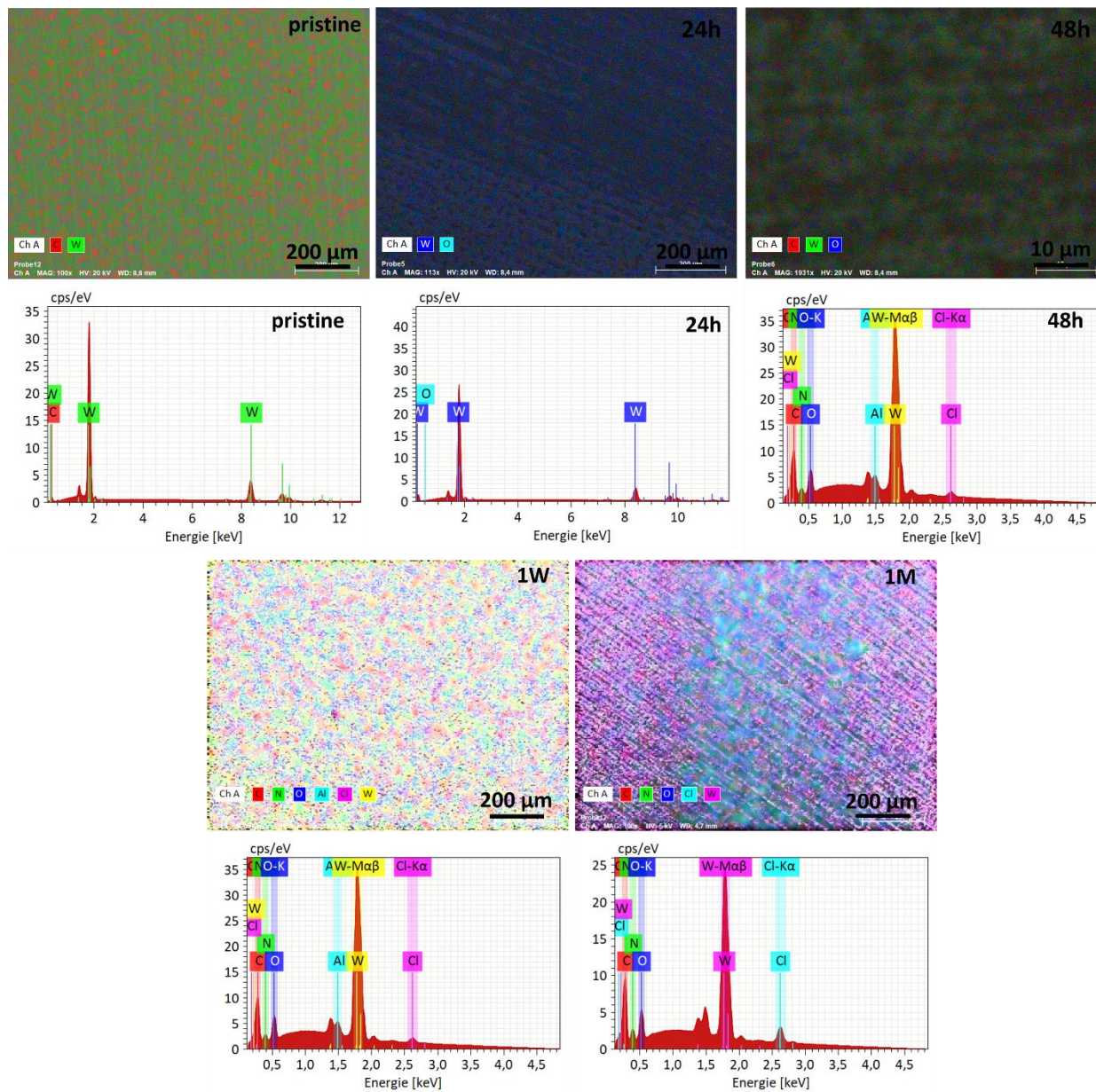


Figure 5-5. EDX images and spectra of the pristine and immersed W foils in AlCl_3 -based ILE.

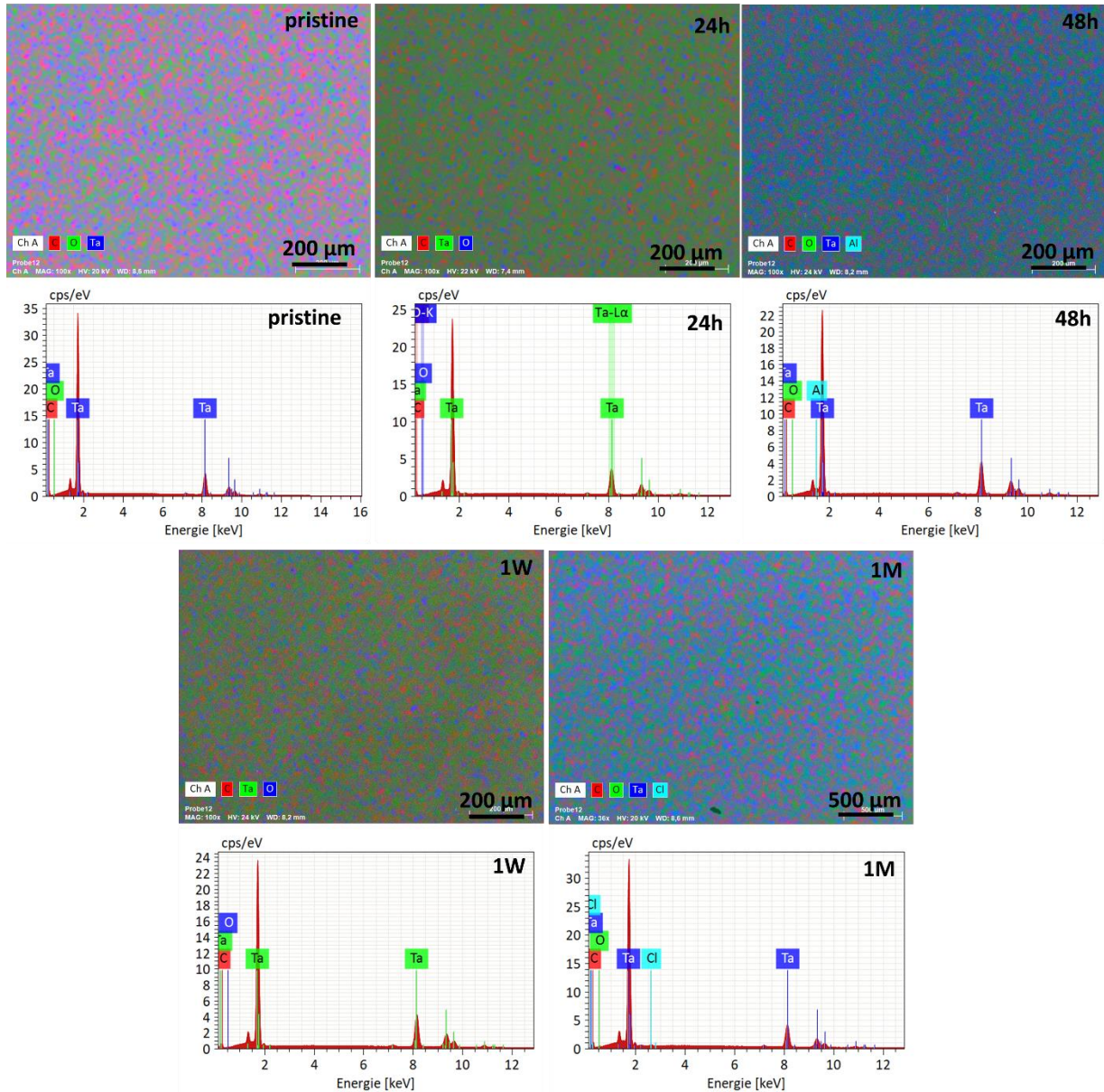


Figure 5-6. EDX images and spectra of the pristine and immersed Ta foils in AlCl_3 -based ILE.

Following up on immersion test, LSV of metal foils as CCs in an acidic electrolyte presents their electrochemical behavior. LSV reveals their corrosion potential, potential range for reactions, presence of passive layers, and current density. This data indicates stability, susceptibility to corrosion, and the impact of the acidic environment that are vital for assessing the foils' long-term performance in batteries and other electrochemical applications. As shown in Figure 5-7, the oxidative doublet peak, specifically between 1 to 1.5 V, indicates the occurrence of electrochemical reactions at the Ni foil's surface within that voltage range. The peak current density of 1.2 mA cm^{-2} represents the rate of these electrochemical reactions. Interpreting this

result in relation to the stability of the Ni foil as a CC in in AlCl_3 -based ILE involves a few key points. The voltage range of 1 to 1.5 V corresponds to the potential range where the oxidative reactions are occurring, suggesting a specific oxidation process at the Ni foil's surface. The doublet peak shape indicates two consecutive or closely related electrochemical processes, possibly due to intermediate species formation during oxidation. The achieved current density of 1.2 mA cm^{-2} indicates the reaction rate. A higher current density could imply higher reactivity, which might impact the Ni foil's stability over time. The presence of oxidative peaks suggests redox reactions on the Ni foil. Depending on the reaction nature, oxide layers or other products might form on the Ni foil's surface, influencing its functionality and corrosion resistance. Correlating this information to Ni foil stability, the oxidative peaks and associated redox reactions raise concerns about potential corrosion susceptibility or surface changes. These reactions might lead to oxide or compound formation, affecting the Ni foil's long-term stability in ILE. Concerning Ti foil, severe corrosion and pitting on the Ti surface after immersion test suggest the susceptibility to degradation in this environment which increases over time. Observed Cl and N in EDX analysis (Figure 5-3), from ILE, supports the corrosive nature. Chlorine ions enhance the corrosion. The identification of Cl and N from the EDX analysis reinforces the aggressive nature of the corrosive electrolyte, substantiating the corrosive-induced degradation trends seen in both the LSV and SEM analyses. The major oxidative peak at 1.7 V, along with the shoulder peak at 2.2 V, signifies electrochemical reactions at the Ti foil's surface within this voltage range. The high current density of 1.38 mA cm^{-2} implies robust reaction kinetics. These reactions contribute to foil degradation. The oxidative peaks depicted in the LSV curve correlate with the corrosive manifestations observed in the SEM images. This suggests that the electrochemical reactions corresponding to the oxidative peaks might be contributing to the observed corrosion and pitting on the Ti foil's surface. However, for Mo, W, Ta foils, the lack of oxidative peaks could imply that these foils are relatively stable within the applied voltage range. The absence of oxidative peaks indicates that the foils might be less susceptible to degradation, which is a positive characteristic for maintaining long-term battery performance. This stability might be attributed to a resistance against reactions that could lead to degradation or corrosion. As potential CCs for cathode materials, the foils' stability within this voltage range of 0 to 3 V is crucial.

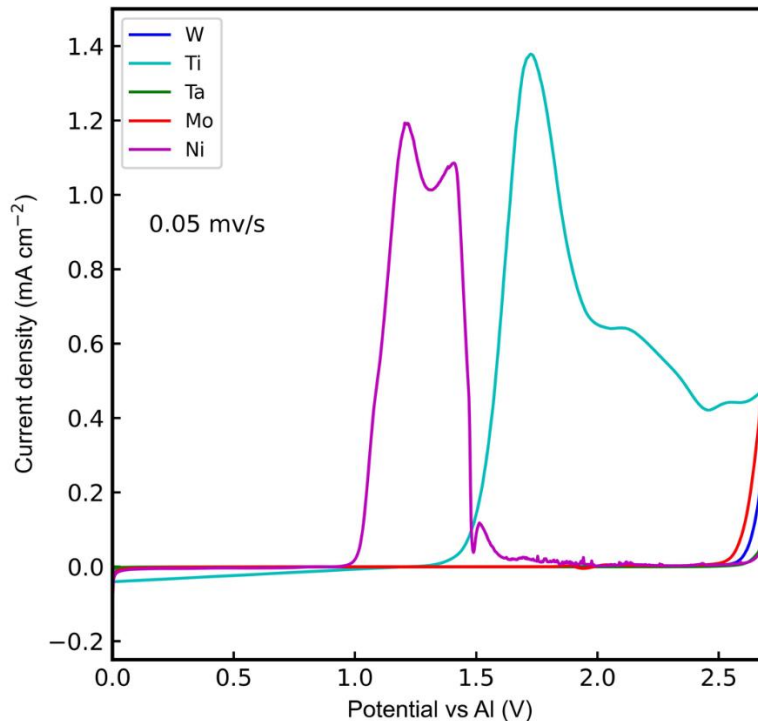


Figure 5-7. Recorded LSV on Ni, Ti, Mo, W, Ta foil in AlCl_3 -based ILE in TSC-SC Al quasi-RE and GC CE.

To assess the electrochemical stability and compatibility of these metallic foils, CVs were conducted. This technique offers valuable information about the foils' stability within the cathodic potential window that is a critical characteristic for their viability (as CCs) of e.g. the graphite cathode material. The initial step involved obtaining LSV profiles for each individual foil. The LSV provided a preliminary indication of the stability of these metallic foils within the potential range of 0 to 2.5 V. Among the tested foils, only Mo, W, and Ta exhibited stability throughout this entire range. The CV experiments were performed using a scan rate of 0.5 mV s^{-1} and a potential range of 0.3 to 2.2 V. This chosen range aligns with the potential window designated for the graphite cathode material, as it is anticipated that these CCs will be utilized to support the deposition of graphite onto their surfaces. The objective of the CV analysis was to probe whether the metallic foils would engage in any undesirable interactions with the electrolyte under the influence of applied potentials or not. By subjecting the foils to repeated potential cycles, the CV technique offers a dynamic perspective on their electrochemical behavior. Specifically, CV provides information about how the current response changes as the potential is swept back and forth within the defined range. In the context of stable foils, a characteristic CV

profile would ideally reveal the absence of redox peaks, instead prominently displaying capacitive current responses. The appearance of capacitive current responses reflects no electrochemical processes occurring at the surface of the foil and implies that the foil remains inert, neither corroding nor reacting with the electrolyte. This type of response is indicative of a compatible and stable metallic CC, making it suitable for its intended role in supporting the graphite cathode material. In Figure 5-8(a) the observable oxidative peaks show the foil's reactivity with the electrolyte, reaffirming earlier indications seen LSV. By synergizing information from both LSV and CV, a clear pattern emerges, characterized by the appearance of three distinct oxidative peaks. These peaks not only reaffirm the interaction between Ni and the AlCl_3 -based ILE but also serve as markers of reactivity. Similar tendencies are evident with the Ti foil (Figure 5-8(b)). The CV profile closely resembles that of the Ni foil with some certain differences. Two primary oxidative peaks are apparent. The larger peak emerges around 1.4 V, accompanied by a current density of 4.2 mA cm^{-2} . This significant peak corresponds to a reversible reaction, and its partner reductive peak appears at about 0.6 V, displaying an approximate -4 mA cm^{-2} current density. Additionally, a secondary oxidative peak, manifesting as a double peak, becomes evident with a lower current density of approximately $+1 \text{ mA cm}^{-2}$, appearing at 2.1 V. This is mirrored by a corresponding reduction peak, similarly presented as a double peak, at 1.8 V and approximately -1 mA cm^{-2} in current density. Considering LSV preliminary assessment of the stability for Mo, W, and Ta foils, further valuating the stability involves a detailed analysis of their CV profiles. These profiles serve as key indicators of their suitability, highlighting electrochemical stability. Examining the CV profile (presented in Figure 5-8(c)) of the Mo foil, distinctive oxidative and reductive peaks are apparent. These peaks are indicators of the foil's reactivity with the ILE. The Mo foil's oxidative and reductive peaks confirm its potential reactivity, which could pose concerns for long-term stability as a CC. The situation changes significantly when it comes to the W and Ta foils. Their respective CV profiles exhibit the prominence of capacitive current responses. Such capacitive current responses align well with the inert attributes of stability in CC materials. As shown in Figure 5-8(f), the captured capacitive current in the CV profiles of W and Ta foils holds paramount significance. It signifies that these foils exhibit minimal interaction with the electrolyte, rendering them stable and well-suited to function as CCs within the potential windows of interest. The capacitive current responses from W and Ta foils not only suggest stability but also align with the

anticipated behavior of an effective CC (to compare the first and fifth cycles see Figure A-5- 5). Lastly, Ni, Ti, and Mo foil's oxidative and reductive peaks reveal reactivity, while the capacitive current responses in W and Ta foil profiles confirm their stability.

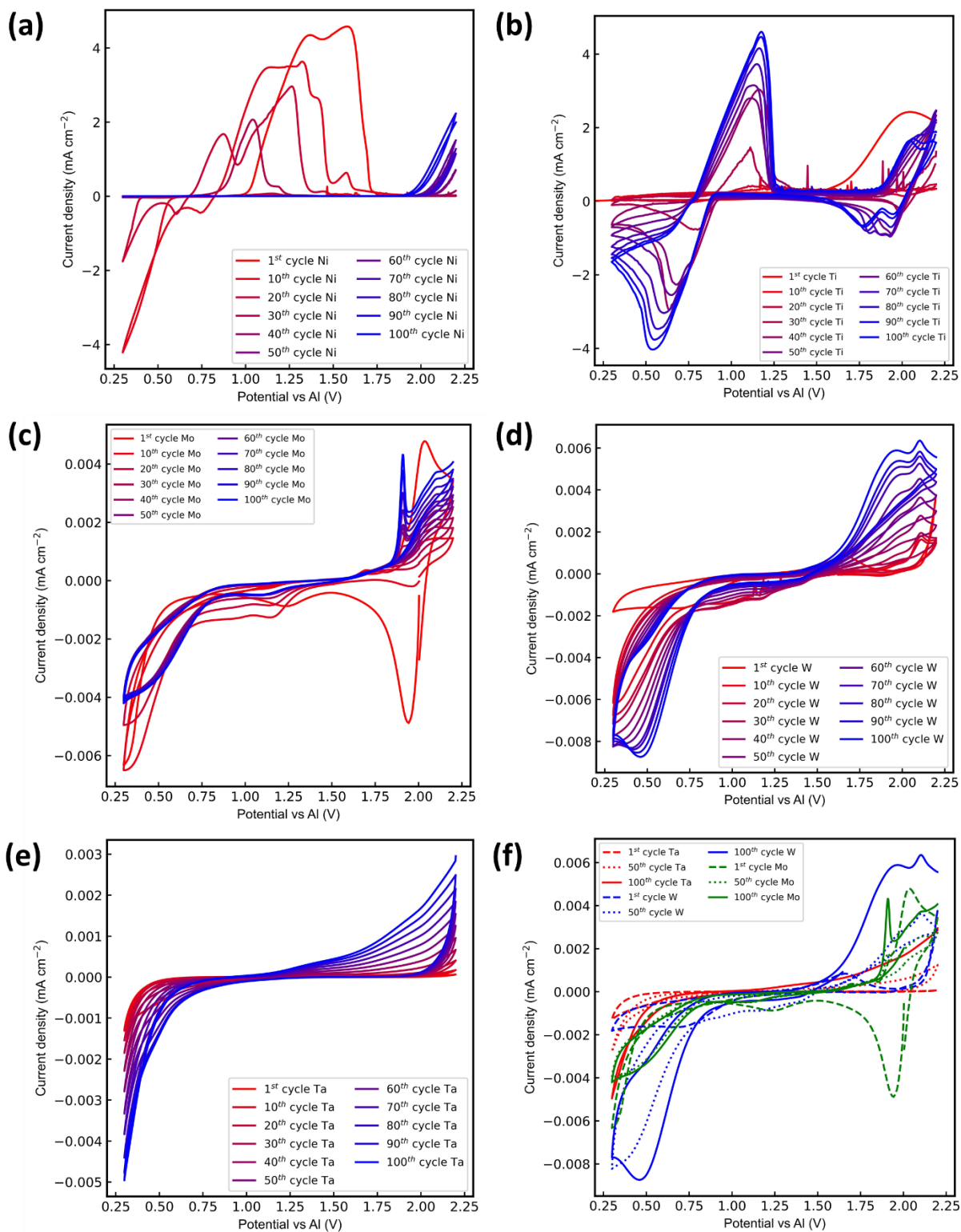


Figure 5-8. Recorded CVs on (a)Ni, (b)Ti, (c)Mo, (d) W (e)Ta (f) CV comparison in AlCl_3 -based ILE in TSC-SC Al quasi-RE and GC CE.

In agreement with the revealed results of recorded CVS on CCs foil, SEM images of the corresponding CCs foil are presented in Figure 5-9. EDX image, spectra of the observed elements on pristine and cycled CCs are presented in Figure A-5-1 to Figure A-5-4. The deposition observed on the surface of the Ni CC is a result of the reaction between Ni and AlCl_4^- , and Al_2Cl_7^- ions. The reactivity of the Ti CC with the ILE leads to severe pulverization of the Ti CC electrode, ultimately resulting in the formation of holes in the Ti CC electrode. On the other hand, the observed pitting corrosion on the Mo CC electrode indicates the reactivity of the Mo substrate with corrosive aluminum complexes present in the electrolyte. This pitting corrosion alters the surface morphology of the Mo CC electrode. In contrast, the surface of the Ta CC undergoes minimal changes in morphology, which is consistent with the observed capacitive current in the recorded CV. The capacitive current suggests that the Ta electrode-electrolyte interface remains relatively stable without significant redox reactions. W CC appears relatively more stable compared to Mo in acidic ILE, while Ta is even more stable compared to W CC.

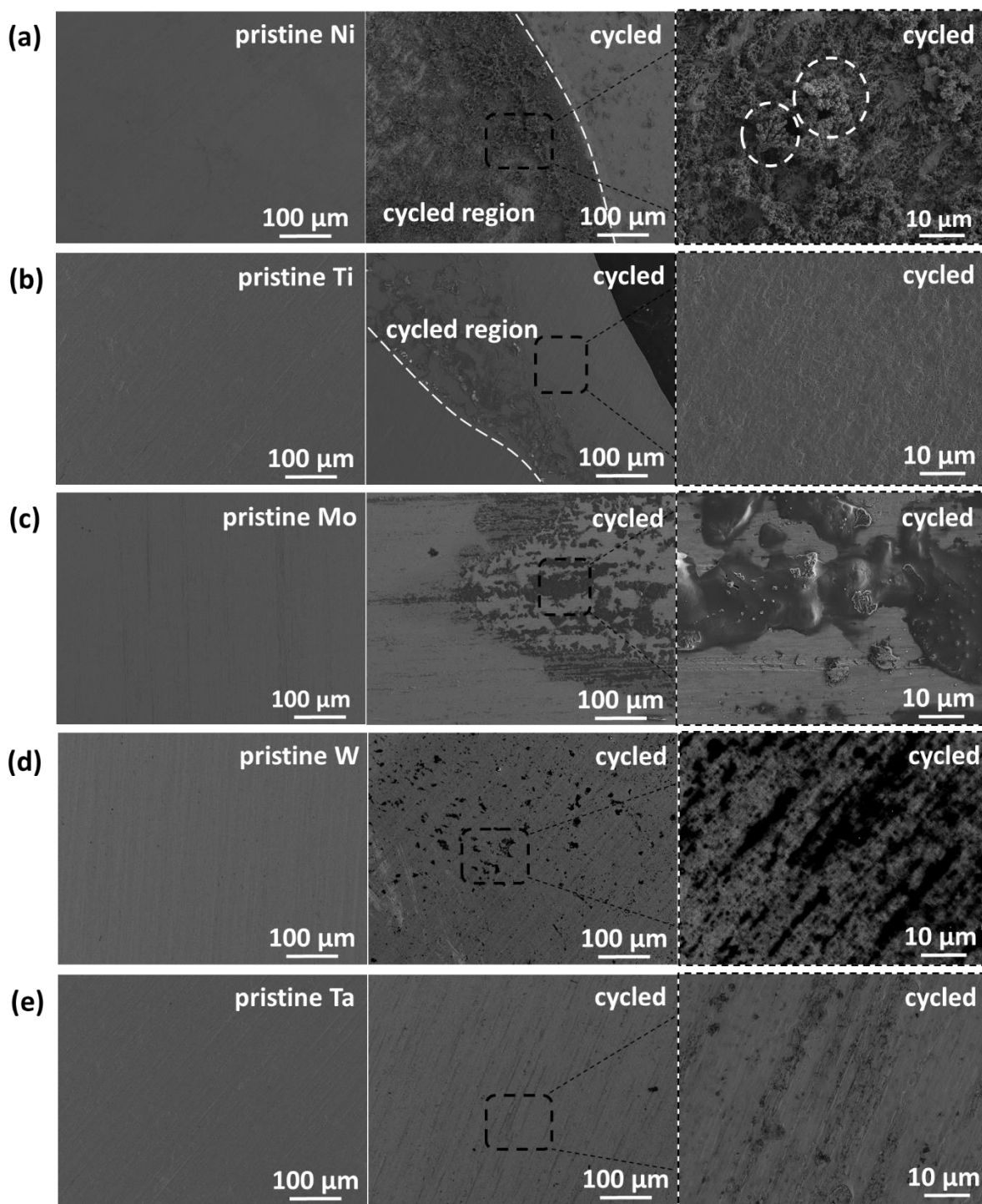


Figure 5-9. SEM images of the cycled Ni, Ti, Mo, W, Ta CC in AlCl_3 -based ILE.

XPS spectra were taken of pristine foils and CCs of Mo, Ta, Ti, and W, and a Ni CC. For the pristine samples, fine spectra were taken of the relevant transition metal, carbon and oxygen, and any visible impurities. An effort was made to measure at the point of greatest corrosion on each current collector, though only the Mo and Ti current collectors showed variation visible to the

naked eye; the Ta and W foils showed no evidence of corrosion, and the Ni foil was fully corroded. All pristine samples were calibrated by setting the primary (C-C) C1s peak to 284.8 eV, with the exception of the Mo sample, for which that peak was already at 284.8 eV. Spectra were fit with CasaXPS [48]; using the CasaXPS LA line shape function for all peaks; non-metals were fit using a standard Gaussian-Lorentzian shape, while conductive metal peaks were fit with ad-hoc asymmetric line shapes. All pristine metal samples had carbon and oxygen peaks, consistent with a metal oxide topped by adventitious hydrocarbons. XPS spectra of all pristine and exposed samples are shown in Figure 5-10, Figure 5-11, Figure 5-12, Figure 5-13, and Figure 5-14. As presented in Figure 5-10, proper fitting of the Ni2*p* spectrum can be challenging due to the complicated satellite structure of some compounds. In our case, the Ni3*p* spectrum was picked up as well, due to overlap with the Al2*p* spectrum, and was used to inform our inferences about the sample. Ni2*p* is fit with a single species with Ni2*p*_{3/2} at 856.5 eV, which alongside the large Cl2*p*_{3/2} peak at 199.3 eV, is consistent with NiCl₂ [109]. We also see a barely resolvable Ni-metal peak at 852.4 eV [109]. The Ni3*p*_{3/2} metal peak at 65.8 eV is substantially larger, as the higher kinetic energy electrons are more likely to make it through the corrosion layer, and we see our NiCl₂ Ni3*p*_{3/2} peak at 68.9 eV [109]. In addition to Ni compounds, Al and N compounds are also visible in the sample, with an Al2*p*_{3/2} Al³⁺ peak at 74.5 eV, likely in large part Al – O, and an N1s peak at 401 eV, likely some degradation product of imidazolium. A single Ni3*p* peak is found to fit much better than a third Ni species; this is obviously a poor approximation of the Ni3*p* satellite structure [181], [182]. However, the locations of the chemical species are not found to be sensitive to the potential presence of additional peaks. Due to higher kinetic energy, the Ni metal peak comes through much more strongly in the Ni3*p* spectrum. As shown in Figure 5-11, the Ti2*p* spectrum of the pristine Ti foil showed a TiO₂ oxide layer above Ti metal [108]. A small titanium carbide peak is also visible in the C1s spectrum. The sample for the current collector is quite similar, with the addition of Al and Cl peaks. The O1s and Cl2*p* spectra suggest that Al and Ti exist in both oxide and chloride form, with more oxide than chloride in both cases. The Cl2*p* spectrum has Cl2*p*_{3/2} peaks at 197.9 eV and 200.1 eV, corresponding to AlCl₃ and TiCl₃ or TiCl₄ respectively [183], [184]. Titanium Chloride cannot be distinguished from TiO₂ in the Ti2*p* spectrum. The Al2*p* spectrum is

fit with two doublets, with $\text{Al}2p_{\frac{3}{2}}$ at 74.2 eV and 75.8 eV respectively. The first of these peaks is clearly an Al^{3+} peak corresponding to both AlCl_3 and Al_2O_3 , while the second could not be identified. Copper contamination peaks are also visible in the sample, possibly due to the copper tape used to affix the sample for XPS analysis. The Ti sample had no visible nitrogen. Concerning the Mo CC, its XPS fine spectra presented in Figure 5-12. The pristine metal foil shows MoO_3 , including a small amount of Mo^{5+} . On the Mo current collector, only Mo metal is visible in the $\text{Mo}3d$ spectrum. We see again an Al^{3+} peak at 74.5 eV, with Al_2O_3 as the majority and AlCl_3 as the minority of this signal, and also assign a small N1s imidazolium peak at 401.5 eV [104], [185]. The $\text{Cl}2p$ spectrum has again a pair of doublets, with $\text{Cl}2p_{\frac{3}{2}}$ peaks at 198.2 eV and 199.2 eV, corresponding to AlCl_3 and either MoCl_2 or MoCl_4 . These Mo – Cl compounds cannot be distinguished in the $\text{Cl}2p$ spectrum and the corresponding peak is not visible in the $\text{Mo}3d$ spectrum. While the major O1s peak at 532.1 eV is assigned to Al – O and C – O, a minor peak at 530 eV also suggests the presence of minimal MoO_3 , though this is also not visible in the $\text{Mo}3d$ spectrum [109], [186]. The pristine W foil spectrum (presented in Figure 5-13) reveal WO_3 over W metal [108], [109]. The $\text{W}4f$ spectrum of the current collector shows only W metal. Trace amounts of Al, Cl, and N are visible on the sample, but it seems clear that the contamination in this case is entirely due to deposited electrolyte – there is no evidence of any W corrosion products. The $\text{Al}2p_{\frac{3}{2}}$ peak at 74.5 eV is likely largely Al – O, as the $\text{Cl}2p_{\frac{3}{2}}$ peak at 197.9 eV implies $[\text{EMIm}]\text{Cl}$ as the primary chloride component. The N1s spectrum has two peaks at 401.4 eV and 399.5 eV, assigned to $[\text{EMIm}]\text{Cl}$ and neutral C-N compounds resulting from the decomposition of $[\text{EMIm}]\text{Cl}$ [104], [185]. As for cycled W, the O1s peak at 530 eV on the CC is too low to originate from C-O or Al-O bonding, suggesting that there may remain a small quantity of residual oxide not visible in the $\text{Mo}3d$ spectrum [109], [187]. Finally, as shown in Figure 5-14, the pristine Ta foil consists of Ta_2O_5 over Ta metal. The Ta current collector is much the same. Tiny $\text{Cl}2p$ and $\text{Al}2p$ peaks are resolvable, at 198.1 eV and 74.5 eV for the $2p_{\frac{3}{2}}$ peaks. The Al content is again much greater than the Cl content, suggesting that the primary Al compound is some form of oxide. Overlap with the $\text{Ta}4p_{\frac{3}{2}}$ peak makes presence of N on the sample impossible to determine. The $\text{Mo}3d$ and $\text{W}4f$ metal spectra showed just bare metal, while the $\text{Ti}2p$ and $\text{Ta}4f$ spectra showed

the same metal-oxide structure as the pristine foils [108]. It seems likely that the metals were exposed to sufficient oxygen to form oxides after cycling, as the presence or absence of the oxide on these foils tracks with the bare metal's air stability. Visible impurities were Si on the W foil, and Ca and TiC on the Ti foil. All CCs showed small residues of nitrogen, aluminum, and chlorine from the cycling, with anionic $\text{Cl}2p_{\frac{3}{2}}$ peaks around 198 eV and cationic $\text{Al}^{3+} \text{Al}2p_{\frac{3}{2}}$ around 74.5 eV. For the most part, CCs showed small residues of nitrogen, aluminum, and chlorine from the cycling, with anionic $\text{Cl}2p_{\frac{3}{2}}$ peaks around 198 eV and cationic $\text{Al}^{3+} \text{Al}2p_{\frac{3}{2}}$ around 74.5 eV. Mo and W both had nitrogen peaks around 401.5 eV, characteristic of cationic imidazolium [104], [185], and the W CC also had a neutral nitrogen peak at 399.4 eV (Figure 5-13). Peaks in a given column are scaled on the same intensity scale. The O1s peak at 530 eV on the CC is too low to originate from C-O or Al-O bonding, suggesting that there may remain a small quantity of residual oxide not visible in the Mo3d spectrum [109], [186]. A comparison of the Cl2p peaks of the foils is shown in Figure 5-15. Peaks around 198 eV, corresponding to AlCl_3 , are rendered in red. Peaks over 199 eV, corresponding to foil corrosion species, are plotted in blue. Analyzing the metal spectra of the foils, the pristine samples showed a thin oxide layer -- MoO_3 , Ta_2O_5 , TiO_2 , and WO_3 [108] with metal beneath. On the CCs, Mo3d and W4f metal spectra showed just bare metal, while the Ti2p and Ta4f spectra showed the same metal-oxide structure as the pristine foils. Given that Ta and titan oxidize much faster than W and Mo, it is likely that these oxide layers formed after cycling. While nothing is visible in their respective metal spectra, the Mo and Ti Cl2p spectra also show secondary species suggestive of a small degree of foil corrosion, at 199.2 eV and 200.1 eV respectively. Lacking visible metal peaks, the precise form of this corrosion is not possible to determine, as MoCl_2 [188], [189] and MoCl_4 [190] cannot be distinguished from the Cl2p spectrum alone, nor can TiCl_3 and TiCl_4 [183], [184]. No attempt is made to unravel the satellite structure of Ni2p. A single Ni3p satellite peak is found to fit much better than a third Ni species; this is obviously a poor approximation of the Ni3p satellite structure [181], [182], but the locations of the chemical species are not found to be sensitive to the potential presence of additional peaks. Due to higher kinetic energy, the Ni metal peak comes through much more strongly in the Ni3p spectrum. A summary and approximate breakdown of the relative signal between spectra can be found in Table 5-3, Table 5-4, Table 5-5, Table 5-6, Table 5-7.

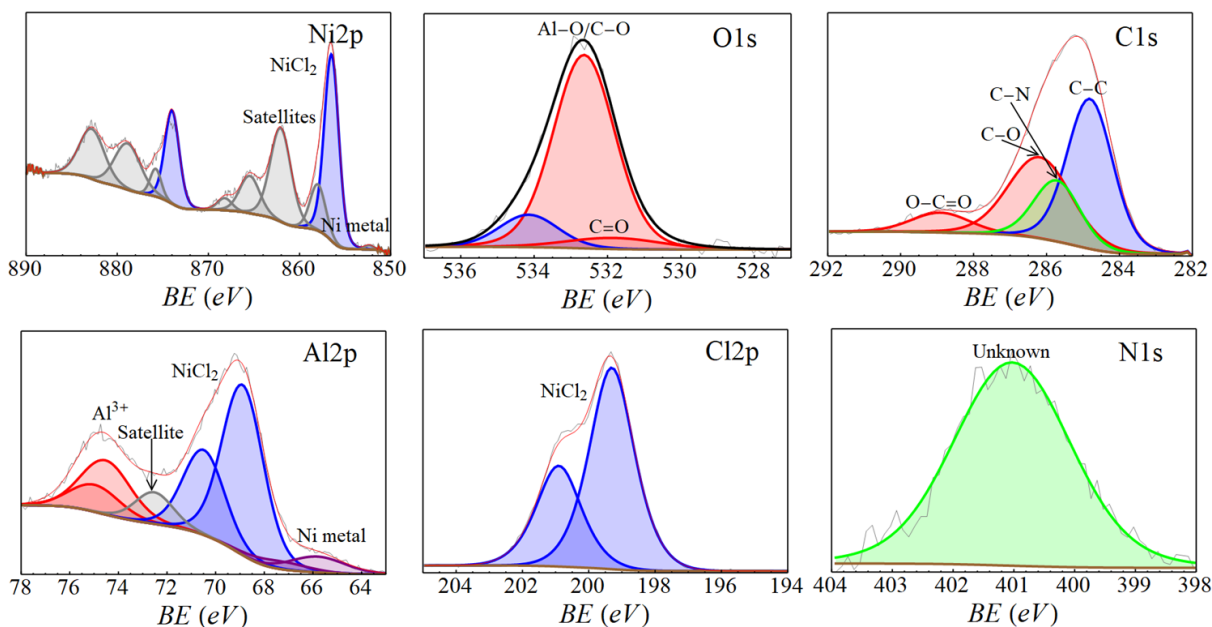


Figure 5-10. Fine spectra from cycled Ni CC AlCl₃-based ILE. Peaks in a given column are scaled on the same intensity scale.

Table 5-3. A table of binding energies in eV, assignments, and % signal content for each species on cycled Ni CC surface.

Spectrum	Binding Energy (eV)	FWHM (eV)	Area (eV*counts)	Sensitivity Factor	Concentration (atomic %)	Assignment
Ni2p _{3/2}	852.4	1.2	46	14.61	0	Ni metal
	856.5	1.9	3436	-	6.1	NiCl ₂
O1s	531.8	3	179	2.93	0.7	C = O
	532.6	2	2041	-	7.7	C - O, Al - O
	534.2	1.9	328	-	1.2	H ₂ O
N1s	401	2.3	543	1.8	3.4	Imidazolium
C1s	284.8	1.5	1675	1	18.6	C - C
	285.7	1.5	688	-	7.6	C - N
	286.2	2	1246	-	13.9	C - O
	288.9	1.9	284	-	3.2	O - C = O or carbonate
Cl2p _{3/2}	199.3	1.6	3974	1.51	29.3	NiCl ₂
Al2p _{3/2}	74.5	2.4	267	0.346	8.3	Al ³⁺
Ni3p _{3/2}	65.8	2.7	87	-	-	Ni metal
	68.9	2	700	-	-	NiCl ₂

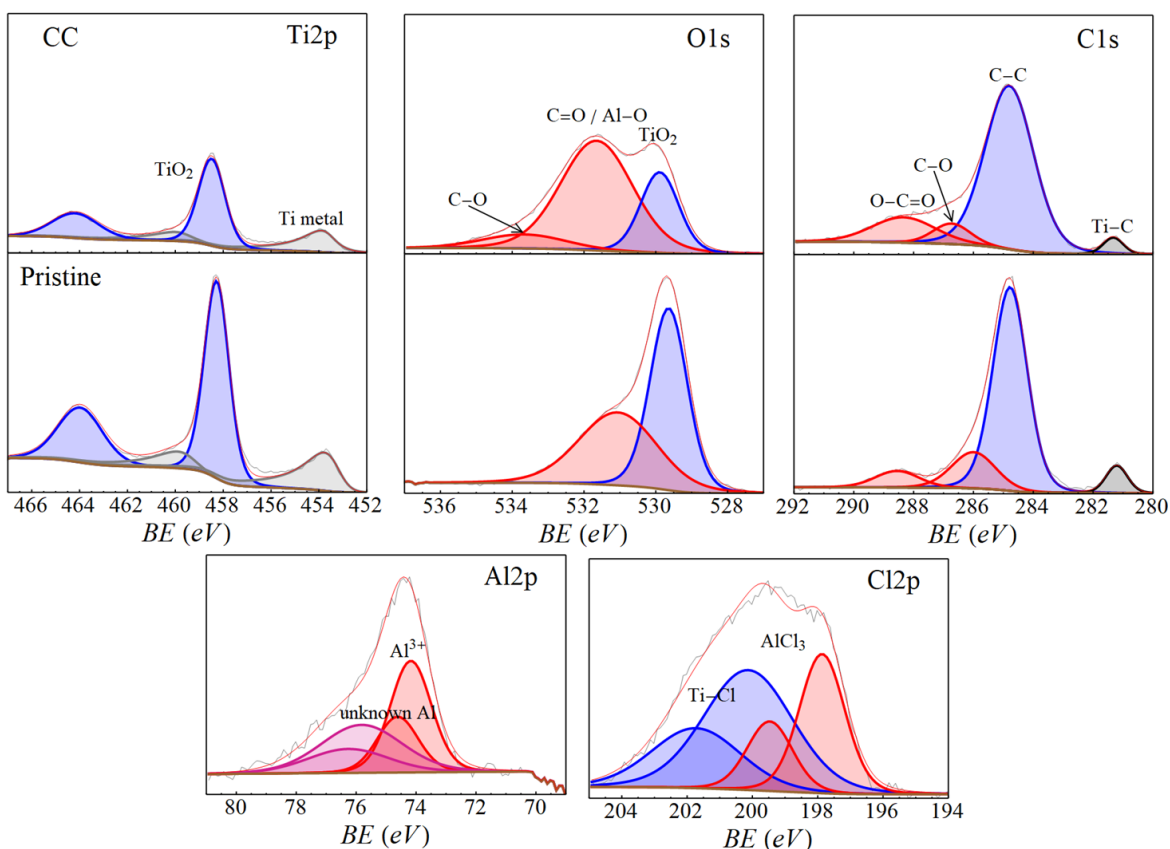


Figure 5-11. Fine spectra from cycled Ti CC in AlCl_3 -based ILE. Peaks in a given column are scaled on the same intensity scale.

Table 5-4. A table of binding energies in eV, assignments, and % signal content for each species on cycled Ti CC surface.

Spectrum	Binding Energy (eV)	FWHM (eV)	Area (eV*counts)	Sensitivity Factor	Concentration (atomic %)	Assignment
O1s	529.9	1.3	2740	2.93	8.4	TiO_2
	531.7	2.4	7041	-	21.7	C = O, Al - O
	533.7	2.7	1040	-	3.2	C - O
$\text{Ti}2p_{3/2}$	453.8	1.3	1397	5.22	2.4	Ti metal
	458.5	1.3	2672	-	4.6	TiO_2
C1s	281.3	0.8	124	1	1.1	Ti - C
	284.8	1.9	2988	-	27	C - C
	286.7	1.5	288	-	2.6	C - O
	288.3	2.5	605	-	5.5	C = O
$\text{Cl}2p_{3/2}$	197.9	1.6	572	1.51	3.4	AlCl_3
	200.1	3.2	963	-	5.8	Ti - Cl
$\text{Al}2p_{3/2}$	74.2	1.6	290	0.356	7.4	Al^{3+}
	75.8	3.2	246	-	6.2	Al^{3+}

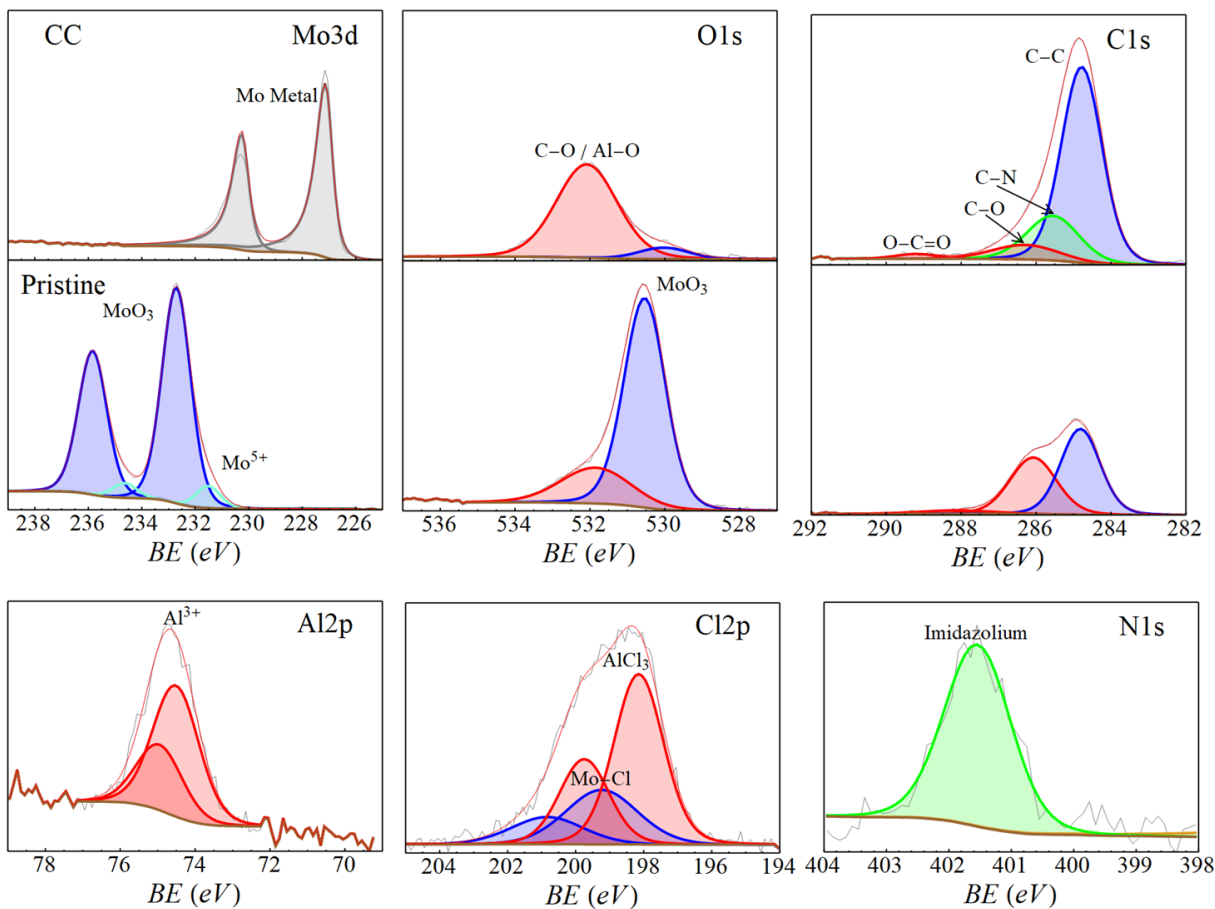


Figure 5-12. Fine spectra from cycled Mo CC in AlCl₃-based ILE. Peaks in a given column are scaled on the same intensity scale.

Table 5-5. A table of binding energies in eV, assignments, and % signal content for each species on Mo CC surface.

Spectrum	Binding Energy (eV)	FWHM (eV)	Area (eV*counts)	Sensitivity Factor	Concentration (atomic %)	Assignment
O1s	530	1.6	490	2.93	1.5	Mo – O
	532.1	1.9	4936	-	15.5	C – O, Al – O
N1s	401.5	1.3	363	1.8	1.9	Imidazolium
C1s	284.8	1.3	4919	1	45.1	C – C
	285.6	1.6	1440	-	13.2	C – N
	286.3	2.1	591	-	5.4	C – O
	289.2	1.3	127	-	1.2	O – C = O or carbonate
Mo3d _{5/2}	227.1	0.6	4844	5.62	7.9	Mo metal
Cl2p _{3/2}	198.2	1.7	451	1.51	2.7	AlCl ₃
	199.2	2.5	204	-	1.2	Mo – Cl
Al2p _{3/2}	74.5	1.5	167	0.356	4.3	Al ³⁺

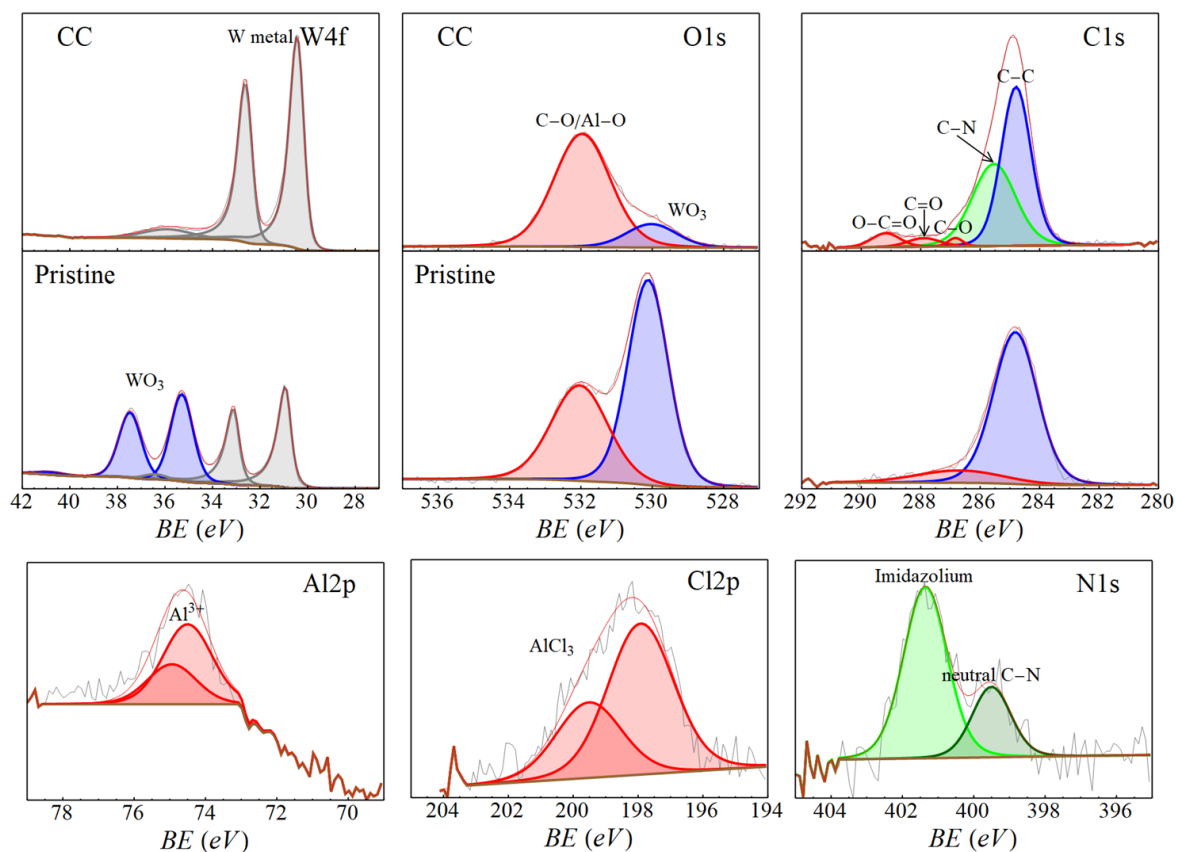


Figure 5-13. Fine spectra from cycled W CC in AlCl_3 -based ILE. Peaks in a given column are scaled on the same intensity scale.

Table 5-6. A table of binding energies in eV, assignments, and % signal content for each species on W CC surface.

Spectrum	Binding Energy (eV)	FWHM (eV)	Area (eV*counts)	Sensitivity Factor	Concentration (atomic %)	Assignment
O1s	530	1.7	810	2.93	3.1	W – O
	532	1.9	4384	-	16.9	C – O, Al – O
N1s	399.5	1.3	145	1.8	0.9	neutral C – N
	401.4	1.4	396	-	2.5	Imidazolium
C1s	284.8	1.2	2568	1	29	C – C
	285.5	1.7	2059	-	23.3	C – N
	286.8	0.6	71	-	0.8	C – O
	287.9	1.2	150	-	1.7	C = O
	289.2	1.1	225	-	2.5	O – C = O or carbonate
$\text{Cl}2p_{3/2}$	197.9	2.4	437	1.51	3.3	AlCl_3
$\text{Al}p_{3/2}$	74.5	1.5	220	0.356	7	Al^{3+}
$\text{W}4f_{7/2}$	30.4	0.7	9356	5.48	19.3	W metal

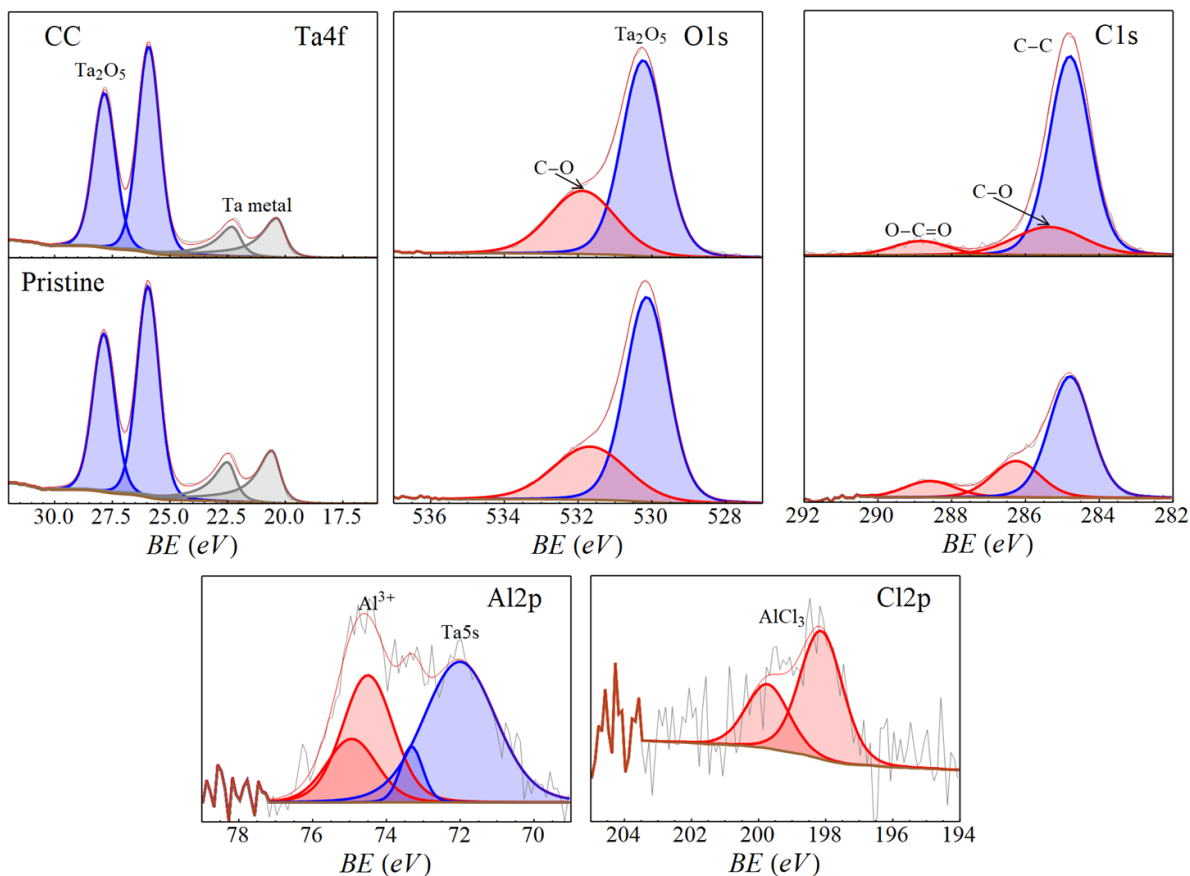


Figure 5-14. Fine spectra from cycled Ta CC in AlCl_3 -based ILE. Peaks in a given column are scaled on the same intensity scale.

Table 5-7. A table of binding energies in eV, assignments, and % signal content for each species on Ta CC surface.

Spectrum	Binding Energy (eV)	FWHM (eV)	Area (eV*counts)	Sensitivity Factor	Concentration (atomic %)	Assignment
O1s	530.2	1.4	9393	2.93	26.8	Ta_2O_5
	531.9	2.1	4708	-	13.4	C-O, Al-O
C1s	284.8	1.3	3029	1	25.3	C-C
	285.4	2.2	734	-	6.1	C-N
	288.4	1.7	284	-	2.4	C=O
$\text{Cl}2p_{3/2}$	198.1	1.5	98	1.51	0.5	AlCl_3
$\text{Al}2p_{3/2}$	74.5	1.6	172	0.356	4	Al^{3+}
$\text{Ta}4f_{7/2}$	20.4	0.9	3035	4.82	5.3	Ta metal
	25.9	1.1	9372	-	16.2	Ta_2O_5

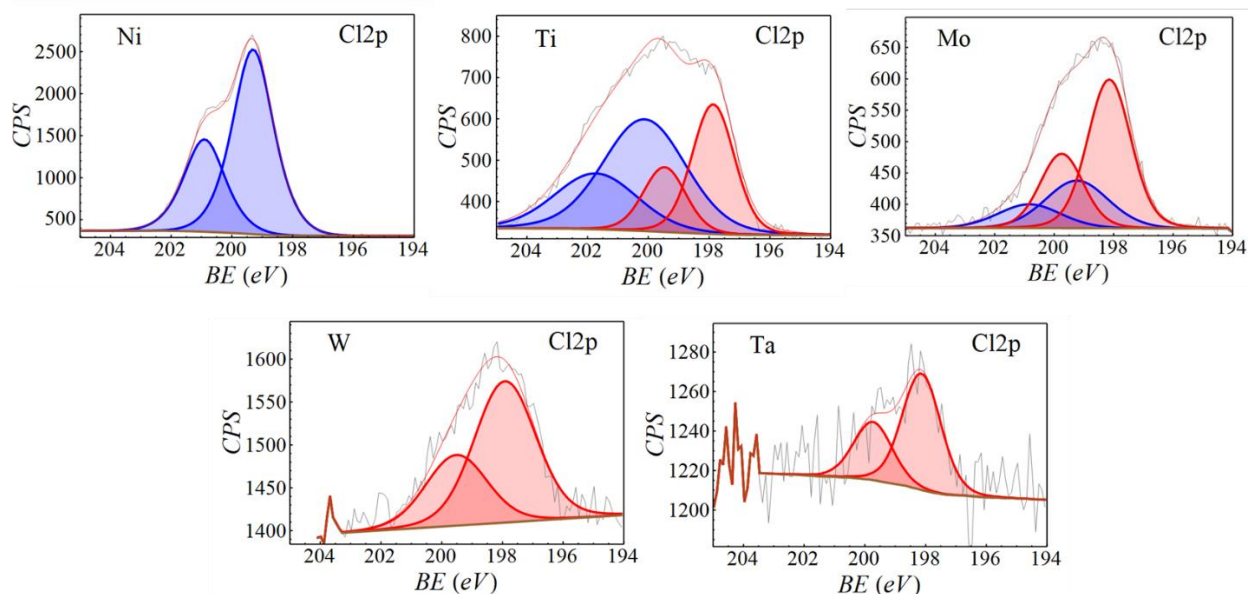


Figure 5-15. The Cl_{2p} fine spectra from each metal foil, displayed on a single intensity scale. Peaks around 198 eV, corresponding to AlCl₃, are rendered in red. Peaks over 199 eV, corresponding to foil corrosion species, are rendered in blue.

Regarding the stability of Mo, and W rods when used as CC in a Swagelok cell configuration, Swagelok cells were constructed in three electrode configurations. Subsequently, CV (Figure 5-16(a)) was employed at various cathodic potentials vs. an Al RE all at a scan rate of 5 mV s⁻¹ within an AlCl₃-based ILE (separated CVs are presented in Figure A-5- 6). The recorded CVs reveals reactivity of the Mo substrate with ILE. Specifically, more reactivity is observed for wider cathodic potential range of 0.5 to 2.5 V. The CCs (Mo, in this case) expected to be relatively inert or unreactive towards the electrolyte. However, as can be seen in Figure A-5- 6(c), the absence of capacitive current indicates complex processes happening at the Mo surface. Instead of capacitive current, we notice the presence of one oxidative peak and two reduction peaks in the CV data. These peaks are characteristic of electrochemical reactions occurring at the Mo surface. Importantly, these reactions are attributed to the interactions between the Mo substrate and the aluminum chloride complexes present in the electrolyte. Upon opening the Swagelok cells, the electrolyte color change was noticed from yellowish to dark red. This color change has been attributed to the reactivity of the Mo substrate (foil and rod) with ILE and subsequently the formation of [Mo₂Cl₉]³⁻ or [Mo₂Cl₈]⁴⁻ complexes [191]. Mo's tendency to form the mentioned complexes with chloride anions results in the reduction in chloride concentration within the

electrolyte upon cycling which agrees with literature [179]. Therefore, Mo rod are not suggested to be taken as CC in Swagelok cells configurations. However, it's important to mentioned that the Mo rod with 99,97% purity contains a series of impurities such as Al, Cr, Cu, Fe, K, Ni, Si, W, C, N, O, Cd, which may affect its compatibility and stability in ionic liquid electrolyte. In Figure 5-16(a), a comparison of recorded CVs for Mo CC in three different potential ranges is presented: 0 to 1.2 V (as cell 1), 0 to 1.5 V (as cell 2), and 0.5 to 2.5 V (as cell 3). This comparison highlights the inert behavior of Mo CC in the 0 to 1.2 V and 0 to 1.5 V potential ranges (cell 1 and cell 2) when compared to the 0.5 to 2.5 V range (cell 3). The presence of redox peaks in the CVs at 0.5 to 2.5 V indicates the reactivity of Mo CC with the AlCl_3 - based ILE. In contrast, no significant reactivity, i.e. no redox reactions were observed in cell 1 and cell 2. In Figure 5-16(b), the reactivity of Mo CC with the ILE is further explored within a potential window of 0.3 to 2.2 V. This reactivity is consistent regardless of the cell configuration: Swagelok cell as the blue curve and a TSC surface cell as the red curve. The Swagelok cell configuration exhibits more pronounced redox peaks, including three oxidation and reduction peaks, even at higher current density. These peaks indicate a higher occurrence of redox reactions not only on the Mo foil but also on the Mo rod in the Swagelok cell. However, it's important to note that even in the TSC surface cell, the reactivity of Mo foil as a CC is evident from the observed redox peaks in the CV. The comparison of the CV data depicted in Figure 5-16(c), conducted at a scan rate of 0.5 mV s^{-1} within the potential range of 0.3 to 2.2 V, highlights the reactivity of both Mo and W rod when used as CCs in the ILE. W CC exhibited a lower current density compared to Mo CC, indicating a difference in their reactivity levels. As in the context of corrosion studies, current density can indicate the rate of corrosion or degradation of a material. Higher current densities can suggest more significant corrosion. Hence, the observed lower current density for W CC indicates that W CC exhibited a slower rate of electrochemical reaction compared to Mo CC. This difference in current density (Figure 5-16(d)) indicates that Mo CC was more reactive or efficient in facilitating the electrochemical processes occurring within the ILE compared to W CC.

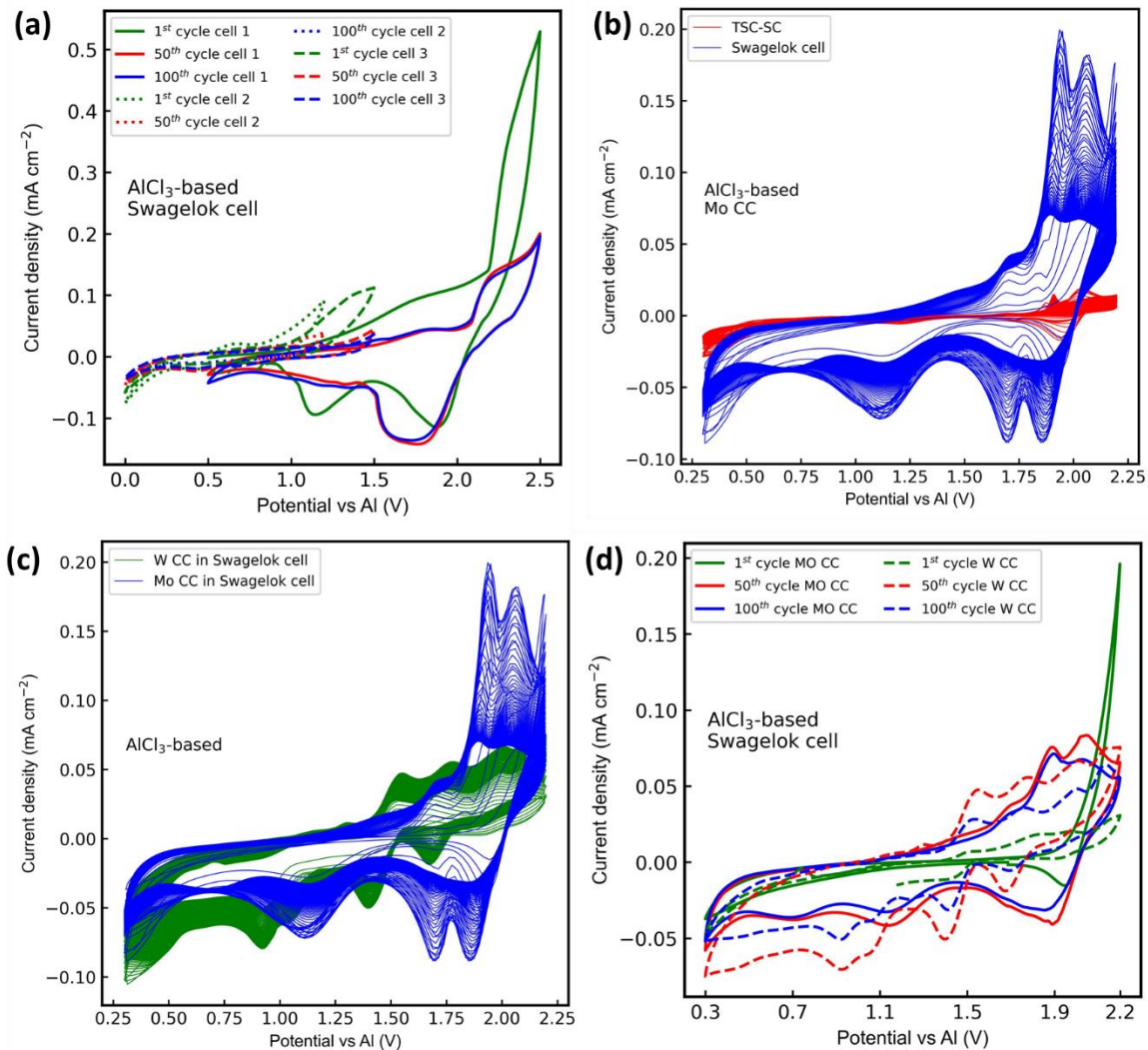


Figure 5-16. Recorded CVs on Mo CC in AlCl₃-based ILE in (a) Swagelok cell 1, cell 2, and cell 3 at 5 mV s⁻¹ and (b) CVs' comparison of Mo CCs in two TSC-SC and Swagelok at 0.5 mV s⁻¹. (c-d) CVs' comparison of Mo and W CC in Swagelok at 0.5 mV s⁻¹.

The presented Figure 5-17 illustrates CVs recorded in an AlCl₃-based ILE at a scan rate of 0.5 mV s⁻¹, using different cell configurations. Three configurations were employed: one with GNP coated on Mo CC in a coin cell, another with Mo foil serving as the CC in a Swagelok cell, and a third with Mo foil as the CC in a TSC-SC cell. Comparing the CVs shown in Figure 5-17(b) and (c), it is noteworthy that they exhibit similarities. However, Figure b displays additional oxidation and reduction peaks. These additional peaks suggest that the Mo rod, in addition to the Mo foil, contribute to reactions with the ILE in Swagelok cell. This indicates that the reactivity of the Mo foil is augmented when the Mo CC includes Mo rod. Furthermore, a comparison of the CVs for Mo foil with and without the GNP active material can provide valuable insights into the role of

Mo CC when it is coated with GNP. Although Figure 5-17(a) and (b), appear quite similar, Figure 5-17(b) exhibits a lower observed current density compared to Figure a. This result aligns with prior literature, which has indicated that the Mo CC has a negligible impact, whereas the reactivity of Mo foil as the CC exerts a predominant influence on electrochemical performance. Our observations after 13 cycles revealed the emergence of noise in the CVs, indicating a certain resistance in the cell. This noise suggests that the coated Mo CC may exhibit reactivity over time, contributing to changes in electrochemical behavior.

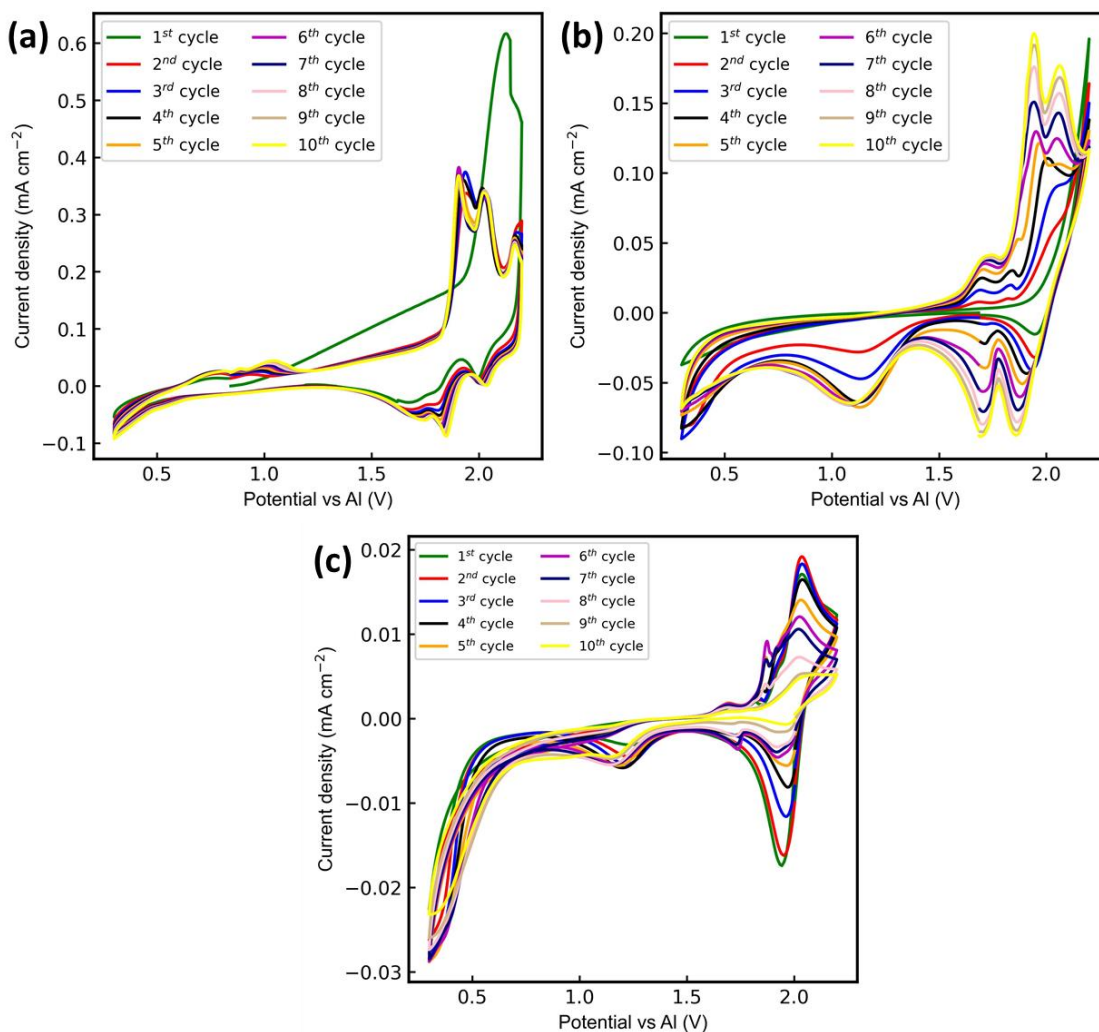


Figure 5-17. Recorded CVs in AlCl₃-based ILE at scan rate of 0.5 mV s⁻¹ on (a) GNP coated on Mo CC in coin cell (contributed by Anastasia Teck from Titirici Group, Imperial College London) (b) Mo foil as CC in Swagelok cell, and (c) Mo foil as CC in TSC-SC.

5.2.2 Conclusions and Outlook

The investigation into the chemical and electrochemical stability of metallic CCs within an AlCl_3 -based ILE has yielded important findings. Ni and Ti foils exhibit significant reactivity, leading to corrosion and alterations in their surface morphology. Mo and W foils also display reactivity, potentially impacting their long-term stability as CCs. In contrast, Ta foils demonstrate remarkable resistance to corrosion and electrochemical reactivity, making them a promising choice for CC applications. LSV and CV profiles align with these observations. CV profiles of Ni and Ti CC display oxidative peaks, while demonstrate capacitive current responses for W and Ta foils indicating their stability. These insights are crucial for selecting appropriate CC materials and ensuring the durability and performance of Al Dual-Ion batteries in practical applications. Moreover, Mo rod (with 99.97% purity and specified impurities as mentioned) is not recommended to be used as CCs in Swagelok cell configurations with an AlCl_3 -based ionic liquid electrolyte due to its unexpected reactivity with the electrolyte, as evidenced by the presence of oxidative and reduction peaks in CV experiments. These interactions between Mo and aluminum chloride complexes suggest potential issues with cell stability and performance. This reactivity persists across different potential ranges and cell configurations, making Mo rod (with 99.97% purity and specified impurities as mentioned) an unsuitable choice. These findings emphasize the need for careful CC material selection to ensure the reliability and efficiency of electrochemical systems.

Addressing the unexpected reactivity of Mo rods (with 99.97% purity and specified impurities as mentioned) in Swagelok cell configurations remains a crucial challenge. Future work could delve into developing strategies to mitigate this reactivity or identifying alternative materials like W and Ta CCs in similar setups.

6 Conclusions

In Chapter 3, the first research study investigates the potential of Al as an alternative to Li for advanced battery applications. Despite its higher theoretical charge capacity than Li, the corrosive nature of conventional AlCl_3 -based electrolyte limits their practicality. To address this limitation, the study introduces $\text{Al}(\text{OTF})_3$ as a non-corrosive substitute for AlCl_3 . The electrolyte's compatibility with urea and NMA for Al plating/stripping is examined. The research compares NMA-based and EiPS-based electrolytes, highlighting challenges in redox reaction reversibility and unexpected behavior with non-Pt or Cu substrates. The influence of temperature and cathodic potential on electrochemical performance is investigated. The study emphasizes the significance of modifying WE surfaces, like Al foil, for practical Al deposition, and underscores ongoing efforts to optimize NMA-based E as $\text{Al}(\text{OTF})_3$ -based electrolytes for advanced AIBs' applications. The second research delves into the challenges on Al plating and stripping in a non-corrosive electrolyte formulation containing urea/NMA/ $\text{Al}(\text{OTF})_3$ as an alternative to AlCl_3 -based E. While avoiding corrosion, this formulation struggles with possibility of Al plating and stripping due to the non-corrosive nature of the electrolyte. Surface modifications on the Al electrode do not mitigate this issue, as they fail to eliminate the persistent Al_2O_3 oxide passivation film. The study stresses the importance of drying electrolyte components to prevent passivation layer formation caused by water content in electrolyte solution. The formation of an interphase layer including $\text{Al}(\text{OH})_3$, AlF_3 , and re-passivated Al oxide impedes successful Al plating and stripping. Insights from CV and XPS underscore the critical role of passivation layer composition and identify limited C-F compound presence in the $\text{Al}(\text{OTF})_3$ -based electrolyte. This thesis suggests exploring strategies to mitigate Al-water interactions and improve Al plating and stripping within the $\text{Al}(\text{OTF})_3$ -based electrolyte, ultimately advancing AIBs' technology. In summary, presented results in chapter 3 highlight the potential of Al as an alternative for LiBs and the challenges associated with developing suitable non-corrosive electrolytes. While the introduction of $\text{Al}(\text{OTF})_3$ as a replacement for corrosive AlCl_3 looks promising, achieving effective Al plating and stripping using non-corrosive electrolyte formulations is still a complicated process. Both parts of chapter 3 emphasize the importance of electrode surface modifications, temperature effects, and careful control of electrolyte components in influencing the interphase layer formation. These findings

collectively contribute to ongoing efforts to enhance the performance and viability of AIBs for sustainable energy storage solutions.

In chapter 4, the study highlights challenges related to the presence of an amorphous Al_2O_3 oxide passivation film on Al substrates, impeding cyclic performance. Surface properties, including initial conditions, treatment, and electrolyte composition, are critical in determining Al electrode performance. The study demonstrates that non-shiny Al foil side, with higher roughness, exhibits enhanced Al plating and stripping due to more active sites. Treatment in an AlCl_3 -based ILE modifies the surface, forming interphase layer rich in Al, Cl, and N. In summary, this study emphasizes the significance of surface properties in Al foil electrochemical behavior within AIBs, underscoring the need to consider factors like initial properties, treatment, and electrolyte composition.

In Chapter 5, the study provides valuable insights into the stability and reactivity of various metallic CCs within an AlCl_3 -based ILE. Through a series of immersion tests and electrochemical analyses, several significant conclusions can be drawn. The investigation reveals different levels of corrosion susceptibility among the tested metallic foils. Ni and Ti foils exhibit pronounced reactivity with the electrolyte, leading to corrosion and surface changes. In contrast, Ta foil exhibits enhanced resistance to corrosion, while Mo and W foils also display reactivity, but to varying degrees. Recorded LSV and CV corroborate these findings, with Ni and Ti foils showing oxidative peaks indicative of reactivity, whereas W and Ta foils exhibit capacitive current responses, suggesting stability. These insights are critical for selecting appropriate CC materials in the development of Al Dual-Ion batteries, as they impact the batteries' long-term stability and performance. The use of SEM-EDX provides visual and compositional evidence of the surface alterations and residues on the CCs, further supporting the observed reactivity. XPS analysis reveals the presence of oxide layers on pristine metal samples and identifies residues of nitrogen, aluminum, and chlorine from cycling on the CCs. This information sheds light on the chemical changes occurring during cycling and their implications for material stability. In a separate investigation, the study assesses the suitability of Mo and W rods as CCs in Swagelok cell configurations using the same AlCl_3 -based ILE. The unexpected reactivity of the Mo substrate with the electrolyte, as evidenced by oxidative and reduction peaks in cyclic voltammetry experiments,

suggests that Mo rod (with 99.97% purity and specified impurities as mentioned) is not recommended for use as CCs in Swagelok cells.

References

- [1] F. Rahide, E. Zemlyanushin, G.-M. Bosch, and S. Dsoke, "Open Challenges on Aluminum Triflate-Based Electrolytes for Aluminum Batteries," *J Electrochem Soc*, vol. 170, no. 3, p. 030546, Mar. 2023, doi: 10.1149/1945-7111/acc762.
- [2] F. Rahide, J. K. Flowers, J. Hao, H. S. Stein, H. Ehrenberg, and S. Dsoke, "Hindered Aluminum Plating and Stripping in Urea/NMA/Al(OTF)₃ as a Cl-Free Electrolyte for Aluminum Batteries," *J Electrochem Soc*, vol. 170, no. 12, p. 120534, Dec. 2023, doi: 10.1149/1945-7111/ad1553.
- [3] F. Rahide *et al.*, "Modification of Al surface via acidic treatment and its impact on plating and stripping," *ChemSusChem*, Oct. 2023, doi: 10.1002/cssc.202301142.
- [4] M. Guidat *et al.*, "In Situ Monitoring of the Al(110)-[EMImCl]:AlCl₃ Interface by Reflection Anisotropy Spectroscopy," *Batter Supercaps*, Oct. 2023, doi: 10.1002/batt.202300394.
- [5] N. Sabi, K. Palanisamy, F. Rahide, S. Daboss, C. Kranz, and S. Dsoke, "Surface Properties-Performance Relationship of Aluminum Foil as Negative Electrode for Rechargeable Aluminum Batteries," *Batter Supercaps*, Sep. 2023, doi: 10.1002/batt.202300298.
- [6] S. Sarmah, Lakhanlal, B. K. Kakati, and D. Deka, "Recent advancement in rechargeable battery technologies," *WIREs Energy and Environment*, vol. 12, no. 2, Mar. 2023, doi: 10.1002/wene.461.
- [7] B. Dunn, H. Kamath, and J.-M. Tarascon, "Electrical Energy Storage for the Grid: A Battery of Choices," *Science (1979)*, vol. 334, no. 6058, pp. 928–935, Nov. 2011, doi: 10.1126/science.1212741.
- [8] F. Wu, H. Yang, Y. Bai, and C. Wu, "Paving the Path toward Reliable Cathode Materials for Aluminum-Ion Batteries," *Advanced Materials*, 2019, doi: 10.1002/adma.201806510.
- [9] H. Yang *et al.*, "The Rechargeable Aluminum Battery: Opportunities and Challenges," *Angewandte Chemie International Edition*, vol. 58, no. 35, pp. 11978–11996, Aug. 2019, doi: 10.1002/anie.201814031.
- [10] W.-J. Zhang, "A review of the electrochemical performance of alloy anodes for lithium-ion batteries," *J Power Sources*, vol. 196, no. 1, pp. 13–24, Jan. 2011, doi: 10.1016/j.jpowsour.2010.07.020.
- [11] Y. Hu, D. Sun, B. Luo, and L. Wang, "Recent Progress and Future Trends of Aluminum Batteries," *Energy Technology*, vol. 7, no. 1, pp. 86–106, Jan. 2019, doi: 10.1002/ente.201800550.
- [12] S. K. Das, S. Mahapatra, and H. Lahan, "Aluminium-ion batteries: developments and challenges," *Journal of Materials Chemistry A*. 2017. doi: 10.1039/c7ta00228a.
- [13] M. C. Lin *et al.*, "An ultrafast rechargeable aluminium-ion battery," *Nature*, 2015, doi: 10.1038/nature14340.

- [14] B. Craig, T. Schoetz, A. Cruden, and C. Ponce de Leon, "Review of current progress in non-aqueous aluminium batteries," *Renewable and Sustainable Energy Reviews*, vol. 133. Elsevier Ltd, Nov. 01, 2020. doi: 10.1016/j.rser.2020.110100.
- [15] Q. Li and N. J. Bjerrum, "Aluminum as anode for energy storage and conversion: a review," *J Power Sources*, vol. 110, no. 1, pp. 1–10, Jul. 2002, doi: 10.1016/S0378-7753(01)01014-X.
- [16] E.-S. Lee, S.-H. Huh, S.-H. Lee, and S.-H. Yu, "On the Road to Stable Electrochemical Metal Deposition in Multivalent Batteries," *ACS Sustain Chem Eng*, vol. 11, no. 6, pp. 2014–2032, Feb. 2023, doi: 10.1021/acssuschemeng.2c05173.
- [17] Y. Zhang, S. Liu, Y. Ji, J. Ma, and H. Yu, "Emerging Nonaqueous Aluminum-Ion Batteries: Challenges, Status, and Perspectives," *Advanced Materials*, vol. 30, no. 38, p. 1706310, Sep. 2018, doi: 10.1002/adma.201706310.
- [18] M.-C. Lin *et al.*, "An ultrafast rechargeable aluminium-ion battery," *Nature*, vol. 520, no. 7547, pp. 324–328, Apr. 2015, doi: 10.1038/nature14340.
- [19] S. Wang *et al.*, "A Novel Aluminum-Ion Battery: Al/AlCl₃-[EMIm]Cl/Ni₃S₂@Graphene," *Adv Energy Mater*, vol. 6, no. 13, p. 1600137, Jul. 2016, doi: 10.1002/aenm.201600137.
- [20] S. K. Das, "Graphene: A Cathode Material of Choice for Aluminum-Ion Batteries," *Angewandte Chemie International Edition*, vol. 57, no. 51, pp. 16606–16617, Dec. 2018, doi: 10.1002/anie.201802595.
- [21] H. Chen *et al.*, "A Defect-Free Principle for Advanced Graphene Cathode of Aluminum-Ion Battery," *Advanced Materials*, vol. 29, no. 12, p. 1605958, Mar. 2017, doi: 10.1002/adma.201605958.
- [22] H. Li *et al.*, "Reversible electrochemical oxidation of sulfur in ionic liquid for high-voltage Al–S batteries," *Nat Commun*, vol. 12, no. 1, p. 5714, Sep. 2021, doi: 10.1038/s41467-021-26056-7.
- [23] A. Eftekhari and P. Corrochano, "Electrochemical energy storage by aluminum as a lightweight and cheap anode/charge carrier," *Sustain Energy Fuels*, vol. 1, no. 6, pp. 1246–1264, 2017, doi: 10.1039/C7SE00050B.
- [24] M. Jiang *et al.*, "Challenges and Strategies of Low-Cost Aluminum Anodes for High-Performance Al-Based Batteries," *Advanced Materials*, vol. 34, no. 2, p. 2102026, Jan. 2022, doi: 10.1002/adma.202102026.
- [25] D. Ma, D. Yuan, C. Ponce de León, Z. Jiang, X. Xia, and J. H. Pan, "Current progress and future perspectives of electrolytes for rechargeable aluminium-ion batteries," *ENERGY & ENVIRONMENTAL MATERIALS*, Oct. 2021, doi: 10.1002/eem2.12301.
- [26] Z. J. Karpinski and R. A. Osteryoung, "Determination of equilibrium constants for the tetrachloroaluminate ion dissociation in ambient-temperature ionic liquids," *Inorg Chem*, vol. 23, no. 10, pp. 1491–1494, May 1984, doi: 10.1021/ic00178a039.
- [27] N. Takami and N. Koura, "Anodic sulfidation of FeS electrode in a NaCl saturated AlCl₃-NaCl melt," *Electrochim Acta*, vol. 33, no. 8, pp. 1137–1142, Aug. 1988, doi: 10.1016/0013-4686(88)80205-6.

- [28] P. R. Gifford and J. B. Palmisano, "An Aluminum/Chlorine Rechargeable Cell Employing a Room Temperature Molten Salt Electrolyte," *J Electrochem Soc*, vol. 135, no. 3, pp. 650–654, Mar. 1988, doi: 10.1149/1.2095685.
- [29] S. Das, S. S. Manna, and B. Pathak, "Role of Additives in Solid Electrolyte Interphase Formation in Al Anode Dual-Ion Batteries," *ACS Appl Energy Mater*, vol. 5, no. 11, pp. 13398–13409, Nov. 2022, doi: 10.1021/acsaem.2c02067.
- [30] S. Das, S. S. Manna, and B. Pathak, "Recent Trends in Electrode and Electrolyte Design for Aluminum Batteries," *ACS Omega*, vol. 6, no. 2, pp. 1043–1053, Jan. 2021, doi: 10.1021/acsomega.0c04163.
- [31] M. Walter, M. V. Kovalenko, and K. V. Kravchyk, "Challenges and benefits of post-lithium-ion batteries," *New Journal of Chemistry*, vol. 44, no. 5, pp. 1677–1683, 2020, doi: 10.1039/C9NJ05682C.
- [32] M.-C. Lin *et al.*, "An ultrafast rechargeable aluminium-ion battery," *Nature*, vol. 520, no. 7547, pp. 324–328, Apr. 2015, doi: 10.1038/nature14340.
- [33] D. Muñoz-Torrero, J. Palma, R. Marcilla, and E. Ventosa, "A critical perspective on rechargeable Al-ion battery technology," *Dalton Transactions*, vol. 48, no. 27, pp. 9906–9911, 2019, doi: 10.1039/C9DT02132A.
- [34] T. Jiang, M. J. Chollier Brym, G. Dubé, A. Lasia, and G. M. Brisard, "Electrodeposition of aluminium from ionic liquids: Part I—electrodeposition and surface morphology of aluminium from aluminium chloride (AlCl₃)–1-ethyl-3-methylimidazolium chloride ([EMIm]Cl) ionic liquids," *Surf Coat Technol*, vol. 201, no. 1–2, pp. 1–9, Sep. 2006, doi: 10.1016/j.surfcoat.2005.10.046.
- [35] T. Schoetz, O. Leung, C. P. de Leon, C. Zaleski, and I. Efimov, "Aluminium Deposition in EMImCl-AlCl₃ Ionic Liquid and Ionogel for Improved Aluminium Batteries," *J Electrochem Soc*, vol. 167, no. 4, p. 040516, Feb. 2020, doi: 10.1149/1945-7111/ab7573.
- [36] R. Böttcher, S. Mai, A. Ispas, and A. Bund, "Aluminum Deposition and Dissolution in [EMIm]Cl-Based Ionic Liquids—Kinetics of Charge—Transfer and the Rate—Determining Step," *J Electrochem Soc*, vol. 167, no. 10, p. 102516, Jan. 2020, doi: 10.1149/1945-7111/ab9c84.
- [37] J. K. Chang, S. Y. Chen, W. T. Tsai, M. J. Deng, and I. W. Sun, "Electrodeposition of aluminum on magnesium alloy in aluminum chloride (AlCl₃)-1-ethyl-3-methylimidazolium chloride (EMIC) ionic liquid and its corrosion behavior," *Electrochem commun*, vol. 9, no. 7, pp. 1602–1606, 2007, doi: 10.1016/j.elecom.2007.03.009.
- [38] D. Yuan, J. Zhao, W. Manalastas, S. Kumar, and M. Srinivasan, "Emerging rechargeable aqueous aluminum ion battery: Status, challenges, and outlooks," *Nano Materials Science*, vol. 2, no. 3, pp. 248–263, Sep. 2020, doi: 10.1016/j.nanoms.2019.11.001.
- [39] C. Ferrara, V. Dall'Asta, V. Berbenni, E. Quartarone, and P. Mustarelli, "Physicochemical Characterization of AlCl₃–1-Ethyl-3-methylimidazolium Chloride Ionic Liquid Electrolytes for Aluminum Rechargeable Batteries," *The Journal of Physical Chemistry C*, vol. 121, no. 48, pp. 26607–26614, Dec. 2017, doi: 10.1021/acs.jpcc.7b07562.

- [40] G. A. Elia *et al.*, "Insights into the reversibility of aluminum graphite batteries," *J Mater Chem A Mater*, vol. 5, no. 20, pp. 9682–9690, 2017, doi: 10.1039/C7TA01018D.
- [41] T. Mandai and P. Johansson, "Al conductive haloaluminate-free non-aqueous room-temperature electrolytes," *J Mater Chem A Mater*, 2015, doi: 10.1039/c5ta01760b.
- [42] H. Chaurasia *et al.*, "Preparation and properties of AlN (aluminum nitride) powder/thin films by single source precursor," *New Journal of Chemistry*, vol. 43, no. 4, pp. 1900–1909, 2019, doi: 10.1039/C8NJ04594A.
- [43] A. K. Lyashchenko *et al.*, "Environment of Al³⁺ Ion and Transsolvation Process in Water–Urea Solutions of Aluminum Chloride," *Russian Journal of Inorganic Chemistry*, vol. 64, no. 7, pp. 924–929, Jul. 2019, doi: 10.1134/S0036023619070118.
- [44] M. F. Brigatti, A. Laurora, D. Malferrari, L. Medici, and L. Poppi, "Adsorption of [Al(Urea)₆]³⁺ and [Cr(Urea)₆]³⁺ complexes in the vermiculite interlayer," *Appl Clay Sci*, vol. 30, no. 1, pp. 21–32, Aug. 2005, doi: 10.1016/j.clay.2005.03.001.
- [45] B. Huber and M. Drüscler, "rhd instruments flexible cell solutions," rhd instruments flexible cell . Accessed: Jan. 30, 2023. [Online]. Available: <https://www.rhd-instruments.de/en/products/cells/tsc-surface>
- [46] J. L. Hutter and J. Bechhoefer, "Calibration of atomic-force microscope tips," *Review of Scientific Instruments*, vol. 64, no. 7, pp. 1868–1873, Jul. 1993, doi: 10.1063/1.1143970.
- [47] P. M. Dietrich, S. Bahr, T. Yamamoto, M. Meyer, and A. Thissen, "Chemical surface analysis on materials and devices under functional conditions – Environmental photoelectron spectroscopy as non-destructive tool for routine characterization," *J Electron Spectros Relat Phenomena*, vol. 231, pp. 118–126, Feb. 2019, doi: 10.1016/j.elspec.2017.12.007.
- [48] N. Fairley *et al.*, "Systematic and collaborative approach to problem solving using X-ray photoelectron spectroscopy," *Applied Surface Science Advances*, vol. 5, p. 100112, Sep. 2021, doi: 10.1016/j.apsadv.2021.100112.
- [49] K. L. Ng, T. Dong, J. Anawati, and G. Azimi, "High-Performance Aluminum Ion Battery Using Cost-Effective AlCl₃-Trimethylamine Hydrochloride Ionic Liquid Electrolyte," *Adv Sustain Syst*, vol. 4, no. 8, p. 2000074, Aug. 2020, doi: 10.1002/adsu.202000074.
- [50] H. Wang, S. Gu, Y. Bai, S. Chen, F. Wu, and C. Wu, "High-Voltage and Noncorrosive Ionic Liquid Electrolyte Used in Rechargeable Aluminum Battery," *ACS Appl Mater Interfaces*, vol. 8, no. 41, pp. 27444–27448, Oct. 2016, doi: 10.1021/acsami.6b10579.
- [51] G. A. Elia *et al.*, "An Overview and Future Perspectives of Aluminum Batteries," *Advanced Materials*, vol. 28, no. 35, pp. 7564–7579, Sep. 2016, doi: 10.1002/adma.201601357.
- [52] M. Chiku, S. Matsumura, H. Takeda, E. Higuchi, and H. Inoue, "Aluminum Bis(trifluoromethanesulfonyl)imide as a Chloride-Free Electrolyte for Rechargeable Aluminum Batteries," *J Electrochem Soc*, vol. 164, no. 9, pp. A1841–A1844, Jun. 2017, doi: 10.1149/2.0701709jes.

- [53] X. Wen *et al.*, "Synthesis and Electrochemical Properties of Aluminum Hexafluorophosphate," *J Phys Chem Lett*, vol. 12, no. 25, pp. 5903–5908, Jul. 2021, doi: 10.1021/acs.jpcllett.1c01236.
- [54] N. Jayaprakash, S. K. Das, and L. A. Archer, "The rechargeable aluminum-ion battery," *Chemical Communications*, vol. 47, no. 47, p. 12610, 2011, doi: 10.1039/c1cc15779e.
- [55] L. D. Reed, S. N. Ortiz, M. Xiong, and E. J. Menke, "A rechargeable aluminum-ion battery utilizing a copper hexacyanoferrate cathode in an organic electrolyte," *Chemical Communications*, vol. 51, no. 76, pp. 14397–14400, 2015, doi: 10.1039/C5CC06053B.
- [56] L. D. Reed, A. Arteaga, and E. J. Menke, "A Combined Experimental and Computational Study of an Aluminum Triflate/Diglyme Electrolyte," *J Phys Chem B*, vol. 119, no. 39, pp. 12677–12681, Oct. 2015, doi: 10.1021/acs.jpccb.5b08501.
- [57] Z. Slim and E. J. Menke, "Comparing Computational Predictions and Experimental Results for Aluminum Triflate in Tetrahydrofuran," *J Phys Chem B*, vol. 124, no. 24, pp. 5002–5008, Jun. 2020, doi: 10.1021/acs.jpccb.0c02570.
- [58] Z. Slim and E. J. Menke, "Aluminum Electrodeposition from Chloride-Rich and Chloride-Free Organic Electrolytes," *The Journal of Physical Chemistry C*, vol. 126, no. 5, pp. 2365–2373, Feb. 2022, doi: 10.1021/acs.jpcc.1c09126.
- [59] T. Mandai and P. Johansson, "Haloaluminate-Free Cationic Aluminum Complexes: Structural Characterization and Physicochemical Properties," *The Journal of Physical Chemistry C*, vol. 120, no. 38, pp. 21285–21292, Sep. 2016, doi: 10.1021/acs.jpcc.6b07235.
- [60] S. Kumar, P. Rama, G. Yang, W. Y. Lieu, D. Chinnadurai, and Z. W. Seh, "Additive-Driven Interfacial Engineering of Aluminum Metal Anode for Ultralong Cycling Life," *Nanomicro Lett*, vol. 15, no. 1, p. 21, Dec. 2023, doi: 10.1007/s40820-022-01000-6.
- [61] H. Wang, S. Gu, Y. Bai, S. Chen, F. Wu, and C. Wu, "High-Voltage and Noncorrosive Ionic Liquid Electrolyte Used in Rechargeable Aluminum Battery," *ACS Appl Mater Interfaces*, 2016, doi: 10.1021/acsami.6b10579.
- [62] X. Zhang *et al.*, "Challenges and Opportunities for Multivalent Metal Anodes in Rechargeable Batteries," *Adv Funct Mater*, vol. 30, no. 45, p. 2004187, Nov. 2020, doi: 10.1002/adfm.202004187.
- [63] L. D. Reed, A. Arteaga, and E. J. Menke, "A Combined Experimental and Computational Study of an Aluminum Triflate/Diglyme Electrolyte," *J Phys Chem B*, vol. 119, no. 39, pp. 12677–12681, Oct. 2015, doi: 10.1021/acs.jpccb.5b08501.
- [64] L. Legrand, A. Tranchant, and R. Messina, "Behaviour of aluminium as anode in dimethylsulfone-based electrolytes," *Electrochim Acta*, vol. 39, no. 10, pp. 1427–1431, Jul. 1994, doi: 10.1016/0013-4686(94)85054-2.
- [65] K. Chiba, T. Ueda, Y. Yamaguchi, Y. Oki, F. Shimodate, and K. Naoi, "Electrolyte Systems for High Withstand Voltage and Durability I. Linear Sulfones for Electric Double-Layer Capacitors," *J Electrochem Soc*, vol. 158, no. 8, p. A872, 2011, doi: 10.1149/1.3593001.

- [66] S.-J. Kang *et al.*, “Non-Grignard and Lewis Acid-Free Sulfone Electrolytes for Rechargeable Magnesium Batteries,” *Chemistry of Materials*, vol. 29, no. 7, pp. 3174–3180, Apr. 2017, doi: 10.1021/acs.chemmater.7b00248.
- [67] J. Alvarado *et al.*, “A carbonate-free, sulfone-based electrolyte for high-voltage Li-ion batteries,” *Materials Today*, vol. 21, no. 4, pp. 341–353, May 2018, doi: 10.1016/j.mattod.2018.02.005.
- [68] M. Nie and B. L. Lucht, “Role of Lithium Salt on Solid Electrolyte Interface (SEI) Formation and Structure in Lithium Ion Batteries,” *J Electrochem Soc*, vol. 161, no. 6, pp. A1001–A1006, 2014, doi: 10.1149/2.054406jes.
- [69] Y. Nakayama *et al.*, “Sulfone-based electrolytes for aluminium rechargeable batteries,” *Physical Chemistry Chemical Physics*, vol. 17, no. 8, pp. 5758–5766, 2015, doi: 10.1039/C4CP02183E.
- [70] S. K. Das, D. Majhi, P. K. Sahu, and M. Sarkar, “Investigation of the influence of alkyl side chain length on the fluorescence response of C153 in a series of room temperature ionic liquids,” *RSC Adv*, vol. 5, no. 52, pp. 41585–41594, 2015, doi: 10.1039/C4RA16864J.
- [71] C. Schütter, A. Bothe, and A. Balducci, “Mixtures of acetonitrile and ethyl isopropyl sulfone as electrolytes for electrochemical double layer capacitors,” *Electrochim Acta*, vol. 331, p. 135421, Jan. 2020, doi: 10.1016/j.electacta.2019.135421.
- [72] N. S. V. Narayanan, B. V. Ashok Raj, and S. Sampath, “Physicochemical, spectroscopic and electrochemical characterization of magnesium ion-conducting, room temperature, ternary molten electrolytes,” *J Power Sources*, vol. 195, no. 13, pp. 4356–4364, Jul. 2010, doi: 10.1016/j.jpowsour.2010.01.070.
- [73] C. Yan *et al.*, “Reversible Al Metal Anodes Enabled by Amorphization for Aqueous Aluminum Batteries,” *J Am Chem Soc*, vol. 144, no. 25, pp. 11444–11455, Jun. 2022, doi: 10.1021/jacs.2c04820.
- [74] Q. Ran *et al.*, “Aluminum-copper alloy anode materials for high-energy aqueous aluminum batteries,” *Nat Commun*, vol. 13, no. 1, p. 576, Jan. 2022, doi: 10.1038/s41467-022-28238-3.
- [75] G. Razaz *et al.*, “Aluminum Alloy Anode with Various Iron Content Influencing the Performance of Aluminum-Ion Batteries,” *Materials*, vol. 16, no. 3, p. 933, Jan. 2023, doi: 10.3390/ma16030933.
- [76] D. Pradhan, D. Mantha, and R. G. Reddy, “The effect of electrode surface modification and cathode overpotential on deposit characteristics in aluminum electrorefining using EMIC–AlCl₃ ionic liquid electrolyte,” *Electrochim Acta*, vol. 54, no. 26, pp. 6661–6667, Nov. 2009, doi: 10.1016/j.electacta.2009.06.059.
- [77] L. C. Loaiza, N. Lindahl, and P. Johansson, “Initial Evolution of Passivation Layers in Non-Aqueous Aluminium Batteries,” *J Electrochem Soc*, Jan. 2023, doi: 10.1149/1945-7111/acb108.
- [78] D.-M. She *et al.*, “Surface Evolution of Aluminum Electrodes in Non-Aqueous Aluminum Batteries,” *J Electrochem Soc*, vol. 167, no. 13, p. 130530, Oct. 2020, doi: 10.1149/1945-7111/abbb09.

- [79] H. Go, M. R. Raj, Y. Tak, and G. Lee, "Electrochemically Surface-modified Aluminum Electrode Enabling High Performance and Ultra-long Cycling Life Al-ion Batteries," *Electroanalysis*, vol. 34, no. 8, pp. 1308–1317, Aug. 2022, doi: 10.1002/elan.202100669.
- [80] A. Zhou *et al.*, "Water-in-Salt Electrolyte Promotes High-Capacity FeFe(CN)₆ Cathode for Aqueous Al-Ion Battery," *ACS Appl Mater Interfaces*, vol. 11, no. 44, pp. 41356–41362, Nov. 2019, doi: 10.1021/acsami.9b14149.
- [81] R. Horia, D.-T. Nguyen, A. Y. S. Eng, and Z. W. Seh, "Using a Chloride-Free Magnesium Battery Electrolyte to Form a Robust Anode–Electrolyte Nanointerface," *Nano Lett*, vol. 21, no. 19, pp. 8220–8228, Oct. 2021, doi: 10.1021/acs.nanolett.1c02655.
- [82] I. Weber, J. Ingenmey, J. Schnaidt, B. Kirchner, and R. J. Behm, "Influence of Complexing Additives on the Reversible Deposition/Dissolution of Magnesium in an Ionic Liquid," *ChemElectroChem*, vol. 8, no. 2, pp. 390–402, Jan. 2021, doi: 10.1002/celec.202001488.
- [83] D.-T. Nguyen *et al.*, "Rechargeable magnesium batteries enabled by conventional electrolytes with multifunctional organic chloride additives," *Energy Storage Mater*, vol. 45, pp. 1120–1132, Mar. 2022, doi: 10.1016/j.ensm.2021.11.011.
- [84] Q. Zhao, M. J. Zachman, W. I. Al Sadat, J. Zheng, L. F. Kourkoutis, and L. Archer, "Solid electrolyte interphases for high-energy aqueous aluminum electrochemical cells," *Sci Adv*, vol. 4, no. 11, Nov. 2018, doi: 10.1126/sciadv.aau8131.
- [85] E. Peled, "The Electrochemical Behavior of Alkali and Alkaline Earth Metals in Nonaqueous Battery Systems—The Solid Electrolyte Interphase Model," *J Electrochem Soc*, vol. 126, no. 12, pp. 2047–2051, Dec. 1979, doi: 10.1149/1.2128859.
- [86] T. Dong, K. L. Ng, Y. Wang, O. Voznyy, and G. Azimi, "Solid Electrolyte Interphase Engineering for Aqueous Aluminum Metal Batteries: A Critical Evaluation," *Adv Energy Mater*, vol. 11, no. 20, p. 2100077, May 2021, doi: 10.1002/aenm.202100077.
- [87] A. Wang, S. Kadam, H. Li, S. Shi, and Y. Qi, "Review on modeling of the anode solid electrolyte interphase (SEI) for lithium-ion batteries," *NPJ Comput Mater*, vol. 4, no. 1, p. 15, Mar. 2018, doi: 10.1038/s41524-018-0064-0.
- [88] L. C. Loaiza, N. Lindahl, and P. Johansson, "Initial Evolution of Passivation Layers in Non-Aqueous Aluminium Batteries," *J Electrochem Soc*, vol. 170, no. 3, p. 030512, Mar. 2023, doi: 10.1149/1945-7111/acb108.
- [89] D. Lee, G. Lee, and Y. Tak, "Hypostatic instability of aluminum anode in acidic ionic liquid for aluminum-ion battery," *Nanotechnology*, vol. 29, no. 36, p. 36LT01, Sep. 2018, doi: 10.1088/1361-6528/aacd7f.
- [90] S. Choi, H. Go, G. Lee, and Y. Tak, "Electrochemical properties of an aluminum anode in an ionic liquid electrolyte for rechargeable aluminum-ion batteries," *Physical Chemistry Chemical Physics*, vol. 19, no. 13, pp. 8653–8656, 2017, doi: 10.1039/C6CP08776K.
- [91] D. Muñoz-Torrero *et al.*, "Investigation of different anode materials for aluminium rechargeable batteries," *J Power Sources*, vol. 374, pp. 77–83, Jan. 2018, doi: 10.1016/j.jpowsour.2017.11.032.

- [92] Y. Long *et al.*, "Suppressing Al dendrite growth towards a long-life Al-metal battery," *Energy Storage Mater*, vol. 34, pp. 194–202, Jan. 2021, doi: 10.1016/j.ensm.2020.09.013.
- [93] H. Chen *et al.*, "Oxide Film Efficiently Suppresses Dendrite Growth in Aluminum-Ion Battery," *ACS Appl Mater Interfaces*, vol. 9, no. 27, pp. 22628–22634, Jul. 2017, doi: 10.1021/acsami.7b07024.
- [94] S. Kumar, V. Verma, H. Arora, W. Manalastas, and M. Srinivasan, "Rechargeable Al-Metal Aqueous Battery Using NaMnHCF as a Cathode: Investigating the Role of Coated-Al Anode Treatments for Superior Battery Cycling Performance," *ACS Appl Energy Mater*, vol. 3, no. 9, pp. 8627–8635, Sep. 2020, doi: 10.1021/acsaem.0c01240.
- [95] J. Świergiel and J. Jadżyn, "Static Dielectric Permittivity and Electric Conductivity of *N*-Methylacetamide + *N,N*-Dimethylacetamide Mixtures," *J Chem Eng Data*, vol. 54, no. 8, pp. 2296–2300, Aug. 2009, doi: 10.1021/je9002515.
- [96] R. Zhang, G. Zhao, and W. Wu, "Structures and Hydrogen Bonding Interactions in Urea-water System Studied by All-atom MD Simulation and Chemical Shifts in NMR Spectrum," *Chinese Journal of Chemical Physics*, vol. 22, no. 5, pp. 511–516, Oct. 2009, doi: 10.1088/1674-0068/22/05/511-516.
- [97] J. K. Carr, L. E. Buchanan, J. R. Schmidt, M. T. Zanni, and J. L. Skinner, "Structure and Dynamics of Urea/Water Mixtures Investigated by Vibrational Spectroscopy and Molecular Dynamics Simulation," *J Phys Chem B*, vol. 117, no. 42, pp. 13291–13300, Oct. 2013, doi: 10.1021/jp4037217.
- [98] W. Peters, H. T. Duong, S. Lee, and J.-F. Drillet, "Investigation of Al(TfO)₃-based deep eutectic solvent electrolytes for aluminium-ion batteries. Part I: understanding the positively charged Al complex formation," *Physical Chemistry Chemical Physics*, vol. 23, no. 38, pp. 21923–21933, 2021, doi: 10.1039/D1CP01711J.
- [99] M. A. Czarnecki and K. Z. Haufa, "Effect of Temperature and Concentration on the Structure of *N*-Methylacetamide–Water Complexes: Near-Infrared Spectroscopic Study," *J Phys Chem A*, vol. 109, no. 6, pp. 1015–1021, Feb. 2005, doi: 10.1021/jp0471150.
- [100] P. M. Schaber, J. Colson, S. Higgins, D. Thielen, B. Anspach, and J. Brauer, "Thermal decomposition (pyrolysis) of urea in an open reaction vessel," *Thermochim Acta*, vol. 424, no. 1–2, pp. 131–142, Dec. 2004, doi: 10.1016/j.tca.2004.05.018.
- [101] Q. Li, J. Sun, L. Zhuang, X. Xu, Y. Sun, and G. Wang, "Effect of urea addition on chitosan dissolution with [Emim]Ac-Urea solution system," *Carbohydr Polym*, vol. 195, pp. 288–297, Sep. 2018, doi: 10.1016/j.carbpol.2018.04.097.
- [102] T. Tsuda, T. Tomioka, and C. L. Hussey, "Physicochemical properties of highly conductive urea–EtMeImCl melts," *Chemical Communications*, no. 25, p. 2908, 2008, doi: 10.1039/b802386g.
- [103] N. Calisi, S. Martinuzzi, A. Giaccherini, C. S. Pomelli, L. Guazzelli, and S. Caporali, "Temperature and angle resolved XPS study of BMIm Cl and BMIm FeCl₄," *J Electron Spectros Relat Phenomena*, vol. 247, p. 147034, Feb. 2021, doi: 10.1016/j.elspec.2020.147034.

- [104] S. Caporali, U. Bardi, and A. Lavacchi, "X-ray photoelectron spectroscopy and low energy ion scattering studies on 1-butyl-3-methyl-imidazolium bis(trifluoromethane) sulfonimide," *J Electron Spectros Relat Phenomena*, vol. 151, no. 1, pp. 4–8, Mar. 2006, doi: 10.1016/j.elspec.2005.09.010.
- [105] J. van den Brand, W. G. Sloof, H. Terryn, and J. H. W. de Wit, "Correlation between hydroxyl fraction and O/Al atomic ratio as determined from XPS spectra of aluminium oxide layers," *Surface and Interface Analysis*, vol. 36, no. 1, pp. 81–88, Jan. 2004, doi: 10.1002/sia.1653.
- [106] J. Tu *et al.*, "Nonaqueous Rechargeable Aluminum Batteries: Progresses, Challenges, and Perspectives," *Chem Rev*, vol. 121, no. 8, pp. 4903–4961, Apr. 2021, doi: 10.1021/acs.chemrev.0c01257.
- [107] M. Textor and M. Amstutz, "Surface analysis of thin films and interfaces in commercial aluminium products," *Anal Chim Acta*, vol. 297, no. 1–2, pp. 15–26, Oct. 1994, doi: 10.1016/0003-2670(93)E0550-Q.
- [108] A. V Naumkin and A. Kraut-Vass, *NIST X-ray Photoelectron Spectroscopy Database*. ational Institute of Standards and Technology, Gaithersburg MD, 2008.
- [109] D. Briggs, "Handbook of X-ray Photoelectron Spectroscopy C. D. Wanger, W. M. Riggs, L. E. Davis, J. F. Moulder and G. E. Muilenberg Perkin-Elmer Corp., Physical Electronics Division, Eden Prairie, Minnesota, USA, 1979. 190 pp. \$195," *Surface and Interface Analysis*, vol. 3, no. 4, pp. v–v, Aug. 1981, doi: 10.1002/sia.740030412.
- [110] L. Suo *et al.*, "'Water-in-salt' electrolyte enables high-voltage aqueous lithium-ion chemistries," *Science (1979)*, vol. 350, no. 6263, pp. 938–943, Nov. 2015, doi: 10.1126/science.aab1595.
- [111] L. Suo *et al.*, "'Water-in-Salt' Electrolyte Makes Aqueous Sodium-Ion Battery Safe, Green, and Long-Lasting," *Adv Energy Mater*, vol. 7, no. 21, p. 1701189, Nov. 2017, doi: 10.1002/aenm.201701189.
- [112] D. D. Macdonald, "The history of the Point Defect Model for the passive state: A brief review of film growth aspects," *Electrochim Acta*, vol. 56, no. 4, pp. 1761–1772, Jan. 2011, doi: 10.1016/j.electacta.2010.11.005.
- [113] Z. Liu *et al.*, "Voltage issue of aqueous rechargeable metal-ion batteries," *Chem Soc Rev*, vol. 49, no. 1, pp. 180–232, 2020, doi: 10.1039/C9CS00131J.
- [114] G. A. Elia *et al.*, "An Overview and Future Perspectives of Aluminum Batteries," *Advanced Materials*, 2016, doi: 10.1002/adma.201601357.
- [115] F. Wang *et al.*, "Highly reversible zinc metal anode for aqueous batteries," *Nat Mater*, vol. 17, no. 6, pp. 543–549, Jun. 2018, doi: 10.1038/s41563-018-0063-z.
- [116] G. A. Elia *et al.*, "An Overview and Future Perspectives of Aluminum Batteries," *Advanced Materials*, vol. 28, no. 35, pp. 7564–7579, Sep. 2016, doi: 10.1002/adma.201601357.
- [117] S. Zaromb, "The Use and Behavior of Aluminum Anodes in Alkaline Primary Batteries," *J Electrochem Soc*, vol. 109, no. 12, p. 1125, 1962, doi: 10.1149/1.2425257.

- [118] Y.-J. Cho, I.-J. Park, H.-J. Lee, and J.-G. Kim, "Aluminum anode for aluminum–air battery – Part I: Influence of aluminum purity," *J Power Sources*, vol. 277, pp. 370–378, Mar. 2015, doi: 10.1016/j.jpowsour.2014.12.026.
- [119] L. Qingfeng, H. A. Hjuler, R. W. Berg, and N. J. Bjerrum, "Electrochemical Deposition of Aluminum from NaCl - AlCl₃ Melts," *J Electrochem Soc*, vol. 137, no. 2, pp. 593–598, Feb. 1990, doi: 10.1149/1.2086512.
- [120] E. Berretti *et al.*, "Aluminium Electrodeposition from Ionic Liquid: Effect of Deposition Temperature and Sonication †," *Materials*, vol. 9, no. 9, p. 719, Aug. 2016, doi: 10.3390/ma9090719.
- [121] H. Yang, F. Wu, Y. Bai, and C. Wu, "Toward better electrode/electrolyte interfaces in the ionic-liquid-based rechargeable aluminum batteries," *Journal of Energy Chemistry*, vol. 45, pp. 98–102, Jun. 2020, doi: 10.1016/j.jechem.2019.10.003.
- [122] M. Jäckle, K. Helmbrecht, M. Smits, D. Stottmeister, and A. Groß, "Self-diffusion barriers: possible descriptors for dendrite growth in batteries?," *Energy Environ Sci*, vol. 11, no. 12, pp. 3400–3407, 2018, doi: 10.1039/C8EE01448E.
- [123] H. Chen *et al.*, "Oxide Film Efficiently Suppresses Dendrite Growth in Aluminum-Ion Battery," *ACS Appl Mater Interfaces*, vol. 9, no. 27, pp. 22628–22634, Jul. 2017, doi: 10.1021/acsami.7b07024.
- [124] S. Choi, H. Go, G. Lee, and Y. Tak, "Electrochemical properties of an aluminum anode in an ionic liquid electrolyte for rechargeable aluminum-ion batteries," *Physical Chemistry Chemical Physics*, vol. 19, no. 13, pp. 8653–8656, 2017, doi: 10.1039/C6CP08776K.
- [125] H. Wang *et al.*, "Anion-effects on electrochemical properties of ionic liquid electrolytes for rechargeable aluminum batteries," *J Mater Chem A Mater*, vol. 3, no. 45, pp. 22677–22686, 2015, doi: 10.1039/C5TA06187C.
- [126] F. Wu, N. Zhu, Y. Bai, Y. Gao, and C. Wu, "An interface-reconstruction effect for rechargeable aluminum battery in ionic liquid electrolyte to enhance cycling performances," *Green Energy & Environment*, vol. 3, no. 1, pp. 71–77, Jan. 2018, doi: 10.1016/j.gee.2017.10.002.
- [127] S. Choi, H. Go, G. Lee, and Y. Tak, "Electrochemical properties of an aluminum anode in an ionic liquid electrolyte for rechargeable aluminum-ion batteries," *Physical Chemistry Chemical Physics*, vol. 19, no. 13, pp. 8653–8656, 2017, doi: 10.1039/C6CP08776K.
- [128] H. Wang *et al.*, "Anion-effects on electrochemical properties of ionic liquid electrolytes for rechargeable aluminum batteries," *J Mater Chem A Mater*, vol. 3, no. 45, pp. 22677–22686, 2015, doi: 10.1039/C5TA06187C.
- [129] F. Wu, N. Zhu, Y. Bai, Y. Gao, and C. Wu, "An interface-reconstruction effect for rechargeable aluminum battery in ionic liquid electrolyte to enhance cycling performances," *Green Energy & Environment*, vol. 3, no. 1, pp. 71–77, Jan. 2018, doi: 10.1016/j.gee.2017.10.002.
- [130] X. Wang *et al.*, "Synthesis of novel nanomaterials and their application in efficient removal of radionuclides," *Sci China Chem*, vol. 62, no. 8, pp. 933–967, Aug. 2019, doi: 10.1007/s11426-019-9492-4.

- [131] S. Choi, H. Go, G. Lee, and Y. Tak, "Electrochemical properties of an aluminum anode in an ionic liquid electrolyte for rechargeable aluminum-ion batteries," *Physical Chemistry Chemical Physics*, vol. 19, no. 13, pp. 8653–8656, 2017, doi: 10.1039/C6CP08776K.
- [132] S. Zein El Abedin, P. Giridhar, P. Schwab, and F. Endres, "Electrodeposition of nanocrystalline aluminium from a chloroaluminate ionic liquid," *Electrochem Commun*, vol. 12, no. 8, pp. 1084–1086, Aug. 2010, doi: 10.1016/j.elecom.2010.05.034.
- [133] L. Gjønnnes, "Development of surface topography during cold rolling of twin-roll cast aluminium," *Wear*, vol. 192, no. 1–2, pp. 216–227, Mar. 1996, doi: 10.1016/0043-1648(95)06809-0.
- [134] S. Xia, X.-M. Zhang, K. Huang, Y.-L. Chen, and Y.-T. Wu, "Ionic liquid electrolytes for aluminium secondary battery: Influence of organic solvents," *Journal of Electroanalytical Chemistry*, vol. 757, pp. 167–175, Nov. 2015, doi: 10.1016/j.jelechem.2015.09.022.
- [135] O. M. E. Ylivaara *et al.*, "Aluminum oxide from trimethylaluminum and water by atomic layer deposition: The temperature dependence of residual stress, elastic modulus, hardness and adhesion," *Thin Solid Films*, vol. 552, pp. 124–135, Feb. 2014, doi: 10.1016/j.tsf.2013.11.112.
- [136] H. Xu *et al.*, "Low-cost AlCl₃/Et₃NHCl electrolyte for high-performance aluminum-ion battery," *Energy Storage Mater*, vol. 17, pp. 38–45, Feb. 2019, doi: 10.1016/j.ensm.2018.08.003.
- [137] D. S. Kim, Y. Y. Yu, and K. Char, "Characterization of aluminum oxyfluoride barrier in magnetic tunnel junctions," *J Appl Phys*, vol. 96, no. 4, pp. 2278–2285, Aug. 2004, doi: 10.1063/1.1771826.
- [138] L. A. Thimons, A. Gujrati, A. Sanner, L. Pastewka, and T. D. B. Jacobs, "Hard-material Adhesion: Which Scales of Roughness Matter?," *Exp Mech*, vol. 61, no. 7, pp. 1109–1120, Sep. 2021, doi: 10.1007/s11340-021-00733-6.
- [139] Y. Liu *et al.*, "Novel Bimetallic Activated Center Alloying Mechanism Positive Electrodes for Aluminum Storage," *Small*, vol. 18, no. 34, Aug. 2022, doi: 10.1002/smll.202203236.
- [140] D. Kong *et al.*, "Polycyclic Aromatic Hydrocarbons as a New Class of Promising Cathode Materials for Aluminum-Ion Batteries," *Angewandte Chemie International Edition*, vol. 61, no. 3, Jan. 2022, doi: 10.1002/anie.202114681.
- [141] Y. Bian *et al.*, "Graphite/copper phthalocyanine composite cathode for overcharge protection and gas evolution suppression in aluminum-ion batteries at room temperature," *Electrochim Acta*, vol. 332, p. 135188, Feb. 2020, doi: 10.1016/j.electacta.2019.135188.
- [142] Y. Du *et al.*, "Interfacial engineering of Bi₂Te₃/Sb₂Te₃ heterojunction enables high-energy cathode for aluminum batteries," *Energy Storage Mater*, vol. 38, pp. 231–240, Jun. 2021, doi: 10.1016/j.ensm.2021.03.012.
- [143] W. Lv, G. Wu, X. Li, J. Li, and Z. Li, "Two-dimensional V₂C@Se (MXene) composite cathode material for high-performance rechargeable aluminum batteries," *Energy Storage Mater*, vol. 46, pp. 138–146, Apr. 2022, doi: 10.1016/j.ensm.2022.01.019.
- [144] B. Zhang, Y. Zhang, J. Li, J. Liu, X. Huo, and F. Kang, "In situ growth of metal-organic framework-derived CoTe₂ nanoparticles@nitrogen-doped porous carbon polyhedral composites as novel

- cathodes for rechargeable aluminum-ion batteries," *J Mater Chem A Mater*, vol. 8, no. 11, pp. 5535–5545, 2020, doi: 10.1039/D0TA00674B.
- [145] H. Hong *et al.*, "Ordered Macro–Microporous Metal–Organic Framework Single Crystals and Their Derivatives for Rechargeable Aluminum-Ion Batteries," *J Am Chem Soc*, vol. 141, no. 37, pp. 14764–14771, Sep. 2019, doi: 10.1021/jacs.9b06957.
- [146] W. Guan, L. Wang, H. Lei, J. Tu, and S. Jiao, "Sb₂Se₃ nanorods with N-doped reduced graphene oxide hybrids as high-capacity positive electrode materials for rechargeable aluminum batteries," *Nanoscale*, vol. 11, no. 35, pp. 16437–16444, 2019, doi: 10.1039/C9NR06481H.
- [147] Y. Zhang, B. Zhang, J. Li, J. Liu, X. Huo, and F. Kang, "SnSe nano-particles as advanced positive electrode materials for rechargeable aluminum-ion batteries," *Chemical Engineering Journal*, vol. 403, p. 126377, Jan. 2021, doi: 10.1016/j.cej.2020.126377.
- [148] R. Zhuang, Z. Huang, S. Wang, J. Qiao, J.-C. Wu, and J. Yang, "Binder-free cobalt sulfide@carbon nanofibers composite films as cathode for rechargeable aluminum-ion batteries," *Chemical Engineering Journal*, vol. 409, p. 128235, Apr. 2021, doi: 10.1016/j.cej.2020.128235.
- [149] Y. Hu *et al.*, "A Binder-Free and Free-Standing Cobalt Sulfide@Carbon Nanotube Cathode Material for Aluminum-Ion Batteries," *Advanced Materials*, vol. 30, no. 2, Jan. 2018, doi: 10.1002/adma.201703824.
- [150] Z. Yu, Z. Kang, Z. Hu, J. Lu, Z. Zhou, and S. Jiao, "Hexagonal NiS nanobelts as advanced cathode materials for rechargeable Al-ion batteries," *Chemical Communications*, vol. 52, no. 68, pp. 10427–10430, 2016, doi: 10.1039/C6CC05974K.
- [151] Y. Hu, B. Luo, D. Ye, X. Zhu, M. Lyu, and L. Wang, "An Innovative Freeze-Dried Reduced Graphene Oxide Supported SnS₂ Cathode Active Material for Aluminum-Ion Batteries," *Advanced Materials*, vol. 29, no. 48, Dec. 2017, doi: 10.1002/adma.201606132.
- [152] S. Wang *et al.*, "A Novel Aluminum-Ion Battery: Al/AlCl₃-[EMIm]Cl/Ni₃S₂@Graphene," *Adv Energy Mater*, vol. 6, no. 13, Jul. 2016, doi: 10.1002/aenm.201600137.
- [153] X. Zhang, G. Zhang, S. Wang, S. Li, and S. Jiao, "Porous CuO microsphere architectures as high-performance cathode materials for aluminum-ion batteries," *J Mater Chem A Mater*, vol. 6, no. 7, pp. 3084–3090, 2018, doi: 10.1039/C7TA10632G.
- [154] J. Kim, M. R. Raj, and G. Lee, "High-Defect-Density Graphite for Superior-Performance Aluminum-Ion Batteries with Ultra-Fast Charging and Stable Long Life," *Nanomicro Lett*, vol. 13, no. 1, p. 171, Dec. 2021, doi: 10.1007/s40820-021-00698-0.
- [155] L. Ellingsen *et al.*, "Environmental Screening of Electrode Materials for a Rechargeable Aluminum Battery with an AlCl₃/EMIMCl Electrolyte," *Materials*, vol. 11, no. 6, p. 936, Jun. 2018, doi: 10.3390/ma11060936.
- [156] N. R. Levy and Y. Ein-Eli, "Aluminum-ion battery technology: a rising star or a devastating fall?," *Journal of Solid State Electrochemistry*, vol. 24, no. 9, pp. 2067–2071, Sep. 2020, doi: 10.1007/s10008-020-04598-y.

- [157] M.-C. Lin *et al.*, "An ultrafast rechargeable aluminium-ion battery," *Nature*, vol. 520, no. 7547, pp. 324–328, Apr. 2015, doi: 10.1038/nature14340.
- [158] H. Sun, W. Wang, Z. Yu, Y. Yuan, S. Wang, and S. Jiao, "A new aluminium-ion battery with high voltage, high safety and low cost," *Chemical Communications*, vol. 51, no. 59, pp. 11892–11895, 2015, doi: 10.1039/C5CC00542F.
- [159] Y. Wu *et al.*, "3D Graphitic Foams Derived from Chloroaluminate Anion Intercalation for Ultrafast Aluminum-Ion Battery," *Advanced Materials*, vol. 28, no. 41, pp. 9218–9222, Nov. 2016, doi: 10.1002/adma.201602958.
- [160] H. Chen *et al.*, "A Defect-Free Principle for Advanced Graphene Cathode of Aluminum-Ion Battery," *Advanced Materials*, vol. 29, no. 12, Mar. 2017, doi: 10.1002/adma.201605958.
- [161] C. Li *et al.*, "Heteroatomic interface engineering in MOF-derived carbon heterostructures with built-in electric-field effects for high performance Al-ion batteries," *Energy Environ Sci*, vol. 11, no. 11, pp. 3201–3211, 2018, doi: 10.1039/C8EE01046C.
- [162] X. Xiao, M. Wang, J. Tu, Y. Luo, and S. Jiao, "Metal–Organic Framework-Derived Co_3O_4 @MWCNTs Polyhedron as Cathode Material for a High-Performance Aluminum-Ion Battery," *ACS Sustain Chem Eng*, vol. 7, no. 19, pp. 16200–16208, Oct. 2019, doi: 10.1021/acssuschemeng.9b03159.
- [163] C. Liu *et al.*, "Binder-free ultrasonicated graphite flakes@carbon fiber cloth cathode for rechargeable aluminum-ion battery," *J Power Sources*, vol. 438, p. 226950, Oct. 2019, doi: 10.1016/j.jpowsour.2019.226950.
- [164] H. Sun, W. Wang, Z. Yu, Y. Yuan, S. Wang, and S. Jiao, "A new aluminium-ion battery with high voltage, high safety and low cost," *Chemical Communications*, vol. 51, no. 59, pp. 11892–11895, 2015, doi: 10.1039/C5CC00542F.
- [165] S. Wang *et al.*, "Aluminum Chloride-Graphite Batteries with Flexible Current Collectors Prepared from Earth-Abundant Elements," *Advanced Science*, vol. 5, no. 4, p. 1700712, Apr. 2018, doi: 10.1002/advs.201700712.
- [166] K. v. Kravchyk, S. Wang, L. Piveteau, and M. v. Kovalenko, "Efficient Aluminum Chloride–Natural Graphite Battery," *Chemistry of Materials*, vol. 29, no. 10, pp. 4484–4492, May 2017, doi: 10.1021/acs.chemmater.7b01060.
- [167] M. Yamada, T. Watanabe, T. Gunji, J. Wu, and F. Matsumoto, "Review of the Design of Current Collectors for Improving the Battery Performance in Lithium-Ion and Post-Lithium-Ion Batteries," *Electrochem*, vol. 1, no. 2, pp. 124–159, May 2020, doi: 10.3390/electrochem1020011.
- [168] M. Walter, M. v. Kovalenko, and K. v. Kravchyk, "Challenges and benefits of post-lithium-ion batteries," *New Journal of Chemistry*, vol. 44, no. 5, pp. 1677–1683, 2020, doi: 10.1039/C9NJ05682C.
- [169] Y. Wang and K. Chen, "Low-cost, lightweight electrodes based on carbon fibers as current collectors for aluminum-ion batteries," *Journal of Electroanalytical Chemistry*, vol. 849, p. 113374, Sep. 2019, doi: 10.1016/j.jelechem.2019.113374.

- [170] S. Zhang, X. Tan, Z. Meng, H. Tian, F. Xu, and W.-Q. Han, "Naturally abundant high-performance rechargeable aluminum/iodine batteries based on conversion reaction chemistry," *J Mater Chem A Mater*, vol. 6, no. 21, pp. 9984–9996, 2018, doi: 10.1039/C8TA00675J.
- [171] Y. Chen *et al.*, "Thick electrodes upon biomass-derivative carbon current collectors: High-areal capacity positive electrodes for aluminum-ion batteries," *Electrochim Acta*, vol. 323, p. 134805, Nov. 2019, doi: 10.1016/j.electacta.2019.134805.
- [172] D. Muñoz-Torrero, M. Anderson, J. Palma, R. Marcilla, and E. Ventosa, "Unexpected Contribution of Current Collector to the Cost of Rechargeable Al-Ion Batteries," *ChemElectroChem*, vol. 6, no. 10, pp. 2766–2770, May 2019, doi: 10.1002/celec.201900679.
- [173] Y. Zhang, S. Liu, Y. Ji, J. Ma, and H. Yu, "Emerging Nonaqueous Aluminum-Ion Batteries: Challenges, Status, and Perspectives," *Advanced Materials*, vol. 30, no. 38, p. 1706310, Sep. 2018, doi: 10.1002/adma.201706310.
- [174] Y. Oh, G. Lee, and Y. Tak, "Stability of Metallic Current Collectors in Acidic Ionic Liquid for Rechargeable Aluminum-Ion Batteries," *ChemElectroChem*, vol. 5, no. 22, pp. 3348–3352, Nov. 2018, doi: 10.1002/celec.201800892.
- [175] L. D. Reed and E. Menke, "The Roles of V_2O_5 and Stainless Steel in Rechargeable Al-Ion Batteries," *J Electrochem Soc*, vol. 160, no. 6, pp. A915–A917, Apr. 2013, doi: 10.1149/2.114306jes.
- [176] L. Chen *et al.*, "Nonmetal Current Collectors: The Key Component for High-Energy-Density Aluminum Batteries," *Advanced Materials*, vol. 32, no. 42, Oct. 2020, doi: 10.1002/adma.202001212.
- [177] Z. Yu, J. Tu, C. Wang, and S. Jiao, "A Rechargeable Al/Graphite Battery Based on $AlCl_3$ /1-butyl-3-methylimidazolium Chloride Ionic Liquid Electrolyte," *ChemistrySelect*, vol. 4, no. 11, pp. 3018–3024, Mar. 2019, doi: 10.1002/slct.201900374.
- [178] S. Divya, J. H. Johnston, and T. Nann, "Molybdenum Dichalcogenide Cathodes for Aluminum-Ion Batteries," *Energy Technology*, vol. 8, no. 6, Jun. 2020, doi: 10.1002/ente.202000038.
- [179] H. Sun, W. Wang, Z. Yu, Y. Yuan, S. Wang, and S. Jiao, "A new aluminium-ion battery with high voltage, high safety and low cost," *Chemical Communications*, vol. 51, no. 59, pp. 11892–11895, 2015, doi: 10.1039/C5CC00542F.
- [180] D. Muñoz-Torrero, J. Palma, R. Marcilla, and E. Ventosa, "A critical perspective on rechargeable Al-ion battery technology," *Dalton Transactions*, vol. 48, no. 27, pp. 9906–9911, 2019, doi: 10.1039/C9DT02132A.
- [181] K. Okada, A. Kotani, H. Ogasawara, Y. Seino, and B. T. Thole, "Auger decay of quasiparticle states: Calculation of the $Ni\ 3p$ photoemission spectrum in $NiCl_2$," *Phys Rev B*, vol. 47, no. 11, pp. 6203–6206, Mar. 1993, doi: 10.1103/PhysRevB.47.6203.

- [182] A. N. Mansour, "Characterization of β -Ni(OH)₂ by XPS," *Surface Science Spectra*, vol. 3, no. 3, pp. 239–246, Jul. 1994, doi: 10.1116/1.1247752.
- [183] C. Sleight, A. P. Pijpers, A. Jaspers, B. Coussens, and R. J. Meier, "On the determination of atomic charge via ESCA including application to organometallics," *J Electron Spectros Relat Phenomena*, vol. 77, no. 1, pp. 41–57, Feb. 1996, doi: 10.1016/0368-2048(95)02392-5.
- [184] A. Siokou and S. Ntais, "Towards the preparation of realistic model Ziegler-Natta catalysts: XPS study of the MgCl₂/TiCl₄ interaction with flat SiO₂/Si(100)," *Surf Sci*, vol. 540, no. 2–3, pp. 379–388, Aug. 2003, doi: 10.1016/S0039-6028(03)00872-0.
- [185] P. Yu, Y. Lin, L. Xiang, L. Su, J. Zhang, and L. Mao, "Molecular Films of Water-Miscible Ionic Liquids Formed on Glassy Carbon Electrodes: Characterization and Electrochemical Applications," *Langmuir*, vol. 21, no. 20, pp. 9000–9006, Sep. 2005, doi: 10.1021/la051089v.
- [186] T. R. Gengenbach, G. H. Major, M. R. Linford, and C. D. Easton, "Practical guides for x-ray photoelectron spectroscopy (XPS): Interpreting the carbon 1s spectrum," *Journal of Vacuum Science & Technology A: Vacuum, Surfaces, and Films*, vol. 39, no. 1, Jan. 2021, doi: 10.1116/6.0000682.
- [187] T. R. Gengenbach, G. H. Major, M. R. Linford, and C. D. Easton, "Practical guides for x-ray photoelectron spectroscopy (XPS): Interpreting the carbon 1s spectrum," *Journal of Vacuum Science & Technology A*, vol. 39, no. 1, p. 013204, Jan. 2021, doi: 10.1116/6.0000682.
- [188] A. D. Hamer and R. A. Walton, "X-ray photoelectron spectra of inorganic molecules. IX. Distinction between bridging and terminal metal-chlorine bonds in metal halide clusters of rhenium(III) and molybdenum(II)," *Inorg Chem*, vol. 13, no. 6, pp. 1446–1451, Jun. 1974, doi: 10.1021/ic50136a038.
- [189] W. W. Beers and R. E. McCarley, "Synthesis, structure and reactivity of .beta.-molybdenum dichloride," *Inorg Chem*, vol. 24, no. 4, pp. 472–475, Feb. 1985, doi: 10.1021/ic00198a008.
- [190] H.-M. Wu and S.-A. Chen, "Dopant-polymer interaction: MoCl₅-doped polyacetylene," *Synth Met*, vol. 26, no. 3, pp. 225–236, Nov. 1988, doi: 10.1016/0379-6779(88)90239-1.
- [191] P. A. Barnard, I. W. Sun, and C. L. Hussey, "Molybdenum(II) chloride in the aluminum chloride-1-methyl-3-ethylimidazolium chloride molten salt. Electrochemical and spectroscopic characterization of the [(Mo₆Cl₈)Cl₆]²⁻ ion in neutral and basic melts," *Inorg Chem*, vol. 29, no. 19, pp. 3670–3674, Sep. 1990, doi: 10.1021/ic00344a010.

Appendix

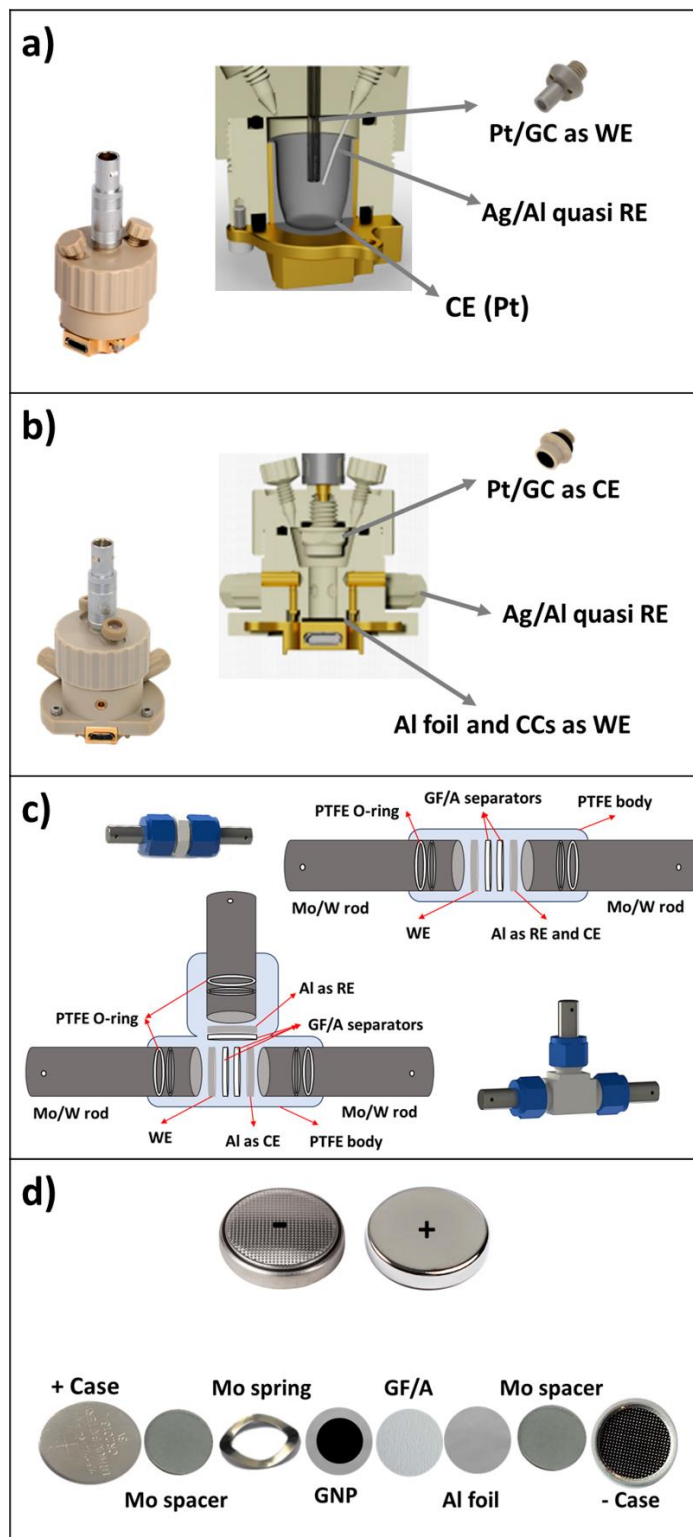
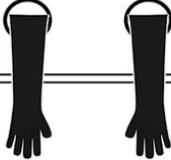
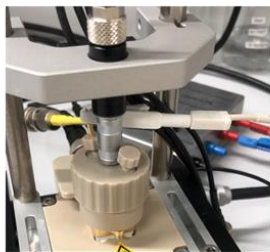


Figure A-2- 1. Schematic drawing of the (a) TSC1600-CC (b) TSC-SC (copyright is with rhd instruments GmbH & Co. KG). (c) Swagelok cell (d) Coin cell.

UNI LAB Glovebox BRAUN

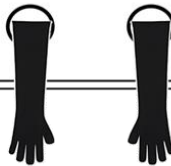
1. Preparation of electrolyte and electrode materials
2. Electrolyte characterization
3. Assembly of TSC 1600 cell

3. Implementation of electrochemical methodology

UNI LAB Glovebox BRAUN

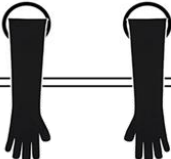
4. Immersion pretreatment procedure, washing and drying the electrodes
5. Assembly of TSC 1600 cell




6. Implementation of electrochemical methodology

UNI LAB Glovebox BRAUN

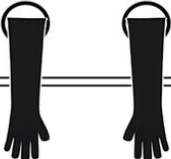
7. Disassembly of TSC1600 closed ad Surface Cell
8. Cleaning and washing of Electrodes




9. Drying of electrodes using BÜCHI Glass Oven B-585

UNI LAB Glovebox BRAUN

10. Mounting electrodes on SEM specimens onto vacuumed SEM specimen holder




11. Recording of SEM Images and EDX spectra using a JEOL JSM 7500F machine

UNI LAB Glovebox BRAUN

12. Conducting XPS measurements using a Specs EnviroESCA NAP-XPS machine

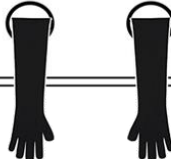
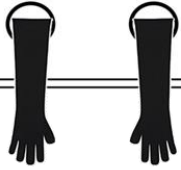


Figure A-2- 2. An overall experimental setup of chapter 3.

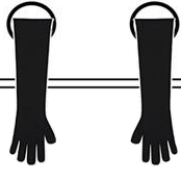
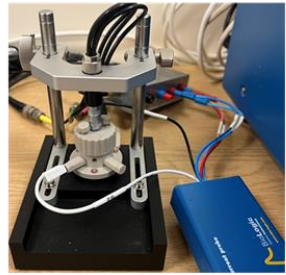
UNI LAB Glovebox BRAUN

1. Preparation of electrolyte and electrode materials
2. Assembly of TSC Surface Cell



UNI LAB Glovebox BRAUN

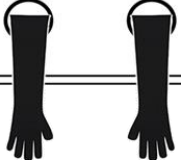
3. Immersion pretreatment procedure, washing and drying the electrodes

4. Implementation of electrochemical methodology

UNI LAB Glovebox BRAUN

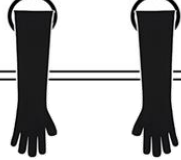
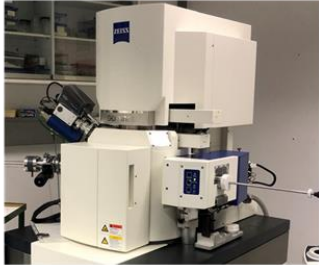
5. Disassembly of TSC Surface Cell
6. Cleaning and Washing of Electrode Materials




7. Drying of electrodes using BÜCHI Glass Oven B-585

UNI LAB Glovebox BRAUN

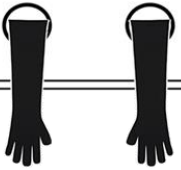
8. Mounting electrodes on SEM specimens onto vacuumed SEM specimen holder

9. Recording of SEM Images and EDX spectra using a JEOL JSM 7500F machine

UNI LAB Glovebox BRAUN

10. Conducting AFM using an AFM microscope (Park NX10, Park Systems)



UNI LAB Glovebox BRAUN

11. Conducting XPS measurements using a Specs EnviroESCA NAP-XPS machine

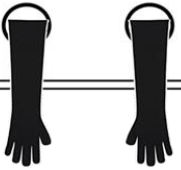


Figure A-2- 3. An overall experimental setup of chapter 4.2.

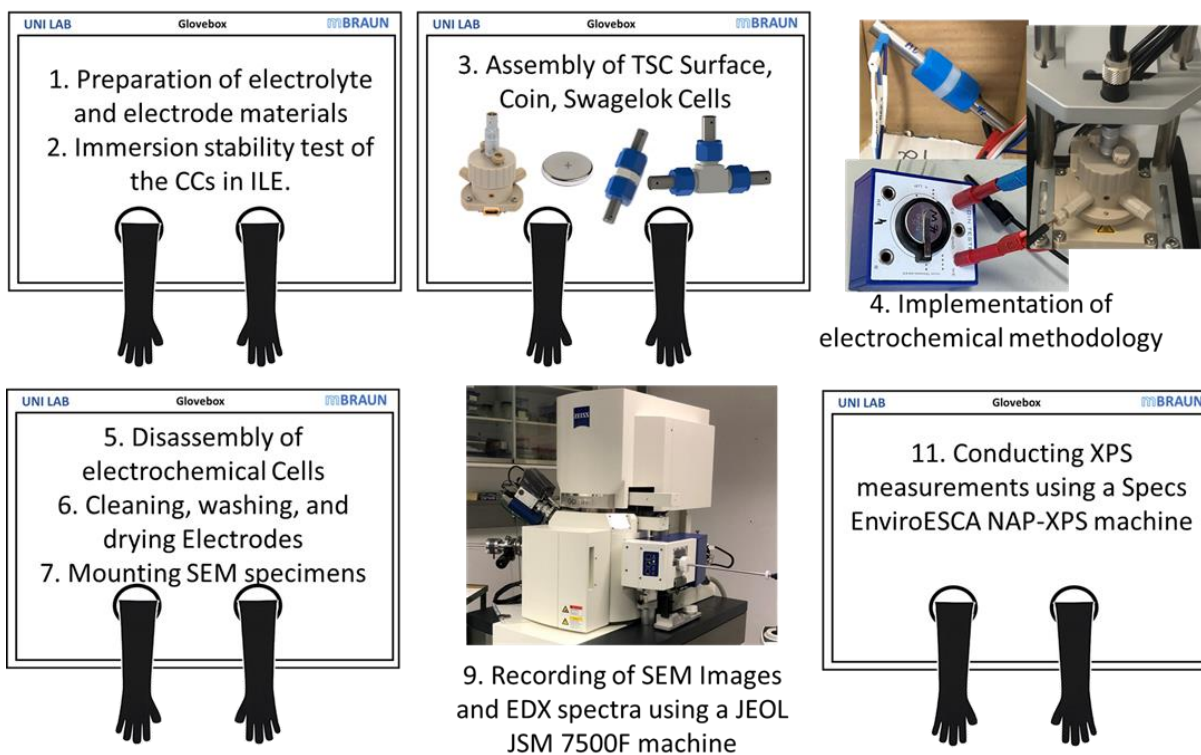


Figure A-2- 4. An overall experimental setup of chapter 5.2.

Table A-3- 1. Viscosity and density values of EiPS-based E at different temperatures

Temperature [°C]	Density [g/cm ³]	Specific Gravity	Lovis Dyn. Viscosity [mPa s]
20.00	1.196	1.2218	82.993
30.00	1.2113	1.2166	50.902
40.00	1.2031	1.2126	34.476
50.00	1.1949	1.2094	24.752
60.00	1.1866	1.2069	18.565
70.00	1.1783	1.2052	13.855
80.00	1.1700	1.2040	10.186

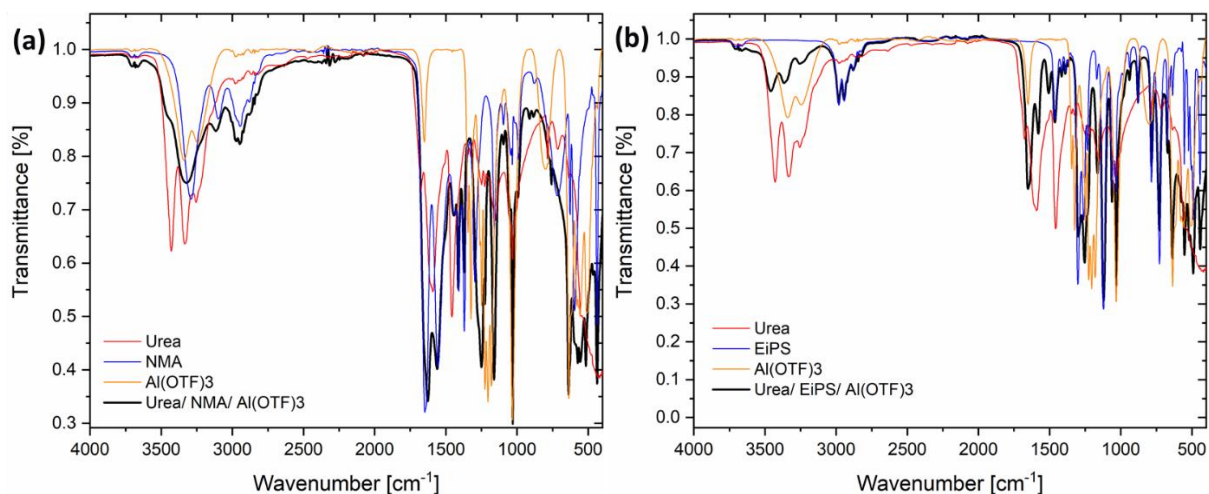


Figure A-3- 1. Full FT-IR spectra of the two electrolyte mixtures compared with the pure chemicals.

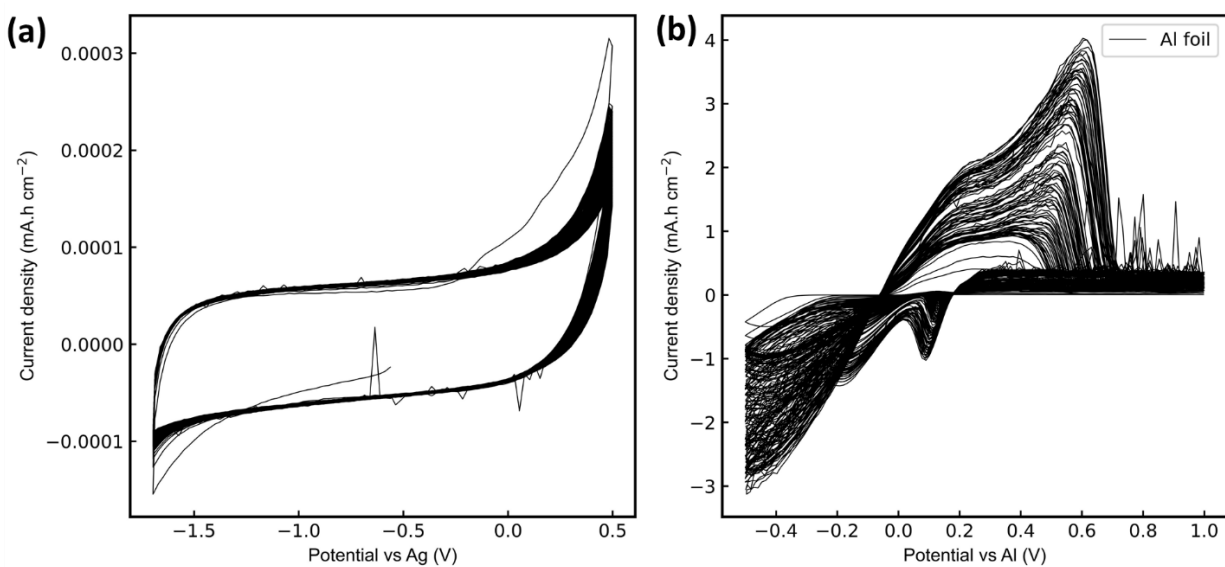


Figure A-3- 2. Recorded CVs with a scan rate of 20 mV s^{-1} on pristine Al WE in TSC-SC with GC CE in (a) NMA-based E vs. Ag quasi-RE and (b) AlCl_3 -based E vs. Al quasi-RE.

Table A-3- 2. EDX results of the elements observed on pristine and cycled Al foil in NMA-based E.

elements	Al					
	pristine		cycled (not M-Al)		cycled M-Al	
	WT	AT	WT	AT	WT	AT
Al	94.59	90.13	95.24	91.54	77.53	65.95
O	3.20	5.14	3.38	5.48	6.87	9.86
C	2.20	4.71	1.38	2.79	7.30	13.96
Cl	-	-	-	-	3.39	2.19
N	-	-	-	-	4.89	8.01

Table A-5- 1. EDX results of the elements observed on pristine and immersed Ni foil in AlCl₃-based E.

element	Ni foil									
	pristine		24 h		48 h		1 W		1 M	
	WT	AT	WT	AT	WT	AT	WT	AT	WT	AT
Ni	93.85	76.32	60.26	30.42	35.85	15.07	93.51	76.29	88.82	67.85
C	5.39	21.41	14.60	36.02	11.10	22.81	5.23	20.86	5.14	19.19
O	0.76	2.27	10.72	19.85	21.62	33.36	0.63	1.88	2.91	8.16
Cl	-	-	8.13	6.80	13.61	9.47	0.35	0.47	1.04	1.31
Al	-	-	6.27	6.89	14.29	13.07	0.27	0.48	2.07	3.45
N	-	-	-	-	3.51	6.18	-	-	-	-

Table A-5- 2. EDX results of the elements observed on pristine and immersed Ti foil in AlCl₃-based E.

element	Ti foil									
	pristine		24 h		48 h		1 W		1 M	
	WT	AT	WT	AT	WT	AT	WT	AT	WT	AT
Ti	95.98	85.70	71.59	47.43	38.59	19.03	94.48	83.40	68.92	45.03
C	4.01	14.29	7.34	19.39	15.59	30.65	4.19	14.77	7.94	20.68
O	-	-	10.59	21.00	16.23	23.96	-	-	10.37	20.28
Cl	-	-	5.79	5.18	17.11	11.39	0.63	0.75	7.98	7.04
Al	-	-	3.30	3.88	7.46	6.53	0.68	1.06	3.46	4.01
N	-	-	1.36	3.09	4.99	8.41	-	-	1.31	2.94

Table A-5- 3. EDX results of the elements observed on pristine and immersed Mo foil in AlCl₃-based E.

element	Mo foil									
	pristine		24 h		48 h		1 W		1 M	
	WT	AT	WT	AT	WT	AT	WT	AT	WT	AT
Ti	89.94	59.86	65.76	25.84	79.38	39.67	68.42	26.90	49.14	14.52
C	10.05	40.13	10.62	25.03	4.08	12.24	7.34	17.31	12.00	21.28
O	-	-	8.24	25.87	7.12	28.45	10.29	32.32	14.68	34.67
Cl	-	-	8.21	8.74	4.63	6.26	6.37	6.78	11.89	9.51
Al	-	-	3.66	5.12	1.81	3.22	2.83	3.96	4.99	5.25
N	-	-	3.47	9.36	2.96	10.14	4.71	12.70	7.28	14.74

Table A-5- 4. EDX results of the elements observed on pristine and immersed W foil in AlCl₃-based E

element	W foil									
	pristine		24 h		48 h		1 W		1 M	
	WT	AT	WT	AT	WT	AT	WT	AT	WT	AT
W	88.74	33.98	98.61	86.09	87.89	32.64	83.77	31.02	75.47	22.24

C	11.25	66.01	-	-	11.07	62.95	6.10	34.60	8.46	38.19
O	-	-	1.38	13.90	1.04	4.42	3.75	15.97	4.47	15.16
Cl	-	-	-	-	-	-	2.84	5.47	8.71	13.31
Al	-	-	-	-	-	-	1.78	4.49	-	-
N	-	-	-	-	-	-	1.73	8.41	2.86	11.09

Table A-5- 5. EDX results of the elements observed on pristine and immersed Ta foil in AlCl₃-based E

element	Ta foil									
	pristine		24 h		48 h		1 W		1 M	
	WT	AT	WT	AT	WT	AT	WT	AT	WT	AT
W	85.31	28.70	83.80	26.37	82.86	25.40	82.02	24.00	82.42	25.00
C	12.18	61.76	13.53	64.15	13.74	63.48	15.01	66.18	13.66	62.45
O	2.50	9.52	2.66	9.46	2.92	10.15	2.96	9.80	3.44	11.81
Cl	-	-	-	-	-	-	-	-	0.46	0.72
Al	-	-	-	-	0.46	0.94	-	-	-	-

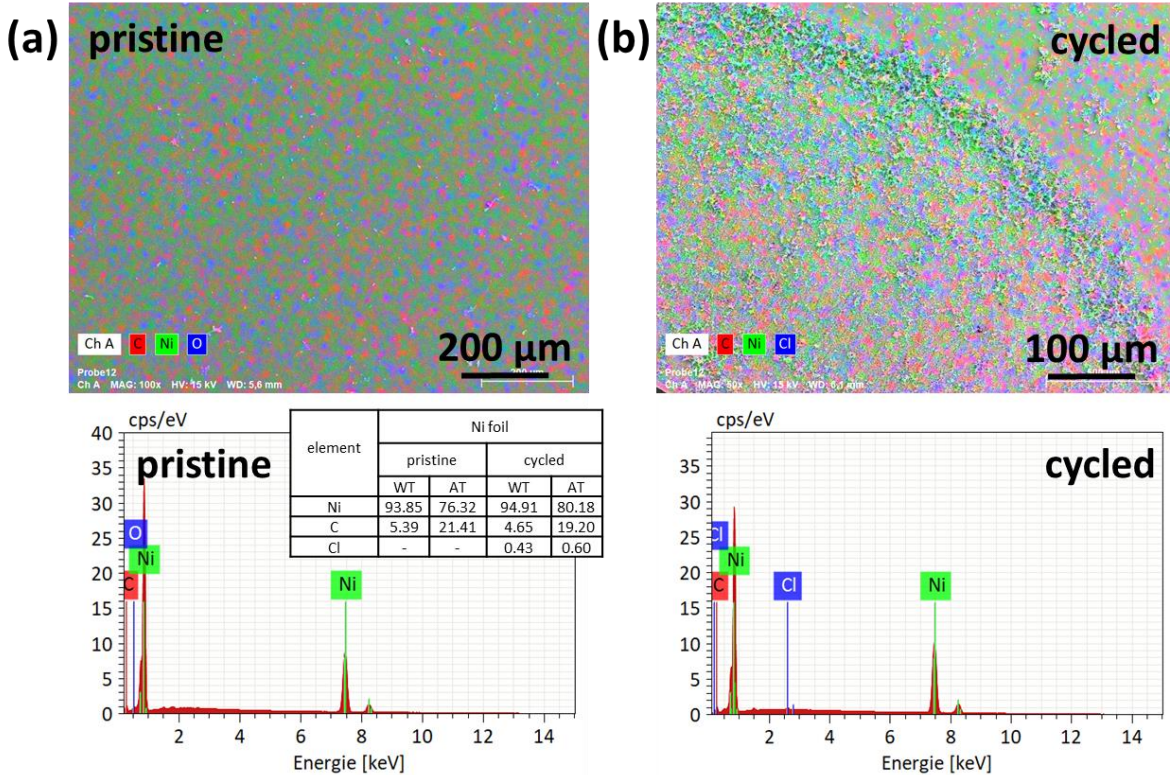


Figure A-5- 1. EDX image, spectra of the observed elements on pristine and cycled Ni CC in AlCl₃-based E.

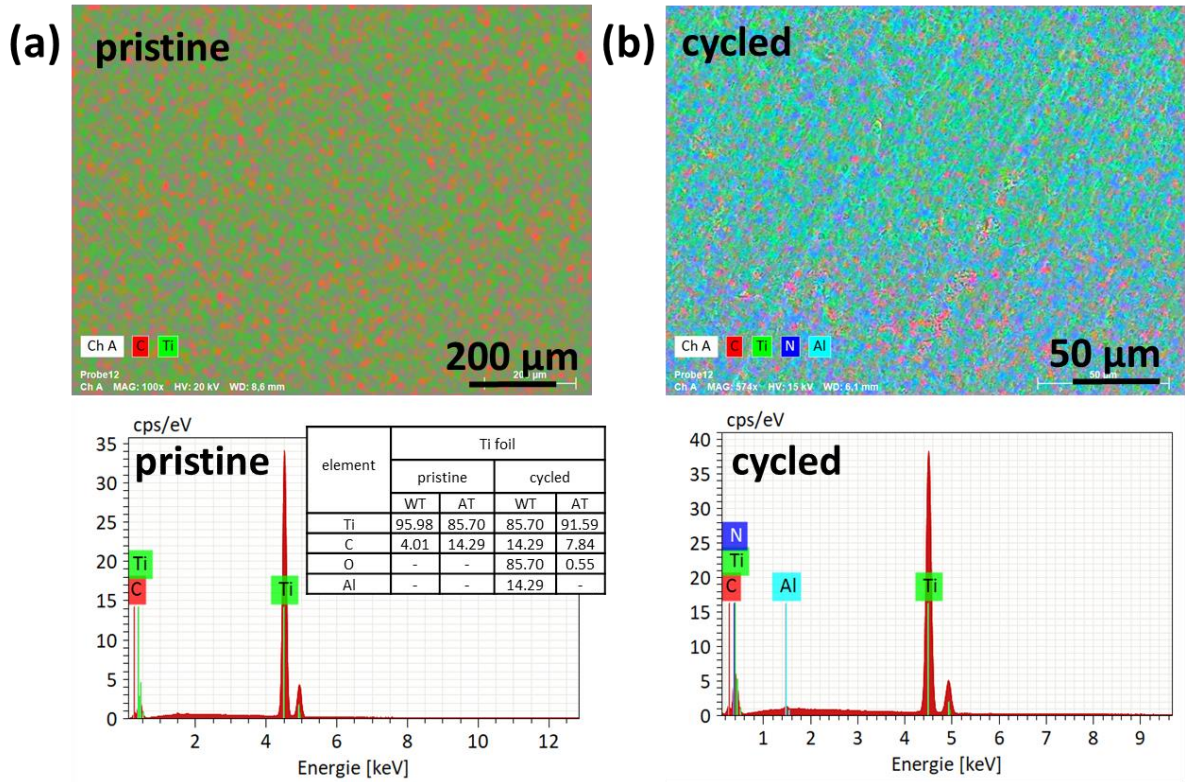


Figure A-5- 2. EDX image, spectra of the observed cycled elements on pristine and cycled Ti CC in AlCl_3 -based E.

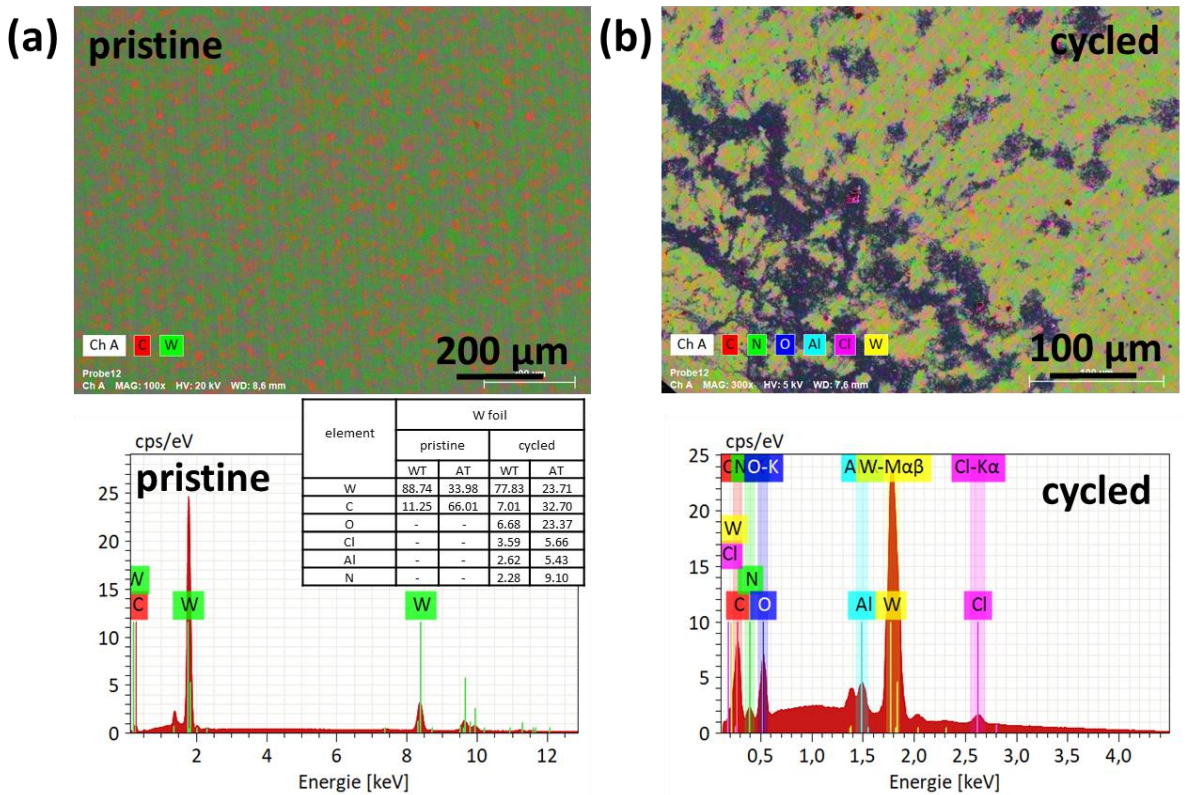


Figure A-5- 3. EDX image, spectra of the observed cycled elements on pristine and cycled W CC in AlCl_3 -based E.

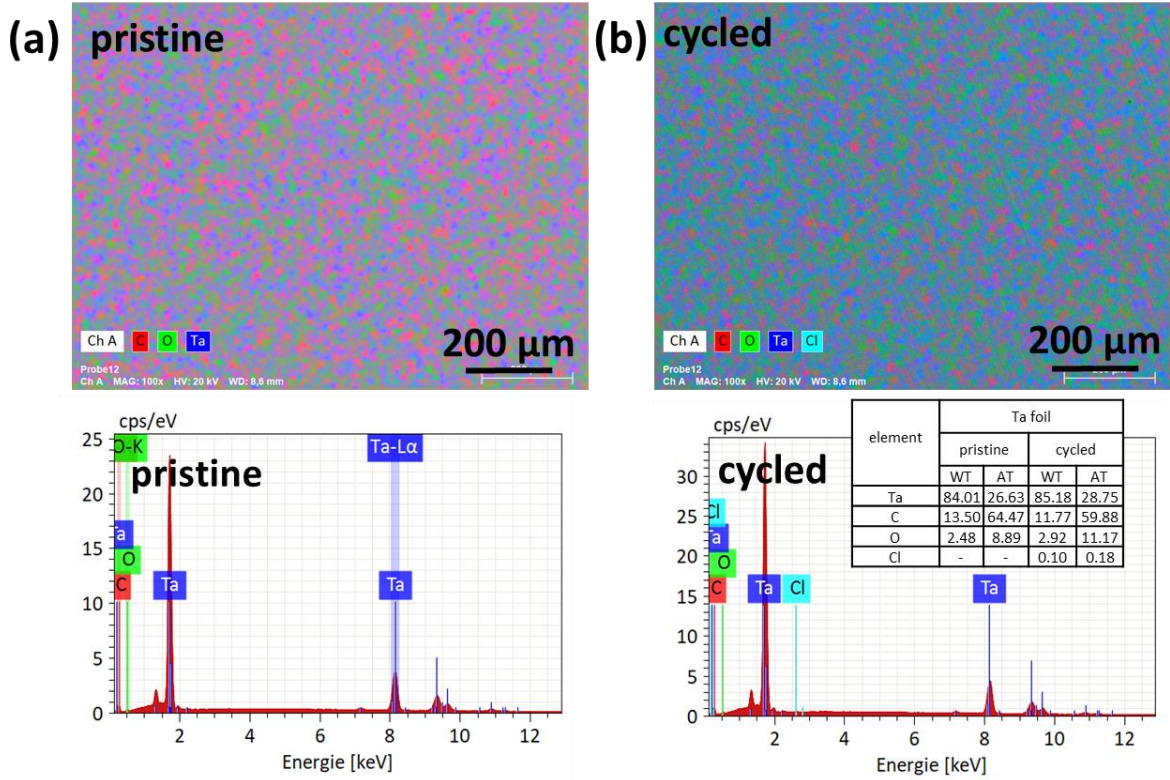


Figure A-5- 4. EDX image, spectra of the observed elements on pristine and cycled Ta CC in AlCl_3 -based E.

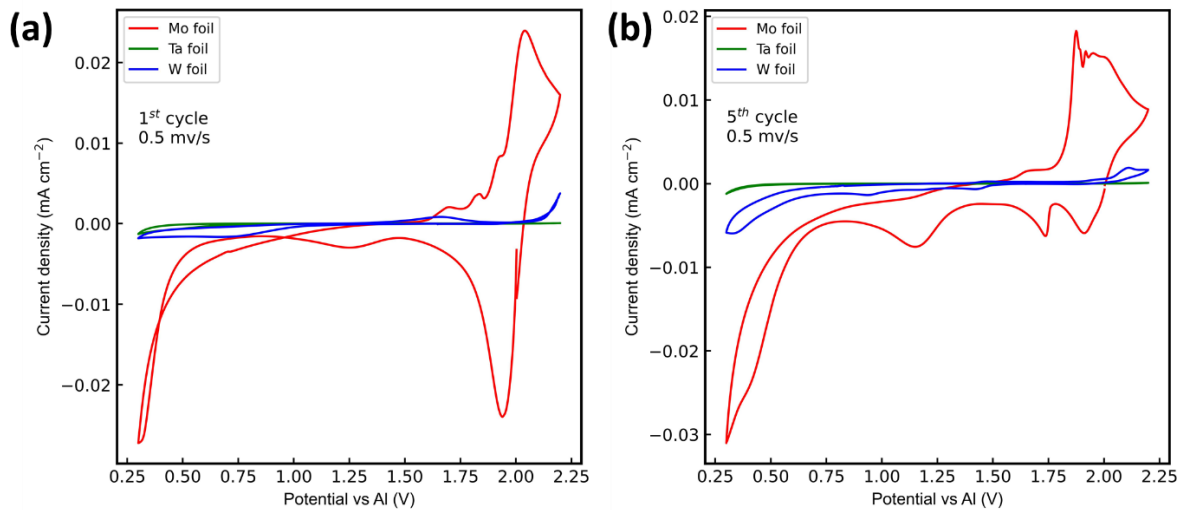


Figure A-5- 5. Recorded CVs' comparison in AlCl_3 -based ILE on Mo, Ta, W CCs (a) 1st cycle (b) 5th cycle.

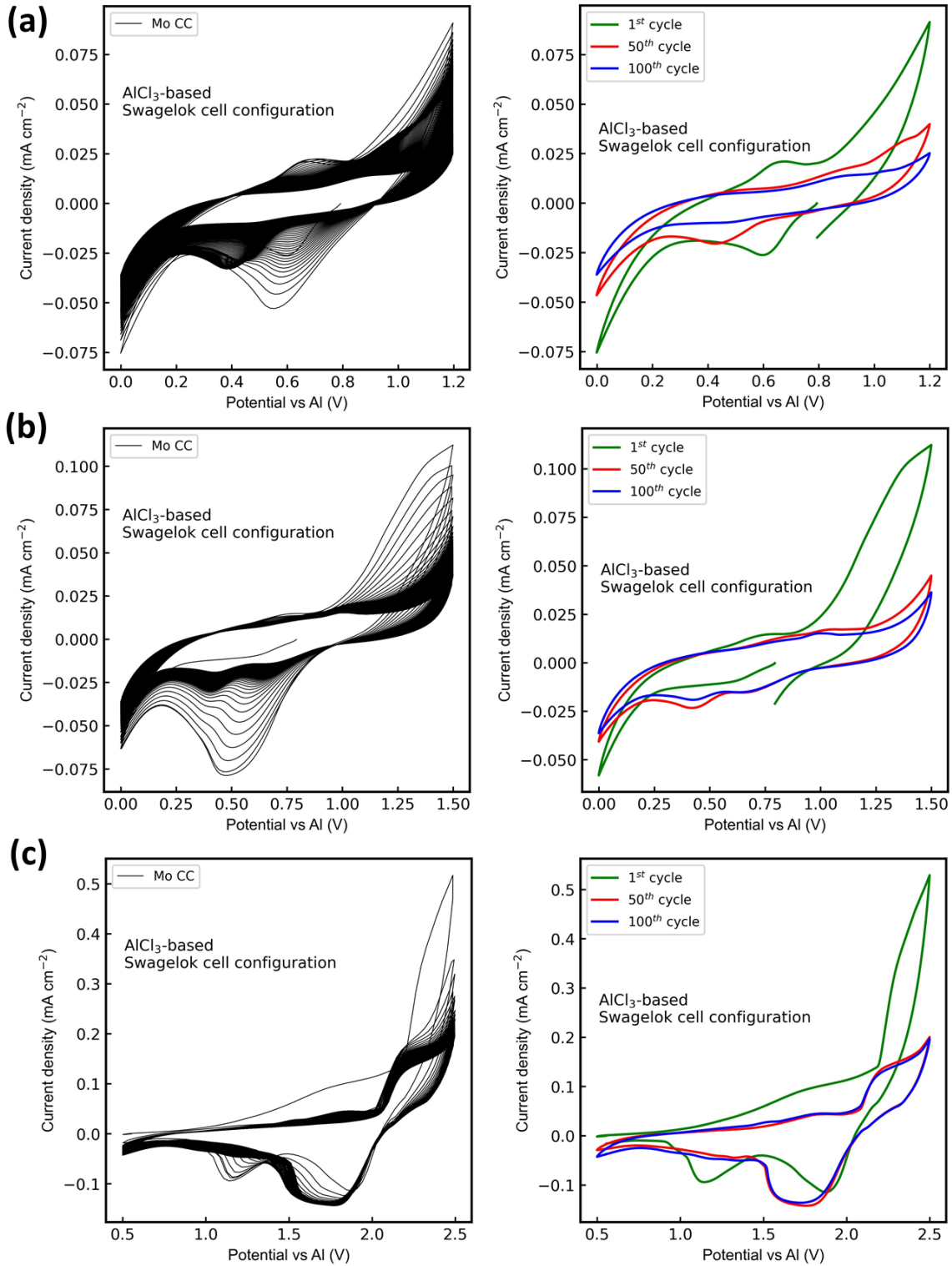


Figure A-5- 6. Recorded CVs' comparison in AlCl₃-based ILE on Mo foils on Mo rods in Swagelok cell setups.